

DEFECT CHEMISTRY AND PHOTO-IONIC EFFECTS IN  
BROMIDE AND IODIDE PEROVSKITES

Von der Fakultät Chemie der Universität Stuttgart  
zur Erlangung der Würde eines Doktors der  
Naturwissenschaften (Dr. rer. nat.)  
genehmigte Abhandlung

vorgelegt von

**YARU WANG (Ya-Ru Wang)**

aus Hebei, China

Hauptberichter: Prof. Dr. Joachim Maier

Mitberichter: Prof. Dr. Thomas Schleid

Prüfungsvorsitzender: Prof. Dr. Joris van Slageren

Tag der Einreichung: 22.05.2023

Tag der mündlichen Prüfung: 26.07.2023

Physikalische Festkörperchemie  
Max-Planck Institut für Festkörperforschung  
Stuttgart, 2023

苟于行之不迷 虽颠沛何其伤

-韩愈

## **Erklärung über die Eigenständigkeit der Dissertation**

Ich versichere, dass ich die vorliegende Arbeit mit dem Titel

“Defektchemie und Photoionische Effekte in Bromid- und Iodidperowskiten”

selbständig verfasst und keine anderen als die angegebenen Quellen und Hilfsmittel benutzt habe; aus fremden Quellen entnommene Passagen und Gedanken sind als solche kenntlich gemacht.

## **Declaration of Authorship**

I hereby certify that the dissertation entitled

“Defect Chemistry and Photo-ionic Effects in Bromide and Iodide Perovskites”

is entirely my own work except where otherwise indicated. Passages and ideas from other sources have been clearly indicated.

Name/Name: Ya-Ru Wang

Unterschrift/Signed:

Datum/Date:





## Acknowledgments

This journey of working as a Ph.D. student in Max Planck Institute in Solid State Research is such a rewarding and enjoyable experience for me. A very important part of it are those people who had accompanied me through all these years. I would like to express my greatest gratitude to all of you.

I would like to thank Prof. Joachim Maier for welcoming me to his group. I appreciate it so much for the insightful discussions, great support and the freedom for me to explore. In addition, I am grateful for the very friendly and international group atmosphere that you had created, which made me feeling as home, especially at the difficult COVID time.

Many thanks to my daily supervisor Dr. Davide Moia for being always supportive and helpful. Thank you for the continuous effort on listening to and trusting on me, without which I cannot go so far. Thank you also for a lot of training and mentorship, those are the very precious experiences and memories that I will value a lot.

A lot of thanks to Dr. Alessandro Senocrate and Dr. Gee Yeong Kim, who I had worked with at the early stage of my PhD. Thank you Ale for always being inspiring and helpful, showing me around in the lab, brainstorming a lot, missing a lot on your contagious laughs. Thank you Gee Yeong for a lot of insightful discussions and collaborative work together. I enjoyed so much working and sharing life with you.

Many thanks to Prof. Michael Grätzel and Prof. Jovana V. Milic for their continuous support and fruitful collaborations on this project. I'm also grateful to Prof. Ursula Röthlisberger and Dr. Marko Mladenovic on the collaborative work on theoretical calculations.

I'm also grateful and indebted to Prof. Bettina Lotsch. Thank you also being a great role model to me. Special thanks for taking the time to talk to me and support me to take the next step of my research.

I owe great thanks to the people who work in nanostructuring lab in MPI-FKF. I would like to thank the head of the lab Jürgen Weis for his commitment on being my external supervisor of my Ph.D. committee and his great and continuous support on my research project. Especially I would like to express the greatest thanks to Bernhard Fenk and Ulrike Waizmann. To Bernhard Fenk: It's always been so much fun and excitement to work with you. Your passion and expertise on the work had inspired me so much. We joked around with Ulli that you are the "nano-master", but I mean it. To Ulrike Waizmann: thank you so much for your dedication to this project, hope that halide perovskites will not appear in your dream anymore. I'm also grateful to Achim Güth for making electrode, Thomas Reindl for training me to use SEM, Marion Hagel for some test on ALD growth.

I'm deeply grateful to the people who I work with in StEM group. To head of the group Peter van Aken: thank you for your support on my project. To Kersten Hahn: thank you so

much for your dedication to the project and your saying about “let’s check our calendar”. To Wilfried Sigle, thank you for always being available for me to ask questions and always asking how is it going when you encounter me in the computer room. To Peter Kopold: thank you for the assistance of the TEM measurements. To Vesna Srot, thank you for training me using the Plasma cleaning instrument in the group.

Special thanks goes to Florian Kaiser for helping me building home-made measurements cells, set ups. I had learnt so much with you on technical stuff. A lot of thanks to Dr. Rotraut Merkle for always being available for any help or support whenever is needed. It truly astounds me how you manage it for everyone. Many thanks to Udo Klock for electronics und auch für Ihre ständige Ermutigung, sich auf Deutsch zu unterhalten. To Uwe Traub, thanks a lot for your support on IT stuff and always updating me some news in Germany. To Armin Sorg and Helga Hoier, thank you so much for help on the numerous XRD measurements during these years. To Dr. Klaus-Dieter Kreuer, thank you for taking the time for reviewing the Zusammenfassung of this thesis, loved a lot for the yearly “Waldmeister” event. Thanks to Prof. Eugene Kotomin for a lot of stimulating discussions and the greetings on Chinese new year almost every year. Thanks to Dr. Igor Moudrakovski, who I had some discussion on NMR. Thanks Armin Schulz for Raman measurements on looking for vibration modes may or may not exist.

Sincerely many thanks go to our secretaries, Madeleine Burkhardt and Sofia Weiglein, who had done tremendous support on the administrative stuff behind the scene. I’m also grateful for Birgit King, who had done a lot of work for my residency in Germany. Special thank also to your kind heart when I’m dealing with housing issues. Furthermore, I would like to thank Dr. Hans-Georg Libuda for his kind help in the IMPRS-CMS program, meeting you in Shanghai and getting to know this program has made my life change in another direction, in a good way. Special thanks to Eva Benckiser, for her kind help in the IMPRS-CMS program and mentor program.

Many thanks to my fellow students and scientists who I shared a lot of same values and experiences with, making my time in MPI extremely joyful. To Mina Jung, thank you very much for sharing and talking both work and life related stuff with me. I like so much of the resonation between us. To Chulian Xiao, I enjoyed so much being as xiaoshimei of you, enjoyed a lot talking with you. To Dr. Algirdas Dučinskas, sharing perspective on books is so much fun! I also like us always on the same page of “5km? Let’s walk home”. To Dr. Yuanye Huang and Dr. Markus Joos, thanks for a lot of activities and laughs together. To Dr. Giulia Raimondi, Sicily is definitely one of the most beautiful place. To Dr. Torben Saatkamp, I like so much of your contagious smile and kind heart, thank you for helping me through some difficult time. To Dr. Andreas Münchinger, thank you for sharing experiences and thoughts

with me. To Dr. Maximilian Hödl, thank you for taking my ‘red face’ pictures in Frühlingsfest 2019 and some laughs. To Dr. Christian Berger, thanks for always being kind to me. To Dr. Dr. Yue Zhu, I liked our talk when encountering in the lab in late evenings. To Dr. Chuanhai Gan and Liyu shi, thanks a lot for inviting me for a lot of delicious food which made me feeling like home. To Dr. Kyungmi Lim, I liked our after-lunch walk and talk. To Dr. Xiaolan Kang, we need to hike together on Alps. To Prof. Jelena Popovic-Neuber, thanks for sharing your opinions and thoughts with me.

To some other friends I met in and out of MPI, who had accompanied me and provided a lot of support. To Liwen Feng, thank you for being around almost my whole period of my PhD, I like your attitude of let’s do it now. To Yu-Jung Wu, so much surprise for the gifts that you brought to me, thanks for always being so sweet to me. To Gabriele Domaine, I enjoyed so much having photography activities with you. To Niklas Windbacher, thank you for a lot of talks and support and the shared laughs. To Dr. Giniyat Khaliullin, thanks for continuous invitation to play table tennis, that made my life much healthier. To Yuanshan Zhang, thanks for being a nice football coach to me. Büsnau Baozi restaurant is a solid idea. To Jihuan Gu, thanks for some shared activities with you. To Prof. Feixiang Wu, the mental picture of you looking back and smiling in Christmas Market 2018 feels like yesterday. To Dr. Qing yu He, I will never forget the email that you replied to me. To Prof. Laifa shen, being a shimei of you is such a joy, thank you for helping me looking for apartments in Germany. To the friends that I met in IS institute: Fan Wang, Dr. Zhen Yin, Dr. Wenbin Kang, Dr. Minchao Zhang and Xianglong Lyu, enjoyed the Friday dinner and supermarket shopping with you.

Many thanks to Prof. Thomas Schleid and Prof. Joris van Slageren for their commitment to be my thesis committee members and to read this thesis.

Lastly, I would like to express my heartfelt gratitude to my parents, my brother for being always supportive and proud of me. Your unconditional love for me has made me being courageous to explore and to adventure. Love you as always.

Stuttgart, May 18<sup>th</sup>, 2023

Ya-Ru Wang (王亚茹)



## Abstract

Bromide and iodide perovskites, especially their mixtures, hold great potential for optoelectronic application due to their optical absorption properties in the visible range. While it is established that these materials are mixed ionic-electronic conductors, their ionic transport properties both in the dark and under light are poorly understood. The present work deals with the defect chemistry and photo-ionic effects in halide perovskites, including iodide and bromide perovskites with special focus on the photo induced phase separation (photo de-mixing) in mixed bromide - iodide perovskites.

The first part covers the defect chemical study of bromide perovskites, including 3D MAPbBr<sub>3</sub> and 2D Dion-Jacobson (PDMA)PbBr<sub>4</sub>. The results reveal that both 3D MAPbBr<sub>3</sub> and 2D (PDMA)PbBr<sub>4</sub> are mixed ionic-electronic conductors. 2D (PDMA)PbBr<sub>4</sub> show three orders of magnitude lower ionic conductivity compared with 3D MAPbBr<sub>3</sub>. This implies that dimensionality reduction is an effective strategy for reducing ion migration in these systems. From a bromine partial pressure dependent study, it is concluded that MAPbBr<sub>3</sub> and 2D(PDMA)PbBr<sub>4</sub> are both P-type conductor and that the surface reaction is the limiting process for the incorporation and exorption of the Br<sub>2</sub> gas. A non-monotonic dependence of the electronic conductivity on bromine partial pressure is detected for both 2D and 3D bromide perovskites. It can be attributed to the reversible formation and dissociation of AuBr<sub>x</sub> on the gold electrode and perovskites interface.

The second part covers the investigation of the thermodynamic properties of the 2D mixed halide perovskites under light. It has been shown that light can be used as a knob for inducing photo de-mixing from single phase 2D mixed halide perovskites to I-rich and Br-rich phases. In the dark, the photo de-mixed phases re-mix with complete reversibility of both their optical and structural properties, demonstrating the full miscibility of mixed bromide-iodide perovskites in the dark. The temperature-dependence of absorption spectra for the photo de-mixed phases gave clear evidence for a miscibility gap under light, from which photo de-mixed phases' compositions are extracted. The photo-miscibility-gap is mapped and confirmed by various methods. The shape of the photo-miscibility-gap shows limited variation in the 0.01 – 0.1 sun illumination intensity range. The non-encapsulation of surface, however, demonstrated a widening of the photo-miscibility gap.

The third part covers the kinetic analysis and mechanistic investigation of photo de-mixing in 2D mixed halide perovskites. Simultaneous monitoring of the electrical conductivity and optical absorption allows for a local probe of electronic and ionic charge carriers, and the composition evolution. Furthermore, time dependent phase distribution is investigated with the aid of top view SEM, showing that I-rich nanodomains forming along the grain boundaries at early times after light exposure with further formation of such domains also within the grain

at longer times. Local elementary distribution is probed with TEM. From the temperature dependent de-mixing half-time, an activation energy for photo de-mixing of 0.39 eV is obtained. Finally, together with DFT calculation on defect formation energy of the mixture of different defect type, a mechanistic description for photo de-mixing, both from molecular and microscopic level is proposed.

The last part deal with the phase stability study of mixed halide perovskites in other dimensionalities, including 3D and nanocrystal based thin films. 3D mixed halide perovskites show that similar to 2D mixed halide perovskites, photo de-mixing occur in two stage. Different from the full reversibility of 2D, photo degradation of 3D perovskites into  $\text{PbI}_2$  in the dark over long time scales is observed. The nanocrystalline mixed halide perovskite ( $\text{BA-MAPb}(\text{I}_{0.5}\text{Br}_{0.5})_3$ ) thin films show no de-mixing in contrast to 2D and 3D under same measurement conditions. Nanocrystals mixtures show superior phase stability under the same illumination condition, with neither degradation nor de-mixing.

This thesis contributes to the understanding of the defect chemistry and ion transport properties of bromide and iodide perovskites, with specific focus on photo de-mixing in mixed halide perovskites. These findings will aid compositional engineering related to halide mixtures to enable optimization of optoelectronic devices as well as the development of other emerging systems exploiting photo-ionic effects.

## Zusammenfassung

Bromid- und Iodidperowskite, insbesondere ihre Mischungen, bergen aufgrund ihrer optischen Absorptionseigenschaften im sichtbaren Spektrum großes Potenzial für optoelektronische Anwendungen. Es steht zwar fest, dass diese Materialien gemischt ionisch-elektronische Leiter sind, jedoch sind ihre Ionentransporteigenschaften sowohl im Dunkeln als auch bei Licht nur unzureichend bekannt. Die vorliegende Arbeit befasst sich mit der Defektchemie und den photoionischen Effekten in Halogenidperowskiten, einschließlich Iodid- und Bromidperowskiten, mit besonderem Schwerpunkt auf der photoinduzierten Phasentrennung (Photoentmischung) in gemischten Bromid-Iodid-Perowskiten.

Der erste Teil behandelt die defektchemische Untersuchung von Bromidperowskiten, einschließlich 3D MAPbBr<sub>3</sub> und 2D Dion-Jacobson (PDMA)PbBr<sub>4</sub>. Die Ergebnisse zeigen, dass sowohl 3D MAPbBr<sub>3</sub> als auch 2D (PDMA)PbBr<sub>4</sub> Mischleiter sind. 2D (PDMA)PbBr<sub>4</sub> zeigt eine um drei Größenordnungen geringere Ionenleitfähigkeit im Vergleich zu 3D MAPbBr<sub>3</sub>. Dies deutet darauf hin, dass die Reduzierung der Dimension eine wirksame Strategie zur Verringerung der Ionenwanderung in diesen Systemen ist. Aus einer Brom-Partialdruck abhängigen Studie wird gefolgert, dass MAPbBr<sub>3</sub> und 2D(PDMA)PbBr<sub>4</sub> beide P-Leiter sind und dass die Oberflächenreaktion der einschränkende Prozess für den Ein- und Austritt des Br<sub>2</sub>-Gases ist. Sowohl für 2D- als auch für 3D-Bromidperowskite wird eine nicht-monotone Abhängigkeit der elektronischen Leitfähigkeit vom Brom-Partialdruck festgestellt. Sie lässt sich auf die reversible Bildung und Dissoziation von AuBr<sub>x</sub> an der Grenzfläche zwischen Goldelektrode und Perowskiten zurückführen.

Der zweite Teil befasst sich mit der Untersuchung der thermodynamischen Eigenschaften der 2D-Mischhalogenidperowskite unter Lichteinwirkung. Es konnte gezeigt werden, dass Licht als Mittel zur Einleitung der Photoentmischung von einphasigen 2D-Mischhalogenidperowskiten zu I-reichen und Br-reichen Phasen verwendet werden kann. In der Dunkelheit vermischen sich die durch Licht entmischten Phasen wieder mit vollständiger Reversibilität ihrer optischen und strukturellen Eigenschaften, was die vollständige Mischbarkeit von gemischten Bromid-Iodid-Perowskiten in der Dunkelheit zeigt. Die Temperaturabhängigkeit der Absorptionsspektren für die photoentmischten Phasen lieferte eindeutige Hinweise auf eine Mischungslücke unter Licht, aus der die Zusammensetzung der photoentmischten Phasen abgeleitet werden kann. Die Fotomischbarkeitslücke wird mit verschiedenen Methoden kartiert und bestätigt. Die Form dieser Lücke zeigt wenig Veränderung im Bereich der Beleuchtungsintensität von 0,01 bis 0,1 Strahlungsleistungen der Sonne. Die Nichtverkapselung der Oberfläche führte jedoch zu einer Vergrößerung der Fotomischbarkeitslücke.

Der dritte Teil befasst sich mit der kinetischen Analyse und der mechanistischen Untersuchung der Photoentmischung in 2D-Perowskiten mit gemischten Halogeniden. Die gleichzeitige Überwachung der elektrischen Leitfähigkeit und der optischen Absorption ermöglicht eine lokale Untersuchung der elektronischen und ionischen Ladungsträger sowie der Entwicklung der Zusammensetzung. Darüber hinaus wird die zeitabhängige Phasenverteilung mit Hilfe von REM-Aufnahmen untersucht, die zeigen, dass sich I-reiche Nanodomänen entlang der Korngrenzen zu frühen Zeiten nach der Lichtexposition bilden, wobei sich solche Domänen nach längerer Zeit auch innerhalb des Korns bilden. Die lokale Elementarverteilung wird mit TEM untersucht. Aus der temperaturabhängigen Halbwertszeit der Entmischung ergibt sich eine Aktivierungsenergie für die Photoentmischung von 0,39 eV. Zusammen mit DFT-Berechnungen zur Defektbildungsenergie der Mischung verschiedener Defekttypen, wird schließlich eine mechanistische Beschreibung der Photoentmischung sowohl auf molekularer als auch auf mikroskopischer Ebene vorgestellt.

Der letzte Teil befasst sich mit der Untersuchung der Phasenstabilität von gemischten Halogenidperowskiten in anderen Dimensionen, einschließlich 3D- und nanokristallbasierten Dünnschichten. 3D-Perowskite mit gemischten Halogeniden zeigen, dass ähnlich wie bei 2D-Perowskiten mit gemischten Halogeniden eine Entmischung in zwei Phasen stattfindet. Im Gegensatz zur vollständigen Reversibilität der 2D-Perowskite wird bei den 3D-Perowskiten im Dunkeln über lange Zeiträume ein Photoabbau zu  $\text{PbI}_2$  beobachtet. Die nanokristallinen Mischhalogenid-Perowskite ( $\text{BA-MAPb}(\text{I}_{0,5}\text{Br}_{0,5})_3$ ) zeigen im Gegensatz zu 2D und 3D unter gleichen Messbedingungen keine Entmischung. Nanokristallmischungen zeigen unter den gleichen Beleuchtungsbedingungen eine bessere Phasenstabilität, ohne dass es zu einer Degradation oder Entmischung kommt.

Diese Arbeit trägt zum Verständnis der Defektchemie und der Ionentransporteigenschaften von Bromid- und Iodidperowskiten bei, wobei der Schwerpunkt auf der Photoentmischung in gemischten Halogenidperowskiten liegt. Diese Erkenntnisse werden bei der Zusammensetzungsentwicklung im Zusammenhang mit Halogenidmischungen helfen, um die Optimierung optoelektronischer Bauelemente sowie die Entwicklung anderer neuer Systeme zu ermöglichen, die opto-ionische Effekte nutzen.



# Contents

Acknowledgments .....	iii
Abstract .....	vii
Zusammenfassung .....	ix
Contents .....	xi
I INTRODUCTORY REMARKS .....	13
1 Introduction .....	1
1.1 Motivation .....	1
1.2 Thesis outline .....	1
II STATE OF RESEARCH .....	3
2.1 Halide perovskites and their application .....	5
2.1.1 Dimensionality engineering .....	6
2.1.2 Halide engineering and mixed halide perovskites .....	7
2.2 Defect chemistry and ion transport in halide perovskites .....	8
2.3 Photo induced ionic effects in halide perovskites .....	9
2.4 De-mixing and photo de-mixing .....	10
2.4.1 Experimental signature of photo de-mixing .....	11
2.4.2 Photo de-mixing and device performance .....	12
2.4.3 Mitigation strategies .....	13
2.4.4 Photo de-mixing models .....	15
2.4.5 Open questions .....	18
III THEORETICAL FRAMEWORK .....	21
3.1 Mixture thermodynamics .....	23
IV MATERIALS AND METHODS .....	27
4 Materials and methods .....	29
4.1 Materials and synthesis .....	29
4.2 Experimental apparatus and techniques .....	30
4.3 Evaluation of the partial conductivities .....	35
V RESULTS AND DISCUSSIONS .....	37
5 Defect chemistry equilibria in bromide and iodide perovskites .....	39
5.1 Introduction .....	39
5.2 Results and discussion .....	40
5.3 Conclusion .....	50
6 Photo de-mixing in 2D mixed halide perovskites: thermodynamics .....	51

6.1 Introduction.....	51
6.2 Results and discussion .....	52
6.3 Conclusion .....	61
7 Photo de-mixing in 2D mixed halide perovskites: kinetics and mechanism .....	63
7.1 Introduction.....	63
7.2 Results and discussion.....	64
7.4 Conclusion .....	77
8 Photo de-mixing in mixed halide perovskites: 3D and nanocrystals .....	79
8.1 Introduction.....	79
8.2 Results and discussion.....	79
8.3 Conclusion .....	87
9 Photo de-mixing in mixed halide perovskites: mechanism.....	89
9.1 Introductory remarks.....	89
9.2 Evaluating the energetics of photo-ionic effects in mixed halide perovskites	90
VI CONCLUSIONS.....	97
10 Concluding remarks .....	99
VII APPENDIX .....	103
A Supporting Material.....	105
A.1 supporting material for Chapter 5.....	105
A.2 supporting material for Chapter 6.....	111
A.3 supporting material for Chapter 7.....	123
A.4 supporting material for Chapter 8.....	135
B Bibliography.....	137
C Curriculum Vitae .....	149

# I INTRODUCTORY REMARKS



## 1 Introduction

### 1.1 Motivation

Organic-inorganic hybrid halide perovskites are regarded as promising light absorbers for a wide range of photovoltaic applications owing to their low cost and easy processibility.<sup>1-3</sup> However, these materials are susceptible to external stimuli, such as humidity, light, and heat, which limits their long-term stability. This remains to be one of the pressing concerns for the future utilization of these photovoltaic materials.<sup>4-7</sup> Unlike traditional semiconductors which conduct electrons and holes only, this class of materials belongs to the category of mixed ionic-electronic conductors with both electron and ion conduction intrinsically involved. In addition, under light, MAPbI<sub>3</sub> (an archetype of halide perovskites) showed huge enhancement in the ionic conductivity.<sup>8</sup> Such photo enhanced ion transport is linked to degradation, influencing long-term stability.<sup>9, 10</sup> It is therefore critical to better understand these materials and the photo-enhanced ionic transport in order to improve their stability and expand their potential. In addition to its application importance, this novel phenomenon of ion transport out of equilibrium is of great interest fundamentally, from both a molecular and microscopic perspective. Another striking example a photo-induced ionic process is the photo-induced phase separation occurring in mixed halide perovskites.<sup>11, 12</sup> This process concerns the change in miscibility of perovskites with two different halides on application of light. Several steps are expected to give rise to this photo induced separation, including photo-induced defect formation, ionic defects transport, and phase transformation. As such, it constitutes a complex problem to unravel as well as a convenient model phenomenon for investigating photo-ionic effects and defect behavior under light.

### 1.2 Thesis outline

The present work deals with the defect chemistry and photo-ionic effects in halide perovskites, specifically in iodide and bromide perovskites, with special focus on the photo-induced phase separation (photo de-mixing) occurring in mixed bromide-iodide perovskites. The thesis has the following structure: the introductory sections summarize the state of research that is related to defect chemistry and photo-ionic effects in iodide and bromide perovskites (Part II, chapter 2) and the theoretical framework of mixture thermodynamics (Part III, chapter 3). Part IV (chapter 4) summarizes the materials and methods as well as the experimental apparatus and measurement techniques.

The results and discussion chapters are presented in Part V:

Chapter 5 covers the defect chemical study of bromide perovskites. Specifically, methylammonium lead bromide (MAPbBr<sub>3</sub>) and 2D Dion-Jacobson 1,4-phenylenedimethan ammonium lead bromide ((PDMA)PbBr<sub>4</sub>) are investigated. Their mixed

conducting properties are measured as a function of varying stoichiometry (controlled via a fixed bromine partial pressure) and temperature. Their properties are discussed in relation to previously investigated iodide perovskites (3D methylammonium lead iodide (MAPbI<sub>3</sub>) and 2D Dion-Jacobson 1,4-phenylenedimethan ammonium lead iodide (PDMA)PbI<sub>4</sub>). Furthermore, this study highlights the range of the bromine partial pressure in which reversible behavior of the bromide perovskites is observed.

Chapter 6 covers the investigation of the phase stability, reversibility and the thermodynamic properties of the 2D Dion-Jacobson mixed halide perovskites ((PDMA)Pb(I<sub>0.5</sub>Br<sub>0.5</sub>)<sub>4</sub>) under light. Temperature dependent absorption measurements are used to identify the photo de-mixed compositions and the photo-miscibility-gap of the mixture. Various experimental methods are developed and compared. Lastly, the effect of encapsulation and light intensity on the shape of the photo-miscibility-gap are also investigated.

Chapter 7 covers the kinetic analysis and mechanistic investigation of photo de-mixing in 2D mixed halide perovskites, by analyzing the time dependent in-situ optical absorption and conductivity changes during illumination. The effect of surface encapsulation is discussed. Furthermore, SEM and TEM are utilized to investigate the morphological changes and the nature of the iodide rich and bromide rich phases resulting from phase segregation. Finally, a mechanistic description for photo de-mixing is proposed.

Chapter 8 covers the investigation on photo de-mixing in mixed bromide-iodide perovskites with different dimensionality: 3D (MAPb(I<sub>0.5</sub>Br<sub>0.5</sub>)<sub>3</sub>) and nanocrystals (BA-MAPb(I<sub>0.5</sub>Br<sub>0.5</sub>)<sub>3</sub>). Their phase properties under light were investigated by optical absorption and XRD. The simultaneous measurements of conductivities are discussed in terms of understanding the electronic and ionic charge carriers' properties during photo de-mixing and dark-remixing.

Chapter 9 covers the mechanism and driving force of photo de-mixing. In particular, various energetic contributions have been considered to drive photo de-mixing in mixed halide perovskites.

Finally, the thesis ends with conclusions (Part VI, chapter 10) and the appendix section (VII).

This thesis contributes to the understanding of the defect chemistry and ion transport properties of bromide and iodide perovskites, with specific focus on photo de-mixing in mixed halide perovskites. These findings will aid compositional engineering related to halide mixtures to enable optimization of optoelectronic devices as well as the development of other emerging systems exploiting photo-ionic effects.

## II STATE OF RESEARCH





## 2.1 Halide perovskites and their application

The term “Perovskite” was named after the Russian scientist Lev A. Perovski by Gustav Rose,<sup>13</sup> who discovered first the perovskite mineral calcium titanate  $\text{CaTiO}_3$  in 1839. Since then, a variety of oxide perovskites  $\text{ABO}_3$  were discovered and investigated, stimulating the technological development of sensors, fuel cells, etc.<sup>14-17</sup> Halide perovskites, with halogen anion instead of oxygen, exhibit the same crystallographic structure. They have the general formula  $\text{ABX}_3$  where  $\text{BX}_6$  halide octahedra form a corner sharing network and A site cations sit in the cavities formed by 12 nearest neighboring X atoms ( $\text{X} = \text{I}, \text{Br}, \text{Cl}$ ) (**Figure 2.1**). The first successful validation of the crystallization of halide perovskites ( $\text{CsPbX}_3$ ,  $\text{X} = \text{I}, \text{Br}, \text{Cl}$ ) was reported by Wells and his collaborators in 1893.<sup>18</sup> In 1978, D. Weber<sup>19</sup> further successfully replaced A site cation  $\text{Cs}^+$  with organic ( $\text{A} = \text{MA}^+$ , methylammonium ion), opening the era of the organic-inorganic hybrid halide perovskites.

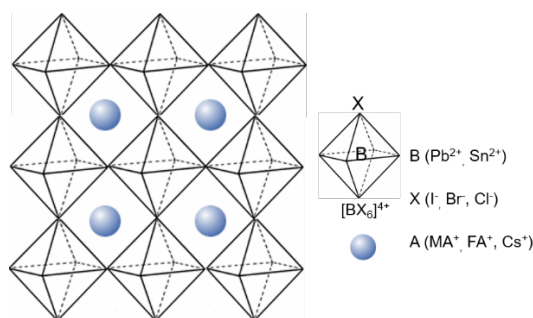


**Figure 2.1.** 3D halide perovskites structure

T. Miyasaka *et al.* were the first to apply these material as “sensitizers” in dye - sensitized photo-electrochemical cells and developed a device with 3.8% solar energy conversion efficiency.<sup>20</sup> After this demonstration, the efficiency of solar cell using halide perovskites as photo-absorbers underwent a significant increase. During the last decade, extensive research in this field led to a record efficiency of 25.7%<sup>21</sup> in 2022. Several strategies have been used to increase the power conversion efficiency (PCE) of halide perovskite based solar cells. These include altering the intrinsic optical and electronic properties of the perovskite active layer and defect passivation / engineering of the interfaces. For the former, tuning the band gap of the halide perovskite has been a pressing requirement for high performance solar cell devices, with the objective of obtaining compounds with a band gap close to the optimal value of 1.1 eV for single junction solar cells under the ideal case that the radiative recombination is the only recombination mechanism.<sup>22</sup> Halide perovskites are also interesting candidates for the development of tandem solar cells.<sup>23, 24</sup> Of particular interest is their use as top solar cell in combination with traditional silicon based devices.<sup>25, 26</sup>

### 2.1.1 Dimensionality engineering

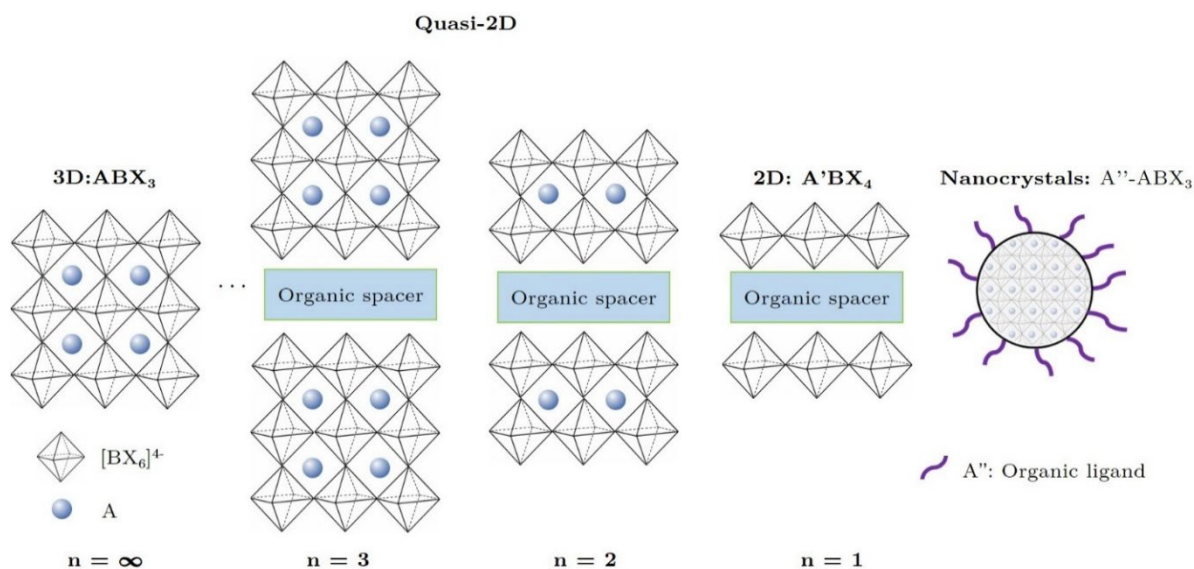


**Figure 2.2.** Halide perovskite structures with different dimensionalities: from 3D to 2D and nanocrystals.

As an additional knob for material design, dimensionality control serves as an effective way to tune the electronic and optical properties, further expanding the halide perovskite family. Compounds with reduced dimensionality are particularly promising for optoelectronic applications.<sup>27</sup> The electrons' and holes' wave functions are confined within these materials, giving rise to quantum confinement effects and, in many cases, to enhanced emission quantum efficiencies.<sup>28-30</sup> By introducing large organic spacer, this confinement can be achieved in 1 dimension (2D halide perovskites,  $A'BX_3$ ) and 3 dimensions (“0D” nanocrystals,  $A''-ABX_3$ ). In both cases large organic cations act as insulating barrier separating semiconducting lead halide sheets (**Figure 2.2**). Depending on the monovalent and bivalent nature of the organic spacer, 2D perovskites can be further classified as Ruddlesden–Popper (RP) and Dion–Jacobson (DJ) (**Figure 2.3**).

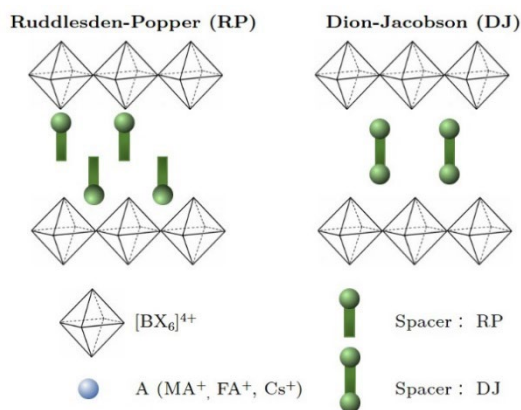


**Figure 2.3.** 2D Halide perovskite structures: Ruddlesden-Popper(RP) and Dion-Jacobson (DJ).

## 2.1.2 Halide engineering and mixed halide perovskites

Halide engineering (mixing and substitution) is used as a facile way for tuning the bandgap of the material. Noh and co-workers have demonstrated the band gap increase linearly with the increase of the Br content. By changing I/Br mixing ratio in  $\text{MAPb}(\text{I}_{1-x}\text{Br}_x)_3$ , (MA = methyl ammonium), almost the entire visible spectrum can be covered.<sup>31</sup> Eperon *et al* replaced methylammonium cation ( $\text{MA}^+$ ) with formamidinium ( $\text{FA}^+$ ) cation, by which a tunable but also slightly red shifted bandgap range between 1.48 and 2.23 eV was achieved.<sup>32</sup> Halide engineering in low dimensional (quasi 2D and nanocrystal system shown in **Figure 2.2**) further expand this range to higher band gap energies<sup>33-35</sup>. In addition to stoichiometry synthesis,<sup>31-33, 35-39</sup>, various other methods, such as halogen gas exchange,<sup>40, 41</sup> halide anion exchange via halide salts,<sup>34, 42, 43</sup> dihalomethane<sup>44</sup> or with physical contact of the two films with pure perovskites are also used for halide mixing.<sup>45-47</sup> **Figure 2.4** summarizes the tunable optical properties achieved by halide engineering and dimensionality control.

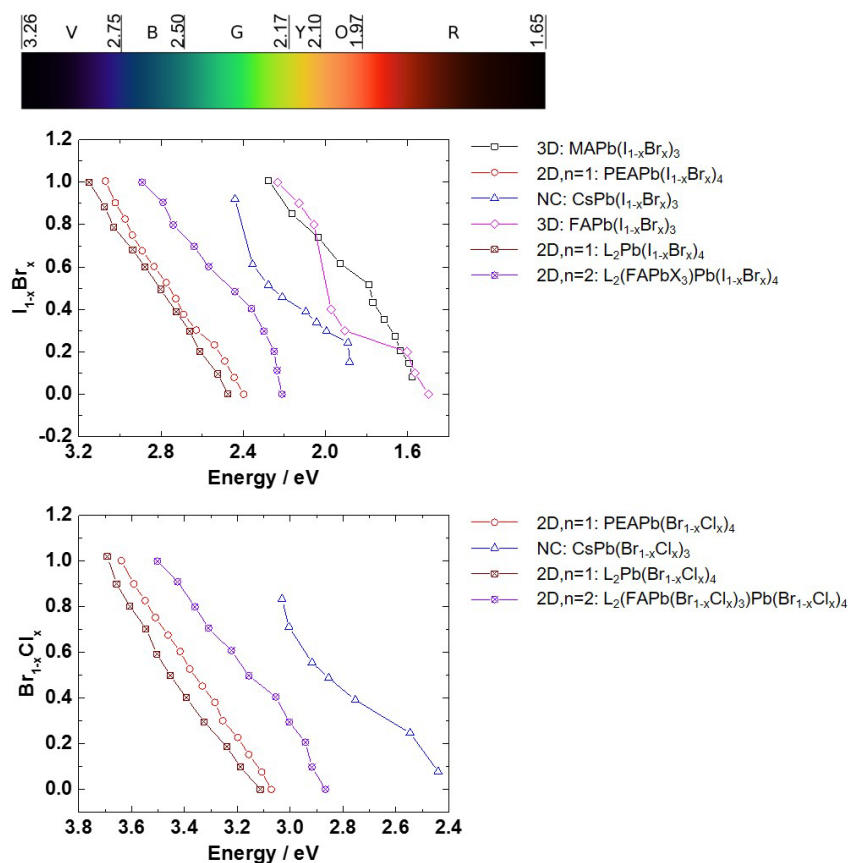


**Figure 2.4.** Tunable optical properties achieved by halide engineering and dimensionality control. Data extracted and replotted with permission, 3D:  $\text{MAPb}(\text{I}_{1-x}\text{Br}_x)_3$  from Ref<sup>31</sup>, the energy here refers to the bang gap energy extracted from Tauc plot of the UV-Vis absorption spectra; 2D, n=1:  $\text{PEAPb}(\text{I}_{1-x}\text{Br}_x)_4$ ,  $\text{PEAPb}(\text{Br}_{1-x}\text{Cl}_x)_4$  from Ref<sup>33</sup>, the energy refers to the low energy excitonic absorption energy ; NC:  $\text{CsPb}(\text{I}_{1-x}\text{Br}_x)_3$  from Ref <sup>34</sup> ; 3D:  $\text{FAPb}(\text{I}_{1-x}\text{Br}_x)_3$  from Ref <sup>32</sup>, the energy here refers to the bang gap energy extracted from Tauc plot of the UV-Vis absorption spectra; 2D, n=1 and n=2:  $\text{L}_2\text{Pb}(\text{I}_{1-x}\text{Br}_x)_4$ ,  $\text{L}_2\text{Pb}(\text{Br}_{1-x}\text{Cl}_x)_4$  from Ref<sup>35</sup>

## 2.2 Defect chemistry and ion transport in halide perovskites

While the mixed ionic-electronic conducting properties of fully inorganic halide perovskites have been investigated as early as 1983,<sup>48</sup> hybrid halide perovskites, such as MAPbI<sub>3</sub>, used in solar cells have initially been treated as traditional electronic semiconductors. In the early years of perovskite solar cells, an anomalous hysteresis behavior in the current–voltage curves was reported for these devices.<sup>49</sup> This hysteresis refers to the fact that the current – voltage curve is significantly different when voltage is scanned in either the forward or the reverse direction (**Figure 2.5**). This effect was found to depend on scan rate, measurement delay time, solar cell architecture/contact.<sup>49-51</sup> In addition, a very large capacitance at low frequency from impedance measurements was also observed.<sup>52-54</sup> The explanation for these observations became clearer only after it was found that, unlike other purely electronic semiconductors, ion conduction in halide perovskites is significant even at room temperatures.<sup>55</sup>

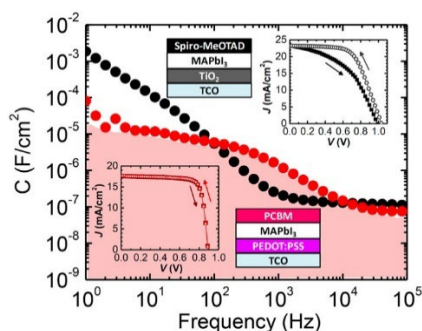


**Figure 2.5.** I–V hysteresis of perovskite solar cell and their Frequency ( $f$ )-dependent capacitance ( $C$ ) properties. TiO<sub>2</sub>/MAPbI<sub>3</sub>/spiro-MeOTAD configuration showed significant  $I$ – $V$  hysteresis along with highest capacitance ( $10^{-2}$  F/cm<sup>2</sup>), see black curve. Substantial reduction in capacitance to  $10^{-3}$  F/cm<sup>2</sup> was observed upon replacing TiO<sub>2</sub> with PCBM (Red). Figure adapted with permission from Ref <sup>50</sup>.

Yang *et al.*<sup>55</sup> showed for the first time that MAPbI<sub>3</sub> is a mixed ionic-electronic conductor, with 4 times higher ionic conductivity compared with its electronic conductivity in the dark. The transient voltage curve measured with a galvanostatic DC polarization experiment fits a square root of time law at short times and an exponential behaviour for longer time, suggesting that the observed long time scale behaviour is due to stoichiometric polarization (**Figure 2.6a**) with chemical diffusion coefficient of  $2.4 \text{ E-}08 \text{ cm}^2 \text{ s}^{-1}$ . Further EMF measurements (**Figure 2.6b**), using MAPbI<sub>3</sub> as electrolyte under an iodine chemical potential gradient, show substantial open circuit voltage, further indicating that MAPbI<sub>3</sub> is a mixed conductor.<sup>55, 56</sup> Doping experiments<sup>57</sup> and atomic modelling<sup>58</sup> revealed that iodine vacancies are the majority ionic charge carriers. The dominant moving ion in this compound is I<sup>-</sup>, as confirmed via Faradaic reaction cell experiments (**Figure 2.6c**), where formation of the metal iodide at the metal/MAPbI<sub>3</sub> contact is observed.<sup>59</sup> Solid state NMR measurements of <sup>14</sup>N, <sup>1</sup>H

and  $^{207}\text{Pb}$  in  $\text{MAPbI}_3$  rule out significant MA long range motion at least in its tetragonal phase ( $T < 327$  K).

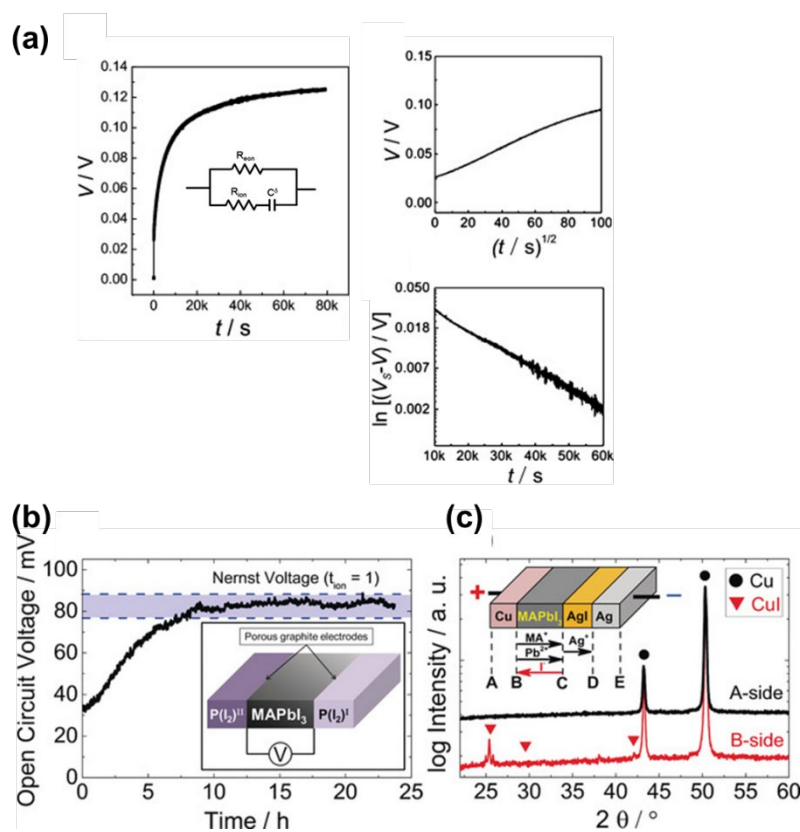


**Figure 2.6.** (a) DC polarization curve for a  $\text{C}|\text{MAPbI}_3|\text{C}$  cell measured by applying a current of 2 nA. Voltage versus square root of time and semi-log plot of voltage versus time at longer time scale was plotted on the right. Figure adapted with permission from Ref<sup>55</sup>. (b) Voltage of an emf cell obtained applying two different  $\text{P}(\text{I}_2)$  (1.7 and 1.5 bar).  $\text{MAPbI}_3$  pellet kept at 403 K. Inset shows the schematics of the experiment. (c) Schematic of a faradaic reaction cell ( $+\text{Cu}|\text{MAPbI}_3|\text{AgI}|\text{Ag}-$ ) and XRD patterns of surfaces A and B of Cu foil after the measurement. Figure adapted with permission from Ref<sup>56</sup>.

### 2.3 Photo induced ionic effects in halide perovskites

Kim *et al.* showed that with above bandgap illumination, the electrical response of  $\text{MAPbI}_3$  is consistent with a significant increase in not only the electronic but also the ionic conductivity (two orders of magnitude in  $\sigma_{\text{ion}}$  and three orders of magnitude in  $\sigma_{\text{eon}}$ , even at a light intensity of only  $1 \text{ mW cm}^{-2}$ ).<sup>8</sup> Such light induced apparent enhancement in the ionic conductivity increases with the increase of the light intensity (**Figure 2.7a**). In addition, such enhancement in ionic conductivity is further confirmed in a permeation cell when applying  $\text{p}(\text{I}_2)$  on one side of the  $\text{MAPbI}_3$  film as  $\text{I}_2$  source, while using Cu on the other side as  $\text{I}_2$  sink under dark and light conditions (**Figure 2.7b**). Compared to the dark situation where the CuI signal is almost at noise level, clear formation of CuI was found at the illumination side. This indicates that transport of iodine flux from one side to another side of  $\text{MAPbI}_3$  is enhanced by light. The ionic conductivities under light were also measured in  $\text{MAPbBr}_3$ . Strikingly, a

different behaviour was observed, whereby in  $\text{MAPbBr}_3$  little or no ionic conductivity enhancement under light is detected.<sup>60</sup> This difference is invoked below in the discussion of the driving force for photo de-mixing in mixed halide perovskites (See Chapter 9).

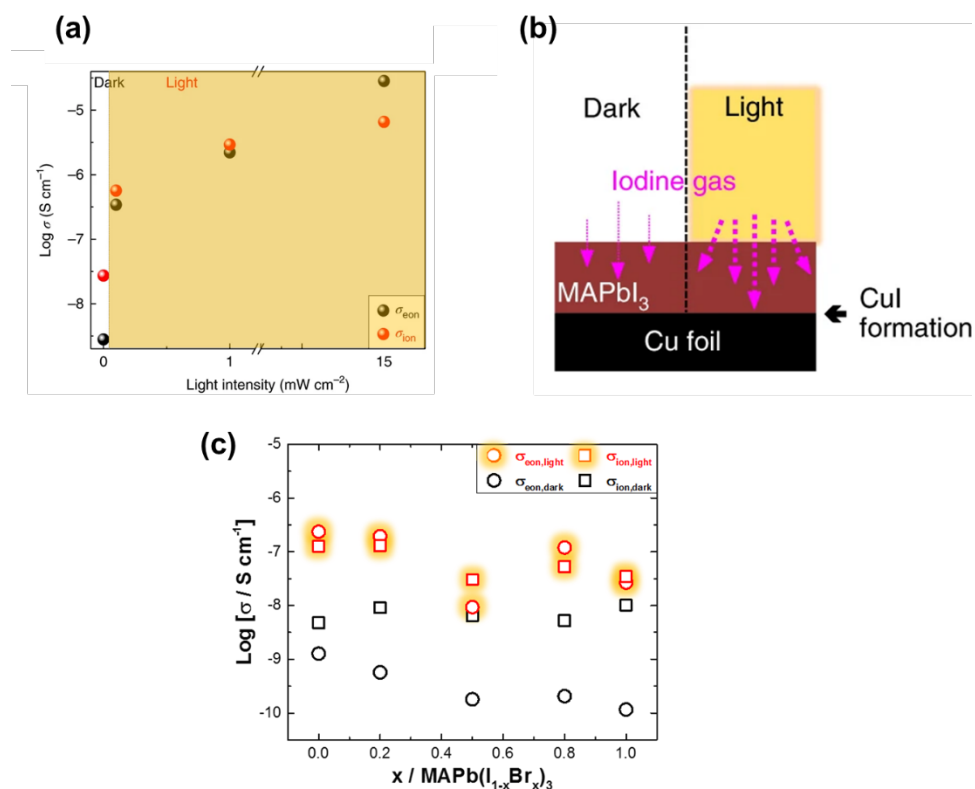


**Figure 2.7.** (a) Electronic and apparent ionic conductivities under different light intensities (extracted from d.c. galvanostatic polarization at 40 °C under an Ar atmosphere). Figure adapted with permission from Ref<sup>8</sup>. (b) Permeation cell in the dark and under light: an iodine flux through a MAPI film is induced by applying a defined iodine partial pressure ( $3.6 \times 10^{-6}$  bar) on one side and Cu as the iodine sink on the other side. (c) Electronic and ionic conductivity of in  $\text{MAPb}(\text{I}_{1-x}\text{Br}_x)_3$  in the dark and under light with light intensity of 1  $\text{mW cm}^{-2}$ .  $\sigma_{\text{ion,light}}$  refers to apparent values calculated from the polarization measurements.

## 2.4 De-mixing and photo de-mixing

De-mixing refers to the process by which two or more components or phases are separated when they are mixed together. This can occur in a variety of contexts, including in chemical mixtures, and particulate systems.<sup>61, 62</sup> In terms of chemical mixtures, de-mixing has been extensively investigated in multicomponent systems including polymer blend, metallic alloys and ionic solid mixtures.<sup>61, 63-65</sup> According to thermodynamics, the stability of the phases relative to one another is determined by the free enthalpy of the phases involved.<sup>66, 67</sup> The free enthalpy is result of the counter-play between enthalpy and entropy of mixing, which depends on pressure (P), temperature (T) and composition(x) (see detailed introduction in Part III).

Recently, Hoke *et al.*<sup>68</sup> reported another de-mixing phenomenon in mixed halide perovskites, whose occurrence depends on the ON/OFF state of the light that shines on the

material, suggesting that light can potentially be another important variable for changing the thermodynamic properties of the mixture. This finding indicates that there might be a link between light and phase thermodynamic properties, which presents great opportunities for studying the out-of-equilibrium thermodynamics with photo-generated charge carriers present in the system.<sup>11</sup>

Specifically, mixed halide perovskites such as  $\text{MAPb}(\text{I}_x\text{Br}_{1-x})_3$  de-mix into I-rich and Br-rich phases under illumination (*photo de-mixing*) and re-mix to the initial composition in the dark (*dark re-mixing*). Anionic mixtures with different A-site cation materials  $\text{CsPb}(\text{Br}_x\text{I}_{1-x})_3$ <sup>43, 69, 70</sup> and  $\text{FAPb}(\text{Br}_x\text{I}_{1-x})_3$ <sup>71-73</sup> have also shown a similar de-mixing behavior. Halide perovskites with multiple mixed A cations and anions  $\text{MA}_z\text{Cs}_y\text{FA}_{(1-y-z)}\text{Pb}(\text{Br}_x\text{I}_{(1-x)})$ <sup>74-76</sup> show a lower tendency to phase segregate. No segregation of cations are observed. Furthermore, de-mixing in these mixtures was found not only to be induced by light but also by voltage bias<sup>77</sup> and high dose electron beam<sup>78</sup>.

#### 2.4.1 Experimental signature of photo de-mixing

Experimentally, the occurrence of photo de-mixing was observed in photoluminescence(PL) emission at low photon energy upon illuminating the mixed halide perovskite accompanied by a simultaneous decrease in intensity of the high photon energy feature, attributed to the bandgap of the mixture (**Figure 2.8 a**).<sup>11, 12</sup> In addition, a recent study from Eva Unger’s group shows the complexity of the evolution in the photoluminescence during phase segregation. A short-lived intense red-shifted band which is close to the pure iodide perovskite’s emission formed within the first few seconds of light exposure, then disappeared followed by emission of I-rich phase with higher energy.<sup>79</sup> UV-Vis absorption measurements shown in **Figure 2.8b** indicate the flattening of the absorption edges after de-mixing, consistent with the formation of phases presenting larger and smaller absorption edge energies. From a structural point of view, XRD measurements show the splitting of a single diffraction peak into two peaks at different diffraction angles indicating Br- rich and I-rich domains (**Figure 2.8c**);<sup>11</sup> Other studies in the literature also report the broadening of these diffraction peaks, evidencing a decrease in crystallinity in the material on de-mixing.<sup>80</sup> Electroluminescence mapping, combined with SEM have also aided the investigation of the phase separation process in terms of spatial distribution of the de-mixed phases (**Figure 2.8d**)<sup>81, 82</sup> Additionally, the long stabilization time of optoelectronic devices using mixed halide compositions compared with its end members has been interpreted as an “electrical signature” for photo de-mixing (**Figure 2.8e**).<sup>68, 83, 84</sup> Various reviews on this topic can be found in the literature.<sup>80, 85-90</sup>



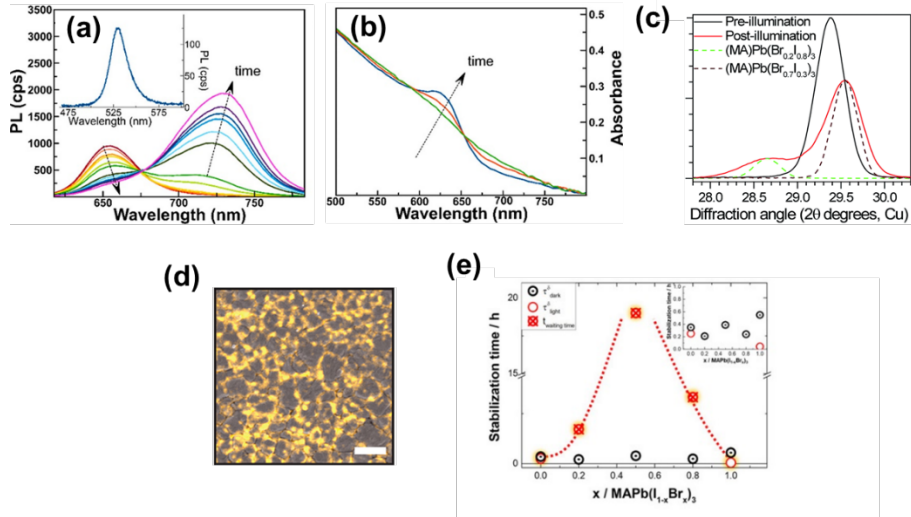


**Figure 2.8.** Key experimental signature for photo de-mixing based on different techniques: (a) Change in photoluminescence of  $\text{MAPb}(\text{I}_{0.5}\text{Br}_{0.5})_3$  under  $\lambda_{\text{exc}} = 405 \text{ nm}$  CW excitation ( $I_{\text{exc}} = 20 \text{ mWcm}^{-2}$ , 3s); Inset show the emission spectra from 475 nm to 600 nm, indicating the formation of the Br-rich domains. Figure adapted with permission from Ref<sup>91</sup>. (b) Change in absorption intensity of  $\text{MAPb}(\text{I}_{0.5}\text{Br}_{0.5})_3$  under  $\lambda_{\text{exc}} = 405 \text{ nm}$  CW excitation ( $I_{\text{exc}} = 20 \text{ mWcm}^{-2}$  time sequence: blue, 0 min; red, 1min; and green 30 min). Figure adapted with permission from Ref<sup>91</sup>; (c) X-ray diffraction of the 200 XRD peak of an  $\text{MAPb}(\text{I}_{0.4}\text{Br}_{0.6})_3$  film before (black) and after (red) under white-light LED ( $\sim 50 \text{ mW cm}^{-2}$ , 5min). Figure adapted with permission from<sup>11</sup> (d) Scanning electron microscope (SEM) and cathodoluminescence (CL) imaging overlay under at 405 nm LED ( $100 \text{ mW/cm}^2$ , 5min). The scale bar is  $2 \mu\text{m}$ . Figure adapted with permission from Ref<sup>81</sup>. (e) Stabilization times of anion mixtures  $\text{MAPb}(\text{I}_{1-x}\text{Br}_x)_3$  in the dark (open symbols) and under light (closed symbols with hollow). Figure adapted with permission from Ref<sup>60</sup>.

#### 2.4.2 Photo de-mixing and device performance

Photo de-mixing causes an undesirable drop in power conversion efficiency of solar cells based on mixed halide perovskites under operation.<sup>68</sup> Early work on this subject shows that, within a period as short as fifteen minutes under continuous visible light, both open circuit voltage (OCV) and short circuit current (SCI) of a mixed halide perovskite based solar cell decrease significantly. As a result, the photo-conversion efficiency of the device decreases (**Figure 2.9a**).<sup>68, 84</sup> By simultaneously recording changes in photoluminescence and solar cell performance under prolonged illumination, it was also demonstrated that, compared with the open-circuit voltage, the loss in short-circuit current density shows a more significant drop, with concurrent red shift, increased lifetime, and higher quantum yield of photoluminescence.<sup>92</sup> This can be attributed to the I-rich phase forming in the active layer, which favors charge carrier trapping and recombination. The funneling of electronic charge carriers into the I-rich domains<sup>93</sup> is enabled by the large diffusion length of the carriers<sup>94</sup> and the favorable valence band offset between the mixture and the I-rich phase (**Figure 2.9b**)<sup>95</sup>.



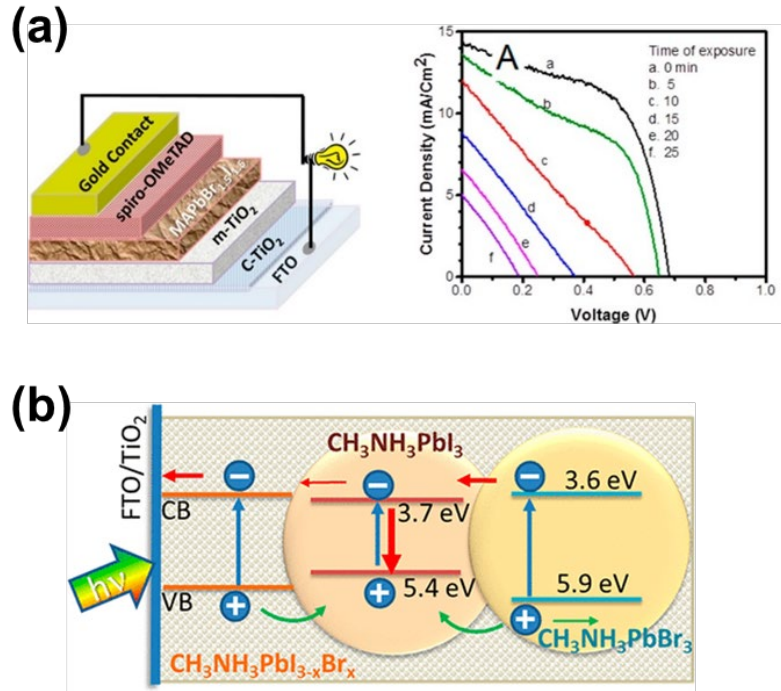


**Figure 2.9.** (a) Left: Schematic illustration of the cell design employed for evaluating photovoltaic performance. Center and Right: J–V characteristics of PSCs with MAPb(Br<sub>1.5</sub>I<sub>1.5</sub>)<sub>3</sub> films under 1 Sun continuous illumination for 25 min. Figure adapted with permission from Ref<sup>84</sup>.

### 2.4.3 Mitigation strategies

A non-uniform distribution of the halides within the perovskite layer due to photo de-mixing can significantly hinder the potential use of mixed-halide perovskites in tandem solar cells and adjustable LED technology. There have been several reported methods in the literature that aim to reduce the segregation of halides in mixed-halide perovskite materials, potentially overcoming this limitation.

#### Stoichiometric engineering:

**Partially replacing A cation** of methylammonium (MA, CH<sub>3</sub>NH<sub>3</sub><sup>+</sup>) with caesium (Cs<sup>+</sup>) or formamidinium (FA, CH(NH<sub>2</sub>)<sub>2</sub><sup>+</sup>) show decrease in de-mixing rate.<sup>75, 96-98</sup> Substituting MA<sup>+</sup> with FA<sup>+</sup> shows a decrease in the rate constant of de-mixing on increasing of the FA<sup>+</sup> content. Significant suppression of such rate constant was observed in the case of 90% substitution.<sup>96</sup> Substituting MA<sup>+</sup> with Cs<sup>+</sup> suppresses phase separation to some extent, although detection of I-rich clusters was confirmed in this case too.<sup>97</sup> Substituting partially or completely MA cation with a mixture of FA and Cs cations also shows a less prominent photo de-mixing, but it does not completely prevent it. The I-rich phases for the mixed (FACs)-perovskites have a similar emission peak as of the MA-perovskites, centered around 740–750 nm.<sup>75</sup> Cs incorporation in (FA<sub>0.83</sub>MA<sub>0.17</sub>)Pb(I<sub>0.83</sub>Br<sub>0.17</sub>)<sub>3</sub> greatly enhances the overall performance of the solar cell<sup>99, 100, 101</sup> Dang *et al.* reported that the addition of Cs<sup>+</sup> and Rb<sup>+</sup> could drastically suppress the segregation of halides.<sup>98</sup>

**Crystallinity control:** Rehman *et al.* demonstrated that the  $\text{Cs}_y\text{FA}_{(1-y)}\text{Pb}(\text{Br}_{0.4}\text{I}_{0.6})_3$  thin films with increased crystallinity (indicated by the width of X-ray diffraction peaks) show improved photostability against photo de-mixing.<sup>74, 77</sup> The grains size of the mixed halide perovskites has also been shown to influence the occurrence of photo de-mixing.  $\text{CsPb}(\text{I}_{0.5}\text{Br}_{0.5})_3$  nanocrystal-based films show no redshift of the PL peak under illumination, indicating the absence of photo de-mixing in this system.<sup>91</sup> According to Zhang *et al.*,  $\text{CsPbBr}_{1.2}\text{I}_{1.8}$  nanocrystal with a lateral size of  $\sim 23$  nm shows no de-mixing.<sup>102</sup> Andrés *et al.* demonstrated the gradual transition from de-mixing free to de-mixing by gradual increase the crystallites' sizes in  $\text{CsPbBr}_{1.56}\text{I}_{1.44}$  nanocube thin films. The threshold grain size of the occurrence of photo de-mixing is  $46 \pm 7$  nm.<sup>103</sup> Similar conclusion have been drawn by Hu *et al.* who showed that a threshold size of phase segregation of approximately 43 nm is relevant to  $\text{CsPbBr}_{1.5}\text{I}_{1.5}$  nanocrystalline films. Consistently, the device performance of solar cells with crystal sizes lower than the threshold size is stable, with the highest PCE achieved at 150 °C annealed films with an average grain size of 106 nm.<sup>104</sup>

Other reports have commented on the beneficial effects of an increased grain size in suppressing photo de-mixing.<sup>105, 106</sup> Hu *et al.* showed that  $\text{MAPb}(\text{Br}_{0.27}\text{I}_{0.73})_3$  perovskite films deposited on poly[bis(4-phenyl)(2,4,6-trimethylphenyl)amine] (PTAA, hole-transport layer, HTL) is more stable against photo de-mixing compared with the same film deposited on poly(3,4-ethylenedioxythiophene) polystyrene sulfonate (PEDOT:PSS). The authors ascribe this effect to the larger grains formed on PTAA when compared to PEDOT:PSS.<sup>105</sup> This study is complicated by the unclear role of the hole transport layer, which influences the charge carrier density in the film (see below).

**Charge carrier manipulation:** The manipulation of the charge carrier recombination, extraction and injection rates is found to influence the occurrence of photo de-mixing. Hole accumulation achieved by contacting mixed halide perovskites with electron transport layers<sup>107, 108</sup> and through electrochemical anodic bias<sup>109</sup> also provide direct experimental evidence for the important role of the hole concentration on the photo de-mixing behaviour in 3D mixed halide perovskites. Belisle *et al.* demonstrated the effect of selective electron/hole extraction by depositing mixed halide perovskites on  $\text{C}_{60}$  (electron transporting layer, ETL)/ poly (triaryl amine) (PTAA, hole-transport layer, HTL). The initial PL of the perovskite is greatly quenched due to its contact with the transport layers. Strikingly, while the perovskite capped with the ETL shows substantial PL from a lower-bandgap phase, the PL of the HTL capped perovskite is largely unaffected.<sup>108</sup> Similarly, Dubose *et al.* discovered that segregation is observed when mixed halide perovskites deposited on an electron transporting layer such as  $\text{TiO}_2$  or insulating  $\text{ZrO}_2$  substrate. By depositing hole transporting layer spiro-OMeTAD on mixed halide perovskites/ $\text{TiO}_2$  film, the halide ion segregation is suppressed.<sup>107</sup> These results

point towards the importance of the photo-generated holes in the mixed halide perovskite layer and indicate that efficient hole extraction greatly suppresses the occurrence of photo de-mixing.

**Defect passivation:** Stranks *et al.* proposed mitigating photo-induced phase segregation by decorating the surfaces and grain boundaries with passivating potassium halide (e.g. KI) layers.<sup>110</sup> They proposed that the excess iodide ions from KI could be able to fill the iodine vacancies in the material and thus suppress halide migration. Belisle *et al.* showed that by coating a  $\text{CH}_3\text{NH}_3\text{PbI}_2\text{Br}$  surface with the electron-donating ligand trioctylphosphine oxide (TOPO)<sup>108, 111</sup>, the rate of halide segregation as monitored by PL of the lower-bandgap iodide-rich domains in the mixed-halide perovskite, is substantially reduced. Based on a similar idea, Kamat *et al.* treated a perovskites solution with  $\text{I}_2$  solution in IPA before spin coating the film to reduce the iodine vacancy concentration. This approach resulted in the mitigation of segregation under light with quick recovery in the dark.<sup>84</sup> These results suggest that carrier trapping and charge accumulation at perovskite surfaces are important components determining the driving force of photo induced halide segregation, and efficiently passivating and treating surfaces are potential pathways towards stabilized wide-bandgap perovskites.<sup>108</sup>

#### 2.4.4 Photo de-mixing models

The mechanism and driving force for photo de-mixing are still under debate. Here is a summary of the models that have been proposed to explain this phenomenon and of how each of the, is (in)consistent with experimental observations:

- i) Dark miscibility gap model (Brivio *et al.*)<sup>112</sup>

Brivio *et al.*<sup>112</sup> performed a thermodynamic analysis of  $\text{MAPb}(\text{Br}_x\text{I}_{1-x})_3$  alloys with DFT calculation. Their work shows a large miscibility gap in the intermediate composition range, predicting the spinodal ( $0.3 < x < 0.6$  at 300 K) and bimodal ( $x = 0.2, 0.7$  at 300 K) decomposition regions and a critical temperature of 343K (**Figure 2.10a**). This model proposes that, thermodynamically, the studied mixture is metastable in the dark and that light simply catalyzes the de-mixing into I-rich and Br-rich phases. In other words, it is the de-mixing kinetics which under light is accelerated, enabling a faster occurrence of de-mixing, which would occur under dark over very long time scales.

This model can explain the independence of the de-mixed I-rich composition after illumination (measured by PL peak) on the initial composition.<sup>11, 113</sup> However, the fact that de-mixing process occurs reversibly, at least partially indicates that the miscibility gap must be influenced by light thermodynamically.<sup>11, 12</sup>

- ii) Bandgap reduction (Draguta *et al.*)<sup>91, 114</sup>

Draguta *et al.* proposed a model whereby the valence band edge difference between the mixture and the demixed phases introduces an energetically favourable path for photogenerated holes. This energy offset counterplays the configurational entropy of mixing

and serves as the driving force of de-mixing. The mixing free energy is calculated between a photoexcited hole in  $\text{MAPb}(\text{I}_{1-x}\text{Br}_x)_3$  and a hole localized in an iodide-rich phase(**Figure 2.10c**).<sup>91, 115, 116</sup>

$$\Delta F^*(x, n) = n(F_{mix}^*(x) - xF_{Br} - F_I^*) = n\Delta F_{GS}(x) + \Delta E_g(x) \quad \text{Eq. 2.4.1}$$

$F_{mix}^*(x)$ ,  $F_{Br}$ , and  $F_I^*$  denote photoexcited  $\text{MAPb}(\text{I}_{1-x}\text{Br}_x)_3$ ,  $\text{MAPbBr}_3$ , and  $\text{MAPbI}_3$  free energies and asterisks denote the presence of a photogenerated hole.  $\Delta E_g(x)$  denotes the band gap differences between the  $\text{MAPb}(\text{I}_{1-x}\text{Br}_x)_3$  and  $\text{MAPbI}_3$ .

According to their calculations, de-mixing is favored thermodynamically and will result in de-mixed compositions  $x_{\text{I-rich}} \sim 0$ . Experimentally, the  $x_{\text{I-rich}}$  is estimated to be  $\sim 0.18 - 0.2$ .<sup>114</sup> The authors argue that kinetic limitations and, specifically, a temperature-independent percolation threshold leads to finite  $x_{\text{I-rich}}$  values. They support their argument by the observation of a limited redshifts  $\sim 10$  meV of the emission arising from parent mixed halide perovskites when de-mixed at a low temperature range between 295 and 185 K. However, this model leaves the observed strong temperature dependence of the threshold light intensity unexplained.<sup>117</sup>

iii) Polaron and strain (Bischak *et al.*)<sup>81, 97, 118</sup>

Bischak *et al.* proposed another thermodynamic model where they considered strain energy as an important component determining miscibility of the iodide and bromide perovskites. Concentrating on the interaction between photo generated electronic charges and the ionic lattice through electron–phonon coupling, they predicted de-mixing based on the standard solid state solution phase transition theory(**Figure 2.10b**).<sup>81</sup> Molecular simulations suggest polaronic strain locally changes the free energy of halide mixing and favors de-mixing, leading to stabilized regions enriched in Iodide. Compared with chemical interaction, the relative energetic contributions to the heat of mixing due to elastic effects from lattice strain are much larger, which leads to a de-mixing transition that depends strongly on strain. This model is consistent with the observation that reducing the electron–phonon coupling in the system by replacing  $\text{MA}^+$  with less polar  $\text{Cs}^+$  reduces the tendency to phase separation.<sup>97</sup>

This model rationalizes the observation that the small clusters enriched in I-rich localize near grain boundaries (in polycrystalline films)<sup>81</sup> or of the edges of the crystals(in single crystals)<sup>2</sup> by releasing strain. The formation of the I-rich domains is stochastic in space is also consistent with the stochastic formation of polarons in space.<sup>119</sup> In addition, this model can explain that a continued presence of photo generated carriers is required for cluster stability as this is also the necessity for polaron formation.<sup>81</sup>

Polarons have also been invoked to rationalize re-mixing at high light intensity due to the merged polarons that leads to the reduced strain gradient that favors mixing thermodynamically.<sup>120</sup> However, it is still not clear if such “photo re-mixing” is not a

illumination induced temperature effect rather than a light induced polaron effect given the high light intensity ( $200 \text{ W cm}^{-2}$ ) used (the fact that a controlled sample show photo de-mixing at  $70 \text{ }^\circ\text{C}$  does not exclude temperature effects).

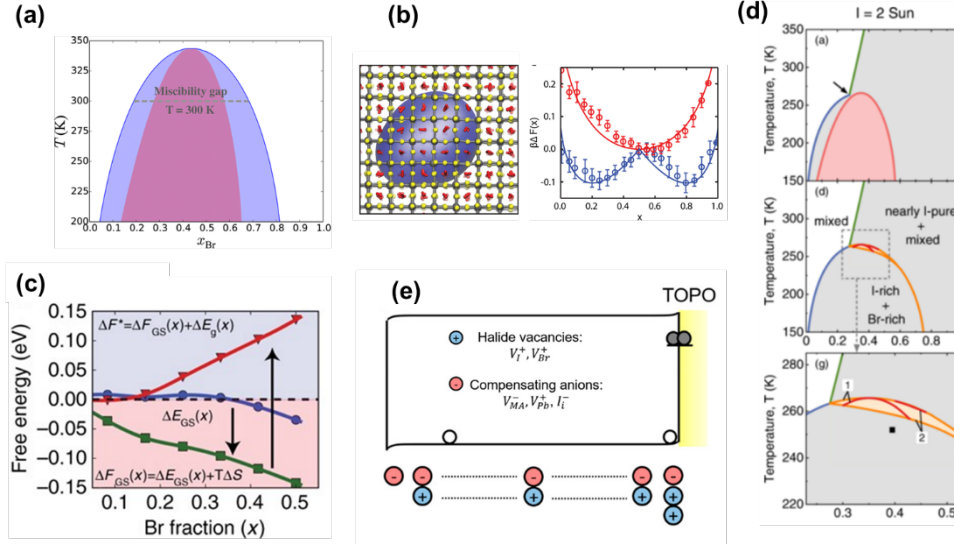


**Figure 2.10.** Photo de-mixing models (a) Dark miscibility gap model(i); (b) polaron and strain model(ii); (c) Bandgap reduction model(iii); (d) Triple phase model(iv); (e) Surface trapping model(v). Figures are adapted with permission.

iv) Triple phase model (Chen *et al.*)<sup>121-123</sup>

Chen *et al.* proposed a model considering the minimization of the total free energy expressed as the sum of the compositional and photocarrier free energy (**Figure 2.10d**). three-phase coexistence is predicted in this model. The phase diagram of the mixture in the dark is calculated by considering the compositional Helmholtz free energy, within the quasi-chemical approximation. Compared with the miscibility gap model in (i), the symmetry lowering by the specific orientation of the MA cations is additionally considered, resulting a  $T_c$  of 266 K, compared with the value of 343 K in (i).

The energy contribution to the free energy from the photo generated electronic charge carriers are further considered by assuming a Boltzmann distribution of photocarriers on different phases.

$$\frac{n_2}{n_1} = \exp\left(-\left(E_g(x_2) - E_g(x_1)\right)/k_B T\right), \quad \text{Eq.2.4.2}$$

where  $n_1$  and  $n_2$  are the photocarrier densities in the two phases. With  $\phi_1$  and  $\phi_2$  the corresponding volume fractions of the two phases, the mixing free energy  $\Delta F^*$  per formula unit under illumination becomes

$$\Delta F^*(x_1, x_2, \phi_1, \phi_2, T) = \phi_1 \Delta F(x_1, T) + \phi_2 \Delta F(x_2, T) + n_1 \phi_1 E_g(x_1) + n_2 \phi_2 E_g(x_2). \quad \text{Eq.2.4.3}$$

In steady state, the rate of generation of photocarriers in the system should be equal to the sum of the rates of photocarrier annihilation by monomolecular and bimolecular recombination in the different phases:

$$G = \phi_1(n_1/\tau + kn_1^2/V) + \phi_2(n_2/\tau + kn_2^2/V) \quad \text{Eq.2.4.4}$$

Based on these equations, a phase diagram under different light intensities in 5 different mixed halide perovskites was constructed. While spinodals change marginally with increasing the photo carrier density, two different bimodals are predicted, The first type (full blue lines) can be viewed as a modification of the dark binodals by illumination, which are referred to as ‘compositional binodals’. Under illumination, a new type of binodals appears (full green lines), named ‘light induced binodals’. A distinct feature of this model is the prediction that triple points exist where two different phases with different halide composition can be nucleated from the parent phase, including one nearly iodine-pure nucleated phase. Furthermore, two types of three-phase coexistence, with the nearly I-pure nuclei being present in (i) both the I-rich and B-rich phase or (ii) only the I-rich phase are discussed<sup>122</sup>. Such prediction has not been confirmed experimentally to date.

v) Surface trapping model (Belisle *et al.*)<sup>108</sup>

Belisle *et al.* propose a model stating that carrier trapping at surface states induces electric fields which impact the movement or accumulation of ionic defects. Such field drives the occurrence of the photo de-mixing (**Figure 2.10e**). Surface treatments with electron donating materials reduce non-radiative recombination or charge accumulation, thus inhibiting halide segregation. The model assumes that mobile halide vacancies are uniformly distributed and are charge compensated by the immobile ions or other ionized point defects and considers a density of surface traps that favor electron trapping at the top surface intrinsically. The model proposes the following: (1) trapping of the electrons at the surface, inducing the formation of an electric field pointing towards the surface of the film; (2) Vacancies migrate towards the surface to shield the trap-induced field; (3) redistribution of the ions and precipitation of I-rich and Br-rich phases occurs. The low activation energy for the formation of bromide vacancy compared with iodide vacancy, combined with the drift of the positively charged vacancies towards the surface and the expulsion of bromide ions away from the surface can result in the formation of the I-rich phase.

### 2.4.5 Open questions

1) Is the origin of photo de-mixing purely thermodynamic in nature or are kinetic effects also involved?

Clarifying the (im)miscibility in mixed halide perovskites in the dark (prior to any illumination) is critical for understanding whether photo de-mixing is purely thermodynamically driven or kinetic effects are also involved. Early studies using normal thin

film X-ray diffraction and synchrotron X-ray powder diffraction showed conflicting results on whether  $\text{CH}_3\text{NH}_3\text{Pb}(\text{I}_{1-x}\text{Br}_x)_3$  exhibits full miscibility or not.<sup>31, 36</sup> Another approach to clarify this question is to investigate whether the process of photo-mixing is completely reversible. The experimental situation is complicated by concomitant photo induced decomposition of the mixture after exposure to light.<sup>124</sup> Decoupling photo de-mixing from light induced decomposition is important and necessary, however, it remains a challenging and unresolved question.

2) What are the properties of the miscibility gap in mixed halide perovskites under light?

It is still unclear whether the lack of miscibility observed under light for mixed halide perovskites follows the traditional properties of a miscibility gap for mixtures at thermodynamic equilibrium. Among the open question in this context the following are of interest: 1) do the de-mixed compositions vary with temperature and can a critical temperature be defined? 2) Are the de-mixed compositions fixed for any starting composition of the pristine mixture? Nandi *et al.* observed that temperature affects the occurrence of photo de-mixing in  $\text{MAPb}(\text{I}_{1-x}\text{Br}_x)_3$  ( $x = 0.15, 0.24, 0.27$ ) differently with different initial composition, where only  $x=0.15$  remains mixed in the temperature range of 77 K – 300 K. For  $x = 0.24$  and  $0.27$ , photo de-mixing only occurs in the intermediate temperature window (200 – 300K).<sup>125</sup> This result implies the possibility to measure such miscibility gap under light. Very small variations in the de-mixed compositions were also observed in  $\text{MAPb}(\text{I}_{0.5}\text{Br}_{0.5})_3$  between 185K and 295K.<sup>114</sup> Therefore, it remains unclear if temperature influences the de-mixed compositions, and what is the shape of such miscibility gap under light. In addition, methods that allows one to measure such miscibility gap are currently missing, also due to the complication from photo-induced decomposition.

3) What is the driving force for photo de-mixing?

Concerning the driving force inducing phase instability in mixed halides perovskites, strain effects and electronic effects are discussed in the literature:

a)The interaction between photo generated charges and the ionic lattice through electron–phonon coupling induces strain effects that changes the free energy of de-mixing.<sup>81, 97, 118</sup>

b)Valence band edge variation and energy gain associated with holes stabilization in I-rich domains influences the free energy of de-mixing.<sup>12, 91</sup>

Fundamentally, the fact that photo de-mixing occurs, indicates that such process involves the formation of (electronic or also ionic) defects and their transport, as well as the formation of new phases. The contribution of ionic effects on the driving force of the photo de-mixing is missing. In addition, what is the dimensionality effect on such contribution?

4) Why do MAPbBr<sub>3</sub> and MAPbI<sub>3</sub> show significant differences in ionic conductivities under light?

MAPbI<sub>3</sub> shows an enormous increase in the apparent ionic conductivity under light (two orders of magnitude in  $\sigma_{\text{ion}}$  even at a light intensities of only 1 mW cm<sup>-2</sup>).<sup>8</sup> Under the same conditions, MAPbBr<sub>3</sub> shows little or no ionic conductivity enhancement.<sup>60</sup> This effect can potentially influence how halide ions are differently distributed and therefore contribute to the driving force of the photo de-mixing. The reason MAPbBr<sub>3</sub> and MAPbI<sub>3</sub> show significant difference on ionic conductivities under light remains unclear. In addition, other than electrical measurements, which are indirect in nature, can these effects be probed directly, e.g. via spectroscopy techniques?

5) What are the differences occur in the defect chemistry of bromide and iodide perovskites?

The defect chemistry of MAPbI<sub>3</sub> has been extensively investigated,<sup>55-57, 126</sup> revealing iodide vacancies to be the majority ionic charge carrier for ion conduction and electron holes for electronic conduction. By substituting iodide with bromide, whether such behavior varies significantly or remains largely unvaried is currently an unanswered question. Given the difference on ionic conductivities under light mentioned in last point, such investigation is even more crucial.

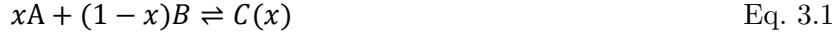


### **III THEORETICAL FRAMEWORK**



### 3.1 Mixture thermodynamics

This section starts with a brief description of the thermodynamics of mixing and de-mixing (for further reading one finds treatments in the literature, e.g. Guggenheim’s book<sup>127</sup>). Let us consider a binary mixture  $C \equiv (A, B)$  that can be thought to be formed according to



For the discussion on mixed halide perovskites, it could be  $\text{MAPb}(\text{I}_{1-x}\text{Br}_x)_3 \equiv (\text{MAPbBr}_3, \text{MAPbI}_3)$ .

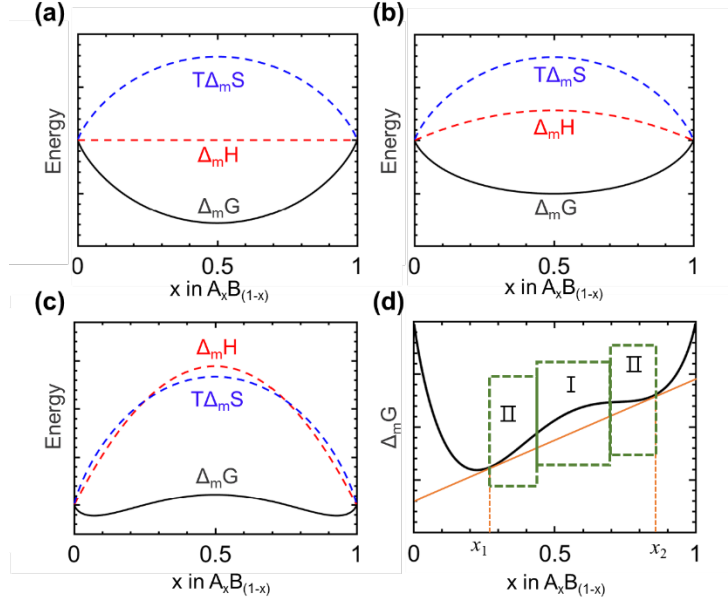
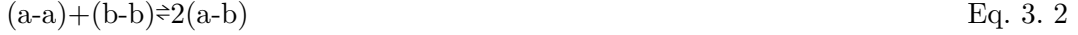


**Figure 3.1.** Mixing free enthalpy ( $\Delta_m G$ ), mixing enthalpy ( $\Delta_m H$ ) and mixing entropy term ( $T\Delta_m S$ ) for mixture  $A_x B_{1-x}$  for the case of (a) an ideal mixture, (b) a regular mixture at high temperature ( $T > T_c$ ) where mixing is favored and (c) a regular mixture at low temperature ( $T < T_c$ ) where de-mixing is favoured. (d) Free enthalpy of mixing of a sub-regular mixture. The two regions in (d) indicated with green dashed squares refer to the (I) spinodal and the (II) binodal regions. By constructing a common tangent to the free enthalpy curve (orange solid line), the de-mixed compositions of  $x_1$  and  $x_2$  can be obtained.

The contributions of the enthalpy ( $\Delta_m H$ ) and entropy ( $\Delta_m S$ ) of mixing to the free enthalpy ( $\Delta_m G$ ) determine if mixing or de-mixing is favored. In ideal mixtures (**Figure 3.1a**), the enthalpy of mixing is zero and mixing is always thermodynamically favorable owing to the contribution of the entropy (if the vibrational contribution to the entropy is neglected). The same applies for a negative mixing enthalpy. If the mixing enthalpy is positive, temperature is a decisive parameter with respect to potential de-mixing. At sufficiently high temperatures, mixing is favored (**Figure 3.1b**). At lower temperatures, where the mixing entropy does not dominate, the free enthalpy of mixing presents a double-minimum profile (**Figure 3.1c**). Such curve will look rather symmetrical (regular mixture) if A and B are similar. **Figure 3.1d** shows the general case where A and B are dissimilar. In either case, the double minimum profile

identifies a region of compositions, referred to as miscibility gap, where the mixed situation is not thermodynamically stable.

A simplified treatment uses a random distribution of A and B atoms for determining the entropy of mixing irrespective of the energetics. Strictly speaking this is only correct for an ideal mixture for which  $\Delta_m H = 0$ . In the general case ( $\Delta_m H \neq 0$ ), the energetics may be described by an interaction parameter  $\Omega$ . Its meaning is obvious when the transition from A and B to C is approximated by resorting to the reaction



Here one assumes that A is constituted by a-a pairs, B by b-b pairs and of that C exhibits also mixed pairs (there may be other structure elements that are common to A and B but not varied by the mixing process). Casting the reaction enthalpy of Eq. 2 and hence  $\Delta_m H$  in the form

$$\Delta_m H = W(x) = x(1-x)\Omega \quad \text{Eq. 3.3}$$

the free enthalpy curve follows as

$$\Delta_m G = RT(x \ln x + (1-x) \ln(1-x)) + x(1-x)\Omega \quad \text{Eq. 3.4}$$

The last term disappears for an ideal mixture ( $\Omega=0$ , i.e., it does not matter whether a is connected with a or b). If there are asymmetrical interactions, but a and b are similar,  $\Omega$  is non-zero but approximately constant and  $\Delta_m G$  is symmetrical about  $x=1/2$ . It is straightforward to show that the critical temperature below which the miscibility gap closes and thus the dome-like form of the free enthalpy of mixing develops into a double minimum form is given by

$$T_c = \Omega / 2R \quad \text{Eq. 3.5}$$

More realistic approximations assume  $\Omega$  to be a function of  $x$  typically making  $\Delta_m H(x)$  and  $\Delta_m G(x)$  asymmetrical (sub-regular mixtures) (**Figure 3.1d**). For temperatures  $T < T_c$ , the coexistence compositions  $x_1$  and  $x_2$  can be obtained from constructing a double tangent to the  $\Delta_m G$  curve. The fact that it is not the minimum values that correspond to the stable compositions but the points of tangency is due to mass conservation which has to be fulfilled. When considering the kinetics of de-mixing, it is relevant to distinguish between regions of positive and negative curvature. In the middle of the phase diagram (**Figure 3.1d, region I**, region between the two inflection points), the curvature is negative such that an infinitesimal compositional fluctuation leads to a decrease in  $\Delta_m G$  and hence to spontaneous de-mixing (this region is called regime of spinodal decomposition). In the two neighboring regions (**Figure 3.1d, region II**, region between  $x_1$  and  $x_2$  where the curvature is positive), a sufficiently large variation in composition is needed to drive de-mixing. In other words, decomposition requires

nucleation and transport of longer range to bring the system into the thermodynamically favored compositional range. It follows that  $T_c$  can be evaluated as the temperature at which the two inflection points coincide (meaning that at the critical composition the third derivative is zero).

The above treatment (Eq. 3.3, 3.4) assumes random distribution of atoms, which is inconsistent with assuming a non-zero interaction energy. A better approach is to only assume random distribution of pairs, and to partially account for the non-zero interaction energy in the evaluation of the enthalpy and entropy of mixing by applying a mass action law for Eq.3.1. The latter approach is termed quasi-chemical approximation and results in a more complex, but more accurate, formulation, in which complete randomness is not assumed. Accurate statistical treatments are very involved. A particular shortcoming of the above treatment is its referring to pair potentials which is not sufficient for coulombic systems. A further shortcoming is the neglect of gradient effects. The latter point has been addressed by the Cahn-Hilliard treatment. Here the free enthalpy exhibits, beyond the homogeneous term (no gradients), a correction term being proportional to  $\int(\nabla c)^2 dV$  (where  $\nabla c$  is effectively the gradient in local composition, which is integrated in the volume of the system). In terms of pair considerations, this is essentially referring to the fact that, in a non-zero compositional gradient, the pair interactions to the “left” are different from the pair interactions to the “right”, as already pointed out by Becker<sup>128</sup>. This theory is more precise in describing the correct transitions between spinodal and binodal behavior. It is also able to predict the influence of the “domain size” in mixtures (see **Figure 3.2**), whereby an additional contribution to the free enthalpy of mixing due to the surface energy associated with the formation of domain boundaries appears in the balance.

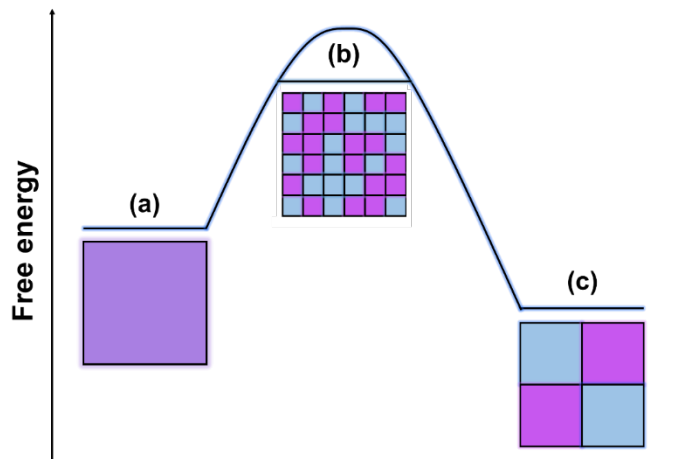


**Figure 3.2.** Schematic of the free energy of a mixture with composition that lies within the miscibility gap for various domain sizes. The influence of domain size is qualitatively shown. (a) Mixed single phase state (atomic “domain size”); (b) de-mixed two-phase state with nanoscopic domain size; (c) de-mixed two-phase state with macroscopic domain size.



## IV MATERIALS AND METHODS





## 4 Materials and methods

### 4.1 Materials and synthesis

**Materials:** Lead iodide ( $\text{PbI}_2$ , 99.9985%) and lead bromide ( $\text{PbBr}_2$ , 99.999%) were purchased from Alfa Aesar. Methylammonium iodide (MAI) and Methylammonium bromide (MABr) were synthesized as reported by Im *et al.*<sup>129</sup> Butylamine Hydroiodide ( $\text{C}_4\text{H}_{11}\text{N} \cdot \text{HI}$ , 97%) was purchased from TCI. 1,4-phenylenedimethan ammonium iodide ((PDMA) $\text{I}_2$ ) spacer, 1,4-phenylenedimethan ammonium bromide ((PDMA) $\text{Br}_2$ ) spacer were synthesized following the procedure reported for the (PDMA) $\text{I}_2$  spacer<sup>130</sup> and the one described below. Dimethylsulfoxide (DMSO, 99.9%), Dimethylformamide (DMF, 99.8%) and Poly(methyl methacrylate (PMMA, average Mw  $\sim 120000$ ) were purchased from Sigma-Aldrich. Chlorobenzene (CB, 99.9%) was purchased in Acros organics. Single crystal sapphire (orientation: (0001), C-plane; single polished and double polished) and quartz (molten isotropic quartz) were purchased from CrysTec.

**Synthesis of 2D (PDMA) $\text{Pb}(\text{I}_{1-x}\text{Br}_x)_4$  precursor solutions:** The precursor solutions with Br content of 0%, 10%, 15%, 20%, 30%, 40%, 50%, 60%, 70%, 80%, 90% and 100% were prepared following the relative stoichiometry of the halides. Specifically, 0.33 M (PDMA) $\text{PbI}_4$  or (PDMA) $\text{PbBr}_4$  solutions were prepared by dissolving 0.33 mmol (PDMA) $\text{I}_2$  ((PDMA) $\text{Br}_2$ ) and 0.33 mmol  $\text{PbI}_2$  ( $\text{PbBr}_2$ ) in the solvent mixture of DMF and DMSO (3:2, (v:v), 200  $\mu\text{L}$ ). The precursor solutions for  $x = 0.1, 0.15, 0.2, 0.3, 0.4, 0.5$  were prepared by dissolving (PDMA) $\text{I}_2$ ,  $\text{PbI}_2$ , and  $\text{PbBr}_2$  with stoichiometry of 1: (1-2x): 2x. For  $x = 0.6, 0.7, 0.8, 0.9$ , (PDMA) $\text{Br}_2$ ,  $\text{PbI}_2$ , and  $\text{PbBr}_2$  with stoichiometry of 1: (2-2x): (2x-1) were used.

**Preparation of 2D (PDMA) $\text{Pb}(\text{I}_{1-x}\text{Br}_x)_4$  films:** The film preparation procedure was conducted in Ar-filled glovebox with controlled atmosphere ( $\text{O}_2$  and  $\text{H}_2\text{O} < 0.1$  ppm). The (PDMA) $\text{Pb}(\text{I}_{1-x}\text{Br}_x)_4$  films were deposited on quartz substrate by spin coating the precursor solution at 9 rps and 66 rps for 2s and 48s, respectively. The films were annealed at 150  $^\circ\text{C}$  for 10 minutes. A PMMA encapsulation layer was deposited on perovskite films, unless stated otherwise, by drop casting a PMMA solution (10 mg/ml, dissolved in chlorobenzene). The coated sample was dried at 40  $^\circ\text{C}$  for 2 hours in the glovebox.

**Synthesis of 3D  $\text{MAPb}(\text{Br}_x\text{I}_{1-x})_3$  precursor solutions:** The mixed iodide-bromide perovskites precursors were prepared by dissolving (1-x) mmol MAI and (1-x) mmol  $\text{PbI}_2$  and x mmol MABr and x mmol  $\text{PbBr}_2$  ( $x=0.0, 0.1, 0.2, 0.3, 0.4, 0.5, 0.6, 0.7, 0.8, 0.9, 1.0$ ) in 1 ml DMSO. After that, the as prepared  $\text{MAPb}(\text{Br}_x\text{I}_{1-x})_3$  precursor solution was filtered by using a PTFE filter (0.45  $\mu\text{m}$ , Whatman) for preparation of the thin film.

**Preparation of 3D  $\text{MAPb}(\text{Br}_x\text{I}_{1-x})_3$  film :** All procedures in this part were conducted in Ar-filled glovebox with well controlled atmosphere ( $\text{O}_2$  and  $\text{H}_2\text{O} < 0.1$  ppm). The  $\text{MAPb}(\text{Br}_x\text{I}_{1-x})_3$  precursor solution are deposited on the  $\text{Al}_2\text{O}_3$  (001) substrate by spin coating

the as synthesized precursor solution at 65 rps and 150 rps for 2s and 180s on Al<sub>2</sub>O<sub>3</sub> substrates. During the spin coating, a 650  $\mu$ L chlorobenzene drop was dropped on the substrate to induce a quick crystallization. Lastly, the films are annealed at 373 K for 2 minutes. PbI<sub>2</sub> and PbBr<sub>2</sub> thin film are prepared using the same procedure. A PMMA encapsulation layer was deposited on perovskite films for encapsulation experiments by drop casting a PMMA solution (10 mg/ml, dissolved in chlorobenzene). The coated sample was dried at 40 °C for 2 hours in the glovebox.

***Synthesis of nanocrystalline BA-MAPb(Br<sub>0.5</sub>I<sub>0.5</sub>)<sub>3</sub> precursor solutions:*** BA based mixed Iodide and bromide halide nanocrystal perovskites precursor were prepared by dissolving 2 mmol MAI, 0.5 mmol PbI<sub>2</sub>, 1.5 mmol PbBr<sub>2</sub> and 0.4 mmol BAI in 2 ml DMF.

***Synthesis of nanocrystalline BA-MAPb(Br<sub>0.5</sub>I<sub>0.5</sub>)<sub>3</sub> thin films:*** The film preparation procedure was conducted in Ar-filled glovebox with controlled atmosphere (O<sub>2</sub> and H<sub>2</sub>O < 0.1 ppm). The BA-MAPb(Br<sub>0.5</sub>I<sub>0.5</sub>)<sub>3</sub> nanocrystal thin films were deposited on sapphire substrate by spin coating the precursor solution at 100 rps for 60 s. a 300  $\mu$ L chlorobenzene drop was dropped at the time of being spun for 6s to induce a quick crystallization. The films were annealed at 65 °C for 5 minutes.

## 4.2 Experimental apparatus and techniques

### ***Optical microscope measurements:***

The OLYMPUS DSX510 digital microscope in glovebox is used for imaging the morphology of the thin film before illumination, after illumination and after SEM measurements. Dark field imaging mode is used.

### ***SEM measurements:***

The samples are transferred via vacuum shuttle from argon glove box after optical microscope imaging to a Zeiss Merlin scanning electron microscope, which is used for imaging the change in morphology down to the nanometer scale. Four independent electron detectors are used to obtain comprehensive information of the perovskites film: 1) Chamber secondary electron detector (Everhardt-Thornley), 2) In-lens secondary electron (SE) detector (available for < 20 keV), 3) In-lens backscattered electron (BSE) detector (available for < 20keV), 4) 4-segment low-angle scattered electron detector. Accelerating voltage of 1.5 kV was used for the measurement.

### **Focus Ion Beam (FIB) Processing:**

Focused Ga Ion Beam processing was used to prepare thin lamella for TEM investigation. Beam-parameter for preparation the blank (cutting of the lamella from substrate): 30kV10nA. Beam-parameter for preparation the rough lamella: 30kV 2nA. Final polishing with 30kV 200pA/ and 30kV 50 pA.

### ***TEM-EDX measurements:***

The TEM-EDX measurements are conducted with JEOL ARM 200CF: Scanning transmission electron microscope equipped with a cold field emission electron source, a DCOR probe corrector (CEOS GmbH), a 100 mm<sup>2</sup> JEOL Centurio EDX Detector, and a Gatan GIF Quantum ERS electron energy-loss spectrometer.

**Ultraviolet–Visible (UV-Vis) spectroscopy experiment under controlled conditions:** UV-Vis experiments were conducted using a Shimadzu UV-2600 spectrometer. The setup was modified to achieve control of the sample temperature (1 °C accuracy) and atmosphere (< 30 ppm O<sub>2</sub>). A LED lamp (MCWHF<sub>2</sub>, Thorlabs) coupled to an optical fiber was used for the illumination during the experiments. The light intensity was measured directly at the exit of the optical fiber using a thermal power meter (PM100 D, Thorlabs).

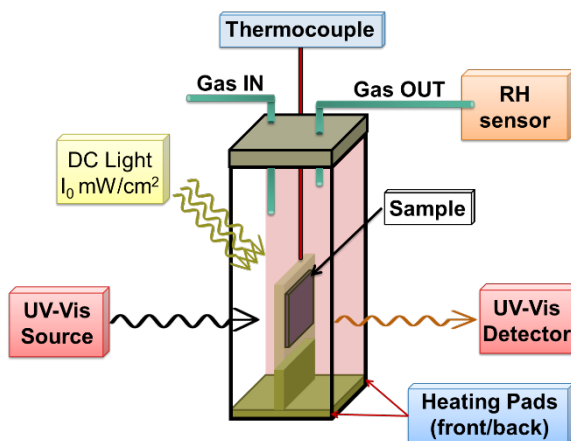


**Figure 4.1.** Schematic of UV-Vis set up under controlled condition.

To estimate the exact light intensity shined on the sample during the experiments, we conducted the calibration as follows (**Figure 4.2**).

$$I = \frac{\left(\frac{D_1}{2}\right)^2}{\left(\frac{a \cdot \tan(\alpha + \beta) - a \cdot \sin(\alpha - \beta)}{2}\right)^2} I_0. \quad \text{Eq. 4.1}$$

where:

$I_0$ : incident light intensity measured directly after the optical fiber;

$I$ : calibrated light intensity hitting the sample;

$D_1$ : diameter of the optical fiber;

$a$ : vertical distance of the optical fiber and the sample;

$\alpha$ : Acceptance angel of the optical fiber ( 22.95° in this case);

$\beta$ : illumination angel of the optical fiber ( 45° in this case);

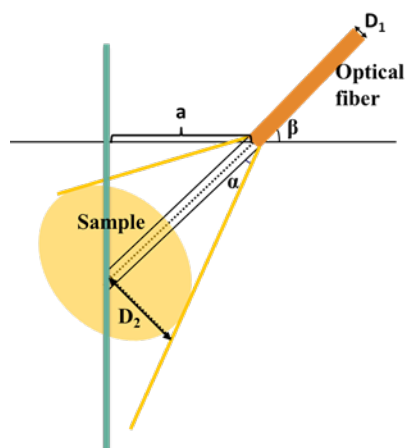


**Figure 4.2.** Calibration of light intensity

Modulation of the bias light to allow for UV-Vis measurements was performed to show in **Figure 4.3**. For each cycle, light was switched on for 900 s followed by a 300 s dark window, during which the UV-Vis measurements were taken.

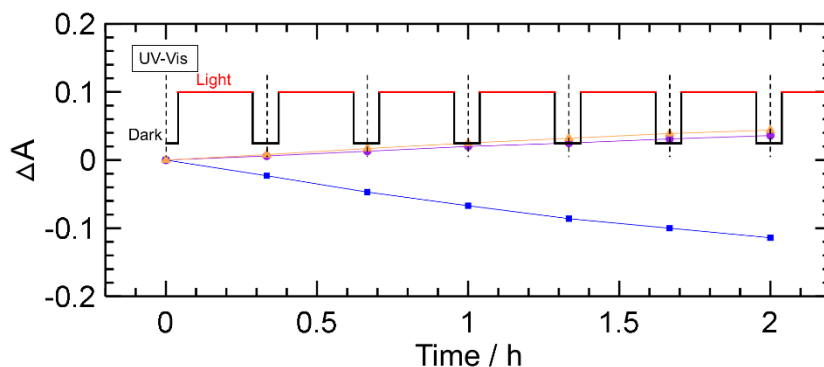


**Figure 4.3.** Representation of the bias light modulation during photo de-mixing experiments (three complete cycles per hour). The black dashed lines indicate the times where the UV-Vis measurements were taken. The blue, yellow and purple data points correspond to the changes in absorbance evaluated by means of the UV-Vis measurements.

**X-Ray Diffraction (XRD):** All the XRD patterns were acquired by a PANalytical diffractometer of Empyrean Series 2 (Cu K $\alpha$  radiation, 40 kV, 40 mA) equipped with a parallel beam mirror and a PIXcel 3D detector. All measurements were conducted in Bragg-Brentano or grazing incidence configuration modules with programmable divergence slits. The Anti scatter slits were used and recorded with a PIXcel 3D detector. The samples that were not encapsulated were mounted in a polycarbonate domed sample holder for protection from ambient atmosphere during the measurements (Panalytical).

## ELECTRICAL MEASUREMENTS

D.C. galvanostatic polarisation measurements were carried out with a Source Meter(Keithley 6430). A.C. impedance spectroscopy data were acquired with Novocontrol Alpha A with electrochemical interface. The impedance data are analyzed in Z view. Two

types of different in-house built measurement cells for characterizing the electrical properties of the materials have been set up.

*Measurement cells for different  $p(\text{Br}_2)$  measurements (Relevant to Chapter 5):*

$\text{Br}_2$  gas have high vapor pressure. The temperature at which  $\text{I}_2$  and  $\text{Br}_2$  present vapor pressure of  $10^{-7}$  bar is  $-50\text{ }^\circ\text{C}$  and  $-130\text{ }^\circ\text{C}$ , respectively.<sup>131</sup> To obtain low partial pressure suitable for  $\text{Br}_2$  partial pressure dependent electrical measurements in Chapter 5, low temperature and gas diluting strategies are used. For the former, a home-made cooling system was implemented. A spiral-shaped cooler element (Thermo Scientific EK 45) immersed in a coolant is used to obtain a temperature of  $-80\text{ }^\circ\text{C}$ . To improve the temperature stability problem, a low power heating element is applied to the system, obtaining a temperature range of  $80 \pm 1\text{ }^\circ\text{C}$ . For the latter, different ratios of Ar carrier gas containing  $\text{Br}_2$  and pure Ar gas are mixed to gain an extra 2 order of magnitude decrease of the  $\text{Br}_2$  partial pressure (See **Figure 4.4** for the design of the  $\text{Br}_2$  set up). Via these two strategies,  $\text{Br}_2$  partial pressure range of  $1 \times 10^{-6}$  bar to  $1 \times 10^{-4}$  bar can be obtained. One should also note it is important to a constant flow of the gas mixture of 100 SCCM used in the measurements cell is maintained for all experiments.

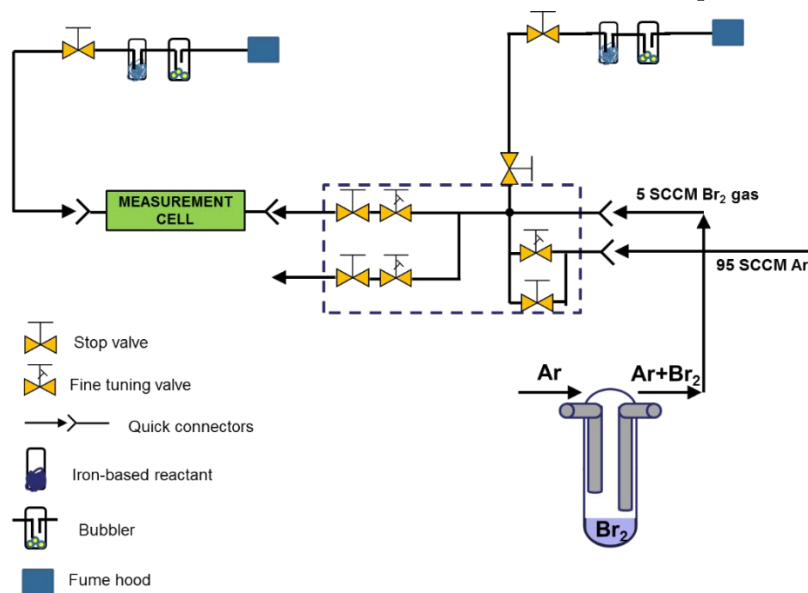


**Figure 4.4.** Schematic for the  $\text{Br}_2$  set up. The gas mixture with 5SCCM  $\text{Br}_2$  and 95 SCCM Ar was used to get a  $p_2(\text{Br}_2)$  of  $5 \times 10^{-6}$  bar.

$\text{Br}_2$  gas also has very high reactivity even at very low partial pressure, which makes corrosion of all other materials being exposed to it a critical issue. This presents challenges for designing the appropriate cells for this measurement. **Figure 4.5** show the the design of such measurement cell with good control of the gas atmosphere and temperature. The main body of the measurement cell (in grey) is constcuted with stainless steel, which had been proved to be resistant to  $\text{Br}_2$  gas the most. Quartz are used for covering the remaining part of the cell, ensuring a gas tight atmosphere.

For electrical measurements, platinum thin wires and copper beryllium coated (additionally coated with Au) contact are utilized. A thermocouple close to the sample is used to constantly monitoring the temperature of the sample. However, even given the best effort to avoid the reaction of  $\text{Br}_2$  gas with other materials of the cell, possible reaction cannot be fully ruled out. Therefore, it is very important to check the ‘health condition’ of the sample by evaluating reversibility of the measurements.

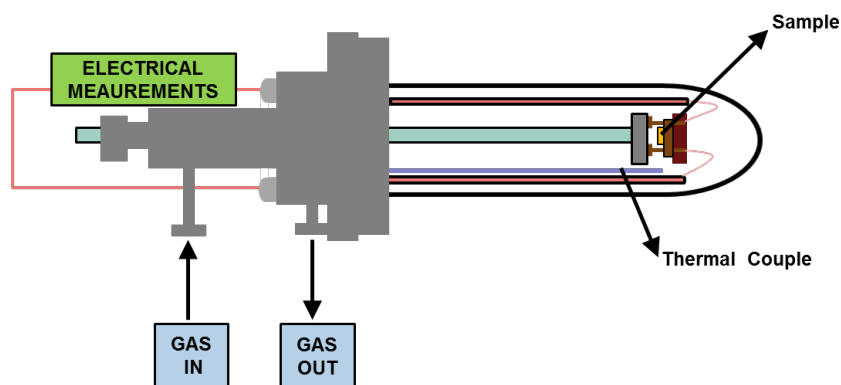


**Figure 4.5.** Schematic for the measurement cell for  $\text{Br}_2$  partial pressure measurements.

*Measurement cell for Photo de-mixing measurements (Relevant to Chapters 7 & 8):*

The measurement cell that could allow for characterizing optical and electrical properties of the materials at controlled temperature, atmosphere and light intensity is shown in **Figure 4.6**.

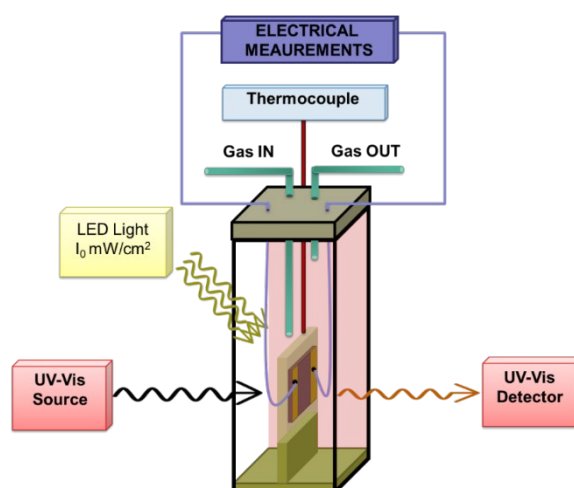


**Figure 4.6.** Schematic for the measurement cell for UV-Vis & Electrical measurements

*Interdigitated electrode for electrical measurements:*

Interdigitated electrode are used for the electrical measurement with the electrode geometry shown in **Figure 4.7**. For 3D halide perovskites, including  $\text{MAPbBr}_3$  and  $\text{MAPb}_{(0.5)\text{Br}_{0.5}}_3$ , electrode geometry of  $L = 10 \mu\text{m}$ ,  $L_c = 5 \mu\text{m}$  and  $W = 80 \mu\text{m}$  is used. For 2D

halide perovskites, including (PDMA)PbBr<sub>4</sub> and (PDMA)Pb(I<sub>0.5</sub>Br<sub>0.5</sub>)<sub>4</sub>, the electrode geometry of L= 5 μm, L<sub>c</sub> = 5 μm and W = 120 μm is used.

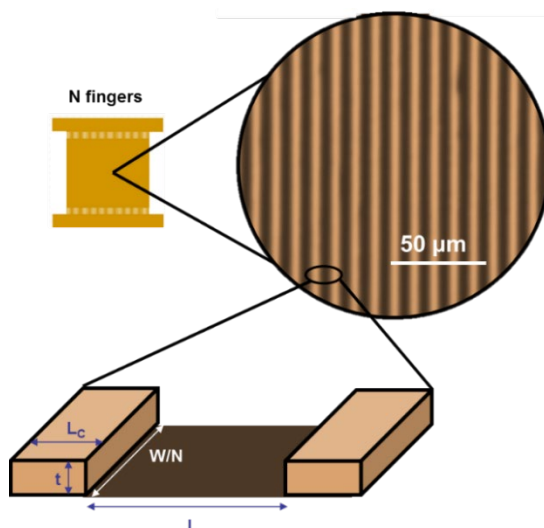


**Figure 4.7.** Schematic for the interdigitated electrode for electrical measurements. L: channel length; L<sub>c</sub>: finger width; t: thickness of the Au fingers; W: overlapping lengths of the fingers; N: number of the fingers.

#### 4.3 Evaluation of the partial conductivities

Chemical diffusion in ionic compounds refers to a charge neutral ambipolar diffusion of at least two chemically different charge species.<sup>132-134</sup> A driving force for such a diffusion can be a voltage difference or a chemical potential difference applied over the material. An internal gradient in stoichiometry is built up over the time, which involves a combination of ionic and electronic transport. Therefore, measuring diffusion process allows us to disclose important information on the mixed ionic – electronic nature of the conductivity in a mixed conductor.<sup>132, 135</sup> DC galvanostatic polarization measurements are helpful for such evaluation in time domain, while impedance characterization allows for such analysis in the frequency domain. I now discuss how the partial conductivities are evaluated with taking MAPbBr<sub>3</sub> as an example (see Chapter 5) and using the electrode geometry discussed above (horizontal device, **Figure 4.7**).<sup>134, 136, 137</sup> **Figure 4.8** shows the DC galvanostatic polarization measurements of MAPbBr<sub>3</sub> thin film measured with ionic blocking electrode. Immediately after applying a constant current, both electrons and ions contributes to the conduction according to their transference number. The initial IR drop (voltage increase,  $U_1 = IR_{tot}$ ) corresponds to the total resistance where both electronic and ionic charge carriers are contributing. With increasing of the time, the partial current of the ionic charge carriers decreases until (ion blocking electrode used) it is completely vanished. Once the steady state is reached ( $U_2 = IR_{eon}$ ), the current is only contributed by the electronic charge carriers.<sup>134, 138</sup> Therefore, ionic and electronic conductivities can be calculated based on ( $\frac{1}{R_{tot}} = \frac{1}{R_{eon}} + \frac{1}{R_{ion}}$ ,  $\sigma = \frac{L}{R \times t \times W}$ ). The  $R_{tot}$  extracted from the initial jump in the DC

measurement depends on time resolution of the instrument used, therefore, one needs to resort to frequency resolved impedance to obtain accurate  $R_{tot}$  by fitting the high frequency semicircle to the equivalent circuit model discussed below.<sup>136</sup> The impedance shown in **Figure 4.8b** involves different processes that can be modeled based on the equivalent circuit that includes bulk and interfacial processes. 1) in the high frequency regime (1E06 Hz - 400 Hz), equivalent circuit = Par ( $R_{eon}$ ,  $R_{ion}$ ,  $C_{bulk}$ ), which results in the first semicircle in the Nyquist plot (Par: parallel,  $R_{eon}$ : electronic resistance,  $R_{ion}$ : ionic resistance,  $C_{bulk}$ : bulk capacitance). The dielectric constant of 280 is calculated based on  $C_{bulk}$  ( $2.48 \text{ E-}08 \text{ F/cm}^2$ ). Such value is higher than the typical value of the halide perovskites, indicating that substrate have a dominant contribution to  $C_{bulk}$ . 2) In the mid-frequency range (15 Hz – 0.03 Hz), equivalent circuit = Ser(Par( $R_{inf}$ ,  $C_{inf}$ ), Par( $R_{bulk}$ ,  $C_{bulk}$ )) (Ser: series,  $R_{inf}$ : interfacial resistance,  $C_{inf}$ : interfacial capacitance ). In such case, an interfacial capacitance of  $1.13\text{E-}04 \text{ F/cm}^2$  is obtained. 3) At low frequencies (0.03 Hz -0.001 Hz), equivalent circuit = Ser(Par( $R_{inf}$ ,  $C_{inf}$ ), Par(Par( $R_{eon}$ , Ser( $R_{ion}$ ,  $C_{ion}$ )),  $C_{bulk}$ )). In this case, a chemical capacitance  $C_{ion} = 1.25\text{E-}04 \text{ F/cm}^2$  is obtained. The electronic resistance obtained from DC polarization and impedance is similar, therefore, the equivalent circuit model mentioned above can well describe such electrochemical response. For situations where the interfacial capacitance at electrode / perovskite interface dominates, the same equivalent circuit can be used. And  $C_{ion}$  can be interpreted as an interfacial capacitance.<sup>136</sup>

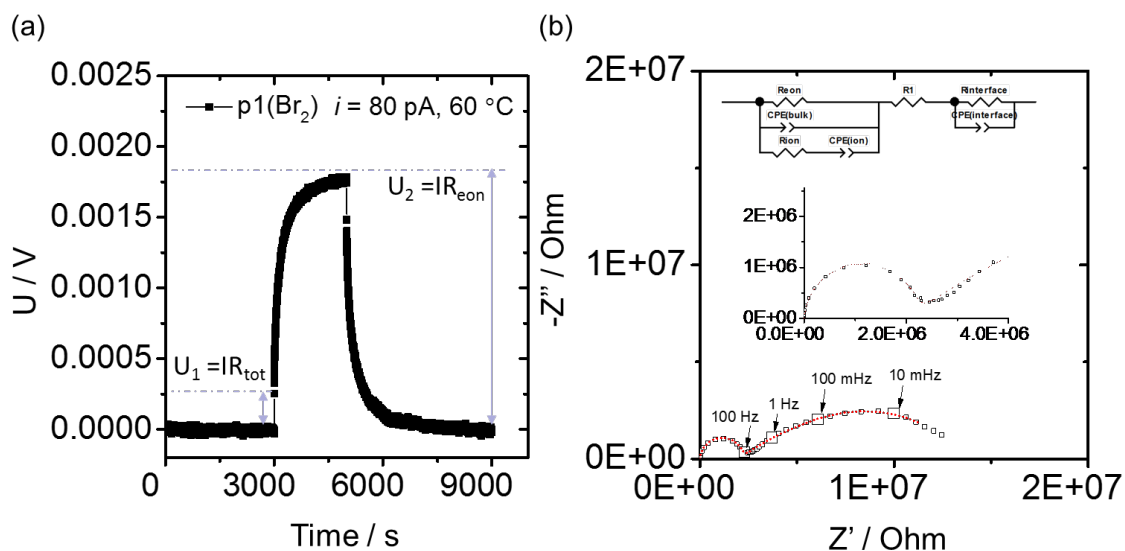


**Figure 4.8.** Electrochemical response of MAPbBr3 thin film measured with ionic blocking electrode (Au, see section 4 for electrode geometry) under  $p_1(\text{Br}_2) = 1\text{E-}06$  bar in the dark at 60 °C. (a) DC galvanostatic polarization measurement when applying current (80 pA) for 3000 s (b) Nyquist plot of impedance spectra (frequency range:  $1\text{E}06 - 1\text{E-}03$ ) after reaching equilibration under such bromine partial pressure and the corresponding equivalent circuits. The read dashed line indicate the fitting of the data.



## V RESULTS AND DISCUSSIONS



## 5 Defect chemistry equilibria in bromide and iodide perovskites

### 5.1 Introduction

Ion migration is a key material property of hybrid halide perovskites.<sup>55</sup> It influences the response of devices based on these materials and it is critical for their stability against illumination, humidity, or heat.<sup>8, 139-142</sup> Understanding the equilibrium charge carrier chemistry of organic-inorganic halide perovskites is a prerequisite for understanding the ion transport behavior of these materials and finding the potential ways to modify it. The defect chemistry of MAPbI<sub>3</sub> has been extensively investigated.<sup>55-57, 126</sup> In this compound, the transport of iodide defects is the dominant factor regarding ionic conduction as discussed in Section 2.2.

Halide substitution<sup>33-35, 45-47</sup> and dimensionality control<sup>127, 143-146</sup> serve as effective methods to adjust the electrical and optical properties of the materials, and to optimize the performance of opto-electronic devices. Especially, mixing iodide and bromide perovskites is of interest, due to the favourable band gap range that becomes accessible through this approach, making this strategy relevant to several device applications (See Section 2.1 for detailed introduction).

In addition, halide substitution and dimensionality tuning can be used to vary the mixed ionic-electronic conducting properties of hybrid perovskites. Previous reports have shown that moving from iodide to bromide perovskite compositions leads to decrease in electronic conductivity and an increase in ionic conductivity.<sup>60</sup> Regarding dimensionality, a number of studies have pointed to a significant decrease in ion conduction in two-dimensional iodide perovskites compared to their three-dimensional counterparts.<sup>45, 147</sup> While these preliminary work showed that both iodide and bromide perovskites show generally similar properties, and that dimensionality reduction is a promising strategy to reduce ion conduction, a detailed investigation of the defect chemistry of bromide perovskites, in the 3D or 2D form, is currently missing.

In this chapter, I present the investigation of the mixed ionic-electronic conducting properties of 3D methylammonium lead bromide (MAPbBr<sub>3</sub>) and 2D Dion-Jacobson 1,4-phenylenedimethan ammonium lead bromide ((PDMA)PbBr<sub>4</sub>). Their electronic and ionic conductivities are measured as a function of varying stoichiometry (controlled via a fixed bromine partial pressure) and temperature. The incorporation and ex-corporation kinetics are investigated. Their properties are discussed in relation to iodide perovskites (3D methylammonium lead iodide (MAPbI<sub>3</sub>) and 2D Dion-Jacobson 1,4-phenylenedimethan ammonium lead iodide (PDMA)PbI<sub>4</sub>). Furthermore, this study highlights the range of the bromine partial pressure in which a reversible behavior of conductivities of bromide perovskites is observed.

## 5.2 Results and discussion

### 5.2.1 Bromine incorporation / ex-corporation and Defect equilibria in MAPbBr<sub>3</sub>

The measurements that I will discuss in the following text are conducted using specially designed cells to prevent Br<sub>2</sub> corrosion (see Section 4.2 and **Figure 4.5**, for detailed description). By using such setup, temperature and the gas flow and the components partial pressures are controlled (**Figure 4.4**), in order to measure the electrochemical properties of the material. Interdigitated gold electrodes that are ion blocking are used for electrical measurements (**Figure 4.7**, see detail electrode geometry in Section 4.2). In the following discussion, the transport properties of the material are evaluated by both DC galvanostatic polarization and impedance measurements.

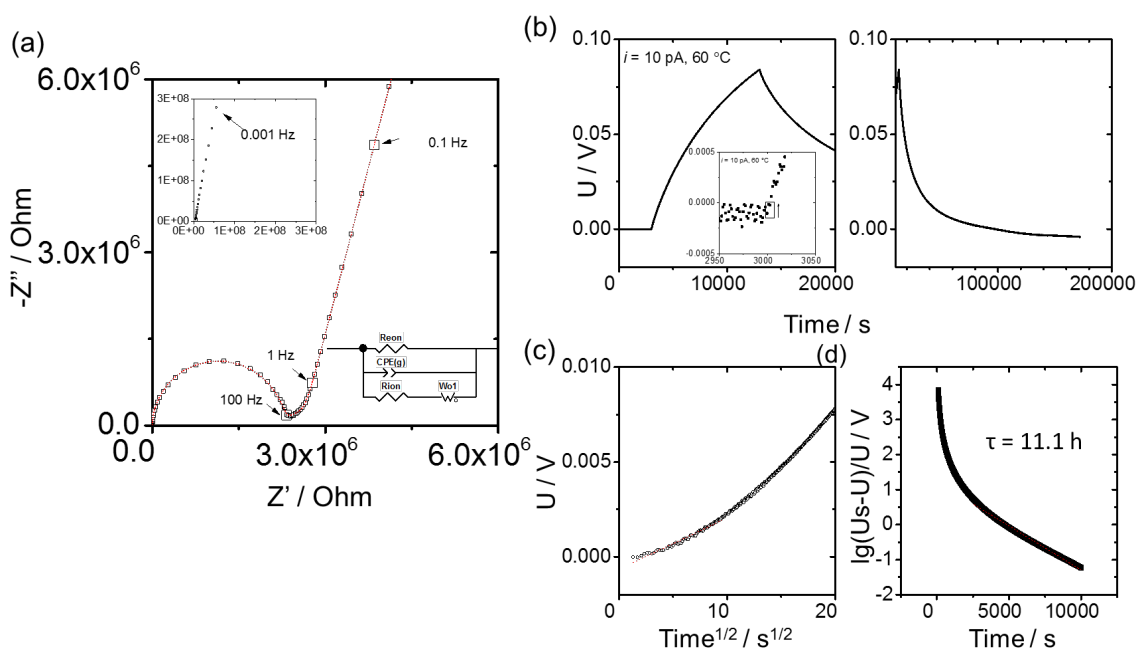


**Figure 5.1.** Electrochemical response of MAPbBr<sub>3</sub> thin film measured with ionic blocking electrode (Au, see section 4 for electrode geometry) under Ar in the dark at 60 °C. (a) Nyquist plot of impedance spectra (frequency range: 1E06 Hz – 1E-03 Hz) after reaching equilibration under Ar. The top left inset figure show the impedance in very low frequency range (0.1 Hz – 0.001 Hz). The bottom right inset figure show the corresponding equivalent circuits that is used to fit the impedance in frequency range of 1E06 – 0.1 Hz.<sup>136</sup> The red dashed line indicates the fitting of using such equivalent circuit to the data. (b) DC galvanostatic measurement: left, polarization (10pA is applied for 10000 s); right, de-polarization (160000s). The time resolution is 1 s. A baseline in voltage of 6 mV is subtracted from the raw data. (c) Short time scale polarization (Voltage vs the square root of time) and (d) long time scale polarization ( $-(U_s - U)/U$  vs time).  $U_s$  is a fitted value representing the saturation voltage when steady state of the polarization is reached.

Let us start with the electrochemical response of MAPbBr<sub>3</sub> thin film in Argon atmosphere (**Figure 5.1**). Impedance characterization allows one to measure the electrical

response in the frequency domain. **Figure 5.1a** shows that such impedance can be modelled by a bulk contribution at high frequencies followed by a low frequency process. DC galvanostatic polarization measurements are used to obtain such response in the time domain. Especially, from the long time polarization behaviour of the material, one can evaluate the electronic charge carriers' properties (ion blocking electrode used). Over the time scale range probed with this measurement (1s – 10000 s) at the available resolution (1 s), the response on current application shows firstly a very tiny IR drop (inset, **Figure 5.1b**) followed by a large polarization with a steady state (not completely reached in this case) at which the ionic current can be assumed to be vanishing.<sup>134, 138</sup> This suggests a very small contribution from electronic charge carriers to the total conductivity, indicating that MAPbBr<sub>3</sub> is very ionic in nature. After switching off the current, a long de-polarization is observed, with a time constant of 40 ks estimated from the plot in **Figure 5.1c**.

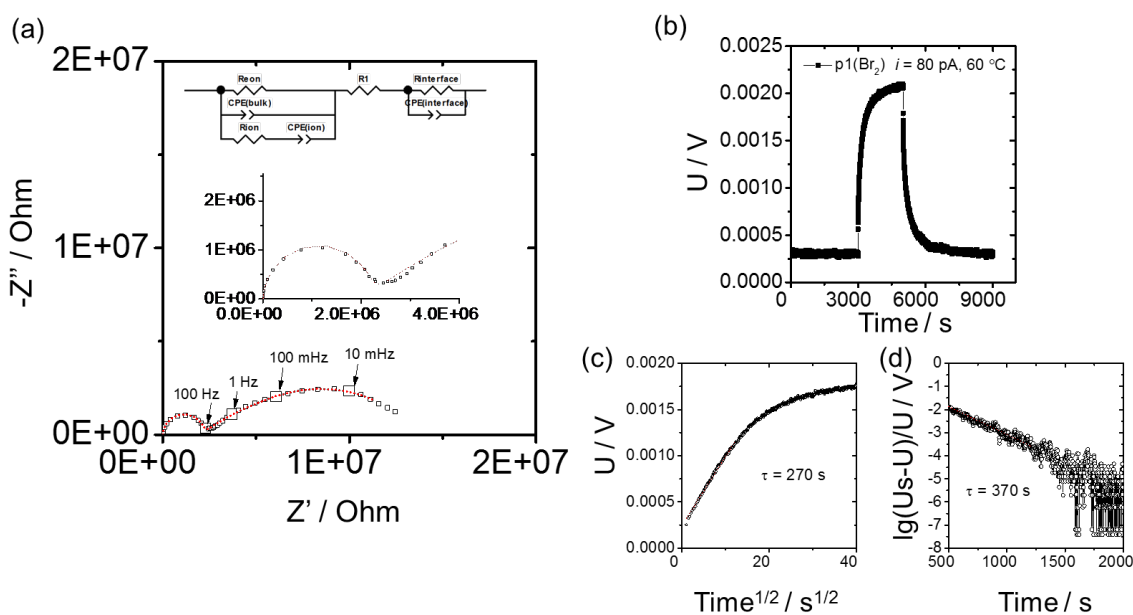
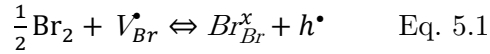


**Figure 5.2.** Electrochemical response of MAPbBr<sub>3</sub> thin film measured with ionic blocking electrode (Au, see section 4 for electrode geometry) under  $p_1(\text{Br}_2) = 1\text{E}-06$  bar in the dark at 60 °C. (a) Nyquist plot of impedance spectra (frequency range: 1E06 – 1E-03) after reaching equilibration under such bromine partial pressure and the corresponding equivalent circuits. The read dashed line indicate the fitting of the data. (b) DC galvanostatic polarization measurement when applying current(80 pA) for 3000 s. (c) Short time scale polarization (Voltage vs the square root of time) and (d) long time scale polarization( ( $U_s - U$ ) /  $U$ ) vs time).  $U_s$  represents the saturation value of the voltage when steady state of the polarization is reached. The time constants are extracted from two polarizations resulting in similar diffusion coefficients ( $D_{\text{short}_t} = 4.08 \text{ E}-10$  and  $D_{\text{long}_t} = 2.65\text{E}-10 \text{ cm}^2 / \text{s}$ ).

When MAPbBr<sub>3</sub> thin film is equilibrated under fixed partial pressure ( $p_1(\text{Br}_2)$ ), **Figure 5.2**), the electrochemical responses change significantly. The impedance (**Figure 5.2a**) show a combination of processes in the middle (15 Hz – 0.03 Hz) and low frequency (0.03 Hz -0.001

Hz), which is modelled by the equivalent circuits where both bulk and interfacial contributions are considered (See section 4.3). The DC galvanostatic polarization (**Figure 5.2b**) exhibits a much shorter time constant  $\tau^\delta$  ( $p_1(\text{Br}_2) = 400 \text{ s}$ ) compared with the argon case (10 ks). The equivalent circuit model is in agreement with the DC galvanostatic polarization measurements showing similar value of  $(R_{\text{eon}}+R_{\text{inf}})$ . Given the fact that  $R_{\text{inf}}$  is small, its effects on the electronic conductivities is very limited (20%).

Based on the above mentioned equivalent circuit models, the partial conductivities of electronic ( $\sigma_{\text{eon}}$ ) and ionic charge carriers ( $\sigma_{\text{ion}}$ ) are evaluated. The ionic conductivity of MAPbBr<sub>3</sub> measured in Ar is almost 4 orders of magnitude greater than the electronic conductivity (**Figure 5.3a**, left). Compared with their iodide counterparts (MAPbI<sub>3</sub>), MAPbBr<sub>3</sub> is much more ionic in nature and behaves more like a solid electrolyte. In addition, such value also indicate that, the mobility of the electronic charge carrier is very low. After exposing the sample to a fixed bromine partial pressure (from Argon to  $p_1(\text{Br}_2) = 1\text{E-}06 \text{ bar}$ ), incorporation of the halogen into the perovskites structure causes the electronic conductivity ( $\sigma_{\text{eon}}$ ) to increase by almost 3 orders of magnitude. This result is consistent with the MAPbBr<sub>3</sub> thin film exhibiting p-type conduction, with electron holes being majority electronic charge carriers. On the other hand, the ionic conductivity shows almost no change when changing the atmosphere from argon to  $p_1(\text{Br}_2)$ . A possible explanation for the observed change is that MAPbBr<sub>3</sub> is intrinsic. In analogy with the study of MAPbI<sub>3</sub>, I hypothesize that ionic conduction in MAPbBr<sub>3</sub> is dominated by bromide vacancies. The incorporation of bromine in its structure should then occur via reducing the concentration of bromide vacancies and increasing the concentration of holes.



The properties of this exchange are investigated further by tracking the kinetics of the change in total resistance during bromine incorporation (**Figure 5.3 b**). To test the reversibility of this process, the atmosphere to which the sample is reverted back to argon. After bromine ex-corporation (from  $p_1(\text{Br}_2) = 1\text{E-}06 \text{ bar}$  to Ar), both electronic and ionic conductivities show rather reversible change (**Figure 5.3 a**, right). Such reversible change is also reflected in terms of the ionic resistance kinetics during bromine ex-corporation (**Figure 5.3 c**). Similar time constant ( $\tau^\delta$  ( $\text{Br}_2$ , in-corporation) = 6.2 h,  $\tau^\delta$  ( $\text{Br}_2$ , ex-corporation) = 5.7 h) are found.

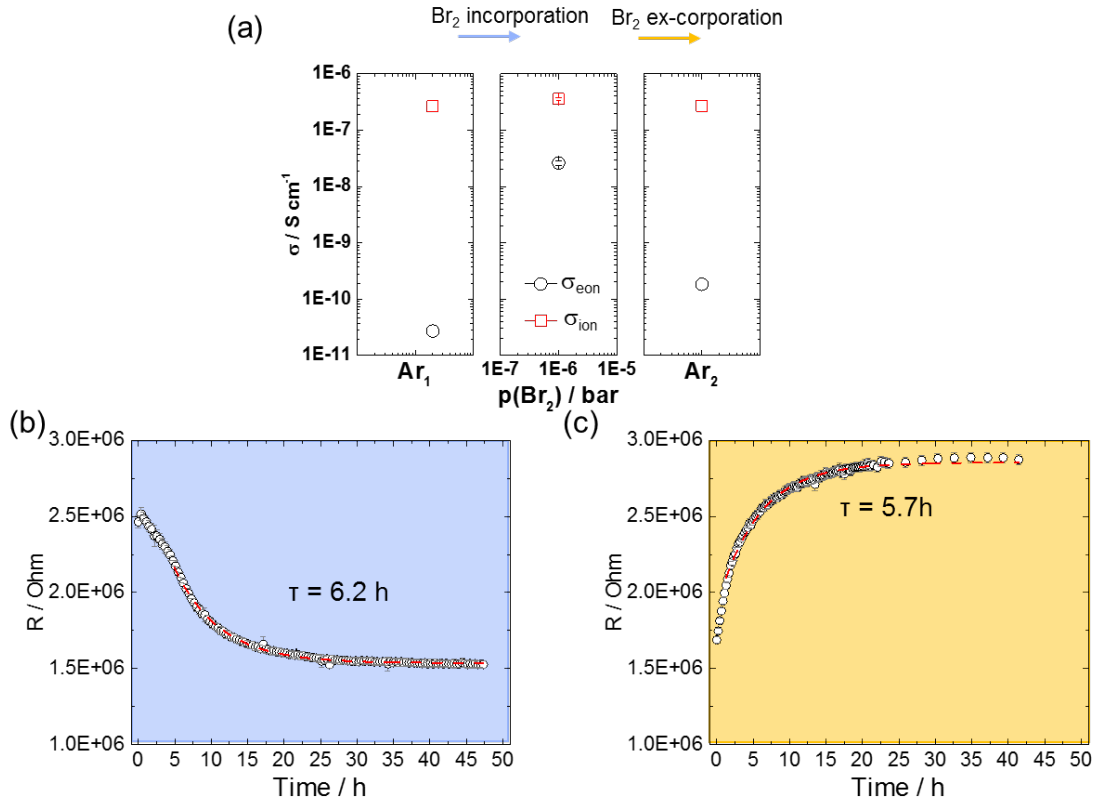


**Figure 5.3.** Bromine incorporation (from argon to  $p_1(\text{Br}_2) = 1\text{E}-06$  bar) and ex-corporation (from  $p_1(\text{Br}_2) = 1\text{E}-06$  bar to Ar) in MAPbBr<sub>3</sub> thin film. (a) Change in electronic and ionic conductivities; (b) incorporation kinetics; (c) ex-corporation kinetics. Such kinetics was evaluated by tracking the fitted value of resistance associated with the first semicircle of the impedance spectrum as function of time after the change in atmosphere was applied. Measurements are conducted at 60 °C.

To further vary the stoichiometry of MAPbBr<sub>3</sub> and to probe the behavior of the material over controlled changes in bromine partial pressure, a higher bromine partial pressure ( $p_2(\text{Br}_2) = 5\text{E}-06$  bar) is applied (**Figure 5.4, 5.5**). Similar equivalent circuit model was intended to be used for the impedance measurements performed under such conditions. However, this was not successful, due to the fact that in the mid-frequency range the data does not fit  $\text{Par}(R_{\text{inf}}, C_{\text{inf}})$ . This can be due to some complicated boundary response in such frequency range that need further clarification. Since the resistance contribution in this region is not significant compared with the total electronic resistance, this problem does not influence the evaluations of the electronic and ionic conductivities very much.

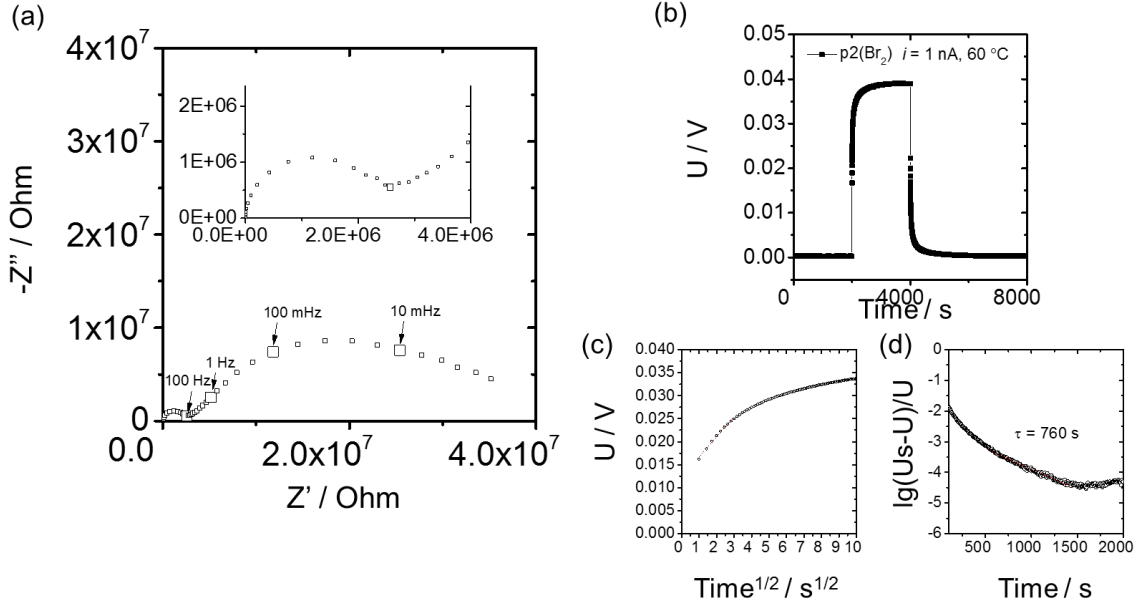


**Figure 5.4.** Electrochemical response of MAPbBr<sub>3</sub> thin film measured with ionic blocking electrode (Au, see section 4 for electrode geometry) under  $p_2(\text{Br}_2) = 5\text{E-}06$  bar in the dark at 60 °C. (a) Nyquist plot of impedance spectra (frequency range:  $1\text{E}06 - 1\text{E-}03$ ) after reaching equilibration under such bromine partial pressure. (b) DC galvanostatic polarization measurement when applying current (1 nA) for 3000 s. (c) Short time scale polarization (Voltage vs the square root of time) and (d) long time scale polarization ( $(U_s - U)/U$  vs time).  $U_s$  represents the saturation value of the voltage when steady state of the polarization is reached.

Similar to the data collected at lower partial pressure, the electronic conductivity increases upon bromine exposure while the ionic conductivity shows a slight increase (**Figure 5.5 a**). The incorporation kinetics is around three times faster (**Figure 5.5b**). This appears to imply that such incorporation process is surface controlled. If it is diffusion controlled, instead, this value should show negligible change for a film thickness of 200 nm. Notably, after a significant drop in the value of the total resistance after equilibration at  $p_2(\text{Br}_2)$ , a slight increase over long times is detected, suggesting slow changes in the sample properties that are not related with reaction R1. The sample's conductivities show a similar behavior as the one illustrated in **Figure 5.3**. On the other hand, when the atmosphere is reverted back to argon, the ex-corporation kinetics show in this case a more complicated behavior (**Figure 5.5c**). In particular, the total resistance after bromine incorporation (last point in **Figure 5.5b**) is smaller than the value of such resistance at the beginning of bromine ex-corporation, implying that during the galvanostatic measurements under  $p_2(\text{Br}_2) = 5\text{E-}06$  bar, the total resistance has increased (**Figure 5.5c**). This suggests that a slow change in properties occurred while the sample was left at  $p_2(\text{Br}_2)$ . Given the fact that reversible change in conductivities is observed when the sample is further equilibrated in argon, there is no evidence that such changes are associated with significant degradation of the sample under investigation. One may also note



that the total resistance after bromine incorporation (last point in **Figure 5.5b**) is smaller than that at the beginning of bromine ex-corporation, implying that during the galvanostatic measurements under  $p_2(\text{Br}_2) = 5\text{E-}06$  bar, the total resistance increases. To account for such changes in the calculation of the electronic and ionic conductivities, the error bar (middle figure, **Figure 5.5a**) is introduced and calculated by using the two values.

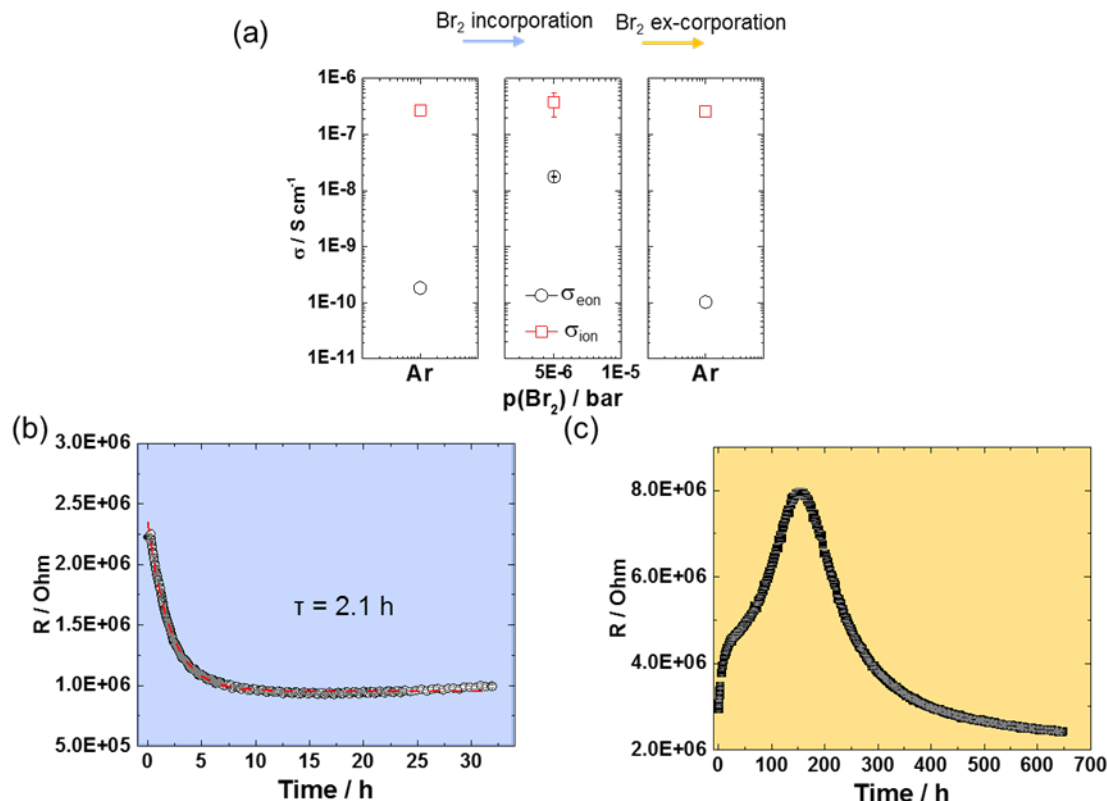


**Figure 5.5.** Bromine incorporation (from argon to  $p_2(\text{Br}_2) = 5\text{E-}06$  bar) and ex-corporation (from  $p_2(\text{Br}_2) = 5\text{E-}06$  bar to Ar) in  $\text{MAPbBr}_3$  thin film. (a) Change in electronic and ionic conductivities; (b) incorporation kinetics; (c) ex-corporation kinetics. Such kinetics was evaluated by the fitting of the first semicircle of the impedance spectra. Measurements are conducted at  $60^\circ\text{C}$ .

The dependence of the electronic and ionic conductivities on bromine partial pressure are further validated by repeating measurements in Ar,  $p_1(\text{Br}_2)$  and  $p_2(\text{Br}_2)$  after the above mentioned measurements (**Figure 5.6a**). The increase of the  $p(\text{Br}_2)$  from  $1\text{E-}06$  bar to  $5\text{E-}06$  bar gives rise to a relatively reproducible trend in the  $p(\text{Br}_2)$  dependence of the conductivities. Specifically, both electronic and ionic conductivities are found to decrease with increasing  $p(\text{Br}_2)$ . While for the ionic conductivity the change is relatively small considering the repeated measurements, the electronic conductivity clearly shows a negative slope with increasing  $p(\text{Br}_2)$ . This non monotonic change in electronic conductivity with increasing  $p(\text{Br}_2)$  seems inconsistent with a p-type conduction in the intrinsic region that I hypothesized for the bromide perovskite

based on the change in conductivity from argon to a fixed  $p(\text{Br}_2)$ . A more complex interaction between the bromine in the gas phase and the solid or the solid/contact interface need to be considered.

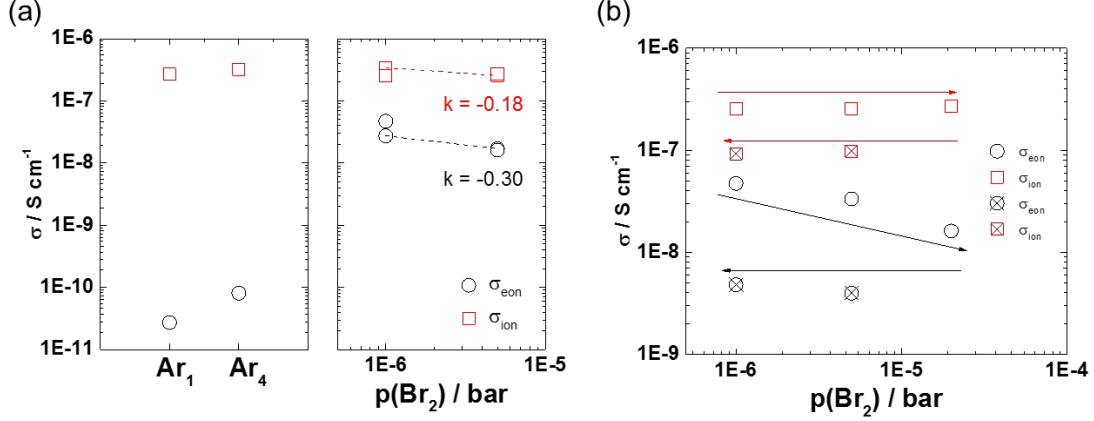
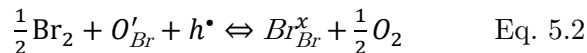


**Figure 5.6.** Bromine partial pressure dependence of electronic ( $\sigma_{\text{eon}}$ ) and ionic ( $\sigma_{\text{ion}}$ ) conductivities in MAPbBr<sub>3</sub> thin film (a) when a reversible range between  $p_1(\text{Br}_2) = 1 \text{ E-}06$  to  $p_2(\text{Br}_2) = 5\text{E-}06$  bar are measured; (b) irreversible range when  $p_3(\text{Br}_2)$  reaches  $2\text{E-}05$  bar. Measurements are conducted at  $60 \text{ }^\circ\text{C}$ .

The first straightforward hypothesis that there is a degradation process occurring on with bromine exposure. However, the reversibility shown in **Figure 5.3 a** and **Figure 5.5a** seems to contradict such hypothesis. In addition, the X-ray diffraction of 3D MAPbBr<sub>3</sub> thin film before and after exposure to bromide gas (measurements before and after  $\text{Ar} \rightarrow p_1(\text{Br}_2) = 1\text{E-}06 \text{ bar} \rightarrow \text{Ar}$ ,  $\text{Ar} \rightarrow p_2(\text{Br}_2) = 5\text{E-}06 \text{ bar} \rightarrow \text{Ar}$ ) in **Figure A.1.3a**(Supporting) show no change for the bulk properties (detected by measurements performed in Bragg-Brentano geometry). One also note that on the surface (detected by Grazing-incidence geometry), two small peaks emerged at the high diffraction angles (**Figure A.1.3a**). Since these peaks are at high angles and with very low intensity, it is difficult to determine their nature. These can potentially be attributed to the different orientations of the perovskite ((114) ( $2\theta = 37^\circ$ ) and (123) ( $2\theta = 41^\circ$ )).

Point defects doping effect in halide perovskites can also potentially induce such decrease in electronic conductivity with  $p(\text{Br}_2)$ . It is possible if bromide replaces an vacancy which requires more holes than bromide during incorporation, which oxygen is most likely involved. Oxygen incorporation have been discussed as an important influencing factor to the defect chemistry of halide perovskites.<sup>57</sup> At very high bromine partial pressure, the incorporation of bromine may result in the ex-corporation of  $\text{O}_2$  with the consumption of holes. Therefore, a decrease in electronic conductivity is possible.



The defect diagram in the appendix highlights this possibility. This explanation is however not consistent with the observed  $\sigma_{\text{ion}} > \sigma_{\text{eon}}$ . It is also cannot explain the invariant ionic conductivity with bromine partial pressure.

Next, the reaction between Au and bromine at the interface is considered. The appearance of the low-frequency feature in the impedance spectrum in  $p_1(\text{Br}_2)$ (**Figure 5.2**) compared with the case in Ar (**Figure 5.1**) suggests the possibility of an interfacial effect. The dielectric constant calculated from the high frequency (bulk) and low frequency (interfacial) 2.8 and 4.5E04, respectively. Considering the electrode geometry (gap length = 10  $\mu\text{m}$ ) and grain size (200 nm) shown in **Figure 4.7**, a thickness of 5E-04 nm is estimated. Such value is too small for a grain boundary thickness. However, if such interfacial contribution is from electrode / perovskites interface, this value is estimated to be around 0.25 nm. Such estimate would be in agreement with the possible formation of a thin layer of  $\text{AuBr}_x$ . Reaction between Au and bromine is thermodynamically favorable.<sup>148</sup> Gold bromide ( $\text{AuBr}_x$ ,  $x = 0.85\text{-}3$ , brown)<sup>149</sup> can be obtained by treating gold powder with liquid bromine at room temperature.<sup>150</sup> In addition, such compound can easily undergo decomposition at elevated temperature into gold monobromide (yellow), and then to metallic gold.<sup>151, 152</sup> The observed reversible change in the low frequency feature can be due to the reversible formation and decomposition of the gold bromide at the gold/perovskites interfaces. When increasing the bromine partial pressure value to  $p_3(\text{Br}_2) = 2\text{E-}05$  bar, the sample shows irreversible behaviour, with a clear deviation between the conductivities probed while changing  $p(\text{Br}_2)$  in different directions(**Figure 5.6b**). This may be explained considering the formation of a more stable  $\text{AuBr}_x$  layer composition under higher bromine partial pressure.

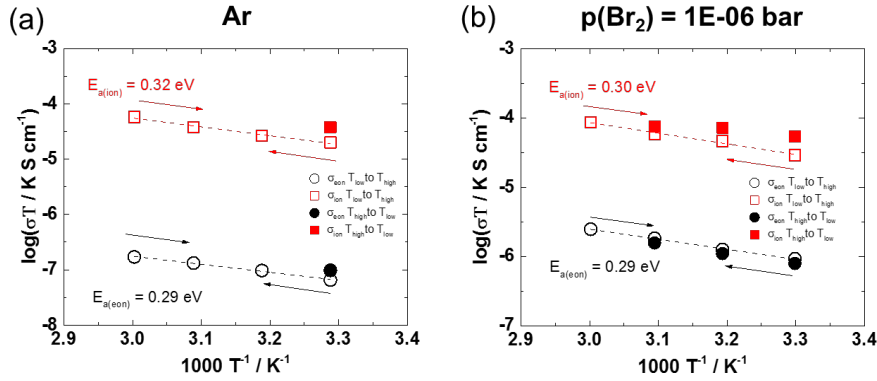


**Figure 5.7.** Temperature dependence of  $\text{MAPbBr}_3$  thin film under (a) Argon (b)  $p(\text{Br}_2) = 1\text{E-}06$  atmosphere. Measurements are conducted in the temperature range from 30 °C to 60 °C with 10 °C temperature step.

The ionic and electronic activation energies of the  $\text{MAPbBr}_3$  thin films were measured under Ar and  $p_1(\text{Br}_2)$  atmosphere in the temperature range  $T =$  from 30 °C to 60 °C. To check the reversibility of the sample during the experiment, after measuring the conductivity

on increasing temperature, additional measurement(s) were run on decreasing temperatures. The obtained Arrhenius plots show similar trends for the two atmospheres, with a much larger value of  $\sigma_{\text{eon}}$  for the measurement under p1(Br<sub>2</sub>), compared with the argon case, as discussed above (**Figure 5.7**). The data show relatively good reversibility when sweeping the temperature to large values and going back to the initial value. The fact that this is observed also for the argon case indicates that a limited change in stoichiometry occurs under these conditions when heating up the film without a fixed p(Br<sub>2</sub>). The electronic activation energies ( $E_{\text{a}}(\text{eon})$ ) and ionic activation energies ( $E_{\text{a}}(\text{ion})$ ) measured under the two conditions show similar values, suggesting that the majority charge carriers are unvaried across these two different situations.

Compared with the activation energies reported for iodide perovskites (MAPbI<sub>3</sub>,  $E_{\text{a}}(\text{eon}) = 0.66$  eV,  $E_{\text{a}}(\text{ion}) = 0.48$  eV)<sup>8</sup>, both of the ionic and electronic activation energies are significantly lower. Since migration energy of halide vacancy transport in MAPbI<sub>3</sub> and MAPbBr<sub>3</sub> are expected to be similar,<sup>153</sup> this indicates that the defect formation energy for MAPbBr<sub>3</sub> is smaller than MAPbI<sub>3</sub>. Such result can be explained by the smaller size of bromide compared with iodide. In addition, the ionic and electronic activation energies are very similar. The possibility that a more complicated mechanism involving association between ionic and electronic charge carriers mediates the transport of either defect is a potentially interesting future research direction.

### 5.2.2 Effects of reduced dimensionality: mixed conductivity in 2D (PDMA)PbBr<sub>4</sub>

To investigate the effect of dimensionality on the electrical properties of bromide perovskites, I conducted similar experiments as the ones reported in the previous section for 2D bromide perovskites. Surprisingly in 2D bromide perovskites, changes in bromine partial pressure did not change the impedance significantly. However, a significant decrease in time constant is observed. (see appendix, **Figure A.1.5**(Ar), A.1.6(p1(Br<sub>2</sub>)), A.1.7(p2(Br<sub>2</sub>))).

The ionic conductivity ( $\sigma_{\text{ion}}$ ) of (PDMA)PbBr<sub>4</sub> measured in Ar show 1-1.5 orders of magnitude greater value than its electronic conductivity ( $\sigma_{\text{eon}}$ )(**Figure 5.8a**, left). Their iodide counterparts ((PDMA)PbI<sub>4</sub>) show similar electronic and ionic conductivities. Such difference suggests that (PDMA)PbBr<sub>4</sub> is a mixed ionic and electronic conductor, but more ionic in nature. This trend is similar to their 3D counterparts MAPbI<sub>3</sub> and MAPbBr<sub>3</sub>. This can be explained based on the wider bandgap of bromide perovskites than their iodide counterparts. Compared with 3D MAPbBr<sub>3</sub>, the electronic conductivity of (PDMA)PbBr<sub>4</sub> is lowered by a factor of four, suggests that introducing an organic spacer between the lead halide slabs suppresses the electronic transport, also consistent with a larger band gap in 2D perovskites. Interestingly, the ionic conductivity shows a significant decrease of almost four orders magnitude compared with MAPbBr<sub>3</sub>. This suggests that the ionic transport is suppressed in 2D

systems even more for the bromide-based systems than the iodide-based ones, the latter showing a factor of about 2 decrease in  $\sigma_{\text{ion}}$  when going from a 3D to a 2D structure.<sup>8</sup> Importantly, the investigated film shows mixed orientation (See supporting chapter, **Figure A.1.4**) and, even though the dominant orientation is parallel to the substrates and the direction of the probed transport, the effect of orientation on the ion migration could be the key to such a large drop in  $\sigma_{\text{ion}}$  between the 3D and the 2D perovskite.

After exposing the 2D bromide perovskites to bromine gas, a similar incorporation reaction as described in eq.5.1 is expected. Indeed, after equilibrium is reached, similar to the 3D MAPbBr<sub>3</sub>, the electronic conductivity increases with one and half order of magnitude while the  $\sigma_{\text{ion}}$  show a minor increase (**Figure 5.8a**). This suggests that 2D (PDMA)PbBr<sub>4</sub> is also an intrinsic mixed conductor with p-type electronic conduction. The estimate of the ionic conductivities here suffers from significant errors due to the very large resistances involved in the analysis. Indeed, the reported value of  $\sigma_{\text{ion}}$  is a lower limit to the ionic conductivity in these materials. Overall, no significant variation in ionic resistance is detected in the cases from Ar to fixed bromine partial pressure (**Figure 5.6 a**, Ar to p1(Br<sub>2</sub>); **Figure 5.6b**, Ar to p2(Br<sub>2</sub>)).

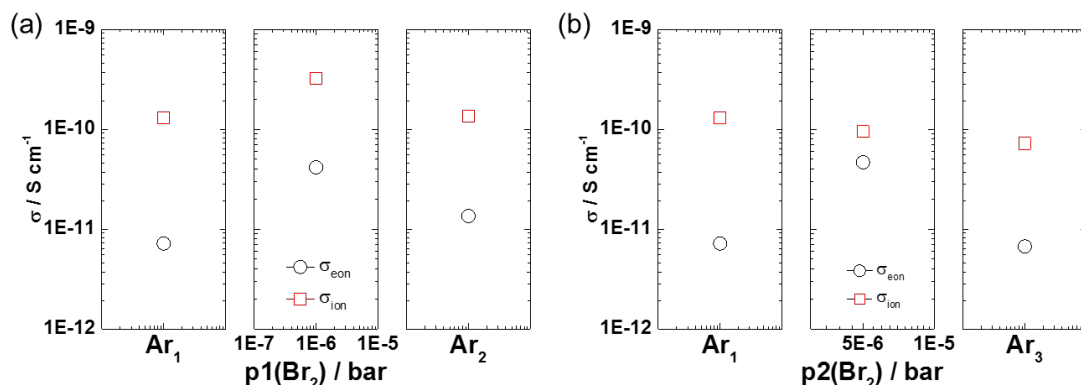


**Figure 5.8.** Change in electronic ( $\sigma_{\text{eon}}$ ) and ionic ( $\sigma_{\text{ion}}$ ) conductivities after bromine incorporation and ex-corporation in 2D (PDMA)PbBr<sub>4</sub> thin film. (a) Change in atmosphere from argon to p1(Br<sub>2</sub>) = 1E-06 bar, ex-corporation from p1(Br<sub>2</sub>) = 1E-06 bar to argon; (b) Change in atmosphere from argon to p2(Br<sub>2</sub>) = 5E-06 bar, ex-corporation from p2(Br<sub>2</sub>) = 5E-06 bar to Argon;

Interestingly, when increasing the bromine partial pressure from p1(Br<sub>2</sub>) = 1 E-06 bar to p2(Br<sub>2</sub>) = 5E-06 bar, there is no significant change for either the electronic conductivity or the ionic conductivities (**Figure 5.9 a**). The XRD analysis also confirms that there is no change in both bulk and the surface properties of the film (See supporting chapter, **Figure A.1.4**). Similar to MAPbBr<sub>3</sub>, when bromine partial pressure increases to p3(Br<sub>2</sub>) = 2E-05 bar, electronic and ionic conductivities show irreversible changes, although some degree of reversibility is detected suggesting a slightly negative slope of the electronic conductivity vs p(Br<sub>2</sub>) also for this compound measured under the given experimental conditions (**Figure 5.9**

b). In this case too, a partially reversible formation of a  $\text{AuBr}_x$  layer at the perovskite Au interface may explain the observed trend.

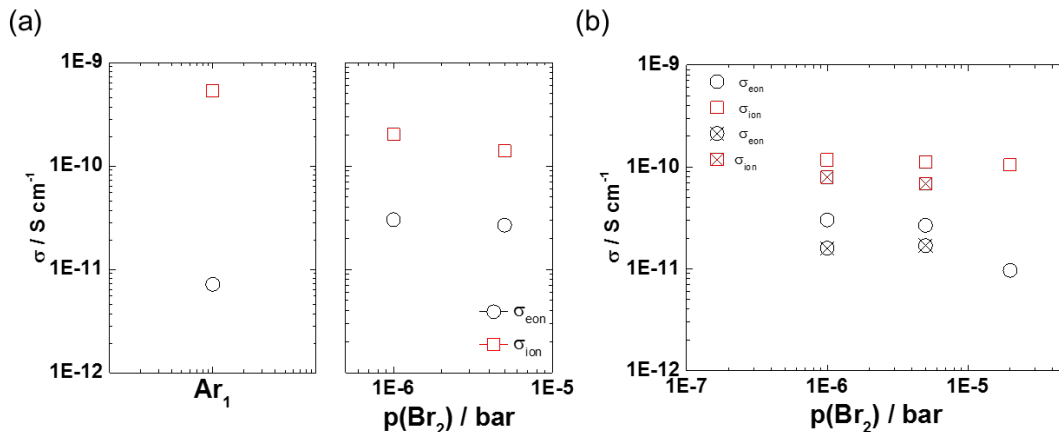


**Figure 5.9.** Bromine partial pressure dependence of electronic( $\sigma_{\text{eon}}$ ) and ionic( $\sigma_{\text{ion}}$ ) conductivities in 2D (PDMA)PbBr<sub>4</sub> thin film (a) when a reversible range between  $p_1(\text{Br}_2) = 1 \text{E-}06$  to  $p_2(\text{Br}_2) = 5 \text{E-}06$  bar are measured; (b) irreversible range when  $p_3(\text{Br}_2)$  reaches  $2 \text{E-}05$  bar.

### 5.3 Conclusion

In this chapter, the charge carrier chemistry and the ion transport properties of 3D MAPbBr<sub>3</sub> and 2D Dion-Jacobson (PDMA)PbBr<sub>4</sub> are investigated. The results reveal that both 3D MAPbBr<sub>3</sub> and 2D (PDMA)PbBr<sub>4</sub> are mixed conductors. 2D (PDMA)PbBr<sub>4</sub> show 3 orders of magnitude lower ionic conductivity compared with 3D MAPbBr<sub>3</sub> when measured in argon at 60°C. This implies that dimensionality reduction is an effective strategy for reducing ion migration in these systems. From a bromine partial pressure dependent study, I conclude that MAPbBr<sub>3</sub> and 2D(PDMA)PbBr<sub>4</sub> are both P-type conductor and that the surface reaction is the limiting process for the incorporation and ex-corporation of bromine at the solid/gas interface. For both compounds, the bromine partial pressure range  $p_1(\text{Br}_2) = 1 \text{E-}06$  bar to  $p_2(\text{Br}_2) = 5 \text{E-}06$  bar is identified as the window where the stoichiometry of the mixed conductors can be changed reversibly. In this regime, a non-monotonic dependence of the electronic conductivity on  $p(\text{Br}_2)$  is detected for both 2D and 3D bromide perovskites. It can be attributed to the reversible formation of  $\text{AuBr}_x$  on the gold electrode and perovskites interface, which introduces an additional contribution on the resistance at low frequency. Further increasing the bromine partial pressure value to  $p_3(\text{Br}_2) = 2 \text{E-}05$  bar, irreversible behaviour in conductivities are observed, which can be explained considering the formation of a more stable  $\text{AuBr}_x$  layer composition under higher bromine partial pressure.

## 6 Photo de-mixing in 2D mixed halide perovskites: thermodynamics

### 6.1 Introduction

Elucidating the origin of photo de-mixing in mixed halide perovskites is of substantial conceptual importance, as it would provide guidelines for suppressing photo-induced phase instability, optimizing halide alloying, and opening up opportunities for new optoelectronic devices.<sup>154</sup> As discussed in Section 2.4.4, clarifying the question of whether photo de-mixing is purely a thermodynamic effect or how far kinetic effects are involved is complicated, as the photo-induced degradation is coupled with photo de-mixing. Evidence for suppressed ion transport in 2D halide perovskites compared with classic 3D hybrid perovskites<sup>155, 156</sup> and improved stability<sup>156</sup> compared to their 3D counterparts provide opportunities to decouple photo de-mixing from light induced degradation.<sup>157</sup> The previous reports on 3D perovskite films<sup>158</sup> show that encapsulation is essential to suppress the degradation of the I-rich phase, improving the reversibility of photo de-mixing and dark re-mixing. Therefore, clarifying (im)miscibility in mixed halide perovskites prior to illumination by investigating the reversibility of photo de-mixing can be possible using more stable 2D mixed halide perovskites as model material with encapsulation of the surface. Various studies investigated photo de-mixing in mixed halide perovskites, some of them describing the materials' miscibility gap based on thermodynamic and kinetic arguments.<sup>112</sup> While the possible existence of a miscibility gap in the dark has been discussed,<sup>31, 36</sup> the fact that this is a reversible process points towards the generally accepted interpretation that illumination changes the thermodynamics of these mixtures. Factors such as polaron formation and strain effects,<sup>81, 97, 159, 160</sup> bandgap reduction due to iodide rich phase formation,<sup>91, 115</sup> influence from local electric fields<sup>108</sup>, halide oxidation<sup>89</sup> were proposed to explain thermodynamic origin of photo de-mixing. However, direct experimental evidence on such effect is missing.

In this chapter, the temperature dependence and composition dependence of the phase behavior of 2D Dion-Jacobson mixed bromide-iodide (PDMA)Pb(I<sub>0.5</sub>Br<sub>0.5</sub>)<sub>4</sub> thin films under light are investigated. All films were measured in Ar atmosphere encapsulated with poly(methyl methacrylate) (PMMA) to minimize photo-induced degradation during the characterization of photo de-mixing. After introducing the material properties, the thermodynamic evaluation of the photo de-mixing process in this mixture is discussed. Various experimental methods that can be used to obtain de-mixed compositions based on the analysis of the temperature-dependent absorption spectra under illumination are developed and compared. Lastly, the information on photo-induced miscibility gap for 2D Dion-Jacobson mixed halide perovskites as well the effect of illumination intensity and surface encapsulation are discussed.

## 6.2 Results and discussion

2D Dion-Jacobson halide perovskite thin films based on  $(\text{PDMA})\text{Pb}(\text{I}_{1-x}\text{Br}_x)_4$  composition (**Figure 6.1a**) with Br content  $x = 0$  ( $(\text{PDMA})\text{PbI}_4$ ),  $x = 0.5$  ( $(\text{PDMA})\text{Pb}(\text{I}_{0.5}\text{Br}_{0.5})_4$ ) and  $x = 1$  ( $(\text{PDMA})\text{PbBr}_4$ ) were fabricated following the procedure described in Section 4.1.

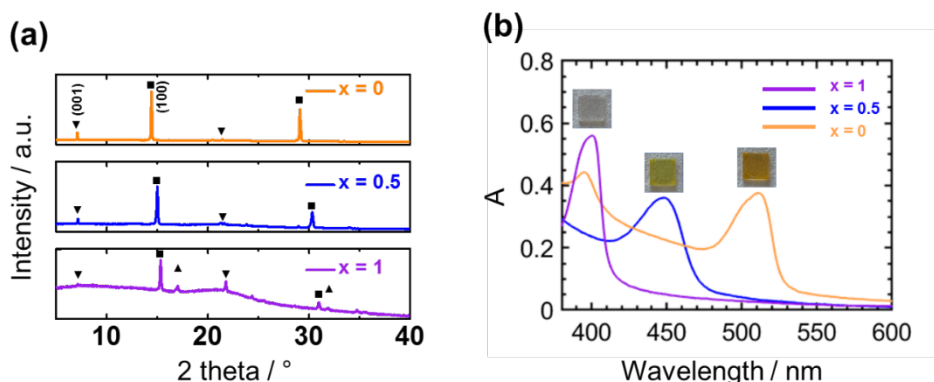


**Figure 6.1.** (a) XRD patterns and (b) UV-Vis spectra of 2D layered  $(\text{PDMA})\text{Pb}(\text{I}_{1-x}\text{Br}_x)_4$  ( $n = 1$ ) perovskite thin films on quartz substrates:  $(\text{PDMA})\text{PbI}_4$  (yellow line),  $(\text{PDMA})\text{Pb}(\text{I}_{0.5}\text{Br}_{0.5})_4$  (blue line),  $(\text{PDMA})\text{PbBr}_4$  (purple line). Diffraction peaks in (b) are labeled with  $\blacktriangledown$ ,  $\blacktriangle$ , and  $\blacksquare$  representing (001), (0k0) and (h00) Bragg planes, respectively. Photographs of relevant thin film samples with corresponding compositions are included in the inset of (b).

**Figure 6.1a** shows the XRD patterns of these films. The diffraction peaks at low angles can be ascribed to reflections from the (001) crystal planes ( $2\theta = 7.11^\circ$ ,  $7.16^\circ$ ,  $7.19^\circ$  for  $x = 0$ , 0.5 and 1, respectively) and correspond to the expected Pb-Pb interlayer distance, indicating the successful preparation of the layered structure for these thin films.<sup>141, 161-163</sup> The increase of the bromide content results in a decrease of such distance ( $12.43 \text{ \AA}$ ,  $12.34 \text{ \AA}$ , and  $12.30 \text{ \AA}$  for  $x = 0$ , 0.5 and 1, respectively), due to the smaller radius of the bromide ion compared with the iodide ion. The successful preparation of the 2D perovskites is also evidenced by UV-Vis absorption spectroscopy (**Figure 6.1b**). The data highlights the pronounced excitonic absorption peak for each of the films, which can be attributed to the optical transitions in the 2D quantum wells.<sup>164</sup> By increasing the Br content, the wavelength associated with the excitonic peak decreases (512 nm, 450 nm, 401 nm), in accordance with the expected changes in the resulting optical properties of layered perovskite materials.<sup>33, 39</sup> Thin films with other intermediate compositions are also successfully prepared (see **Figure A.2.1** in the Supporting Information).

### 6.2.1 Reversibility

Having evidenced the formation of 2D structures in thin films, the in-situ evolution of their optical response changes under illumination using UV-Vis is monitored. This technique



enables in-situ non-destructive evaluation of optical and structural properties<sup>165</sup> and is commonly used to probe photo de-mixing in mixed halide perovskites.<sup>116, 166</sup> The exposure to light induces no significant change of the optical absorption spectrum of the  $x = 0$  (iodide) and minor changes for the  $x = 1$  (bromide) 2D perovskite thin films (**Figure A.1.2**, supporting information). Such changes are not related to de-mixing (only one halide involved) or to temperature variations and have been also observed for pure I- and pure Br-RP films under light.<sup>167</sup> On the other hand, a pronounced change of the absorbance for a thin film of the 50% iodide 50% bromide composition under illumination is observed. In the following, I refer to the initial homogeneous composition of the film before exposure to light as  $x_{\text{initial}}$  (in this case  $x_{\text{initial}} = 0.5$ ). The spectral evolution indicates a gradual phase transformation from the pristine phase (PDMA)Pb(I<sub>0.5</sub>Br<sub>0.5</sub>)<sub>4</sub> to Br-rich and I-rich phases (**Figure 6.2a**; the curves' color gradient from black to red refers to early to long time scale of illumination). The change in absorbance  $\Delta A$  (**Figure 6.1c**), obtained by subtracting the initial absorbance spectrum before illumination from each subsequent spectrum, clearly shows formation of I-rich and Br-rich phases and a bleaching of the feature assigned to (PDMA)Pb(I<sub>0.5</sub>Br<sub>0.5</sub>)<sub>4</sub>. The shape of  $\Delta A$  remains approximately similar as a function of illumination time, suggesting that the phases that form at early time scales are already close in composition to the final quasi-equilibrium phases.

After photo de-mixing, illumination was stopped and the sample was left in the dark. As a result, the de-mixed phases underwent re-mixing (**Figure 6.2 b**). Only a small difference between the pristine absorption spectrum and the one after re-mixing for  $\sim 330$  h in the dark (blue and red dashed lines in **Figure 6.2b**) was observed, indicating almost full reversibility for the sample's optical properties. The kinetics of the change in absorbance  $\Delta A$  during the experiment (displayed in **Figure 6.2e, f**) emphasizes the difference in time scale between the de-mixing ( $\sim 10$  h) and re-mixing ( $\sim 330$  h) processes.

To further clarify the optical and structural reversibility of photo de-mixing in these 2D mixtures, the UV-vis and XRD measurements on a (PDMA)Pb(I<sub>0.5</sub>Br<sub>0.5</sub>)<sub>4</sub> thin film sample in its pristine state and after 4 consecutive treatments were conducted. These include a photo de-mixing and 3 dark re-mixing steps, as shown in **Figure 6.3a**. The UV-Vis and XRD data were collected at room temperature and are shown in **Figure 6.3b-c**. After illumination at 80 °C for 20 hours (step(1)), the emergence of both longer (I-rich) and shorter (Br-rich) wavelength optical absorption features is observed, consistently with **Figure 6.2**, accompanied by a decrease in the diffraction intensity and broadening of some XRD peaks. The structural change seems to affect predominantly peaks that correspond to the (h00) orientation (Pb-Pb intralayer distance). Regarding the dark re-mixing experiment, only limited changes are detected when storing the thin film in argon in the dark at room temperature for 6 months (step(2)). On the other hand, after leaving the thin film at 80 °C for 30 days (step(3) and

step(4)), the de-mixed phases re-mixed reaching a state close to the pristine phase, from both absorption and structural analysis.

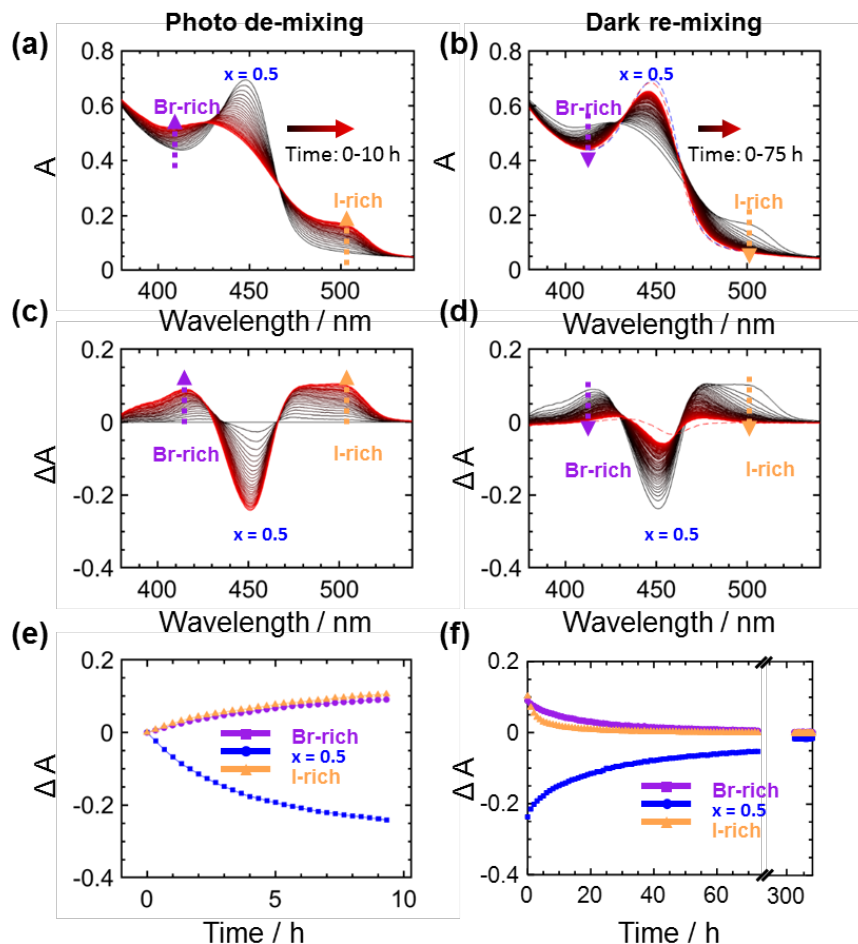


**Figure 6.2.** UV-Vis spectra evolution of  $(\text{PDMA})\text{Pb}(\text{I}_{0.5}\text{Br}_{0.5})_4$  thin films (with PMMA encapsulation and in Ar atmosphere to exclude possible degradation) (a) under light ( $1.5 \text{ mW}/\text{cm}^2$ ) at  $80 \text{ }^\circ\text{C}$  for  $\sim 10 \text{ h}$  with  $20 \text{ min}$  interval and (b) in the dark at  $80 \text{ }^\circ\text{C}$  for  $\sim 75 \text{ h}$  with  $1 \text{ h}$  time interval between spectra. For the case under light, within each interval, spectra were collected by switching off the bias light for  $300 \text{ s}$  (see **Figure 4.3** from the Material and Methods). The gradient from black to red in (a – d) denotes the time sequence. In (b), the blue dashed line represents the absorption spectra of the sample before illumination (also shown in (a) for Time =  $0 \text{ h}$ ), while the red dashed line corresponds to the absorbance after photo de-mixing and  $330 \text{ hours}$  of re-mixing in the dark. (c, d) Change in absorbance obtained by subtracting the reference spectrum of the pristine sample from each absorbance spectrum shown in (a) and (b), respectively. (e, f) Kinetics of the photo de-mixing and dark re-mixing processes highlighting the change in absorbance at wavelengths associated to  $(\text{PDMA})\text{Pb}(\text{I}_{0.5}\text{Br}_{0.5})_4$  ( $450 \text{ nm}$ , blue), Br-rich ( $414 \text{ nm}$ , purple) and I-rich ( $501 \text{ nm}$ , yellow) phases.

To investigate the dependence of the observed reversibility in the optical and structural properties on the de-mixing temperature, the same experiment illustrated in **Figure 6.3a**, but using different temperatures for step(1) is performed. The decrease in intensity and broadening

of some diffraction peaks is more pronounced for higher photo de-mixing temperatures, consistent with a larger fraction of the film undergoing phase separation (see peak intensity and FWHM of the (h00) orientation in **Figure 6.3d**). As for the re-mixing in the dark, once again there is limited changes in properties after step(2), while complete reversibility to the mixed state is gradually reached after step(3) and (4). This experiment highlights the long-term reversible behavior associated with photo de-mixing and dark re-mixing in these 2D mixed-halide perovskite thin films when compare with 3D systems.<sup>158</sup> In particular, (i) a large degree of reversibility in terms of optical properties for samples that were de-mixed at different temperatures and for over 20 hours is observed; (ii) for some of the samples the reversibility is complete also concerning their structural properties; (iii) the data show the possibility to kinetically trap the photo de-mixing state by storing the sample in the dark at room temperature.

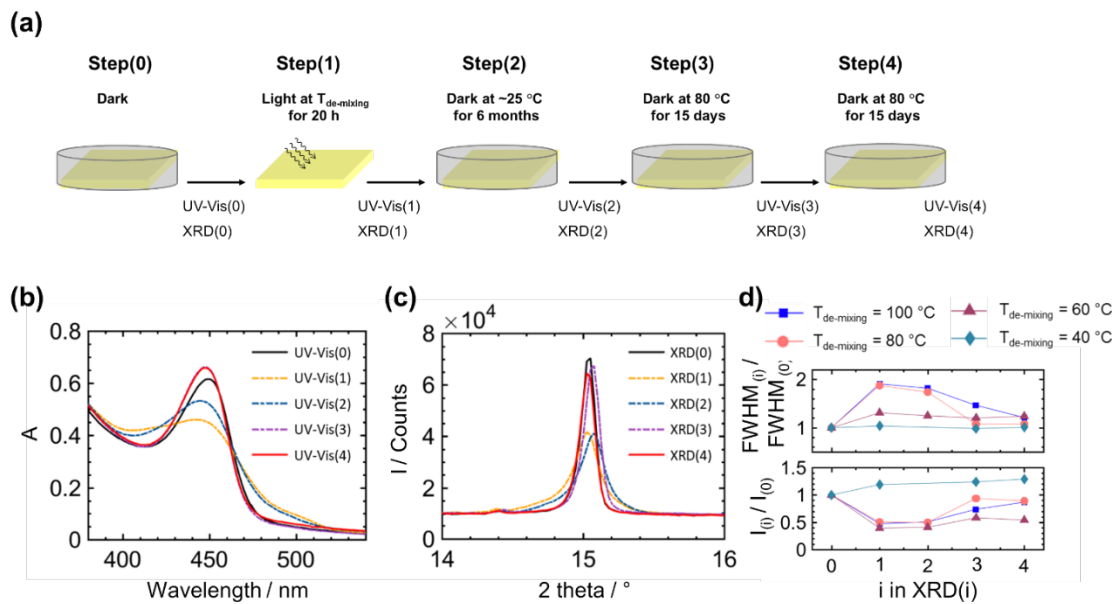


**Figure 6.3.** (a) Schematics showing the experimental procedure performed on  $(\text{PDMA})\text{Pb}(\text{I}_{0.5}\text{Br}_{0.5})_4$  thin films (with PMMA encapsulation). All steps were performed in argon atmosphere. Step(0): pristine film in the dark; step(1): illuminating the thin film using cold white LED with  $1.5 \text{ mW}/\text{cm}^2$  for 20 h at a temperature of  $T_{\text{de-mixing}}$ ; step(2): thin film stored in the dark at room temperature for 6 months; step(3): thin film left at  $80 \text{ }^\circ\text{C}$  for 15 days in the dark; step(4): thin film left at  $80 \text{ }^\circ\text{C}$  for another 15 days in the dark. Both XRD and UV-Vis measurements were conducted at room temperature after each step. (b) UV-Vis and (c) XRD performed after each treatment step shown in (a) on a thin films  $T_{\text{de-mixing}} = 80 \text{ }^\circ\text{C}$ . (d) Changes in relative FWHM and intensity for XRD peak  $2\theta = 13^\circ - 17^\circ$  after each step, for thin films that were de-mixed at different temperatures.

### 6.2.2 Temperature dependence of photo de-mixing

In order to evaluate the thermodynamic or kinetic origin for photo de-mixing in mixed halide perovskites, the temperature-dependent UV-Vis absorption measurements of a thin film with  $x_{\text{initial}} = 0.5$  were carried out. After exposing the sample at 100 °C. for 20 hours, the temperature was gradually decreased to 40 °C, with the illumination intensity being kept constant. As shown in **Figure 6.4a,c**, while no significant change is observed for the shape of the feature associated with the Br-rich phase, the absorption signal detected for the I-rich phase showed a significant red shift with decreasing temperature. The reversibility of the process was inspected by performing a second temperature scan back to high temperature under the same conditions (**Figure 6.4b, d**). Strikingly, the absorption features of the I-rich phase shifted back to the same wavelength region as originally observed for the same temperature, suggesting a reversible behavior.

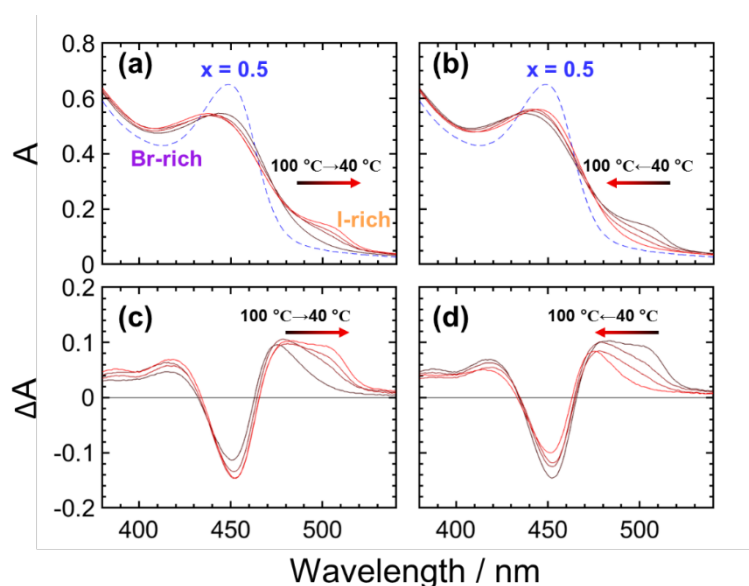


**Figure 6.4.** Temperature-dependent UV-Vis measurements of (PDMA)Pb(I<sub>0.5</sub>Br<sub>0.5</sub>)<sub>4</sub> thin film (with PMMA encapsulation) under light (1.5 mW/cm<sup>2</sup>) at temperature varying as follows: (a) 100°C 80°C 60°C 40 °C, (b) 40 °C 60°C 80°C 100 °C (displayed spectra were recorded after 20 hours at each temperature). The gradient color from black to red denotes the sequence of the temperature step. The dashed blue lines indicate the absorption spectrum of the pristine (PDMA)Pb(I<sub>0.5</sub>Br<sub>0.5</sub>)<sub>4</sub> phase ( $x_{\text{initial}} = 0.5$ ) at 100°C. (c–d) Change in absorbance  $\Delta A$  spectra (obtained by subtracting from each absorption spectrum the spectrum of the pristine sample).

### 6.2.3 Photo-miscibility-gap

After confirming that the temperature dependence of the photo de-mixed absorption occur in a reversible manner, it is necessary to attempt on a quantitative evaluation of the de-mixed compositions under light, which is referred here as *photo-miscibility-gap*. The characteristic absorption wavelengths of Br-rich phases were determined based on the peak position of the  $\Delta A$  spectra at short wavelengths. These values are then converted into

compositions ( $x_{Br}$ ) by using a calibration dataset obtained from calculated  $\Delta A$  spectra based on the absorption of films with different compositions at different temperatures. This method allows one to account for the overlapping absorption features from different phases at short wavelengths and possible temperature effects. For the I-rich phase, the position of the (negative) peak in slope of the experimental  $\Delta A$  is considered, which can be then converted into composition ( $x_I$ ) based on the calibration data obtained from the calculated  $\Delta A$  spectra described above. For detailed information on the method used to extract the composition of the de-mixed phases, see Supporting information A.2.

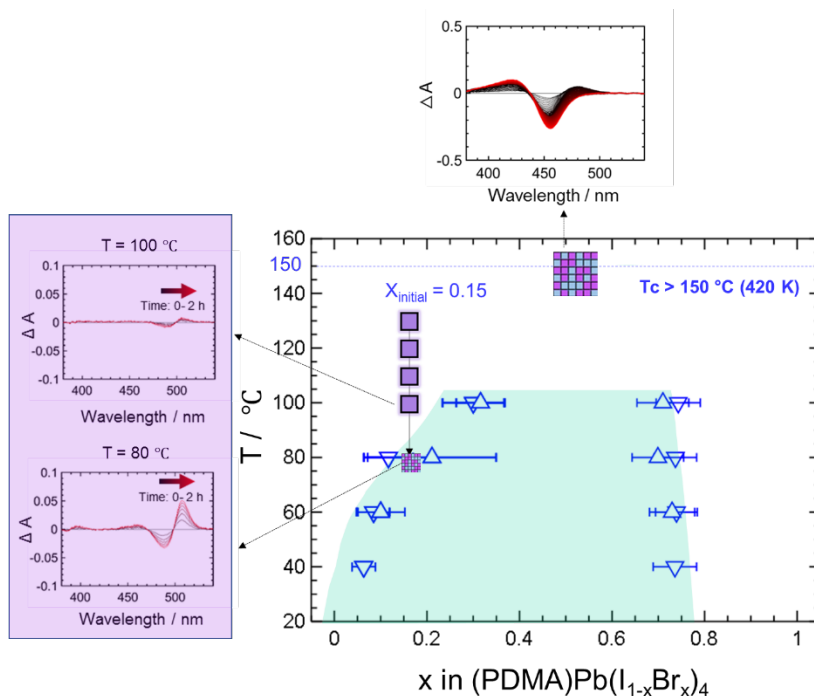


**Figure 6.5.** Photo-miscibility-gap extracted from temperature dependent UV-Vis measurements shown in Figure 6.4a–d; Downward-pointing ( $\nabla$ ) and upward-pointing ( $\Delta$ ) triangles denote data collected during a downward and upward temperature scan respectively (for details on the method to evaluate the photo-miscibility gap, see supporting information A.2).

The data (summarized in **Figure 6.5**) show that, by decreasing the temperature, the gap for the de-mixed compositions widens. The photo de-mixed composition for the I-rich domain approaches the value corresponding to the end member composition ( $x = 0$ ). The feature associated with the Br-rich domain undergoes much more limited changes over the probed temperature range. This indicates that the degree of de-mixing, and therefore the range of immiscible compositions, increases in width with decreasing temperature, which is consistent with the decrease of the mixing entropy contribution to the free energy on decreasing temperature. As discussed above, the analysis of the upward temperature scan (shown by  $\Delta$ ) displays an analogous trend. The critical temperature of this photo-miscibility gap, above which the entropic contribution would be large enough to prevent de-mixing, is an important

parameter. The investigation of long time-scale photo de-mixing is limited to temperatures up to 100 °C, to avoid possible changes in the film’s properties (annealing temperature of 150 °C was used during film preparation). However, it is worth commenting on the fact that the UV-Vis measurements performed on a sample with  $x_{\text{initial}} = 0.5$  under light at 150 °C show the appearance of absorption features associated with Br-rich and I-rich phases at early time scales. One cannot easily extract photo de-mixed compositions for such phases due to the disappearance of the I-rich feature at long time scales. Nevertheless, this experiment suggests a critical temperature higher than 150 °C and provides a lower bound estimate of 0.07 eV for the interaction parameter  $\Omega$  ( $\Omega = T_c/2R$ , where  $R$  is the gas constant, see Section 3.1 for more details).<sup>168</sup> Importantly, the “bending” of the miscibility gap observed in **Figure 6.5** for the temperature dependence of  $x$  is verified by monitoring the kinetics of photo de-mixing in a 2D perovskite thin film with  $x_{\text{initial}} = 0.15$ . When decreasing the temperature gradually from 130°C to 80 °C, more pronounced changes in absorbance and characteristic feature for both I-rich and Br-rich phases only for measurements at 80 °C are observed. This suggests the transition from a phase stable to a phase instable region when boundary of miscibility gap is crossed.

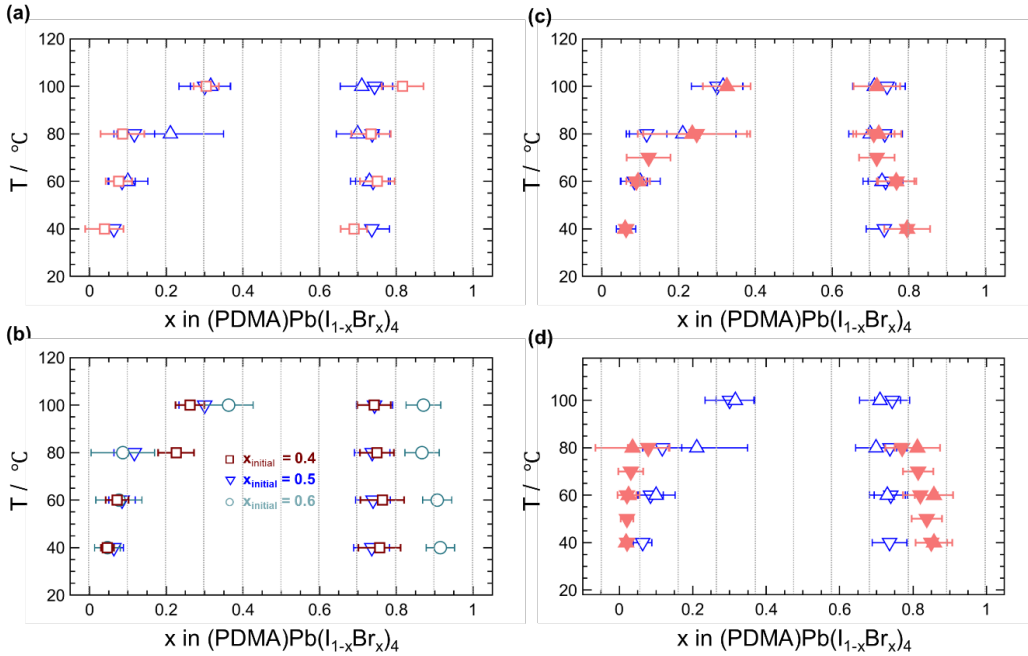


**Figure 6.6.** Photo-miscibility-gap (a) mapped using multiple samples (pink squares,  $\square$ ) compared with the data shown in **Figure 6.5** in the main text obtained for a single sample (blue empty upwards  $\triangle$  and downwards pointing triangles  $\nabla$ ); (b) of thin films  $(\text{PDMA})\text{Pb}(\text{I}_{1-x}\text{Br}_x)_4$  with different initial composition performed under illumination ( $1.5 \text{ mW cm}^{-2}$ ). Films with  $x_{\text{initial}} = 0.4$  (brown),  $x_{\text{initial}} = 0.5$  (blue) and  $x_{\text{initial}} = 0.6$  (cyan) were considered. The data correspond to measurements of the films taken after 20 hours at each temperature under continuous illumination; (c) mapped under  $\times 10$  times higher illumination intensity ( $15 \text{ mW cm}^{-2}$ , pink filled triangles) than the one shown in **Figure 6.5** ( $1.5 \text{ mW cm}^{-2}$ , Blue empty upwards and downwards pointing triangles); (d) mapped for a  $(\text{PDMA})\text{Pb}(\text{I}_{0.5}\text{Br}_{0.5})_4$  thin film without

encapsulation (pink filled triangles). The case of an encapsulated sample as shown in **Figure 6.5** is also shown for comparison (Blue empty upwards and downwards pointing triangles). Downward-pointing and upward-pointing triangle symbols denote data collected during a downward and upward temperature scan respectively.

This photo-miscibility gap is further confirmed by analysing the de-mixed compositions of different pristine samples that are photo de-mixed under different temperatures. The obtained de-mixed compositions for I-rich and Br-rich phases (see **Figure 6.6a**) show a comparable shape of the photo-miscibility-gap as in Figure 6.5. Furthermore, the sensitivity of the boundaries for the extracted photo-miscibility-gap to the initial composition of the 2D perovskite thin film is evaluated by performing temperature-dependent photo de-mixing on films with  $x_{\text{initial}} = 0.4$  and  $0.6$  (see **Figure 6.6**), analogously to the experiment shown in **Figure 6.5**. Obviously the composition associated with the I-rich phase forming after photo de-mixing is rather insensitive to the value of  $x_{\text{initial}}$ . In contrast, the composition datasets extracted for the Br-rich phase seems to vary significantly depending on the pristine film composition. While the error associated with such estimates is relatively large for some of the data, this may suggest slight variations in the steady-state photo de-mixed compositions depending on the starting condition.

While the methods described above have the potential to map the miscibility gap of samples under a given illumination intensity, the situation is more complicated compared to a study of a system in the dark at equilibrium. De-mixing is likely to depend on the concentration of photo-generated electronic charge carriers, and this may vary during the experiment, for example due to changes in recombination. To test the sensitivity of the measured photo-miscibility-gap to the bias light, a similar experiment as the one shown in **Figure 6.6c** with 10-times higher light intensity was investigated. Slight differences in the shape of the temperature-dependent absorbance of the thin film under the two light conditions are observed, with a more pronounced excitonic signature associated to the I-rich domain at low temperatures (See appendix, **Figure A.2.11**). However, the analysis using the method described above results in surprisingly similar de-mixed compositions for the two different light intensities, suggesting limited variation in the stable compositions while varying the optical perturbation in this range.

Finally, the effect of encapsulation of the sample on the photo de-mixing behavior of these 2D perovskite thin films is investigated (**Figure 6.6d**). Similar to the previous reports on 3D perovskite films,<sup>158</sup> encapsulation was found to be essential to suppress the degradation of the I-rich phase, improving the reversibility of photo de-mixing and dark re-mixing. Interestingly, the non-encapsulated sample demonstrated a widening of the photo-miscibility gap when compared to a reference sample encapsulated with PMMA (data in **Figure 6.5**). Changes in absorbance for the non-encapsulated sample highlight a drop in the signature

associated to I-rich domains(See appendix, **Figure A.2.12**), suggesting the presence of a loss mechanism for such phase, likely due to ex-corporation of iodine-based species. These observations highlight that the role of nonstoichiometry on the thermodynamics of photo demixing remains a key issue and point to the importance of encapsulation in the analysis of the behavior of halide perovskite material. The impact of surface encapsulation will also be discussed in Chapter 7.

### 6.2.4 Composition dependence of phase stability under light

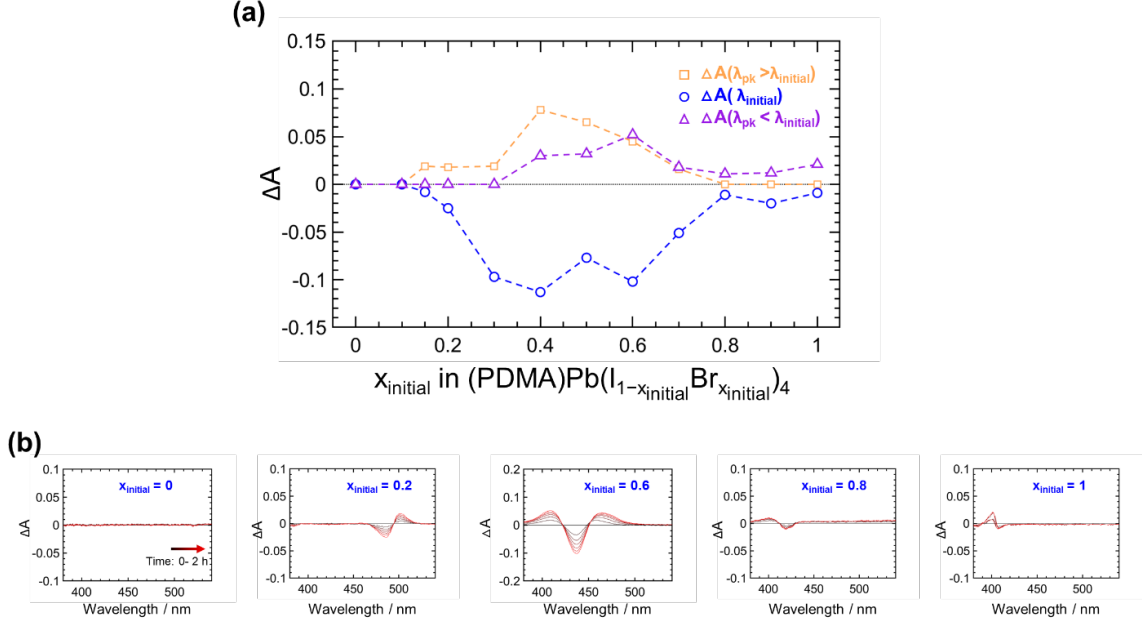


**Figure 6.7.** (a) Changes in absorbance measured at 100°C and after 2 hours of illumination plotted as function of the films' initial composition. The dataset indicated by the blue circles displays the bleach in the absorption at (peak wavelength of the pristine film). The yellow squares and the purple triangles indicate the peak values of features that emerged during illumination at wavelengths that are longer or shorter than, respectively. When no feature was detected, a value of is shown.(b) Some examples of absorption spectra were shown for readers' clarity.

The accuracy of the methods described above is further validated by investigating the phase stability of samples with  $x_{\text{initial}}$  spanning the full range between 0 and 1. The photo demixing of samples at 100 °C after 2 hours under  $1.5 \text{ mW cm}^{-2}$  illumination intensity is considered. **Figure 6.7** illustrates the changes in absorbance associated to the bleach of the main excitonic peak (at the peak wavelength of the pristine film) as well as the peaks of features emerging due to red-shift or blue-shift of the absorption spectrum. The data reveal that changes in absorbance, and therefore possible phase instability, under light occur for films with  $x_{\text{initial}} = 0.15$ . However, the emergence of a clear Br-rich phase is only observed for  $x_{\text{initial}} = 0.3$ , which is consistent with our previous analysis at this temperature. Furthermore, for samples with  $x_{\text{initial}} = 0.8$ , no feature associated to an I-rich phase compared to the initial



composition was detected, suggesting that no de-mixing occurred in such cases. This boundary falls within the uncertainty region of the data in **Figure 6.5**. A slight blue-shift in absorption still occurs for  $x_{\text{initial}} = 0.8$  and even for  $x_{\text{initial}} = 1$ , which deserve future investigation.

### 6.3 Conclusion

In summary, it is demonstrated that 2D Dion-Jacobson mixed-halide perovskites undergo photo de-mixing with phase transformation from the pristine (PDMA)Pb(I<sub>0.5</sub>Br<sub>0.5</sub>)<sub>4</sub> to I-rich and Br-rich phases under illumination. In the dark, the photo de-mixed phases re-mix with complete reversibility of both their optical and structural properties, indicating full miscibility in the dark. This result confirms that photo de-mixing is a thermodynamic effect rather than a photo catalytic effect. The temperature-dependent absorption for the photo de-mixed phases show a reversible red shift for I-rich at low temperature while no significant change observed for Br-rich phase, evidencing existence of miscibility gap under light. Photo de-mixed phases' compositions are extracted from the temperature-dependent absorption spectra based on a calibration method developed in this thesis. Such method uses calculated  $\Delta A$  spectra that is based on the reference absorption spectra of mixed halide perovskites with different compositions at different temperatures to correlate characteristic wavelengths of the de-mixed phases with compositions. The photo-miscibility-gap is mapped and confirmed by various methods in a temperature range relevant for applications of these materials in optoelectronic devices. Limited variation in the photo-miscibility-gap is observed when using 10 times higher illumination intensities. Lack of encapsulation of the surface of the mixed halide perovskites prior to illumination, however, induces a widening of such gap as well as partial degradation.



## 7 Photo de-mixing in 2D mixed halide perovskites: kinetics and mechanism

### 7.1 Introduction

Photo de-mixing in mixed halide perovskites involves electronic charge carrier generation and recombination, defect formation, transport. Consequently, the formation of the new phases is a result of combination of both electronic and ionic effects. Therefore, it is important to clarify both electronic and ionic charge carrier transport properties during photo de-mixing. Motti *et al.* investigated the impact of halide segregation on the electronic charge-carrier dynamics and transport properties on mixed halide perovskite films ( $\text{MAPb}(\text{I}_{0.5}\text{Br}_{0.5})_3$ ). These results reveal that, halide segregation results in negligible impact on the THz charge-carrier mobilities and in enhanced lattice anharmonicity in the segregated I-rich domains.<sup>93</sup> The latter can be regarded as a signature of ion transport. In single halide perovskites ( $\text{MAPbI}_3$ ), Kim *et al.* provided evidence for increased ionic conductivity and iodine transport upon illumination.<sup>8, 60</sup> A later study focusing on the discrepancies in such light effect between iodide and bromide perovskites suggested that photo de-mixing appears to be a direct consequence of the photo-induced ionic effect.<sup>60</sup> However, a direct measurement of the electronic and ionic charge carriers' properties and their correlation is still missing.

In addition, the change in morphology including spatial distribution and domain size is critical for identifying the nature of ionic transport. The latter can also be important for evaluating the thermodynamic properties relevant to the de-mixing regime. Early report by Bischak *et al.* demonstrated that low energy emission feature stemming from grain boundaries zones appeared upon illuminating  $\text{MAPb}(\text{I}_{0.5}\text{Br}_{0.5})_3$ . This can be attributed to the formation of the I-rich domains close to the grain boundaries.<sup>81</sup> However, direct measurements of the domain composition and domain size remains missing. Linking the charge carrier transport properties to the change in morphology and phase within the mixture is of ultimate importance in order to shed light on the mechanism of photo de-mixing.

In this chapter, 2D Dion-Jacobson mixed halide perovskites  $(\text{PDMA})\text{Pb}(\text{Br}_{0.5}\text{I}_{0.5})_4$  (PDMA: 1,4-phenylenedimethan ammonium spacer) is used to investigate de-mixing under light and re-mixing in the dark. Using 2D Dion-Jacobson mixed iodide-bromide perovskites as model material has not only the advantage of superior stability compared with 3D perovskites, more importantly, the fact that their thin films with grain size in the micrometer range offers the opportunity of probing the same grain before and after illumination, giving accurate information on phase or morphology. The phase behavior of the mixture is investigated both under light and in the dark using a wide range of in-situ and ex-situ experimental techniques. Firstly, the conductivity changes during de-mixing is monitored. This allows for the direct probing of the ionic and electronic conductivities while the charge carrier or phase properties are varied during photo de-mixing. Simultaneously, the compositional evolution is tracked

during de-mixing and re-mixing by analyzing the time dependent in-situ optical absorption properties, as described in chapter 6. Furthermore, SEM and TEM are used to investigate the morphological changes and the nature of the iodide rich and bromide rich phases resulting from phase segregation. The investigation is carried out for samples that are encapsulated with a thin layer of PMMA. The effect of surface encapsulation is also discussed based on with results obtained for non-encapsulated samples.

## 7.2 Results and discussion

### 7.2.1 Morphological change

Ex-situ SEM measurements are conducted to examine the changes in morphology and phase properties pre- and post-illumination. In this study, silicon substrates that had a thin layer of  $\text{Si}_3\text{N}_4$  on top is used. The substrates exhibits several "windows" where no silicon is present and consisted only of the  $\text{Si}_3\text{N}_4$  film (15 nm thickness) (**Figure A.3.1**). The use of  $\text{Si}_3\text{N}_4$  as a substrate provided two advantages: (1) the thin substrate layer allows imaging measurements to be conducted in transmission mode; (2) the window positions ( $100 \times 100 \mu\text{m}$ ) could be used to identify the grain under consideration (**Figure A3.1b**).

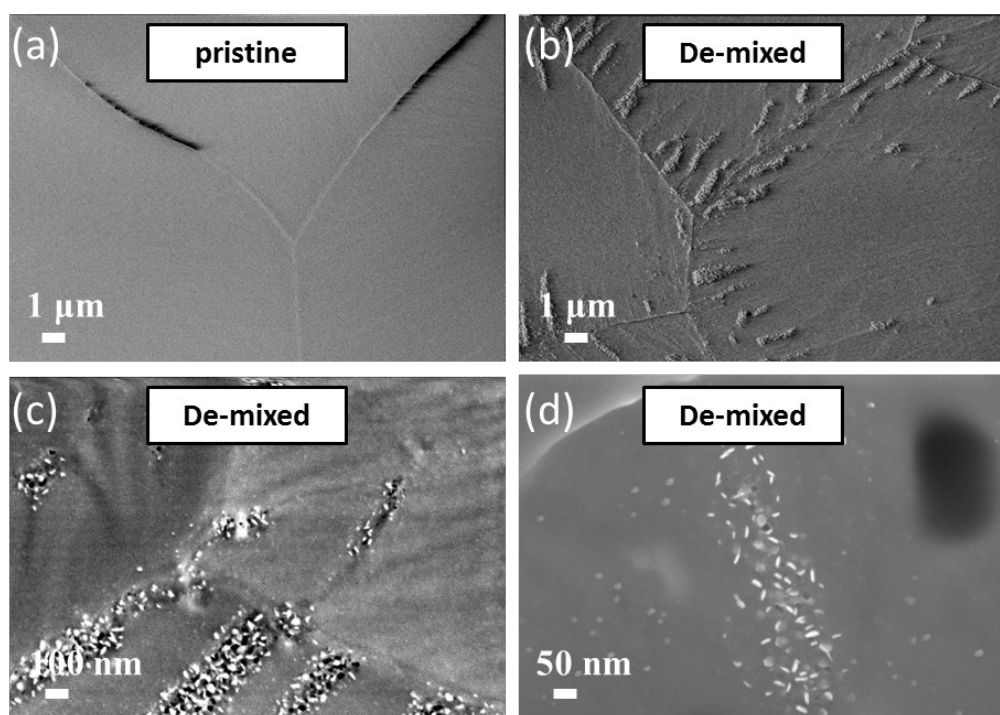


**Figure 7.1.** SEM of  $(\text{PDMA})\text{Pb}(\text{I}_{0.5}\text{Br}_{0.5})_4$  thin film in pristine (a) and de-mixed state (b) (illumination intensity  $1.5 \text{ mW}/\text{cm}^2$  at  $80^\circ\text{C}$ ). Images from InLens detector are used (see detailed discussion on detectors) with the magnification of 5K. See complete data set in **Figure A.3.3** and **Figure A.3.4** supporting information.

In order to obtain comprehensive information on both surface and bulk properties, Inlens, SE2, and BSE detectors were employed during SEM measurements. The SE2 detector provides information on surface texture and roughness by detecting emitted secondary

electrons from the surface. The BSE detector is sensitive to backscattered electrons, which provide topographical and phase information on the sample. The Inlens detector can detect the high-resolution secondary and high-energy backscattered electrons (see Chapter 4.2 for further details). The morphology of the  $(\text{PDMA})\text{Pb}(\text{I}_{0.5}\text{Br}_{0.5})_4$  thin film prior to illumination show homogeneous contrast within the grain (Figure 7.1a, triple junction), with a mean grain size of 3-5  $\mu\text{m}$  (Figure A.3.2). After de-mixing under light, crystallites with different contrast formed close to the grain boundaries (Figure 7.1b, c, d). Such small crystallites exhibits a width of approximately 30 – 70 nm (Figure 7.1d). To study the changes in perovskite thin film morphology during photo de-mixing, the illumination time was varied (0 h, 1 h, 20 h, 50 h) as shown in Figure 7.2 (see full measurements with other detectors in supporting information: Figure A.3.3 and A.3.4).

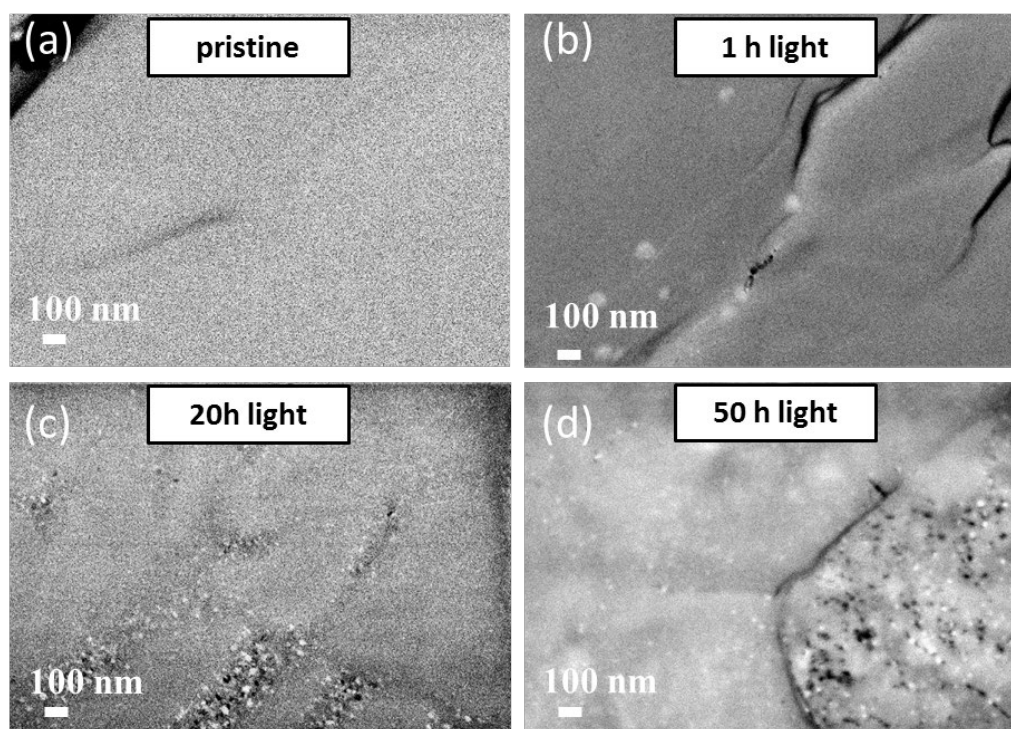


**Figure 7.2** SEM of  $(\text{PDMA})\text{Pb}(\text{I}_{0.5}\text{Br}_{0.5})_4$  thin film with different de-mixing time (illumination intensity  $1.5 \text{ mW}/\text{cm}^2$  at  $80^\circ\text{C}$ ). (a) pristine; (b) de-mixed for 1 h; (c) de-mixed for 20 h; (d) de-mixed for 50 h. Images from BSE detector are used (see detailed discussion on detectors). The imaging Magnification: 30K.

With 1 h illumination, no significant changes are observed. However, after 20 h of illumination, small crystallites with a width of approximately 30 – 70 nm formed close to the grain boundaries in the films. With 50 h illumination, the small crystallites formed not only close to the grain boundaries but also inside the grains. Intriguingly, the crystallites increased in concentration with longer illumination time, but their size remained approximately constant. Figure A.3.5 shows the morphology of the crystallites that are formed using transmission mode measurements (measurements of bulk) and further confirms these findings. Limited

contrast is obtained for measurements performed in transmission mode, as they represent an average over the whole thickness of the film. More cracks are present after illumination in the areas that are close to the grain boundaries, which can be due to the strain induced when new phases are formed. These results suggest that heterogeneous nucleation occurs firstly in competition with homogeneous nucleation. This indicates the presence of special sites close to the grain boundaries that are capable of significantly lowering the free energy associated with the nucleation process.

Such domains show tendency to disappear in the dark (glovebox at room temperature for 6 months). This indicates that photo de-mixing is reversible, at least partially, (**Figure 7.3**). It is also consistent with the results of full optical and structural reversibility (See Chapter 6). Full reversibility from a morphological point of view is difficult to prove, due to the need of non-encapsulated surfaces for SEM measurements. Under such conditions, halogen exchange with the gas atmosphere during the experiment is expected to occur, inducing irreversible degradation.

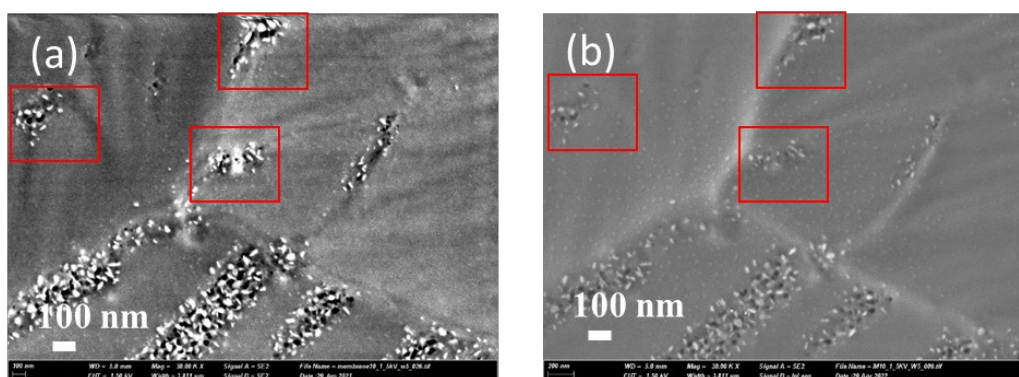


**Figure 7.3.** SEM for  $(\text{PDMA})\text{Pb}(\text{I}_{0.5}\text{Br}_{0.5})_4$  thin film (a) de-mixed for 50 h at  $1.5 \text{ mW}/\text{cm}^2$  at  $80^\circ\text{C}$ ; (b) re-mixed in the dark in the glovebox at room temperature for 6 months. The red square indicates the disappearance of the crystallites after dark storage treatment mentioned above. Images from SE2 detector are used (see detailed discussion on detectors). Magnification: 30K.

To investigate the chemical nature of the crystallites detected with SEM after photo de-mixing, cross sectional TEM is conducted. Au electrode substrates are used here to decrease the charging effect from a insulating substrates. **Figure 7.4 a** shows a top view SEM image of a de-mixed film. Similar to the above mentioned results, white crystallites are observed close the grain boundaries. One single crystalite is marked with two carbon dot and two carbon pillar markers (**Figure 7.4a, b**). **Figure 7.4 b** shows the TEM image of the cross section of such region with the grain boundary is identified between the two markers (black in this case). **Figure 7.4d** shows the TEM image with higher magnification. EDX mapping evidenced that I-rich domains are found to nucleate close to the grain boundary groove on the substrate / perovskites interface. This experiment provides direct evidence that the nanodomains forming



upon photo de-mixing of the investigated 2D mixed-halide perovskite are related to I-rich phases, an observation that is qualitatively consistent with previous work on 3D systems.<sup>81</sup> Surprisingly, Au nanoparticles are found in the perovskite film region. These particles are present only at the place where the I-rich phase is formed. This remains further experiments to clarify if such effect is reproducible. Surprisingly, Au nanoparticles are also found in the perovskite film region based on the TEM characterization. These particles are present only where the I-rich phase is formed, highlighting a more complex interaction between the film during photo de-mixing and the gold contact.

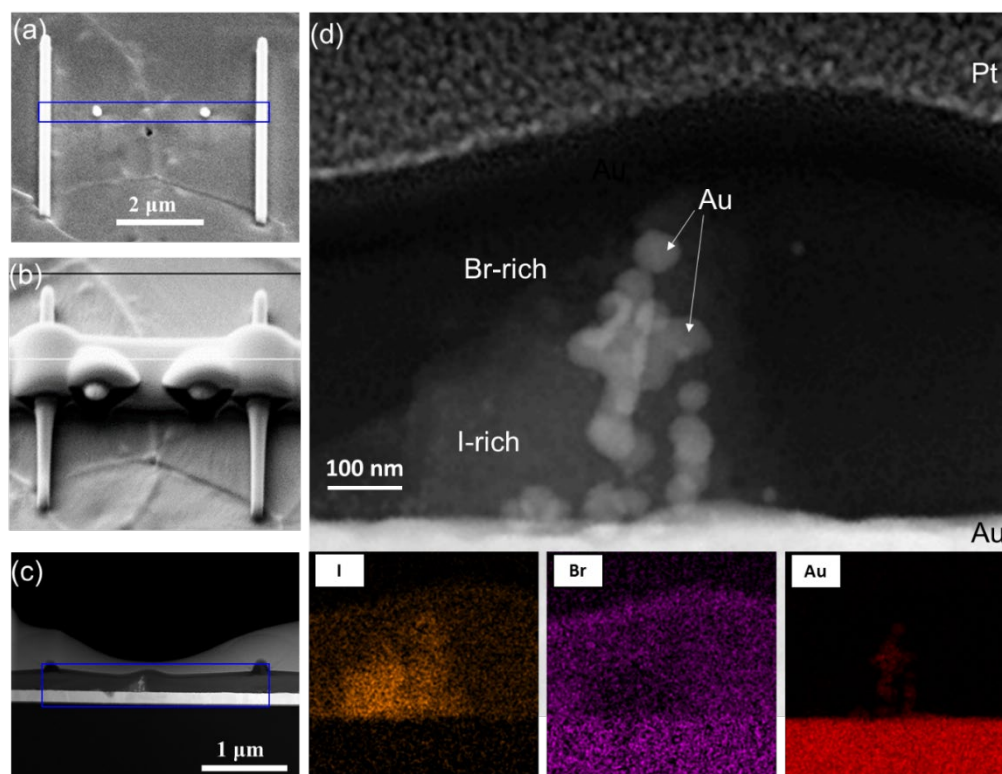


**Figure 7.4** Identification of the white crystallites formed after photo de-mixing under light ( $1.5 \text{ mW/cm}^2$ ) at  $80 \text{ }^\circ\text{C}$  for 20 h (a) Top view SEM image on the surface after depositing carbon markers to identify the position of the target crystallite. The carbon pillars are used to mark the position of the grain boundary area and the carbon dots to mark the size of the crystallites for FIB lamella preparation. (b) Top view SEM image after depositing Pt. (c) TEM image for such an area shown in (a), the black spots in this image are the cross sections of the carbon pillars in a. (d) TEM image with higher resolution highlighting the crystallites on the grain boundary is I-rich domain (the bottom panel show the EDX mapping)

In addition, the analysis of the halide distribution across two phases using EDX shows vertical segregation, whereby iodide preferentially segregates to the substrate/perovskite interface while bromide segregates to the free perovskite surface (**Figure 7.5**). The compositional distribution across the potential phase boundary is observed to be almost linear. The data correspond to an average composition across the lamella thickness.

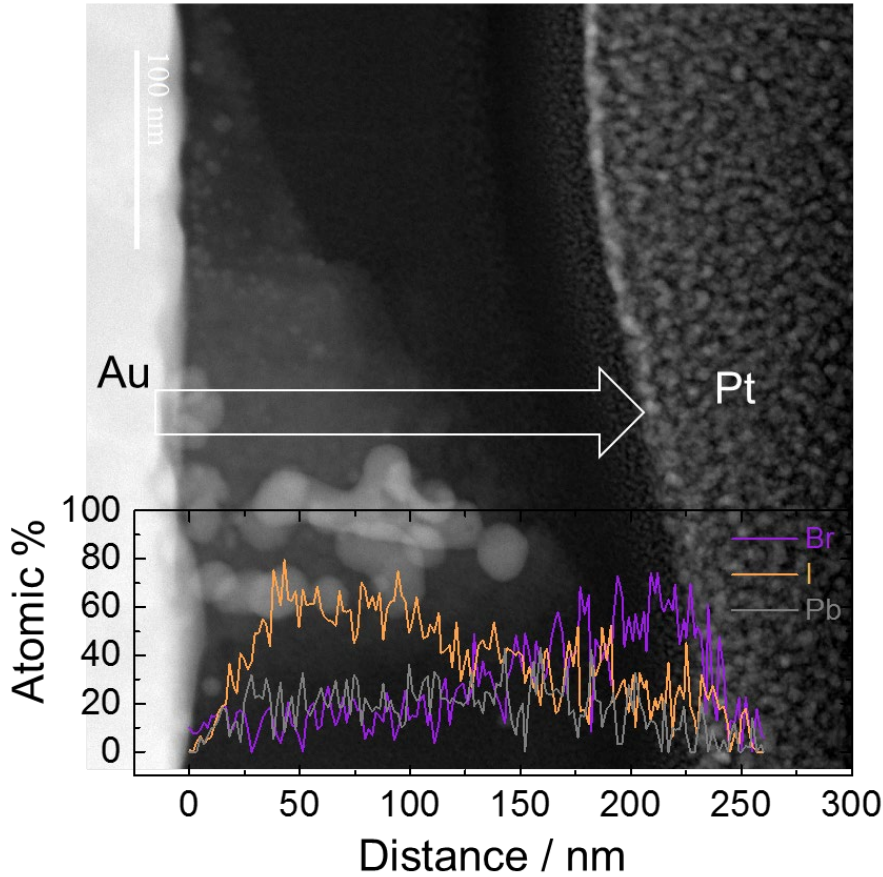


**Figure 7.5.** Elementary distribution across the de-mixed thin film (From left to right: Au→perovskites→Pt), showing that iodine is preferentially de-mixed close to the Au / perovskites interface while bromide tend to be accumulated on the free perovskites surface.

### 7.2.2 Optical and conductivity changes

Now let us move to the results and discussion of the conductivities and phase properties during photo de-mixing. Monitoring the optical and conductivity changes simultaneously during de-mixing allows for tracking the optical features of the two separated phases during their formation and the local probing of changes in both the ionic and electronic charge carrier concentration. This is achieved by the modulation of the bias light (**Figure 7.6a**), that is illumination is stopped periodically for short time during which UV-Vis is taken allowing one to measure the change in impedance during photo de-mixing as a function of time both in the dark (**Figure 7.7 a**) and under light (**Figure 7.7b**). The impedance spectra are further fitted with an equivalent circuit model including a resistor in parallel to a constant phase element (R-CPE). This resistance in the dark ( $R$ ) may be attributed to the ionic transport due to  $\sigma_{\text{ion}} > \sigma_{\text{eon}}$  under such conditions for the pristine film ( $\sigma_{\text{eon}} = 1.92\text{E-}11 \text{ S/cm}^2$ ,  $\sigma_{\text{ion}} = 8.49\text{E-}11 \text{ S/cm}^2$ ) (the time constant extracted from the polarization in this case is  $\tau = 4000 \text{ s}$  extracted from **Figure 7.6 b, c**). The resistance under light ( $R^*$ ) can be attributed to the electronic resistance,



as indicated by a limited change in voltage during a DC polarization measurement (the time constant extracted from the polarization in this case is  $\tau = 50$  s, **Figure 7.6 d, e**).

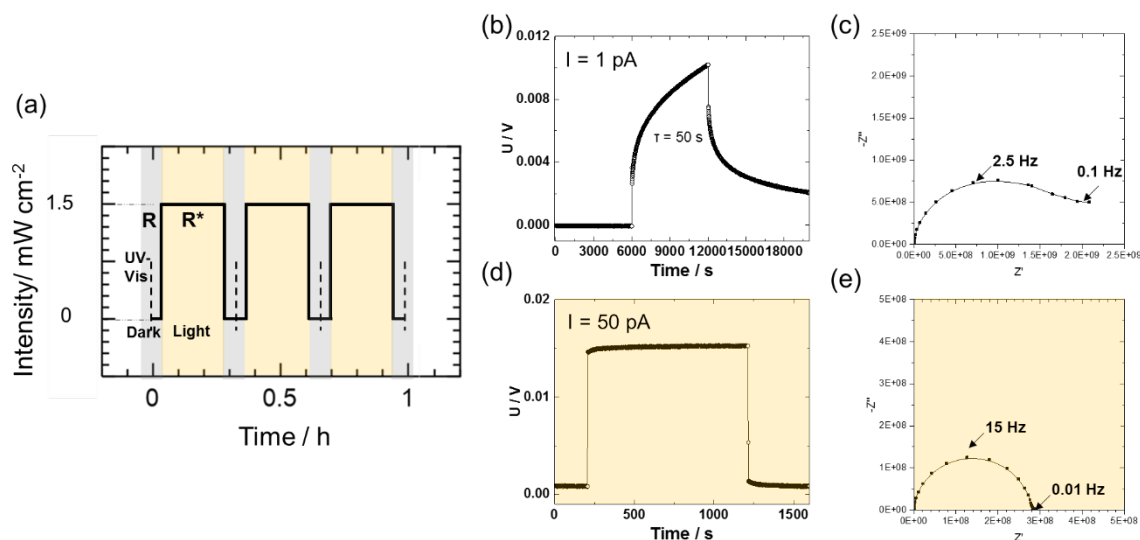


**Figure 7.6.** (a) Representation of the modulation of the bias light that allows for simultaneous measurements of UV-Vis and impedance during photo de-mixing. The light ON/OFF conditions are modulated such that there are three complete cycles per hour (150 s dark, 900 s light, 150 s dark). For each cycle, UV-Vis measurements were taken when the sample is in dark (indicated by black dashed line). Impedance measurements were conducted 2 times in the dark (grey background) and 6 times under light (1.5 mW/cm<sup>2</sup>, yellow background). (b) and (c) show the DC galvanostatic polarization and impedance measurements of (PDMA)Pb(I<sub>0.5</sub>Br<sub>0.5</sub>)<sub>4</sub> thin film in the dark, from which ionic and electronic conductivities ( $\sigma_{\text{eon}} = 1.92\text{E-}11$  S/cm<sup>2</sup>,  $\sigma_{\text{ion}} = 8.49\text{E-}11$  S/cm<sup>2</sup>) are extracted. This suggest that total resistance (first semi-circle) in the impedance is mainly contributed by the ionic transport. Therefore, such resistance can be considered as ionic resistance (R) in **Figure 7.7c**. (d) and (e) show the galvanostatic polarization and impedance measurements of (PDMA)Pb(I<sub>0.5</sub>Br<sub>0.5</sub>)<sub>4</sub> thin film under light, respectively, which evidence that the total resistance (first semi-circle) in the impedance is mainly contributed by the electronic transport. Therefore, such resistance can be attributed to the electronic resistance (R\*) in **Figure 7.7c**.

Upon illumination, the ionic resistance in the dark (R, upper figure in **Figure 7.7c**) decreases by more than one order of magnitude within the first 15 minutes. Further de-mixing leads to an increase in the ionic resistance. The electronic resistance under light (R\*, lower figure in **Figure 7.7c**) decreases abruptly within the first 15 minutes of illumination, it then remains approximately stable until about 1 h of illumination, and lastly it decreases slowly with longer time constant.

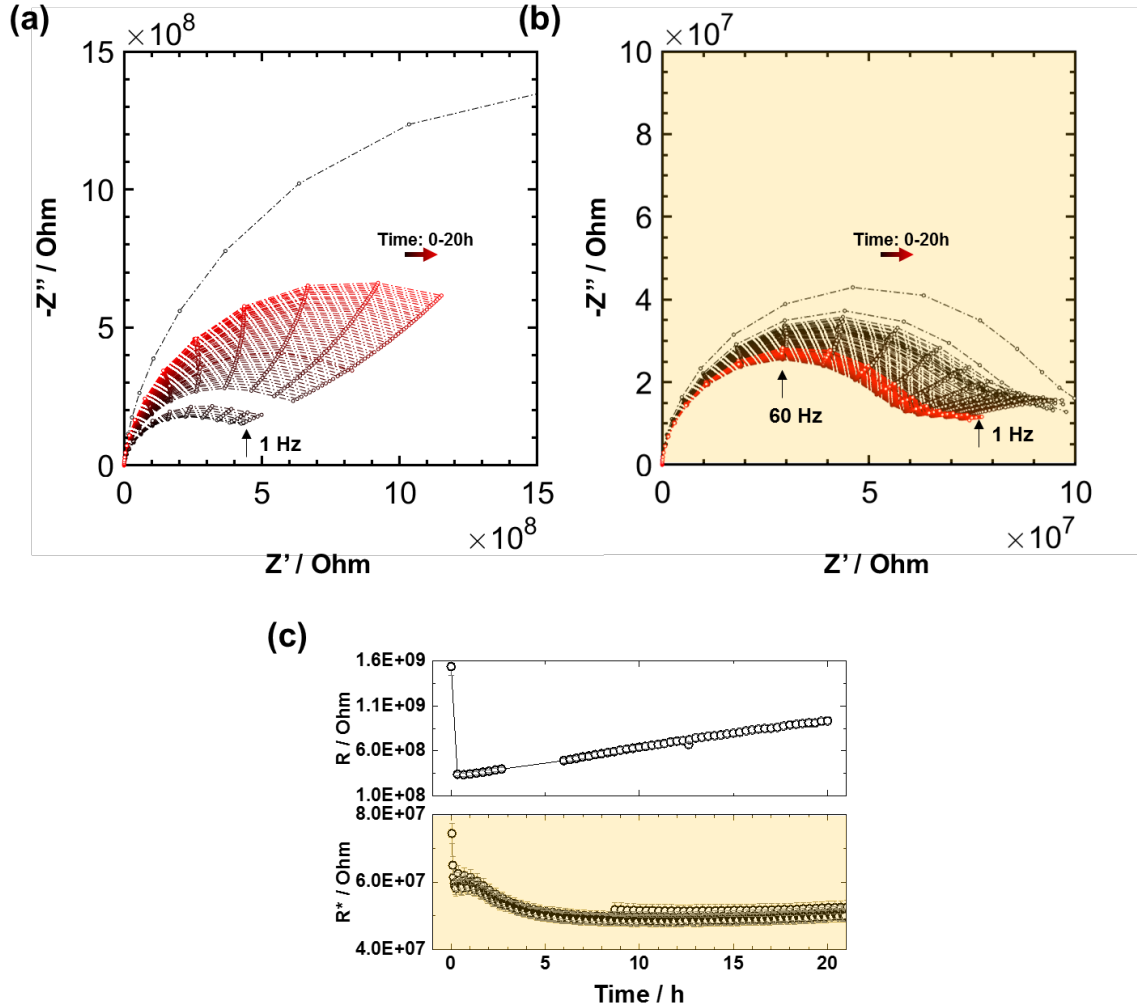


**Figure 7.7.** Impedance spectra of (PDMA)Pb(I<sub>0.5</sub>Br<sub>0.5</sub>)<sub>4</sub> thin film (with PMMA encapsulation,  $\sim 60$  nm): (a) measured in the dark (b) measured under light ( $1.5 \text{ mW/cm}^2$ ) during photo demixing (at  $80^\circ\text{C}$  for 20 h, in Ar atmosphere). (c) Evolution of the resistance extracted from the high frequency semi-circle of the impedance. measured in the dark ( $R$ ) and under light ( $R^*$ ). (d) Transient in resistance ( $R^*$  in yellow background) when quasi equilibrium of the photo demixing is reached during multiple cycles when the bias light is switched ON and OFF.

**Figure 7.8 a,b** show the absorption change during photo de-mixing indicating that the single phase mixed halide perovskite separates into Br-rich and I-rich phases under illumination (see also Chapter 6). It is worthy to note that within the first 15 min illumination, only an absorption feature that is close to the initial mixture appear (**Figure 7.8b**, upper figure). This indicates the composition broadening close to the initial composition of the mixture occurs at this time scale. With continuous illumination, an I-rich phase forms with the composition that is close to the equilibrium composition while the Br-rich phase shows larger composition variation (**Figure 7.8c**).

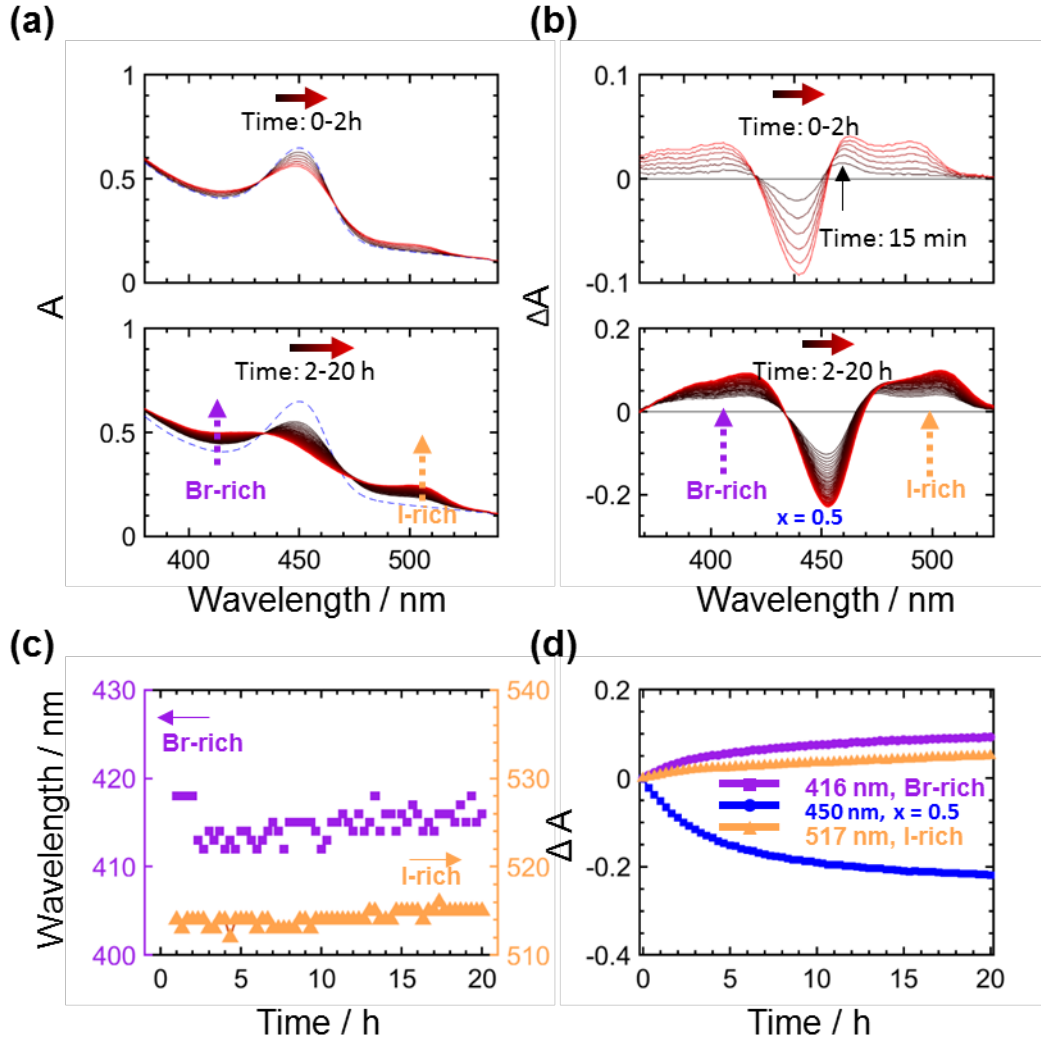


**Figure 7.8.** UV-Vis spectra evolution of (PDMA)Pb(I<sub>0.5</sub>Br<sub>0.5</sub>)<sub>4</sub> thin films (with PMMA encapsulation and in Ar atmosphere) during photo de-mixing under light (1.5 mW/cm<sup>2</sup>) at 80 °C for ~20 h (a) Absorbance and (b) Change in absorbance obtained by subtracting the reference spectrum of the pristine sample from each absorbance spectrum shown in (a). (c) characteristic wavelengths of the Br-rich and I-rich phases as a functions of illumination time. The peak wavelengths of the  $\Delta A$  and the peak wavelengths of the slope of  $\Delta A$  are used to characterize the absorption change for Br-rich and I-rich, respectively. (d) Kinetics of the photo de-mixing highlighting the change in absorbance at wavelengths associated to (PDMA)Pb(I<sub>0.5</sub>Br<sub>0.5</sub>)<sub>4</sub> (450 nm, blue), Br-rich (416 nm, purple) and I-rich (517 nm, yellow) phases.

This result, together with the electrical measurements mentioned above, suggests that within the first 15 min illumination, composition broadening close to the initial composition occurs, inducing an abrupt decrease in ionic resistance and electronic resistance. Different stage de-mixed has also been observed by Suchan *et al.* that a short-lived intense red-shifted band which is close to the pure iodide perovskite's emission formed within the first few seconds of light exposure (first stage), then disappeared followed by emission of I-rich phase with higher

energy(second stage).<sup>79</sup> Therefore, the composition fluctuation can be due to the local formation of pure iodide clusters due to hole trapping. Such trapping process will result in an increase in the ionic concentration. The change in electronic resistance under light in this case is potentially a combined effect of hole trapping increasing the electronic resistance and of increased concentration of electronic carriers due to the formation of the I-rich clusters(phases). These I-rich clusters(phases) have lower bandgap, increasing the photo-generation rate of electrons and holes and therefore decreasing the electronic resistance (assuming unchanged mobility<sup>93</sup>). The different stages shown in the electronic resistance evolution can potentially be attributed to the different generation rates associated with the composition of the pure iodide clusters(first stage) and I-rich phases (second stage). Within the initial stage locally pure iodide clusters form, due to the lower bandgap, the generation rate of the electronic charge carriers is very high, such that the electronic resistance decreases abruptly. However, when the demixing continues with the two phases forming, I-rich domains with composition close to the final composition form, the generation rate decrease. Therefore, the electronic resistance decreases but in a more moderate manner.

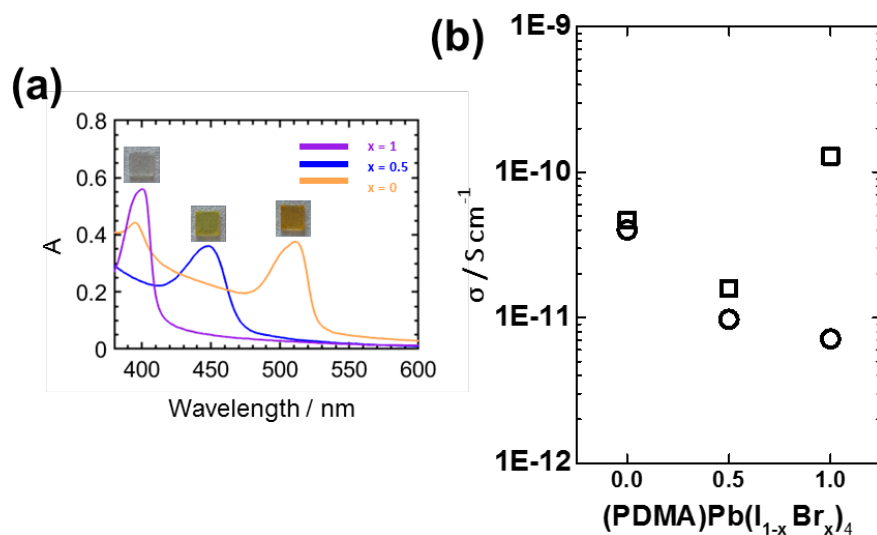


**Figure 7.9.** (a) UV-Vis spectra of 2D layered perovskite thin films on quartz substrates:  $(\text{PDMA})\text{PbI}_4$  (yellow line),  $(\text{PDMA})\text{Pb}(\text{I}_{0.5}\text{Br}_{0.5})_4$  (blue line),  $(\text{PDMA})\text{PbBr}_4$  (purple line). Photographs of relevant thin film samples with corresponding compositions are included in the inset. (b) Electronic(circle) and ionic conductivities(square) of  $(\text{PDMA})\text{PbI}_4$  (A. Ducinkas's thesis),  $(\text{PDMA})\text{Pb}(\text{I}_{0.5}\text{Br}_{0.5})_4$  and  $(\text{PDMA})\text{PbBr}_4$  measured in the dark in Ar atmosphere at 60°C.

To further correlate the change in ionic and electronic resistance with the phase composition and morphology, the conductivity of the pure 2D I and Br perovskites are measured. **Figure 7.9 a** shows the optical absorption of these films  $(\text{PDMA})\text{Pb}(\text{I}_{1-x}\text{Br}_x)_4$ , where  $x = 0, 0.5$  and 1. **Figure 7.9 b** shows that by increasing the bromide content in the 2D film,

the electronic conductivity decreases while the ionic conductivity in  $x = 0.5$  shows a dip compared to its end members. (Note that iodide data were measured at  $60^\circ\text{C}$ <sup>169</sup> while the experiments discussed above were performed at  $80^\circ\text{C}$ ). This result, together with the above discussed increase in the ionic resistance at the second stage of the photo de-mixing where both two phase formed, points towards that an overall lower ionic conductivity of the de-mixed state is possibly due to an insulating nature of the formed phase boundary.

In order to correlate the above-mentioned conductivities and absorption properties with the microscopy results, it is important to evaluate if de-mixing occurs following a similar multi-stage process from a morphological point of view. To do this,  $(\text{PDMA})\text{Pb}(\text{I}_{0.5}\text{Br}_{0.5})_4$  thin film is deposited on Au interdigitated electrodes (necessary for the electrical measurements) with the same preparation procedures as the one used for the  $\text{Si}_3\text{N}_4$  substrates (**Figure 7.1**). **Figure 7.10** shows the top view SEM images for a  $(\text{PDMA})\text{Pb}(\text{I}_{0.5}\text{Br}_{0.5})_4$  thin film on Au interdigitated electrodes in two states: prior to illumination and after 20 h of illumination. Similarly, to the films on  $\text{Si}_3\text{N}_4$  substrates, crystallites form close to the grain boundaries after illumination also in this case.

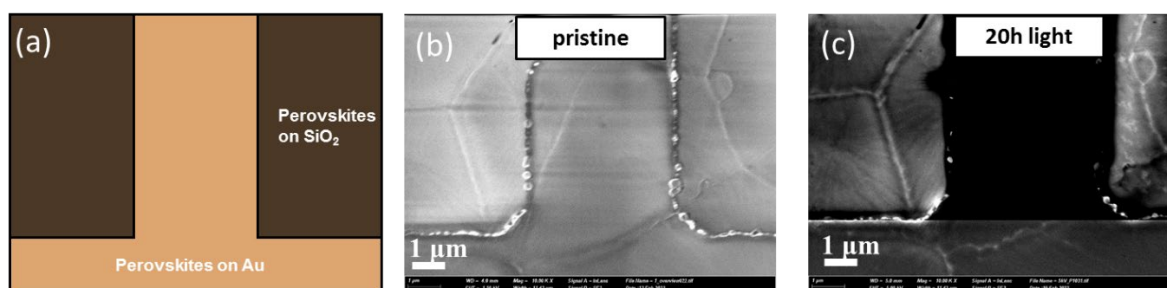


**Figure 7.10** SEM (InLens) for  $(\text{PDMA})\text{Pb}(\text{I}_{0.5}\text{Br}_{0.5})_4$  thin film. (a) Schematic showing different regions: perovskites on Au and perovskites on  $\text{SiO}_2$  (b) Pristine; (c) de-mixed for 20 h at  $1.5 \text{ mW/cm}^2$  at  $80^\circ\text{C}$ . Magnification: 10K.

As the SEM investigation was carried out on samples without encapsulation, the effect of such parameter on photo de-mixing was also evaluated by conducting the same experiment discussed above, but without adding the thin layer of PMMA after the deposition of the 2D mixture (see **Figure A.3.9** and **A.3.10** for optical and impedance data in supporting information). Importantly, XRD measurements performed before and after de-mixing show that no degradation products like of  $\text{PbI}_2$  or  $\text{PbBr}_2$  are observed (**A.3.12**, compared with **Figure 6.3**), indicating that no significant photo induced degradation occurs in this time scale without encapsulation. Also, as evidenced by the negligible changes in absorption over the last three hours of the experiment (Appendix, **Figure A.3.11**), the photo de-mixing process reaches a state of quasi-equilibrium for both cases with and without surface encapsulation.

As the SEM investigation was carried out on samples without encapsulation, the effect of such parameter on photo de-mixing was also evaluated by conducting the same experiment discussed above, but without adding the thin layer of PMMA after the deposition of the 2D

mixture (see **Figure A.3.9** and **A.3.10** for optical and impedance data in supporting information). Importantly, XRD measurements performed before and after de-mixing show that no degradation products like of  $\text{PbI}_2$  or  $\text{PbBr}_2$  are observed (**A.3.12**, compared with Figure 6.3), indicating that no significant photo induced degradation occurs in this time scale without encapsulation. Also, as evidenced by the negligible changes in absorption over the last three hours of the experiment (Appendix, **Figure A.3.11**), the photo de-mixing process reaches a state of quasi-equilibrium for both cases with and without surface encapsulation.

**Figure 7.11a** shows the difference of ionic and electronic resistance during photo de-mixing with and without PMMA encapsulation on the surface prior to illumination. Contrary to the abrupt decrease in ionic resistance within the first 15 min with PMMA, an increase of the ionic resistance was observed without PMMA encapsulation. Such distinct difference suggests that surface effects play an important role on the photo de-mixing behavior. PMMA has often been used as passivation layer in the literature. As photo de-mixing is sensitive to the electronic charge carrier concentration, it is very likely that photo de-mixing is also influenced by the presence of this encapsulant. It is worthy to notice that the ionic resistance in the dark (the first point in **Figure 7.11a**, upper figure) is the same as prior to illumination for both the encapsulated and the non-encapsulated samples. The electronic resistance under light ( $R^*$ , the first point in **Figure 7.11a**, lower figure) shows higher resistance compared with the with PMMA case. Given the very thin layer of the PMMA ( $\sim 60$  nm, See Appendix **Figure A3.13**) and its optical properties (largely transparent in the visible), it can be safely excluded that this increase in resistance is due to optical transparency and blocking of such layer. Instead, the observed increase in resistance under light suggests that encapsulation with a thin layer of PMMA may decrease the electronic charge carrier concentration within the film. Such results can potentially be explained by an enhanced charge carrier recombination at the interface between perovskites and PMMA layer. The electronic resistance under light ( $R^*$ ), without PMMA shows decrease in resistance within the first hour and then increase as a function of de-mixing time. After long time scales ( $\sim 4$ h),  $R^*(\text{PMMA})$  is larger than  $R^*$  (w/o PMMA).

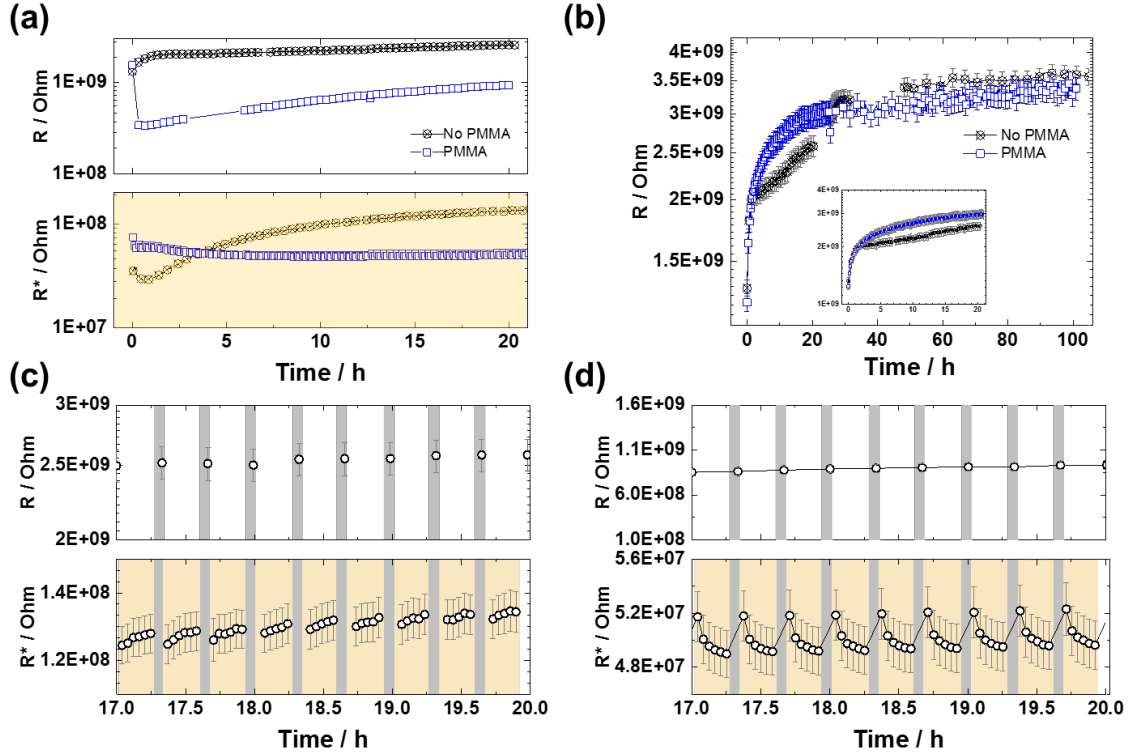
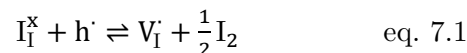


**Figure 7.11** The effect of encapsulation on ionic ( $R$ ) and electronic resistance ( $R^*$ , in yellow background) response of  $(\text{PDMA})\text{Pb}(\text{I}_{0.5}\text{Br}_{0.5})_4$  thin film during photo de-mixing (white LED illumination:  $1.5 \text{ mW}/\text{cm}^2$ , at  $80 \text{ }^\circ\text{C}$  for 20 h, in Ar atmosphere). (b) Ionic resistance ( $R$ ) during dark re-mixing. Black open circle with crossing denotes absence of PMMA encapsulation; blue open squares denote the situation presence of PMMA encapsulation. (c, d) show the transient in electronic resistance ( $R^*$  in yellow background) when quasi equilibrium of the photo de-mixing is reached. (c) Without PMMA encapsulation (d) with PMMA encapsulation on the surface prior to illumination.

A more detailed examination of the collected data highlights the influence of the light modulation from dark to light during photo de-mixing on ionic and electronic resistance (as depicted in **Figure 7.11c** and d for the samples with and without PMMA). It is interesting to notice that throughout the measurement, a transient in the value of resistance under light is observed ( $R^*$  in yellow background) when the light is switched off and on. **Figure 7.11c** indicates that with an uncovered surface, the electronic resistance shows periodic increases during the illumination cycle. Following the 150-second dark period during which impedance measurements were taken, the electric resistance once again decreases, followed by another cycle of increased electronic resistance. The opposite trend is discovered for the encapsulated film. This trend is consistent with the overall trend of  $R^*$  shown in **Figure 7.11a**. Such observed difference in the change in  $R^*$  between the two samples may be attributed to the trapping of electronic charge carriers under light and the subsequent excorporation of iodine into the gas phase (according to defect equation below).



Such process is prohibited when the surface is encapsulated with PMMA. Therefore, a transient involving an increase in the charge carrier density with prolonged illumination time is observed. Such hypothesis is consistent with earlier studies on PL intensity with and without PMMA encapsulation during repeated de-mixing and remixing cycles in which the PL intensity slightly decreases without encapsulation.<sup>170</sup> The change in resistance in the dark during dark re-mixing is also measured and displayed in **Figure 7.11b**. Without PMMA encapsulation, the re-mixing kinetics exhibit more complex re-mixing steps, but the ultimate resistance and the time constant are nearly same in both cases, indicating that surface passivation may affect the kinetics of dark re-mixing. The ultimate resistance increases with a factor of two compared with the pristine prior to photo de-mixing and dark re-mixing, suggesting that minor degradation occurs. Importantly, this is the case also for the encapsulated sample. This suggests that, even though complete reversibility is observed for the optical and structural properties of these 2D mixed halide perovskites with encapsulation, the electrical response after photo de-mixing and dark re-mixing does not completely recover. On the other hand, the experiment in **Figure 7.11b** was run for only 100 hours. Further changes may occur over the 300 hour time scales cannot be excluded (see Chapter 6).

In addition to the above kinetic analysis, the kinetics for the change in the absorbance obtained during photo de-mixing at different temperatures (**Figure A.3.14- A.3.16**) are tracked and fitted a bi-exponential functions to the data (**Figure A.3.17**). From the analysis of the temperature dependent half-time we obtain an activation energy of 0.39 eV (**Figure A.3.18**). This value is slightly larger than the value reported for photo de-mixing in 3D (0.27 and 0.30 eV)<sup>11, 117</sup> and 2D RP case (0.22 eV)<sup>171</sup> mixed halide perovskites.

Finally, a microscopic picture of the mechanism of photo de-mixing is proposed (**Figure 7.12**) based on the experimental and computational results shown above. We have shown evidence that photo de-mixing of 2D mixed halide perovskites occurs in multiple stages. In a first stage, a composition broadening close to the initial composition occurs, a process potentially consistent with spinodal decomposition of the mixture. This is accompanied by significant decrease in the resistance measured in the dark, possibly due to an increase in concentration of mobile ionic defects or to electronic trapping effects. In a second stage, direct transformation of the mixed halide perovskite to the final composition for either the I-rich or the Br-rich phase (or possibly for both of them) occurs via nucleation and growth of these phases. The existence of the nucleation centres along the grain boundaries, but also within the grains, can significantly lower the energy barrier of the final phase formation, triggering nucleation processes that compete with the spinodal decomposition. Such mechanism in a simplified free energy diagram is shown below.<sup>17, 20, 21, 49</sup>



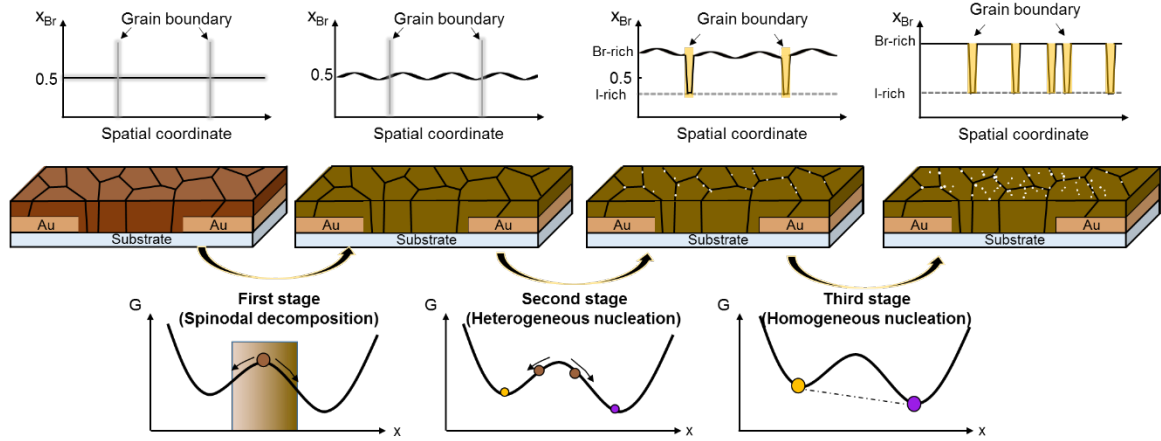


**Figure 7.12** Microscopic schematic representation of the proposed mechanism for photo de-mixing in the 2D PDMAPb(I<sub>1-x</sub>Br<sub>x</sub>)<sub>4</sub> perovskite, showing spinodal decomposition (first stage) followed by nucleation (second and third stage). Upper panel: composition distribution in spatial coordinate; middle panel: change in film morphology at different stages; bottom panel: compositional variation at different stages illustrated schematically in a free energy (under light) vs composition plot.

## 7.4 Conclusion

In this chapter, complementary experimental techniques are used to unveil the role of electronic and ionic effects on photo de-mixing in 2D mixed halide perovskites. Morphologically, the spatial distribution of the de-mixed domains highlight heterogeneous nucleation of nano-domains that are rich in iodide. These domains are ~30-70 nm and form between the boundary layers of the adjacent grains and close to the film/substrate interface. Homogeneous nucleation occurs with prolonged illumination, where such domains also form within the grains. Interestingly, increasing photo de-mixing time results in increase in the density of such domains while their size remains limited to <100 nm.

When the sample is encapsulated with PMMA (reducing the effect of slow degradation and excorporation of iodine under light) a decrease in the (ionic) resistance in the dark by more than one order of magnitude within the first 15 min of illumination is observed. Such decrease in resistance is accompanied by the composition broadening close to initial mixture composition. This can be rationalized based on a substantial concentration of holes that are trapped, resulting in an increase of the ionic defect concentration. A decrease of the (electronic) resistance under light is also detected, which can be attributed to the electronic charge generation and subsequent funneling to the almost pure iodide clusters. Further illumination increases the (ionic) resistance in the dark and decreases the (electronic) resistance under light, suggesting that the de-mixed situation becomes gradually more ionically insulating and the formation of the I-rich phase are dominating the electronic response. In this stage (illumination times longer than ~1 h), I-rich phases with compositions close to the final quasi-equilibrium compositions are formed.

The effect of a non-encapsulation surface has also been investigated. During photo de-mixing, in contrast to the case with PMMA encapsulation, both of the (ionic) resistance in the dark and electronic resistance under light increase as a function of illumination time. This difference in the electrical response can be attributed to the influence from the surface charge recombination and from the ex-corporation reaction of iodine into the gas phase by surface encapsulation. Without PMMA encapsulation, the re-mixing kinetics exhibit more complex re-mixing steps, but the ultimate resistance and the time constant are nearly same in both cases, indicating that surface passivation may affect the kinetics pathway of dark re-mixing.

Lastly, the kinetics investigation of photo de-mixing in 2D DJ mixed halide perovskites shows an activation energy for photo de-mixing of 0.39 eV, slightly larger than the value reported for photo de-mixing in 3D (0.27 and 0.30 eV) and 2D RP type (0.22 eV) mixed halide perovskites.

## 8 Photo de-mixing in mixed halide perovskites: 3D and nanocrystals

### 8.1 Introduction

As introduced in the previous chapters, phase transformation of mixed halide perovskites to de-mixed phases with different bandgaps occurs upon illumination.<sup>11</sup> This phase transformation involves the generation and recombination of electronic charge carriers and their interaction with the lattice that induces ionic defect formation and transport. Therefore, the process of photo de-mixing is a result of both electronic and ionic effects. Dimensionality control serves as an effective way to tune the electronic and optical properties of halide perovskites (See Section 2.1). For example, the electrons' and holes' wave functions are confined and varied by introducing large organic spacer. This confinement can be achieved in various dimensions. Of particular interest are the compounds where confinement occurs in 1 dimension (two dimensional (2D) halide perovskites,  $A'BX_3$ ) and three dimensions (3D nanocrystals (NC),  $A''-ABX_3$ ) (See **Figure 1.2**). Notably, the introduction of a 2D layer in 3D mixed halide perovskites has shown, in several instances, improved stability and performance in devices.<sup>172-174</sup> In such context, understanding photo de-mixing in mixed halide perovskites with different dimensionality is crucial.

In this chapter, the dependence of the phase behavior of mixed halide perovskites with different dimensionality (3D, and nanocrystals, see Section 1.2 for introduction of the materials) under light is investigated. The changes in absorption properties and conductivities when the films are exposed to light are probed simultaneously. These results are compared and discussed with the results shown for 2D perovskites in Chapter 6 and 7.

### 8.2 Results and discussion

The structure of mixed halide perovskites with different dimensionalities used in this work are shown in **Figure 8.1a**. Compared with 3D mixed halide perovskites ( $\text{MAPb}(\text{I}_{0.5}\text{Br}_{0.5})_3$ ), 2D mixed halide perovskites ( $(\text{PDMA})\text{Pb}(\text{I}_{0.5}\text{Br}_{0.5})_4$ ) exhibit a structure involving organic spacers which separate corner-sharing  $[\text{PbX}_6]^{4-}$  slabs, leading to their confinement in the direction perpendicular to such lead halide octahedral planes. 3D nanocrystals are confined in three dimension with organic ligand surrounding the three dimensional perovskites. **Figure 8.1b** shows the thin film morphology of these mixed halide perovskites. The grain size are around 150-200 nm, 3-5  $\mu\text{m}$ , 10 nm for 3D, 2D and NC mixed halide perovskites, respectively. The XRD and UV-Vis of mixed halide perovskites are shown in **Figure 8.1 c and d**. A distinct feature of 2D mixed halide perovskites is the appearance of the XRD peak at very low angle, which corresponds to the distance of the lead halide octahedral slabs. Compared with 3D mixed halide perovskites, 3D NCs exhibits absorption at higher photon energies while 2D mixed halide perovskites show a sharp excitonic peak.

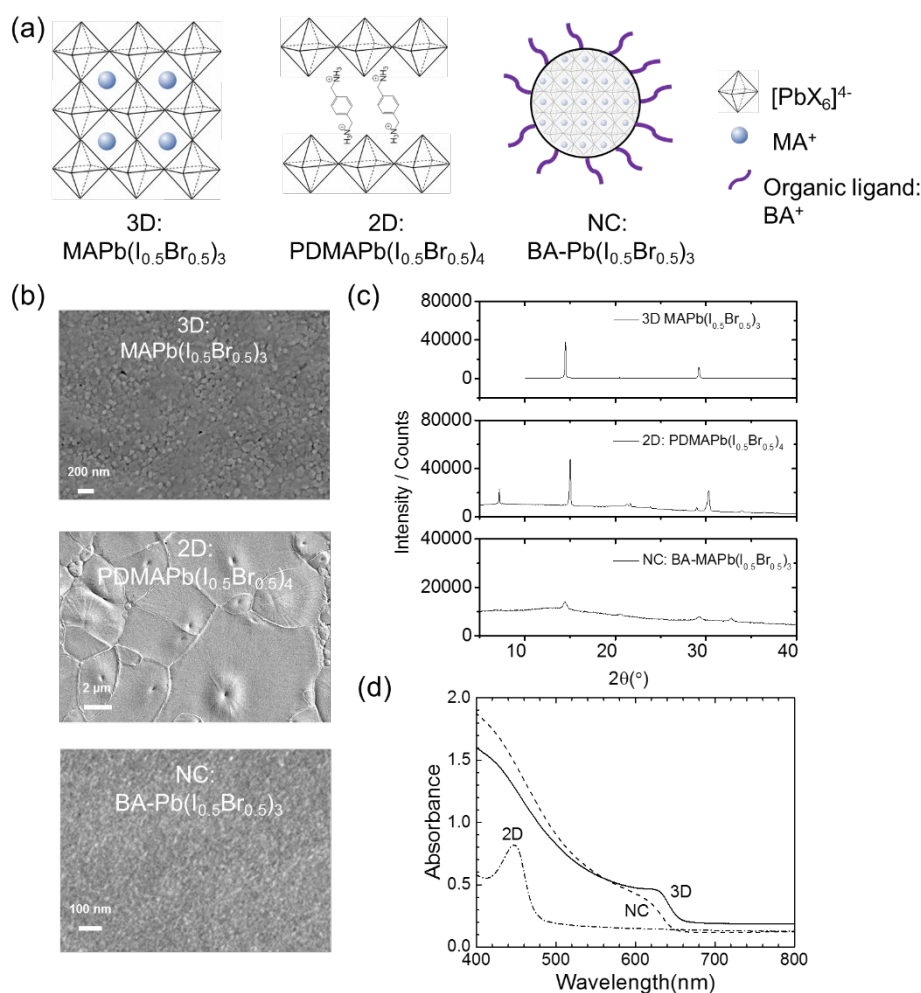


**Figure 8.1.** (a) Mixed halide perovskite structures with different dimensionalities: from three dimensional (3D):  $\text{MAPb}(\text{I}_{0.5}\text{Br}_{0.5})_3$  to two dimensional (2D):  $(\text{PDMA})\text{Pb}(\text{I}_{0.5}\text{Br}_{0.5})_4$  and nanocrystals (NC):  $\text{BA-MAPb}(\text{I}_{0.5}\text{Br}_{0.5})_3$ . MA, PDMA and BA represents methyl ammonium ( $\text{MA}^+$ ), 1,4-phenylenedimethan ammonium ( $\text{PDMA}^{2+}$ ) and n-butyl ammonium ( $\text{BA}^+$ ). (b) Top view SEM image (c) XRD (d) UV-Vis spectrum of the above mentioned mixed halide perovskites.

### 8.2.1 Photo de-mixing in 3D mixed halide perovskites: $\text{MAPb}(\text{I}_{1-x}\text{Br}_x)_3$

In this chapter, I present results obtained by applying a similar method as the one shown in chapter 7 to 3D and nanocrystalline mixed-halide perovskite thin films. By combining UV-Vis and impedance measurements, in-situ non-destructive evaluation of optical and electrical properties<sup>165</sup> during photo de-mixing in the samples is possible. **Figure 8.2** shows the UV-Vis spectral evolution of  $\text{MAPb}(\text{I}_{0.5}\text{Br}_{0.5})_3$  during photo de-mixing.

The absorption spectrum of 3D  $\text{MAPb}(\text{I}_{0.5}\text{Br}_{0.5})_3$  thin film shows composition fluctuation that is close to the initial composition on illumination at early time scales (~1h). Continuous illumination results in the formation of two distinct absorption features, previously identified as I-rich and Br-rich phases.<sup>11</sup> Such two-stage absorption behavior has also been observed in 2D mixed halide perovskites (Chapter 7), suggesting that the mechanism of photo

de-mixing may remain unchanged while varying the dimensionality. The kinetics of photo de-mixing is further monitored based on their characteristic absorption wavelengths (**Figure 8.2e**). On consumption of the mixed phase, the I-rich phase form first, followed by a slower increase in the signal associated with the Br-rich phase. This further suggests a two-stage de-mixing mechanism occurring in the 3D mixed halide perovskites system. Photo de-mixing reaches a quasi-equilibrium state after approximately 15 hours, as confirmed by the change in absorption and its derivative with respect to time, referred to as  $(A_n - A_0)$  and  $(A_n - A_{n-1})$  (**Figure 8.2e and f**).

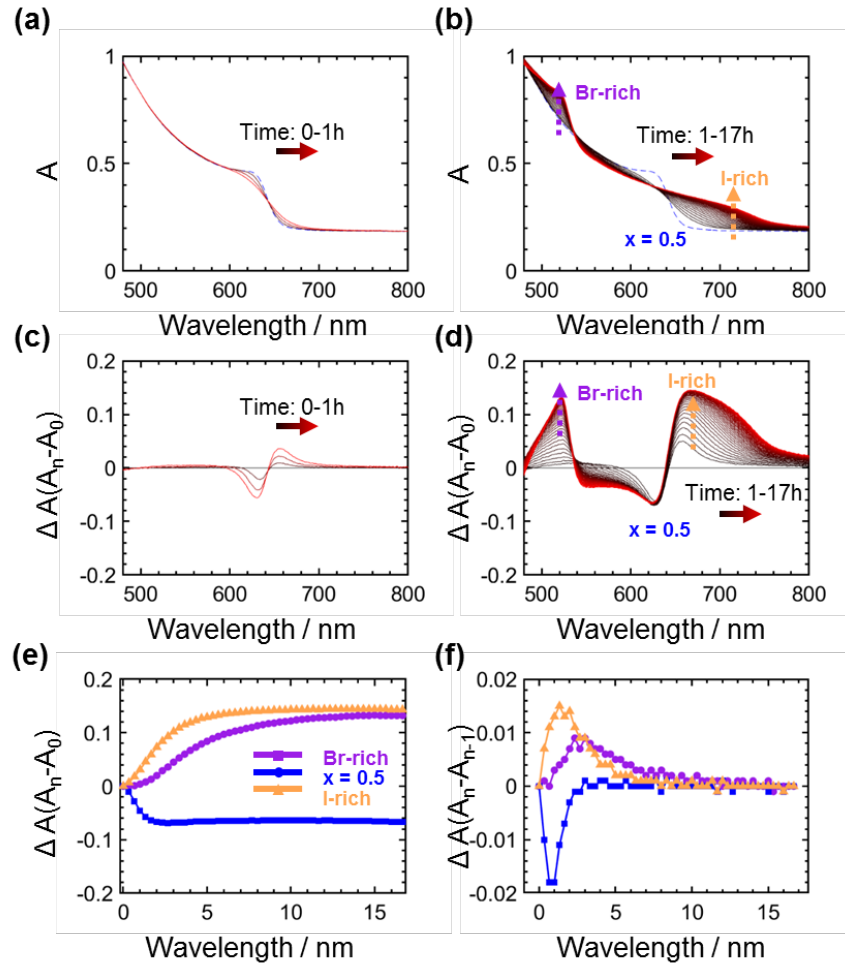


**Figure 8.2.** UV-Vis spectral evolution of  $\text{MAPb}(\text{I}_{0.5}\text{Br}_{0.5})_3$  thin films (without PMMA encapsulation and in Ar atmosphere to exclude possible) under light ( $1.5 \text{ mW/cm}^2$ ) at  $40^\circ \text{C}$  for 17 h. Measurements were performed with 20 min interval. See Chapter 4 for details about the dark and light modulation procedure. (a) First stage of photo de-mixing: illumination induces composition fluctuation close to the initial composition; (b) Second stage of photo de-mixing: formation of the two distinct absorption features that correspond to the final Br-rich and I-rich phases; (c, d) Change in absorbance obtained by subtracting the reference spectrum of the pristine sample from each absorbance spectrum shown in (a) and (b), respectively. Kinetics of the change in absorbance during the photo de-mixing process (e)  $\Delta A(A_n - A_0)$  (f)

$\Delta A(A_n - A_{n-1})$  at wavelengths associated to  $\text{MAPb}(\text{I}_{0.5}\text{Br}_{0.5})_3$  (623 nm, blue), Br-rich (523 nm, purple) and I-rich (663 nm, yellow) phases.

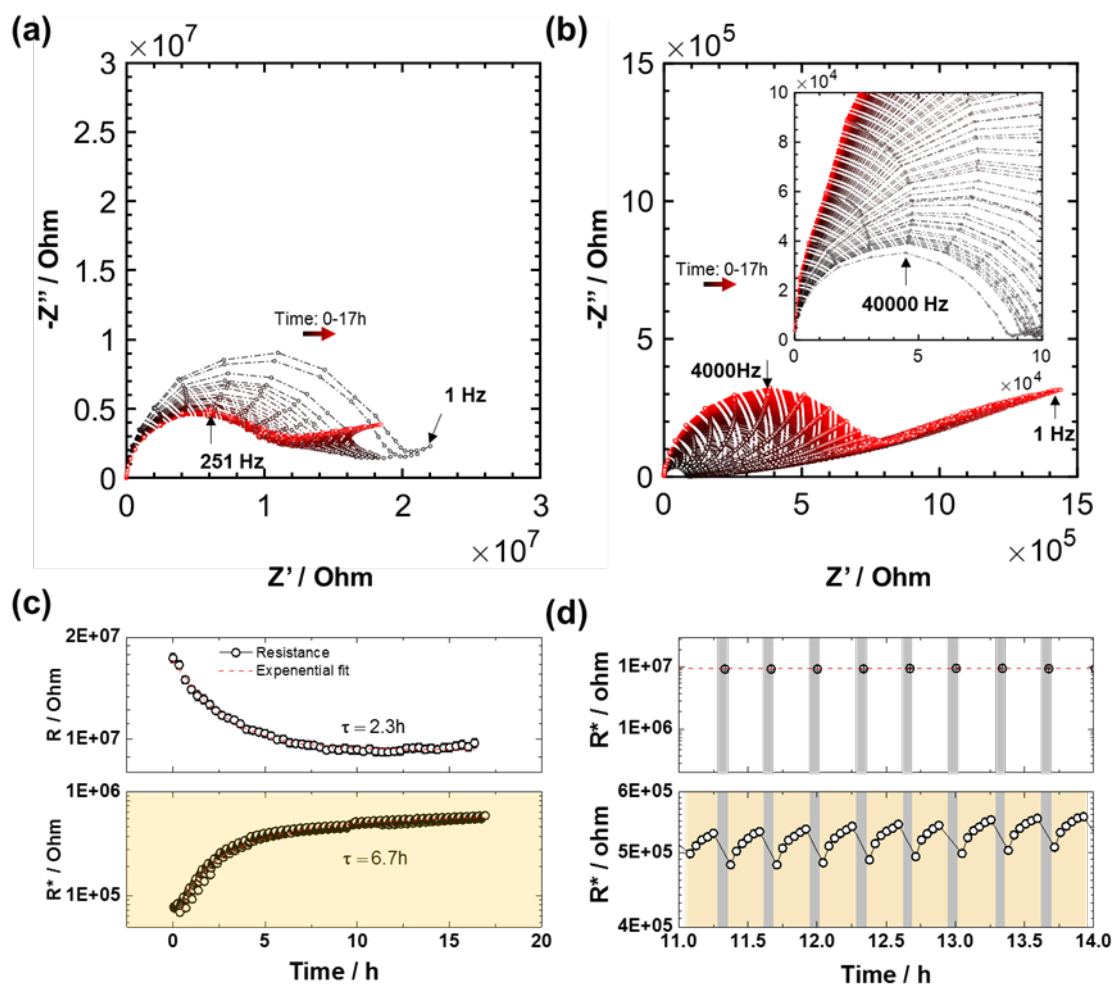


**Figure 8.3.** Impedance spectra evolution of  $\text{MAPb}(\text{I}_{0.5}\text{Br}_{0.5})_3$  thin films (without PMMA encapsulation and in Ar atmosphere) during photo de-mixing ( $1.5 \text{ mW}/\text{cm}^2$ ) at  $40^\circ\text{C}$  for 17 h. (a) measured in the dark (b) and measured under light. Black to red data denote the time sequence. (c) Change in the value of resistance during photo de-mixing: upper (in the dark), below (under light). The resistance is obtained from fitting a circuit model including a resistor and a constant phase element to the high frequency semi-circle of the data shown in a and b. (e) Transient of the resistance under light observed during the light modulation when quasi-equilibrium of the photo de-mixing is reached.

Figures 8.3 a, b show the changes in the impedance in the dark and under light during photo de-mixing. The resistance in the dark ( $R$ , upper figure in **Figure 8.3 c**) can primarily be attributed to ionic transport while the resistance under light ( $R^*$ , lower figure in **Figure 8.3c**) can be attributed to electronic transport. The (ionic) resistance in the dark decreases while the (electronic) resistance under light increases as function of illumination time. Interestingly, no distinct separation of the two stages observed in absorption is observable from this electrical response.

Next, the effect of the surface encapsulation is evaluated by conducting photo de-mixing experiments under the same conditions but encapsulating a PMMA layer on the surface. In this case, interestingly, only the first stage photo de-mixing appears (**Figure 8.4 a, c**), even under long illumination times under the same conditions as for the experiment in **Figure 8.2**. This result suggests that encapsulation plays an important role in the reaction pathway of photo de-mixing in 3D mixed halide perovskites. The observed first stage of photo de-mixing shows reversible behaviour when the sample is in the dark (**Figure 8.4 b,d**). The sample without PMMA, however, shows partial reversibility in the absorption feature with the formation of the  $\text{PbI}_2$  (**Figure A.4.2**, supporting information).

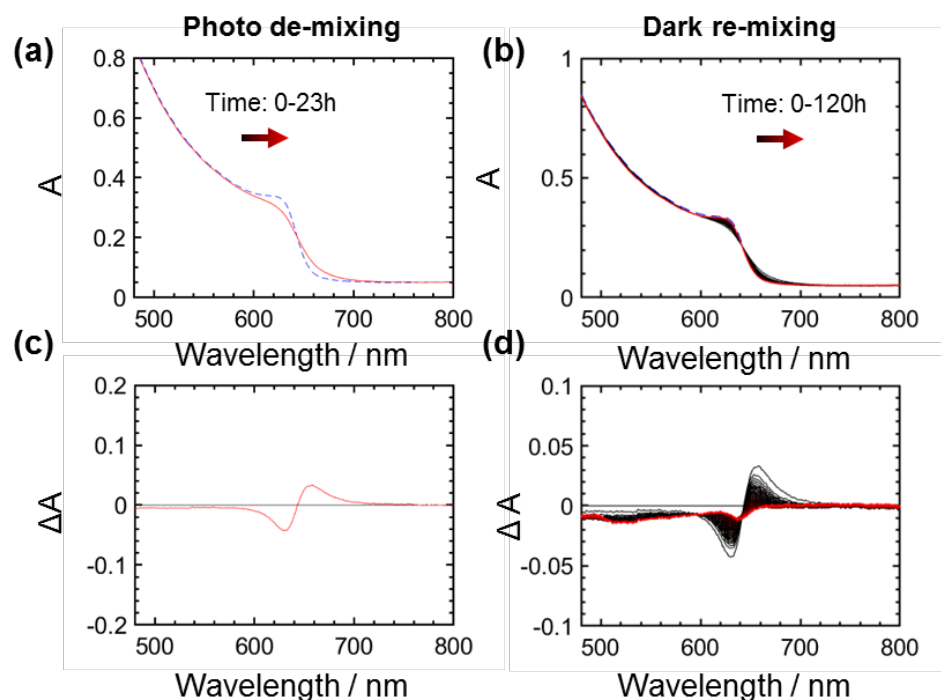


**Figure 8.4.** UV-Vis spectra evolution of  $\text{MAPb}(\text{I}_{0.5}\text{Br}_{0.5})_3$  thin films (with PMMA encapsulation and in Ar atmosphere) (a) under light ( $1.5 \text{ mW}/\text{cm}^2$ ) at  $40 \text{ }^\circ\text{C}$  for  $\sim 23 \text{ h}$  with 20 min intervals (within each interval, spectra were collected by switching off the bias light for 300 s) and (b) in the dark at  $40 \text{ }^\circ\text{C}$  for  $\sim 120 \text{ h}$  with 1 h time interval between spectra. (c, d) Change in absorbance obtained by subtracting the reference spectrum of the pristine sample from each absorbance spectrum shown in (a) and (b), respectively.

To study the effect of encapsulation on the electrical response during photo de-mixing and to check the reversibility of the process further, the impedance of the two samples discussed above is measured during illumination and after light has been switched off. The kinetics of the ionic resistance evolution in the dark during photo de-mixing (yellow) and re-mixing (black) under these two conditions (non-encapsulated / encapsulated with PMMA) are displayed in **Figure 8.5a**. Firstly, regardless of encapsulation, the ionic resistance ( $R$ , dark) shows a (almost) complete reversible behaviour. Given the observed degradation without PMMA, this indicates that the electrical response is not as sensitive than absorption and XRD

to the degradation of the sample. The time scale of the recovery is slower by a factor of six compared with the de-mixing. In addition, the re-mixing kinetics shows an almost linear trend followed by a plateau when the steady state is reached, possibly suggesting that re-mixing occurs in the form of a zero order reaction.

With encapsulation, after the first stage of photo de-mixing, the ionic resistance decreases by 7%. When the sample is not encapsulated, however, after completion of the two-stage photo de-mixing, the ionic resistance decreases by a factor of two. Interestingly, the ionic resistance after 1h (completion of the first stage) is the same compared with the encapsulated value after 23 h illumination. This indicates that there is good correspondence between the electrical and the optical response and that the two samples reach similar conditions on completion of the first stage of photo de-mixing. The data associated with the non-encapsulated mixed halide perovskite film in **Figure 8.5b** show that the electronic resistance during photo de-mixing (total resistance under light,  $R^*$ ) undergoes an increase of almost one order of magnitude. This implies that I-rich phase formation in this case is not percolating within the bulk film and that the rate of recombination increases the more the de-mixing advances. On the other hand, for the film with PMMA encapsulation, the electronic resistance under light remains almost constant with respect of time during the photo de-mixing process. This may be related with possible changes in surface properties (e.g. formation of trap states potentially related to the process of iodine exchange with the gas phase) occurring when the film is not encapsulated, an effect that can be reduced by encapsulation.

Next, I discuss the possible mechanism of photo de-mixing in 3D mixed halide perovskites ( $\text{MAPb}(\text{I}_{0.5}\text{Br}_{0.5})_3$ ). Firstly, in-situ optical spectroscopy indicates that photo de-mixing in the 3D mixed halide perovskites occurs in two stages, with composition variations that are close to the initial composition (stage one) followed by formation of the Br-rich and I-rich phases (stage 2). This behavior is observed when the perovskite's surface is not encapsulated. A similar two-stage behavior was also found in 2D mixed halide perovskites (Chapter 7, with and without encapsulation), indicating that introducing insulating organic spacers to the system does not affect the mechanism of the photo de-mixing. With encapsulation, however, under the same conditions, only the first stage photo de-mixing is observed, occurring at a slower rate. This can be a thermodynamic effect that with the presence of encapsulation, the second-stage de-mixing is not favored energetically. It is also consistent with the observed narrowing of the photo-miscibility-gap with encapsulation in 2D (Chapter 7).



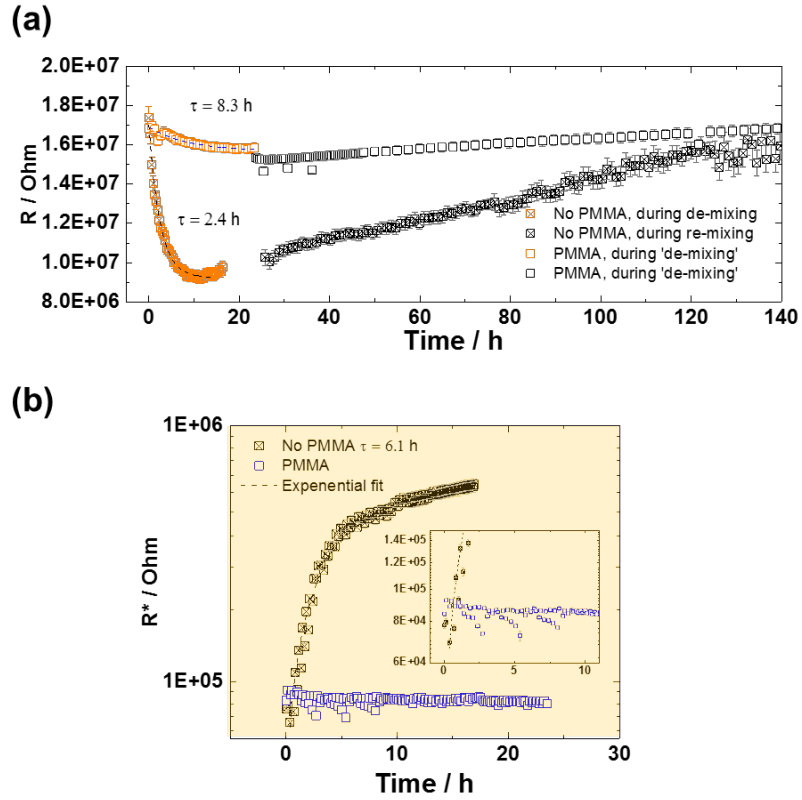


**Figure 8.5.** (a) Kinetics of change in resistance measured in the dark ( $R$ ): photo de-mixing (orange) and dark re-mixing (black) of  $\text{MAPb}(\text{I}_{0.5}\text{Br}_{0.5})_3$  thin films under two conditions that surface is encapsulated (square) and non-encapsulated (crossed square) with PMMA before photo de-mixing. (b) Kinetics of the changes in resistance measured under light ( $R^*$ ).

## 8.2.2 Phase stability of BA-MAPb(I<sub>0.5</sub>Br<sub>0.5</sub>)<sub>3</sub> nanocrystals under light

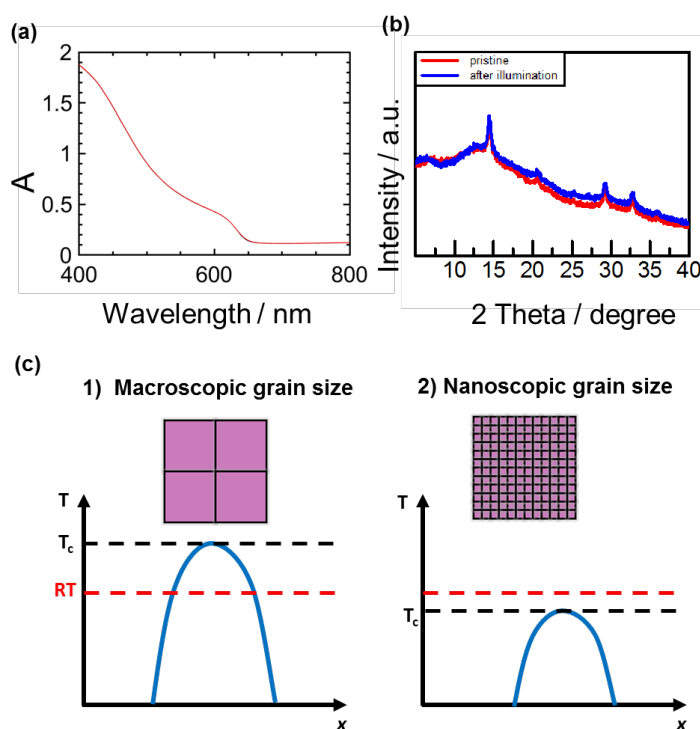


**Figure 8.6.** (a) UV-Vis spectra evolution of BA-MAPb(I<sub>0.5</sub>Br<sub>0.5</sub>)<sub>3</sub> nanocrystal thin films (without PMMA encapsulation and in Ar atmosphere to exclude possible degradation) (a) under light (1.5 mW/cm<sup>2</sup>) at 40 °C for ~20 h with 20 min interval. (b) X-Ray diffraction of the film before and after illumination. (c) Representation of the influence of grain size on the critical temperature  $T_c$ . In (c) RT indicates room temperature.

The phase stability of BA-MAPb(I<sub>0.5</sub>Br<sub>0.5</sub>)<sub>3</sub> nanocrystals is investigated using a similar procedure as discussed above. Thin film of the nanocrystalline mixture was deposited on sapphire substrates and exposed to the same illumination used for all experiments described above. Before and after the in-situ optical absorption measurement during light treatment, the structure of the film is assessed via XRD and UV-Vis. As shown in **Figure 8.6 a b**, no change in both of the optical and structural properties are observed on illumination of the film for 20 hours with the same illumination conditions used for the study of the 3D and the 2D samples (1.5 mW cm<sup>-2</sup>). This result, consistent with previous observations,<sup>103, 104</sup> suggests that, by reducing grain size, photo de-mixing can be suppressed. This can be explained from an energetic point of view by considering the surface energy contribution from the additional phase boundary that would form upon de-mixing to the mixing free energy. This contribution is significant for a small grain where the energetics is strongly influenced by surfaces and interfaces. As a result, this suppresses the critical temperature associated with the photo-miscibility-gap (see further discussion in chapter 9). It is possible that, with larger illumination intensities, the value of the critical temperature increases and that photo de-mixing in such system can occur as well.

### 8.3 Conclusion

In this chapter, the phase stability of mixed halide perovskites exposed to light is investigated as a function of the compound's dimensionalities. Results for 3D and nanocrystalline perovskites are presented and compared with the results obtained for the 2D system in Chapter 7.

Firstly, in-situ optical spectroscopy indicates that photo de-mixing in 3D mixed halide perovskites ( $\text{MAPb}(\text{I}_{0.5}\text{Br}_{0.5})_3$ ) occurs with two stages, including composition variations that are close to the initial composition (stage one) followed by formation of the Br-rich and I-rich phases (stage 2). This behavior is observed when the perovskite's surface is not encapsulated and is accompanied by partial degradation of the film. With encapsulation, however, under the same conditions, only the first stage of photo de-mixing is observed, occurring at a slower rate compared with the non-encapsulated system. In both cases, the ionic resistance under dark shows almost complete reversibility on re-mixing of the phases despite the partial reversibility in optical and structural properties observed for the non-encapsulated case. This indicates that the electrical properties measured under dark are not sensitive to the observed degradation.

During photo de-mixing, the ionic resistance decreases throughout the first-stage of photo de-mixing followed by further decrease during the second stage and a slight increase over time scale  $>10$  hours. This may imply that the first-stage photo de-mixing results in an increase in defect concentration while the second stage is a result of further ion migration and the formation of the phase boundary between the iodide and bromide-rich domains with (close to) final compositions. The electronic resistance under light shows significant increase during photo de-mixing, implying that I-rich phase formation in this case is not percolating within the bulk film. Interestingly, no change in the resistance under light is observed for the encapsulated sample.

Finally, the nanocrystalline mixed halide perovskite ( $\text{BA-MAPb}(\text{I}_{0.5}\text{Br}_{0.5})_3$ ) thin film shows no de-mixing under comparable conditions, in contrast to the behavior observed for the 2D and 3D systems. This is consistent with previous observations<sup>103, 104</sup> and with the role of interfacial energy in the formation of the de-mixed phases, as will be further discussed in Chapter 9.<sup>60, 168</sup>



## 9 Photo de-mixing in mixed halide perovskites: mechanism

In this chapter, a theoretical analysis of the ionic and electronic effects involved in the phase behavior of mixed halide perovskite under light is discussed. Various energetic contributions as potential driving force of photo de-mixing in these compounds are discussed: photostriction and strain effects, hole stabilization due to high valence band edge in I-rich environment compared with the mixed phase, hole stabilization by ionic defect formation and structure relaxation (photo-ionic effects). Particularly, photo-ionic effects, and the effect of surface energy are also included in the following discussion.<sup>60, 168</sup>

### 9.1 Introductory remarks

On a very general level there are two possibilities to explain the role of light for the observed de-mixing in mixed halide perovskites when exposed to light (see also Section 2.4):

i) The mixtures in the dark are metastable and illumination enables faster kinetics of de-mixing.<sup>112</sup> ii) the energetic input from illumination drives the initially stable mixture into instability.

Clarifying the presence or absence of a miscibility gap for mixed halide perovskites in the dark at room temperature is critical to this discussion. Early studies using normal thin film X-ray diffraction and synchrotron X-ray powder diffraction showed conflicting results on whether  $\text{CH}_3\text{NH}_3\text{Pb}(\text{I}_{1-x}\text{Br}_x)_3$  exhibits full miscibility or not.<sup>31, 36</sup> The conclusion drawn from Chapter 6 that 2D DJ mixed halide perovskites undergo reversible photo de-mixing both optically and structurally however suggests full miscibility in the dark. This leaves us with (ii), which indeed currently represents the most accredited interpretation.

Concerning the driving force which induces phase instability in mixed halides perovskites, various aspects can act as contributing factors regarding the de-mixing mechanism:

c) The formation of small clusters, identified as I-rich domains, near grain boundaries has been related to possible polaron-induced strain effects. Molecular and mean-field phenomenological models were used to show that this localized strain can change the free energy landscape and favor de-mixing.<sup>81, 97, 118</sup>

d) The energy of photo-generated electrons and holes in these mixtures are given by the edges of conduction and valence band (CBM and VBM), both of which depend on composition. Therefore, de-mixing brings about an energy change that depends on light intensity (concentration of electrons and holes). In Ref.<sup>12, 91</sup> the greater portion of the photo de-mixing driving force is attributed to the valence band edge variation and to the energy gain associated with holes stabilization in I-rich domains.

e) An additional photo-ionic effect has been proposed to contribute to the photo de-mixing. The defect chemical mechanism, corroborated by calculations<sup>60, 175-177</sup>, involves holes self-trapping on iodide sites in the I-rich domains further leading to the formation of iodine

interstitials, dumbbells or even higher aggregates via ionic rearrangement. For the Br-analogue, the same mechanism does not occur to the same extent as holes tend to be more delocalized.

In addition to these aspects, concentration gradients of halide species resulting from the photo-generated charge carriers concentration gradient have also been described as a factor underlying the photo de-mixing process.<sup>178-180</sup> Surface defect carrier trapping leading to electric-field-induced anion drift have additionally been proposed as a possible driving force for phase separation.<sup>108</sup> The fact that photo de-mixing is observed in mixed halide perovskites under uniform illumination<sup>181</sup> as well as in the bulk of single crystal samples<sup>82</sup> suggests that these aspects, while insightful for the analysis of experiments, are not critical in terms of fundamental driving force of the process.

## 9.2 Evaluating the energetics of photo-ionic effects in mixed halide perovskites

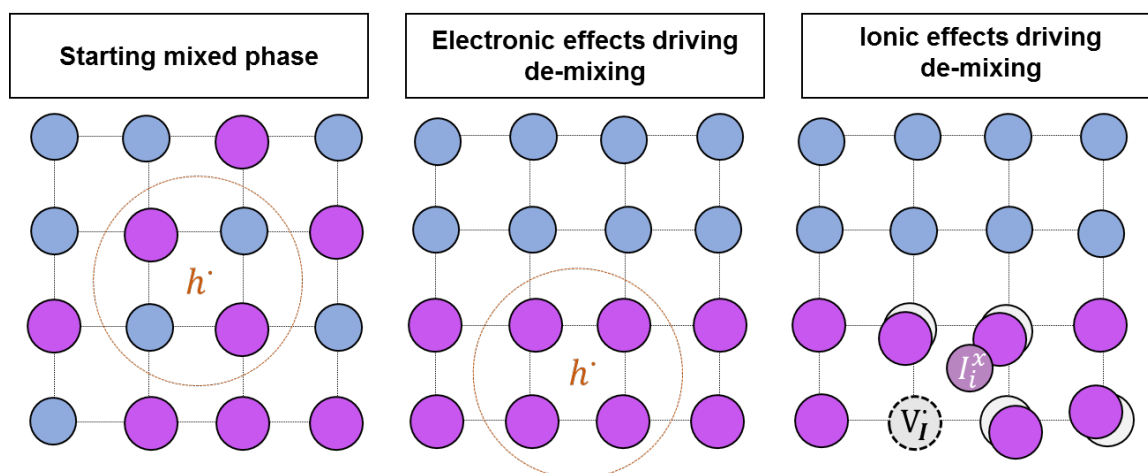


**Figure 9.1.** Energetic effects owing to electronic and ionic processes. (a) Photo-generated hole in a mixed domain of a mixed halide perovskites; (b) Scenario associated with de-mixed situation due to local fluctuation of composition into I-rich and Br-rich environment. The photo-generated hole is stabilized in the I-rich domain due to its higher valence band edge compared to the Br-rich domain. (c) Further stabilization of the de-mixed phases occurs when the photo-generated hole localizes on an I-site, resulting in the reduction of the ionic radius of the corresponding I - I pairs (formation of the singly-charged I-I dumbbell or other higher order defects) and displacements of the surrounding atoms.

The energetic contributions stemming from electronic and ionic effects described above is summarized in **Figure 9.1**. Compared with the situation in the dark, energy variations due to electronic effects are related to electronic energy variations of electron and hole transfer between phases. A higher VB-edge and a lower CB-edge are related to electronic stabilization for holes and electrons, respectively. As the halide composition predominantly affects the position of the VB-edge,<sup>182</sup> the focus is on hole stabilization here (electron stabilization is also discussed at the end of this chapter). This involves the difference in the energy of the valence

band maximum between the mixed halide perovskites and the I-rich phase ( $\Delta E_{\text{HT}}$ : HT stands for hole transfer). In 3D MAPb(I<sub>1-x</sub>Br<sub>x</sub>)<sub>3</sub>, such offset between  $x = 0.5$  to  $x = 0$  is -0.2 eV. The interested reader may refer to the literature for more details on the electronic driving force concerning a) and b) above,<sup>81, 91, 112, 183</sup> while below I discuss c) in more detail. As mentioned in the previous section, photo-generated holes in an I-rich phase can be further stabilized by the formation of complex defects involving ionic relaxation. Let us inspect in more detail the energetics of hole localization and of ionic/electronic relaxation.

When considering the process in which a photo-generated delocalized hole localizes on an iodide site and participates in the formation of singly-charged I-I dumbbell, a number of contributions have to be taken into account. Firstly, the delocalization energy ( $\Delta E_{\text{loc}}$ ) has to be overcome. This is usually taken as half the (valence) band width (corresponding to the difference of the lowest bonding orbital energy to the non-bonded state or to the difference to the highest anti-bonding orbital state to the non-bonded state). Secondly, the energy gain due to the formation energy of the dumbbell ( $\Delta E_{\text{f}}$ ) and to the following polarization energy ( $\Delta E_{\text{p}}$ ) of the crystal due to electronic shells and ionic defect displacement needs to be considered.  $I_i^{\times}$  (relaxed) is short for the final complex defect which is approximately an iodine dumbbell (involving another formerly regular iodine) with covalent contributions. In defect notation this sequence is written as:



$I_i^{\times}$  (relaxed) is short for the final complex defect which is approximately an iodine dumbbell (involving another formerly regular iodine) with covalent contributions.

The reaction energy for (R1.1) is roughly half the valence band width ( $\sim \frac{4eV}{2}$ )<sup>184</sup> (the localization energy can even be smaller than this value for accurate consideration<sup>185</sup>). The reaction energy of (R1.3) may be estimated from the energy of forming a dumbbell (-molecule). As the reaction energy of (R1.2) is not available, (R1) can be alternatively composed as follows

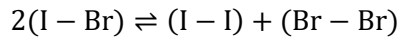


where (R2.1) describes the excorporation of an iodine atom ( $I_g$  corresponds to an iodine atom in the gas phase, is called F center), (R2.2) refers to the ionization energy of a neutral

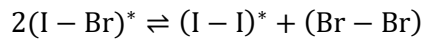
vacancy minus the bandgap, (R2.3) refers to iodine incorporation from the gas phase to an interstitial.

The following text discusses the relevance of the ionic driving force in 3D and 2D situation. Firstly, the estimate for the reaction energy for the defect reactions mentioned above is obtained by using data from Ref.<sup>177</sup>, where CsPbI<sub>3</sub> was theoretically investigated. While it has been shown that A-site substitution can vary significantly the kinetics of ion transport and de-mixing,<sup>186, 187</sup> this analysis based on CsPbI<sub>3</sub> may still be representative in terms of the energetics involved in the de-mixing process (hole trapping is mostly influenced by the halide orbitals). The reaction energy for (R2.1) is estimated as 3.0 eV (formation energy of F center), the energy for (R2.2) as -1.6 eV (ionization energy of a neutral iodide vacancy by hole) and the energy for (R2.3) as -0.4 eV (formation of H center), so that the total energy balance is slightly positive, +1.0 eV. Notably, if this value is taken for granted, the reaction energy for (R1.2) & (R1.3), describing the transfer of a neutral iodine from a regular site to a relaxed interstitial position, follows as -1.0 eV. This value refers to the process where  $V_I^\times$  and  $I_i^\times$  are independent. If however an associated pair ( $V_I^\times I_i^\times$ ) is formed, which is a more likely scenario, the value is substantially lower. For CsPbI<sub>3</sub> a relaxation energy of the order of  $\sim 1.8$  eV can be calculated from (Formation energy of Frenkel pair) minus formation energy of the H center and F center) and is consistent with the value reported in alkali halides.<sup>177, 188</sup> Considering such value in our treatment would indeed change the sign of the energy associated to (R1) = (R2) from positive to negative ( $\sim -0.8$  eV). In addition, if the majority of self-trapped hole centers is associated with the vacancies, it is clear that such dissociation adds a high value (association energy/2 eV) to the ion migration process. When considering the complete picture, additional interactions of the trapped hole center with trapped electrons (see below) may lower this value. What remains however clear is that the inclusion of ionic defect formation leads to a stronger de-mixing tendency. The above mentioned calculation is based on the calculation of the CsPbI<sub>3</sub> in cubic symmetry, the potential consequences of ionic driving force for photo de-mixing in other symmetry, different halide compositions and dimensionality will be included and discussed in Ref.<sup>189</sup>

If one simplifies the de-mixing problem by considering pairs, as described in Chapter 3, and neglects the illumination effects in the bromide-rich domains, two reactions have to be distinguished,



which refers to the sites that are hole-free and



which refers to the sites where photo-generated holes are present.



It is clear that the reaction of (I - Br) to (I - I)\* and Br - Br brings about a slight energy gain due to electronic but also to the ionic relaxation. Its reaction free energy is characterized not only by an electronic, but also an ionic contribution. Nonetheless, the overall value is rather small. An evident first conclusion is that defect formation effects depend, similarly to the electronic contribution, on the total hole concentration and hence on light intensity. Secondly, in order to have appreciable energetics that drive de-mixing, a large fraction of holes should be trapped (possibly the vast majority of the holes are not free). Thirdly, the fact that both de-mixing kinetics and photostriction effect show saturation when increasing light intensity may also be correlated with a saturated concentration for self-trapped holes.<sup>91, 160</sup>

At this point the following points are to be highlighted resulting from the analysis of photo de-mixing in mixed halide perovskites based on a non-ideal solution model: (i) the  $\Omega$  parameter (See Chapter 3, Eq. 3.5) includes hole stabilization by the higher valence band edge of the iodide plus the self-trapping energy. (ii)  $\Omega$  is proportional to the self-trapped hole concentration. (iii)  $T_c$  in 2D mixed halide perovskites is estimated from photo-miscibility-gap to be above 420 K (see Chapter 6)<sup>113</sup>, which provides a lower bound estimate of 0.07 eV for  $\Omega$ ; (iv) the fact that the de-mixing phenomenon disappears in the nano-crystals ( $\leq 50$  nm) at room temperature (see Chapter 9)<sup>103, 104</sup> ( $T_c \leq 300$  K) can be attributed to the additional G-cost of forming an interface.<sup>190-193</sup> This is also consistent with the self-limiting de-mixed I-rich domain size (40nm - 70 nm), as shown Chapter 7.

The additional interfacial energy cost of forming the interface between de-mixed domains should be considered in more detail:

According to (iv), the free energy of (de-)mixing (Eq. 4) is, at the critical temperature, compensated by the additional interfacial energy cost of forming the interface between de-mixed domains. The latter can be expressed as  $G_{ex} = 2 \frac{\gamma}{L} V_m$  ( $\gamma$  is the interfacial tension of the domains,  $L$  is the domain size and  $V_m$  is the molar volume), and it is significant for small  $L$ . In view of Eq. 3.4, one can then write for the interaction parameter  $\Omega$

$$\Omega = \frac{[2 \frac{\gamma}{L} V_m - RT_c (x \ln x + (1-x) \ln(1-x))]}{x(1-x)} \quad \text{Eq. 9.1}$$

Therefore, the absence of photo de-mixing in nanocrystals at room temperature allows us to estimate an upper limit for the interaction parameter ( $\Omega_{max}$ ). By evaluating Eq. 9.1 for  $T_c = 300$  K,  $x = 0.5$ ,  $L = 50$  nm, and using an estimate of the halide molar volume for mixed halide perovskites,<sup>194, 195</sup> one obtains  $\Omega_{max} = 4 \left[ 1.8 \frac{m^2}{J} \gamma + 1.7 \right]$  kJ mol<sup>-1</sup>. If one then considers values of surface tension in the range of 0.1-1 J/m<sup>2</sup>,<sup>193, 196</sup>  $\Omega_{max} = 0.07 - 0.14$  eV. The  $\Omega$  parameter is a property related to the interaction between the halides in this model, and therefore it is not expected, to a first order approximation, to vary with the domain size. It

follows that the same value of  $\Omega_{max}$  obtained above is relevant also to the macroscopic domain case, where negligible interfacial contributions are expected, resulting in an estimate for  $T_{c,max} = 420 - 840$  K. The lower bound of such critical temperature is consistent with the experimental results shown in Chap 6 that the critical temperature is above 420 K.

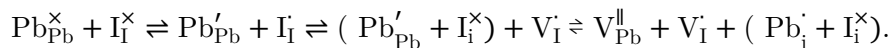
Large concentration of the self-trapped holes and higher order defects formation in soft, ionic halide perovskites lattice,<sup>197</sup> can be responsible for large lattice strain and lattice deformation as already mentioned above.<sup>159, 160, 198-201</sup> It is also worthy to note that the photo-induced strain<sup>200</sup> and photo-ionic effect<sup>60</sup> decrease on substituting iodide with bromide in these perovskites. The extent to which defect formation may be playing a role on the observed photo-induced strain is therefore an interesting question for future research.<sup>60</sup> In this context, it is revealing to refer to Darken's model of de-mixing in alloys when oversize-substitutions are introduced.<sup>202</sup> Here the effect of "squeezing" an additional volume element into a solid is considered. The oversize  $\Delta V'$  converts into a volume increase of the matrix  $\Delta V$ , given by  $\Delta V = \Delta V' \cdot 3(1-\nu)/(1+\nu)$ . A typical Poisson ratio ( $\nu$ ) of 0.3 leads to  $\Delta V$  exceeding  $\Delta V'$  by 60%. By considering the oversize introduced by a large substitutional impurity and applying the regular solution model, Darken could explain Hume-Rothery's rule stating that the substituting atom in alloy systems should not have a size exceeding the one of the substituted atom by more than 15% in order for it to be stable<sup>202, 203</sup>. The reasoning is as follows: if the volume is increased by  $\Delta V' = V' - V$ , the elastic energy density can be estimated according to ( $M_s$ :shear modulus)

$$E = \frac{2}{3} M_s V \left( \frac{V' - V}{V} \right)^2 \quad \text{Eq. 9.2}$$

This energy may be equated to  $\Omega$  and hence to  $2RT_c$  in order to get an estimate of  $T_c$  within the regular solution model. Interestingly, if  $(V'/V)$  is replaced by  $(r'/r)^3$  with  $r$  being the radius of the introduced oversized sphere, and representative values for alloys of  $M_s V$  are introduced, a critical radius of 15% can be assessed to be a necessary upper bound for the size mismatch of substitutional impurities in order to obtain miscibility at 1000 K. In our case the experimentally found photo-contraction effect can be transferred into a de-mixing tendency: if the self-trapping effect is the cause,  $(I - I)^*$  takes the role of the impurity substituting for  $(I - I)^*$ . However, the above consideration is too crude to be quantitatively applied in our case, let alone the fact that the decisive materials parameters are not known.

Having considered the consequences of holes being trapped and of the formation of higher order defects, one question that arises naturally concerns the potential role of electrons in the de-mixing process. Given the fact that the conduction band edge decreases when increasing the iodide content,<sup>31, 182, 204</sup> it is reasonable to assume that electrons will also locate themselves in I-rich domains.<sup>205</sup> Since the conduction band in MAPbI<sub>3</sub> is predominantly formed by Pb-orbitals, e'-trapping on Pb<sup>2+</sup> would favor localization within the already formed I-rich

domains and contribute to the de-mixing tendency. Further interactions with I interstitials would make the balance more favorable (see below). The formation of  $\text{Pb}^0$  has been reported in mixed halide perovskites under illumination.<sup>206-208</sup> However, the aggregation tendency of  $\text{Pb}^0$  is expected to be lower than that of  $\text{I}^0$  due to its larger size. Yet the interaction of  $\text{I}^0$  and  $\text{Pb}^+$  or even  $\text{Pb}^0$  in the I-rich domains might play an important but underrated role here. In the limit of a symmetrical situation, one would assume interstitial  $(\text{PbI})^+$  or  $\text{PbI}_2$  molecules. The excitation could be then solely written in terms of trapped defects, e.g. as



Such massive trapping might also have important consequences on the charge carrier life-times in these materials<sup>209-211</sup>. Pb-I interactions could influence the extent to which iodide vacancies are mobile, rather than associated with the iodine interstitial. Testing these possibilities via spectroscopic methods will clarify the extent to which such defect formation routes are favorable and elucidate their contribution to the phase behavior, but also to the charge carrier dynamics of hybrid perovskites. Such investigation also requires further theoretical work to understand self-trapping effects in photo-active ionic materials<sup>212</sup>.



## VI CONCLUSIONS



## 10 Concluding remarks

In summary, this thesis investigated the defect chemistry and photo-ionic effects in iodide and bromide perovskites, with special focus on the photo de-mixing occurring in mixed bromide-iodide perovskites. The main aspects investigated are:

- **Defect chemistry equilibria in bromide vs iodide perovskites** (Chapter 5): the aim is to elucidate the charge carrier chemistry in 3D MAPbBr<sub>3</sub> and 2D (PDMA)PbBr<sub>4</sub> in comparison to iodide perovskites.
- **Thermodynamics of photo de-mixing in 2D mixed halide perovskites** (Chapter 6): the aim is to investigate phase stability, reversibility and thermodynamic properties of the 2D Dion-Jacobson mixed halide perovskites ((PDMA)Pb(I<sub>0.5</sub>Br<sub>0.5</sub>)<sub>4</sub>) under light.
- **Kinetics aspects of photo de-mixing in 2D mixed halide perovskites** (Chapter 7): the aim is to study the kinetics of photo de-mixing in terms of composition, electronic and ionic conductivity, and morphology (phase) evolution.
- **Dimensionality effect on photo de-mixing in 3D and nanocrystalline mixed halide perovskites** (Chapter 8): the aim is to clarify how the process of photo de-mixing depends on the dimensionality of the perovskite.

This thesis provides advance in the understanding of these aspects based on the following:

The defect chemistry study of bromide perovskites revealed that, similar to the case of iodide perovskites, 3D MAPbBr<sub>3</sub> and 2D (PDMA)PbBr<sub>4</sub> are P-type mixed conductors (electron holes are dominant electronic charge carriers). Compared with 3D MAPbBr<sub>3</sub>, 2D (PDMA)PbBr<sub>4</sub> shows 3 orders of magnitude lower ionic conductivity, indicating significantly suppressed ion migration by dimensionality reduction. For both compounds, stoichiometry of the mixed conductors can be changed reversibly up to a bromine partial pressure  $p_2(\text{Br}_2) = 5\text{E-}06$  bar, while larger value of  $p(\text{Br}_2)$  induce irreversible changes in the conductivity of the samples. In the reversible regime, a non-monotonic dependence of the electronic conductivity on  $p(\text{Br}_2)$  is detected for both 2D and 3D bromide perovskites. It can be attributed to the reversible formation of AuBr<sub>x</sub> on the gold electrode and perovskites interfaces, which introduces an additional contribution to the resistance at low frequency.

The thermodynamic investigation of photo de-mixing in 2D mixed halide perovskites demonstrates that, despite their improved stability compared with 3D perovskites, phase transformation from single phase to de-mixed phases occurs under light also for these materials. The complete reversibility of photo de-mixing is verified experimentally both optically and structurally, suggesting full miscibility of mixed halide perovskites in the dark. This result confirms that photo de-mixing is a thermodynamic effect rather than a photo catalytic effect, settling a debate that has been discussed in the community since the first observation of the photo de-mixing. Furthermore, the de-mixed compositions of the two phases are found to be

dependent on temperature, which fits the thermodynamic description of de-mixing, and the presence of a miscibility gap. Such photo-miscibility gap is therefore introduced, mapped and carefully evaluated via multiple methods. A lower limit of 150 °C is found for the critical temperature of this system under 0.01 sun illumination. Limited variation in the photo-miscibility-gap is observed when using 10 times higher illumination intensity. Lack of encapsulation of the surface of the mixed halide perovskites prior to illumination, however, induces a widening of such gap as well as partial degradation.

The kinetics investigation of photo de-mixing in 2D DJ mixed halide perovskites shows an activation energy of 0.39 eV, slightly larger than the value reported for photo de-mixing in 3D (0.27 and 0.30 eV) and 2D RP type (0.22 eV) mixed halide perovskites. Photo de-mixing in 2D mixed halide perovskites (with surface encapsulation) is found to occur in multiple stages. In a first stage, a composition fluctuation close to the initial composition is discovered. This is accompanied by a significant decrease in ionic resistance in the dark. Such decrease in (ionic) resistance is attributed to an increase in the ionic defect concentration induced by hole trapping during illumination. The (electronic) resistance under light also decreases rapidly due to the increase of photo generated electronic charge concentration. In a second stage and third stage, direct transformation of the mixed halide perovskites to the final I-rich and Br-rich compositions occurs. Heterogeneous nucleation of I-rich domains on the grain boundaries that is at the interface between the perovskite and substrate occurs first, followed by homogeneous nucleation inside the grains. During this process, interdiffusion of iodine and bromine occurs, resulting in vertical segregation of the halides where iodide preferentially segregates close to the perovskite / substrate interface. In this stage, the ionic resistance in the dark increases, while the electronic resistance under light keeps decreasing, which can be linked to the formation of an (ionically) insulating phase boundary and the fact that I-rich phases are dominating the electronic response.

The investigation of the dimensionality effect on the phase stability in 3D and nanocrystalline mixed halide perovskites shows that 3D mixed halide perovskites ( $\text{MAPb}(\text{I}_{0.5}\text{Br}_{0.5})_3$ ) undergo similar two-stage de-mixing under light as for 2D mixed halide perovskites. In contrast to the full reversibility of 2D systems, photo degradation of 3D perovskites into  $\text{PbI}_2$  (degradation occurring also in the dark over long time scales) is observed. The nanocrystalline mixed halide perovskite ( $\text{BA-MAPb}(\text{I}_{0.5}\text{Br}_{0.5})_3$ ) thin films show no de-mixing in contrast to 2D and 3D under same measurement conditions. The results are consistent with previous reports suggesting that nanocrystalline mixtures show superior phase stability, with neither degradation nor de-mixing on illumination.

Lastly, a mechanism describing the various driving force contributions of photo de-mixing is proposed. In addition to the photostriction and strain effects, and the electronic



effects (hole stabilization due to high valence band edge in I-rich environment compared with the mixed phase), it is emphasized that an additional driving force contribution should be included accounting for ionic effects. One such effect is hole stabilization by ionic defect formation and structure relaxation (photo-ionic effects). Such contribution can provide up to -1 eV further stabilization of the de-mixed phases compared to the mixed situation, larger than the value estimated for the electronic driving force. In addition, the effect of surface energy and the electron trapping can also contribute to the driving force of the photo de-mixing.

The defect chemical investigation of photo-ionic effects (specifically photo de-mixing) discussed in this thesis contributes to the fundamental understanding of the behavior of ionic and electronic charge carriers under light in iodide and bromide perovskites and as a function of material dimensionality. Such understanding will enable progress in the optimization of optoelectronic devices as well as the development of other emerging systems exploiting opto-ionic effects.



## VII APPENDIX



## A Supporting Material

### A.1 supporting material for Chapter 5

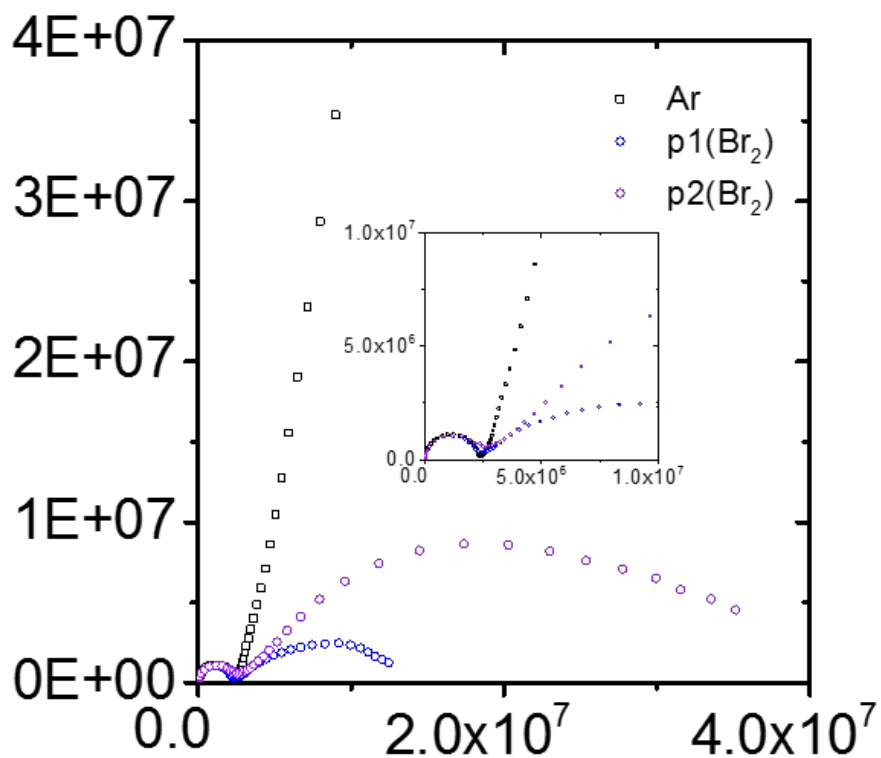


**Figure A.1.1.** Comparison of the impedance spectra (Nyquist plot) under different atmosphere measured with ionic blocking electrode in the dark at 60 °C (frequency range: 1E06 – 1E-03). The black, blue and purple data points denote the impedance of the sample after being equilibrated under Ar,  $p_1(\text{Br}_2) = 1\text{E-}06$  bar,  $p_2(\text{Br}_2) = 5\text{E-}06$  bar, respectively.

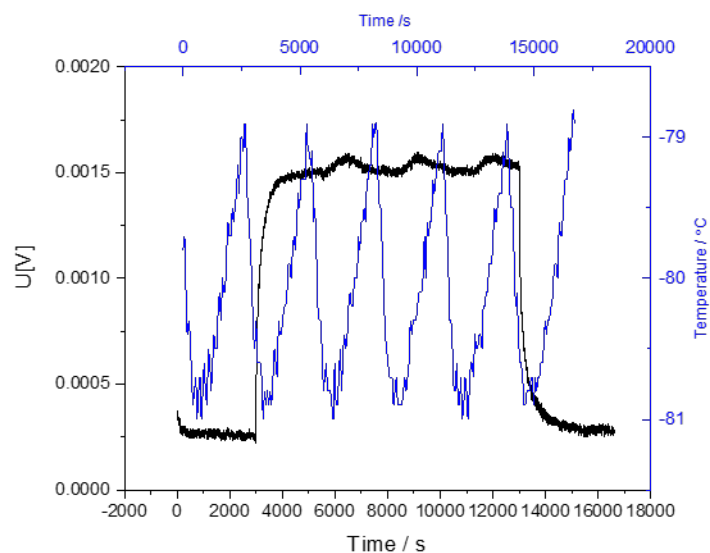


**Figure A.1.2.** DC galvanostatic polarization measurement of MAPbBr<sub>3</sub> thin film measured with long time showing the influence of the voltage at long time scale due to small temperature fluctuation (2 °C) induced bromine partial pressure difference(5 E-08 bar). The measured is conducted with ionic blocking electrode in the dark at 60 °C under  $p_1(\text{Br}_2) = 1\text{E-}06$  bar.

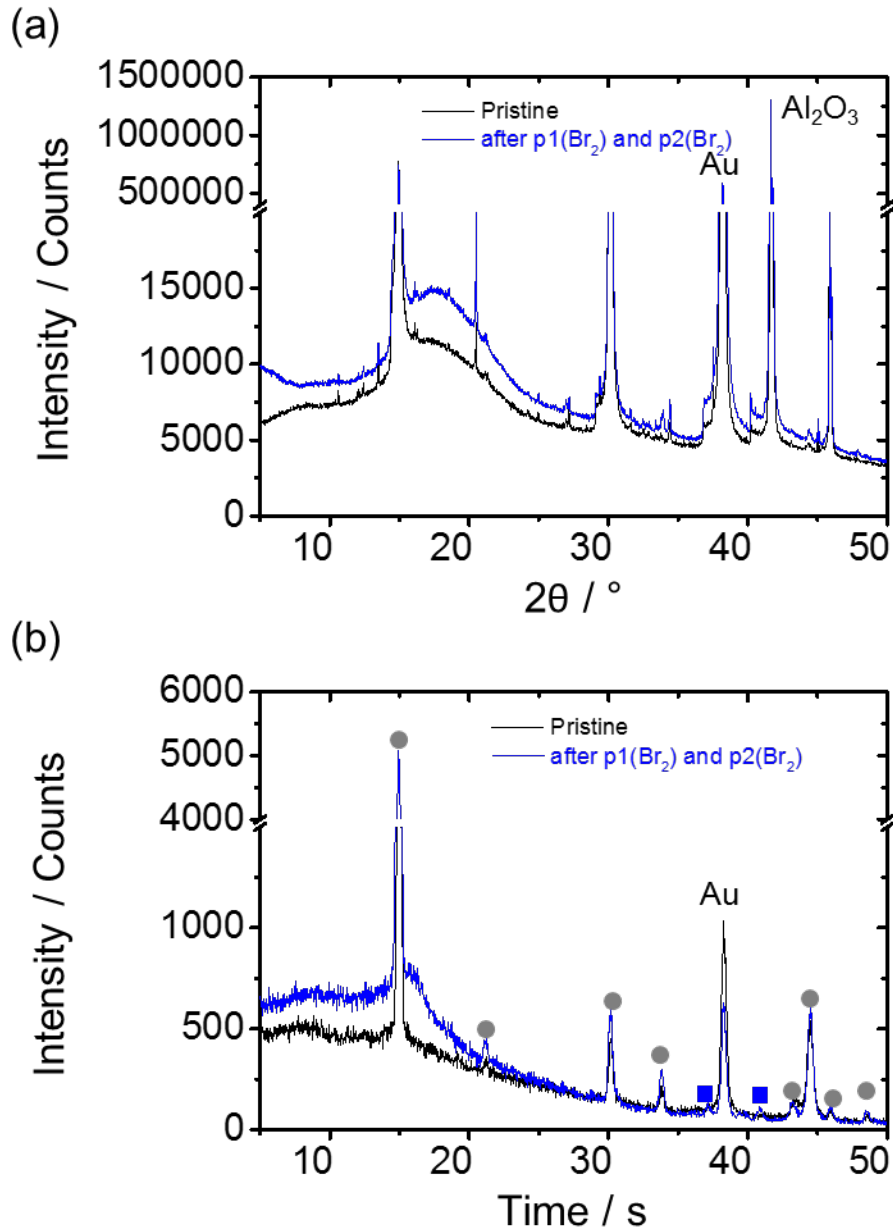


**Figure A.1.3.** X-ray diffraction of 3D MAPbBr<sub>3</sub> thin film before (black) and after exposure to bromide gas (blue, measurements was taken after Ar  $\rightarrow$  p1(Br<sub>2</sub>) = 1E-06 bar  $\rightarrow$  Ar, Ar  $\rightarrow$  p2(Br<sub>2</sub>) = 5E-06 bar  $\rightarrow$  Ar) (a) Bragg-Brentano and (b) Grazing-incidence geometry. All measurements were measured when samples are in a gas-tight dome with argon to exclude air exposure. Grey circles indicate the peaks that are not changed after exposure to bromine gas, while the blue squares indicate the newly emerged peaks that corresponds to the orientation of: (114) ( $2\theta = 37^\circ$ ) and (123) ( $2\theta = 41^\circ$ ). The substrate for these measurements on the interdigitated gold on Al<sub>2</sub>O<sub>3</sub>.

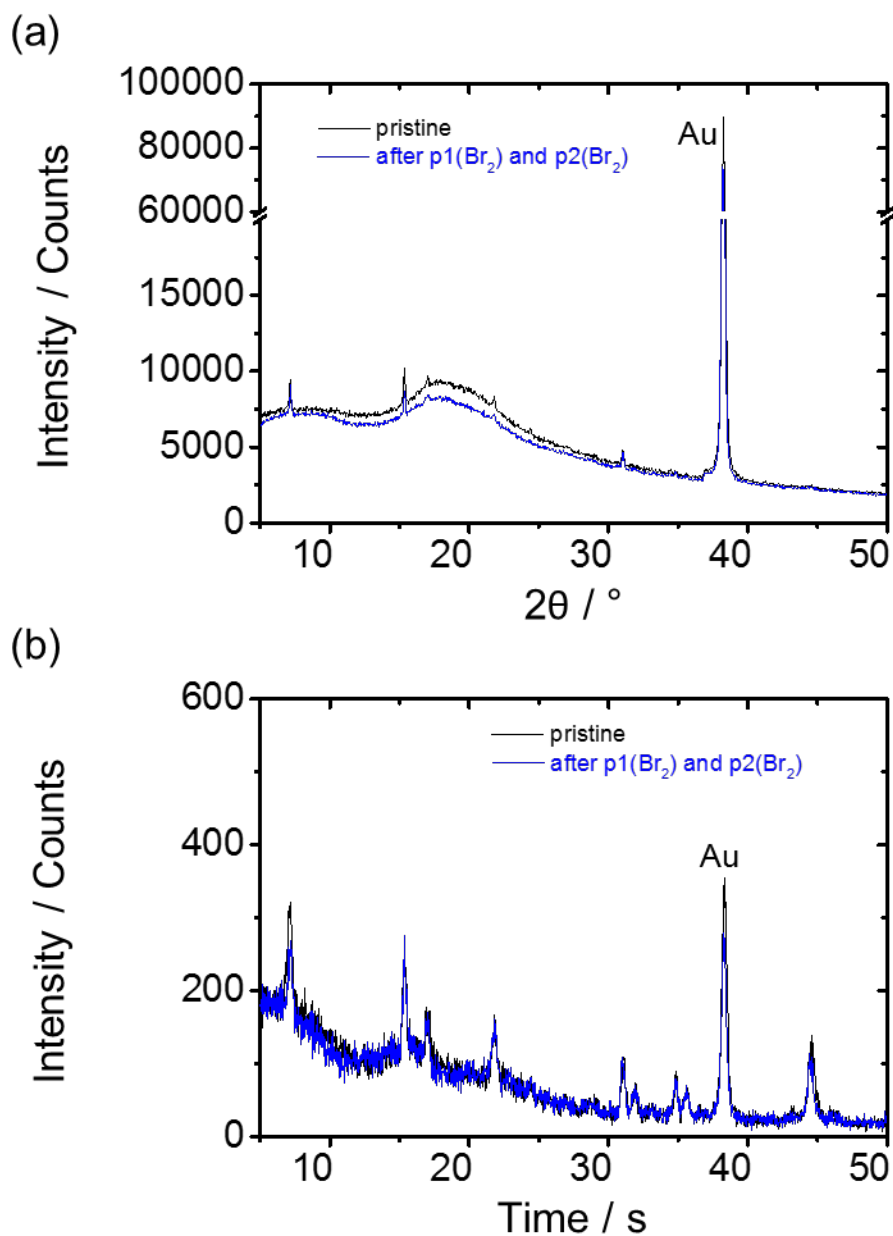


**Figure A.1.4.** X-ray diffraction of 2D (PDMA)PbBr<sub>4</sub> thin film before (black) and after exposure to bromide gas (blue, measurements was taken after Ar  $\rightarrow$  p1(Br<sub>2</sub>) = 1E-06 bar  $\rightarrow$  Ar, Ar  $\rightarrow$  p2(Br<sub>2</sub>) = 5E-06 bar  $\rightarrow$  Ar) (a) Bragg-Brentano and (b) Grazing-incidence geometry. All measurements were measured when samples are in a gas-tight dome with argon to exclude air exposure. No change is observed both in the bulk and surface of the film. The substrate for these measurements on the interdigitated gold on quartz.



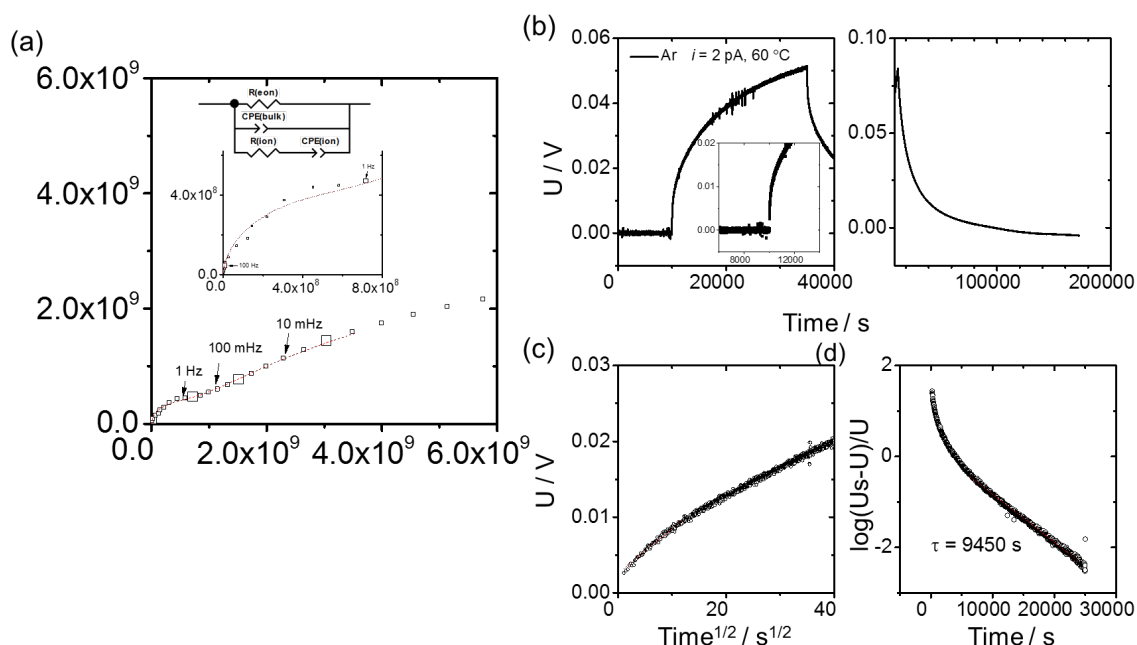


**Figure A.1.5.** Electrochemical response of 2D (PDMA)PbBr<sub>4</sub> thin film measured with ionic blocking electrode (Au, see section 4 for electrode geometry) in argon in the dark at 60 °C. (a) Nyquist plot of impedance spectra (frequency range: 1E06 – 1E-03) after reaching equilibration and the corresponding equivalent circuits. The read dashed line indicate the fitting of the data. (b) DC galvanostatic polarization measurement when applying current(2 pA) for 20000 s. (c) Short time scale polarization (Voltage vs the square root of time) and (d) long time scale polarization(  $(U_s - U)/U$  vs time).  $U_s$  represents the saturation value of the voltage when steady state of the polarization is reached. 2.6749e-12

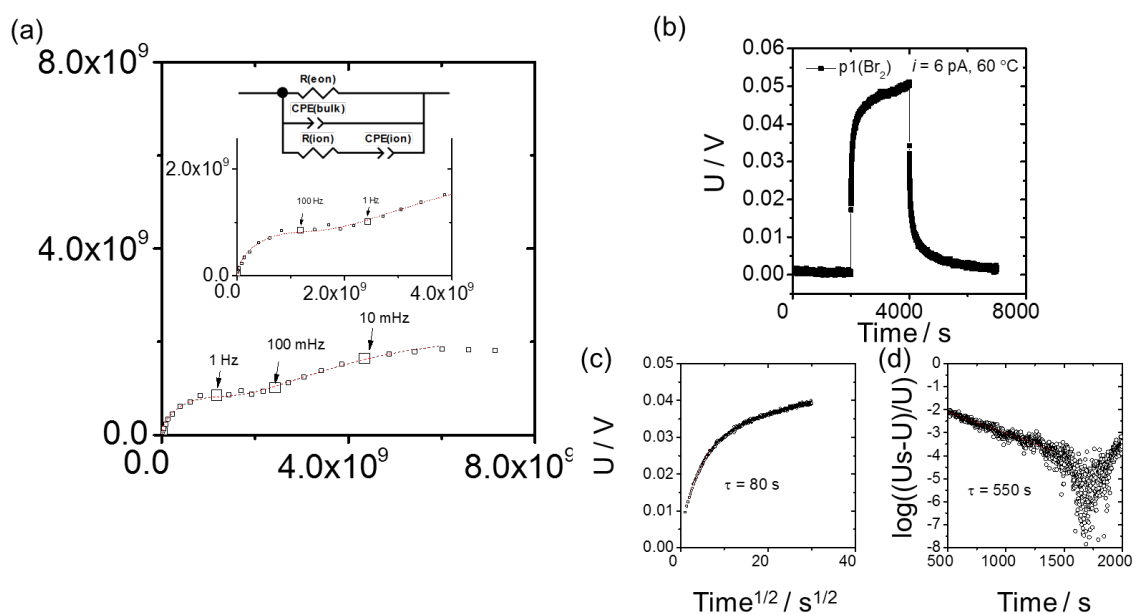


**Figure A.1.6.** Electrochemical response of 2D (PDMA)PbBr<sub>4</sub> thin film measured with ionic blocking electrode (Au, see section 4 for electrode geometry) under  $p_1(\text{Br}_2) = 1\text{E}-06$  bar in the dark at 60 °C. (a) Nyquist plot of impedance spectra (frequency range: 1E06 – 1E-03) after

reaching equilibration under such bromine partial pressure and the corresponding equivalent circuits. The read dashed line indicate the fitting of the data. (b) DC galvanostatic polarization measurement when applying current(6 pA) for 2000 s. (c) Short time scale polarization (Voltage vs the square root of time) and (d) long time scale polarization(  $(U_s - U)/U$  vs time).  $U_s$  represents the saturation value of the voltage when steady state of the polarization is reached.

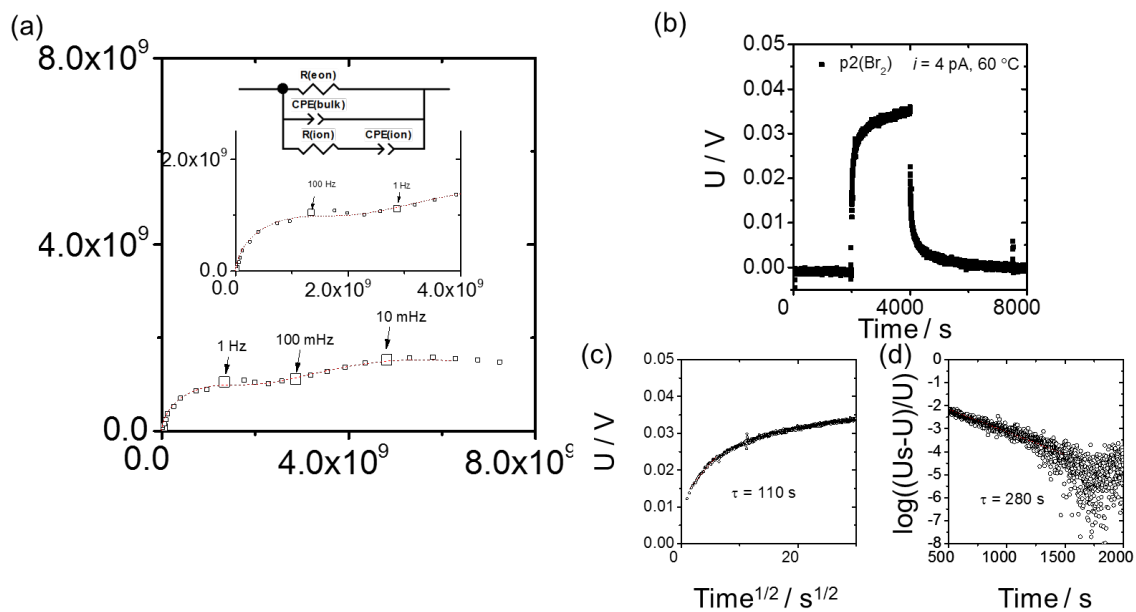


**Figure A.1.7.** Electrochemical response of 2D (PDMA)PbBr<sub>4</sub> thin film measured with ionic blocking electrode (Au, see section 4 for electrode geometry) under  $p_2(\text{Br}_2) = 5\text{E-}06$  bar in the dark at 60 °C. (a) Nyquist plot of impedance spectra (frequency range: 1E06 – 1E-03) after reaching equilibration under such bromine partial pressure and the corresponding equivalent circuits. The read dashed line indicate the fitting of the data. (b) DC galvanostatic polarization measurement when applying current(4 pA) for 2000 s. (c) Short time scale polarization (Voltage vs the square root of time) and (d) long time scale polarization(  $(U_s - U)/U$  vs time).  $U_s$  represents the saturation value of the voltage when steady state of the polarization is reached.

## A.2 supporting material for Chapter 6

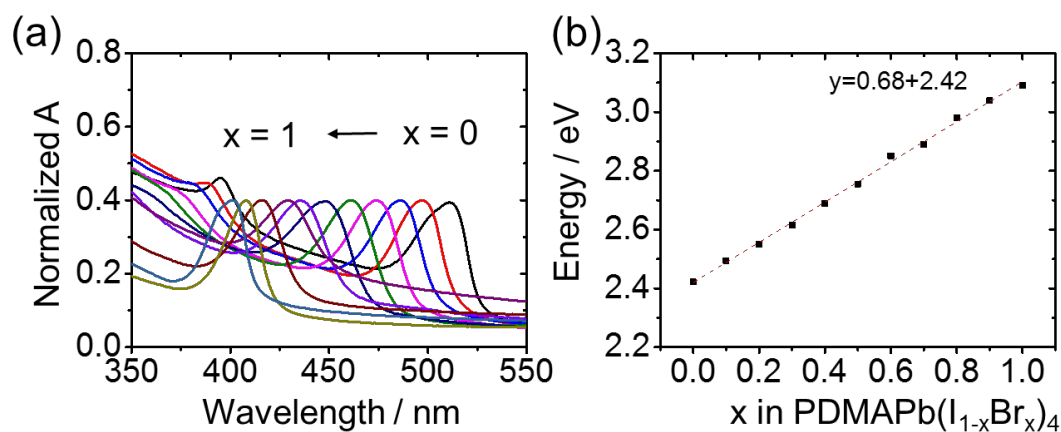


**Figure A.2.1.** (a) UV-Vis spectra for (PDMA)Pb(I<sub>1-x</sub>Br<sub>x</sub>)<sub>4</sub> thin films (b) absorption energy as a function of bromide content, and the corresponding fitting.

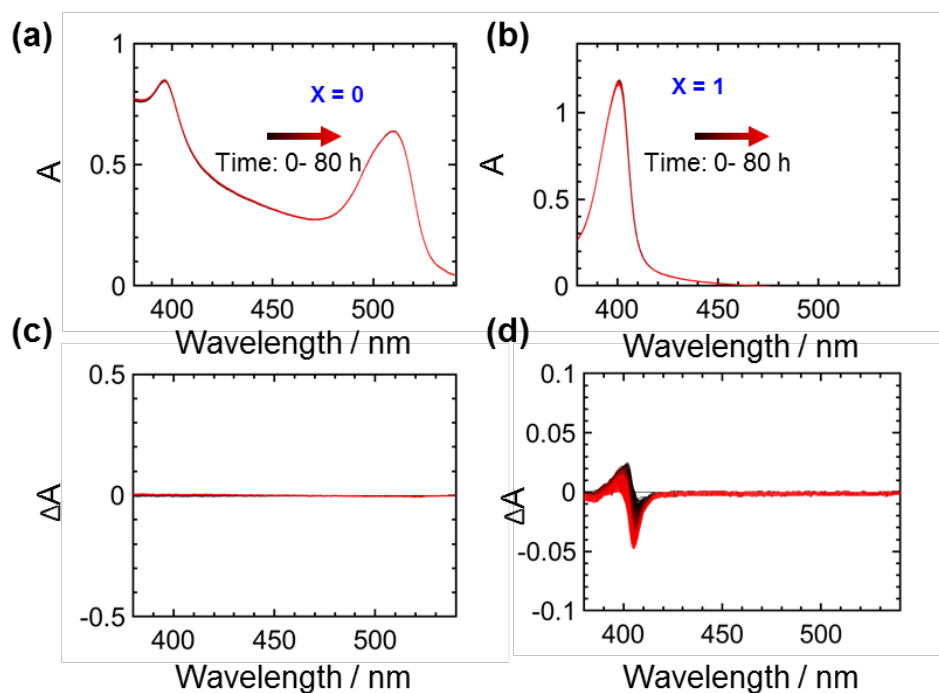


**Figure A.2.2.** UV-Vis spectra for (PDMA)PbI<sub>4</sub> (a) and (PDMA)PbBr<sub>4</sub> (b) thin films at 80 °C (with PMMA encapsulation in Ar atmosphere) with 1.5 mW/cm<sup>2</sup> for 80 h. No absorption change is detected for (PDMA)PbI<sub>4</sub>. For (PDMA)PbBr<sub>4</sub>, a slight blue shift in absorption is detected. (c) and (d) are the corresponding  $\Delta A$  spectra (obtained by subtracting the reference spectrum of the pristine sample from each absorption spectrum).

### Methods for composition extraction of de-mixed phases

Here, I discuss the methods used for extracting the characteristic absorption wavelengths for Br-rich and I-rich phases referred to the photo de-mixing experiments in the main text. The estimate of the compositions associated with these features is also discussed in detail below.

#### *Estimation of the characteristic wavelengths for I-rich and Br-rich phases*

**Figure A.2.3a, b** show the absorbance and the change in absorbance evolution of a 2D DJ perovskite with  $x_{\text{initial}} = 0.5$  performed at 100 °C for 20 hours. Both graphs highlight the emergence of features that can be assigned to I-rich and Br-rich phases as discussed in the main text. For the I-rich domain, a clear excitonic peak could not be resolved in most cases. Therefore, characteristic wavelengths for the I-rich absorption signature were defined based on the (negative) peak of the slope of the A signal with respect to wavelength (**Figure A.2.3c**). Such wavelength is used to determine the composition of the I-rich phase, according to the method discussed below.

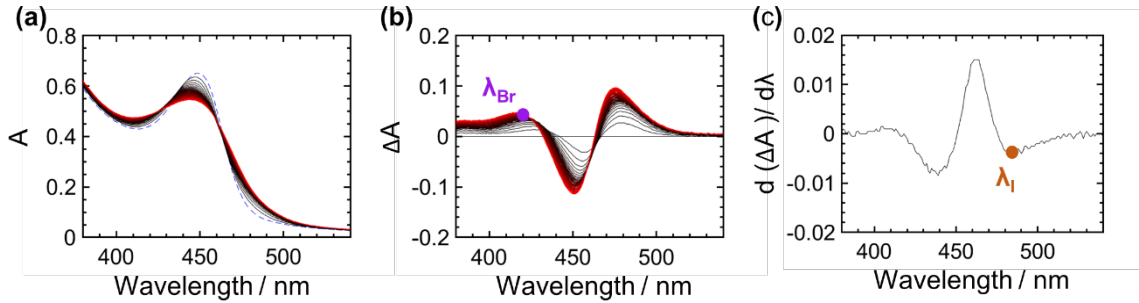


**Figure A.2.3.** (a) Raw UV-Vis (b)  $\Delta A$  and (c) spectra for photo de-mixing performed at 100°C. The graphs show examples of the characteristic wavelengths corresponding to Br-rich ( $\lambda_{\text{Br}}$ ) and I-rich ( $\lambda_{\text{I}}$ ).  $\lambda_{\text{Br}}$  was obtained from the peak of the A at short wavelengths, while  $\lambda_{\text{I}}$  was obtained from the peak of the slope of A.

**Figure A.2.4** displays the derivative of the change in absorbance for the sample, after 20 hours of illumination and for the four temperatures. The derivative of  $\Delta A$  does not always show a sharp peak, also due to the noise in the data after differentiation. The peak position is determined by smoothing the data using the Savitzky-Golay method (15 point window). I then evaluate the error associated to the determination of such peak position considering the root mean square (rms) of the residual obtained from the smoothing and evaluate the wavelength range where the value of the smoothed data is close to the peak value within 2 times the rms.

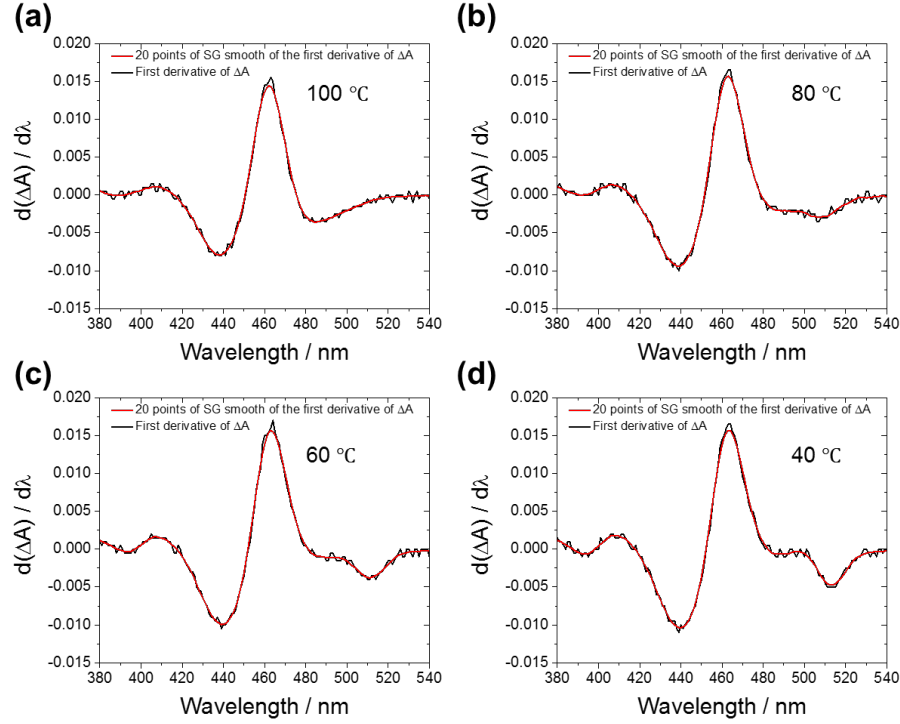


**Figure A.2.4.** Derivative of  $\Delta A$  with respect to wavelength for the samples de-mixed at different temperatures: (a) 100 °C; (b) 80 °C; (c) 60 °C; (d) 40 °C. The black and the red lines denote the raw data and the smoothed data. The latter were obtained using the Savitzky-Golay method (number of points used for smoothing window = 15).

The characteristic absorption wavelengths of Br-rich phases were determined based on the peak position of the A spectra at short wavelengths (**Figure A.2.3b**). It is noted that changes in the shape and peak position related to the absorbance of the Br-rich phase upon variations in the absorption magnitude associated to the starting phase and I-rich phase during the experiment would be expected. Due to this, the value of should not be directly used to estimate the Br-rich phase composition. Instead, we proceed by accounting for the influence from the emergence of the I-rich phase and from the consumption of the pristine phase during de-mixing by calculating the A spectra for different I-rich and Br-rich compositions (see full description in the next section).

*Correlating the characteristic wavelengths with compositions for Br-rich and I-rich phases*

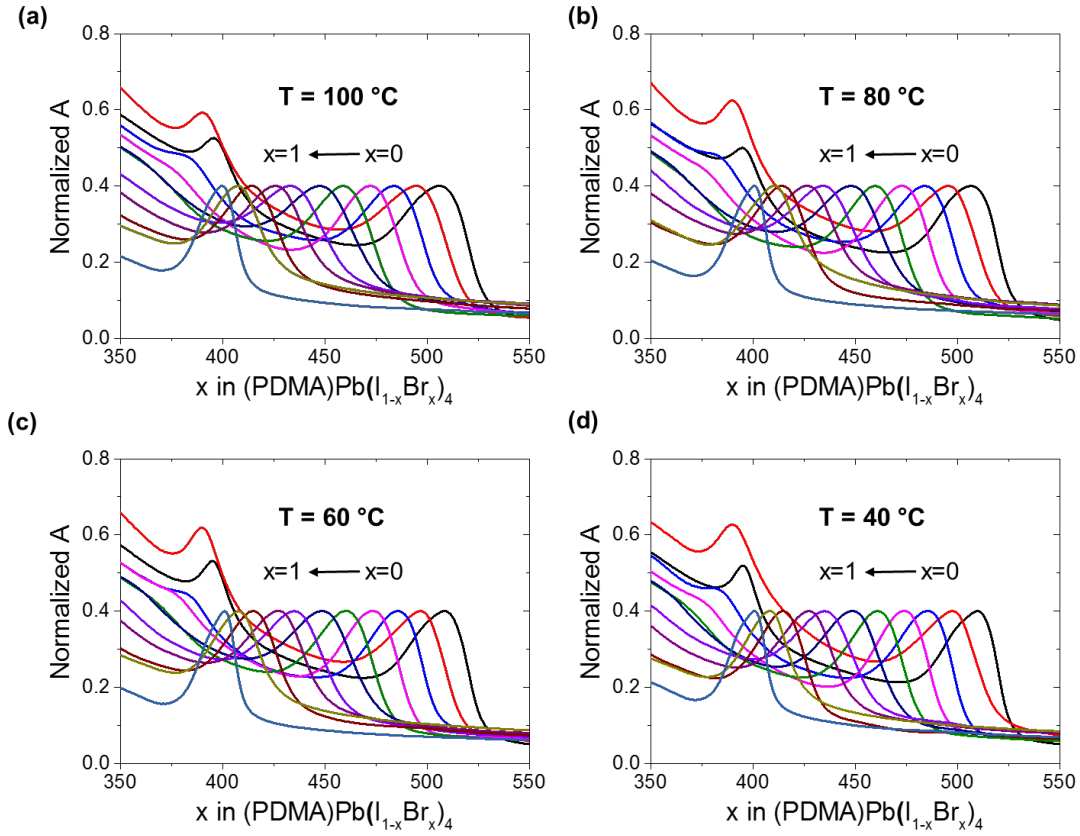
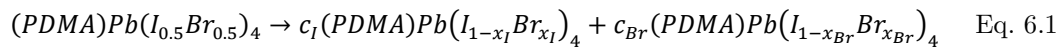


**Figure A.2.5.** Normalized absorbance spectra for  $(\text{PDMA})\text{Pb}(\text{I}_{1-x}\text{Br}_x)_4$  thin films with  $x = 0, 0.1, 0.2, 0.3, 0.4, 0.5, 0.6, 0.7, 0.8, 0.9, 1$  measured at (a)  $100\text{ }^\circ\text{C}$ ; (b)  $80\text{ }^\circ\text{C}$ ; (c)  $60\text{ }^\circ\text{C}$ ; (d)  $40\text{ }^\circ\text{C}$ .

In order to correlate the characteristic wavelengths for Br-rich and I-rich phases with their corresponding compositions, UV-Vis measurements are conducted for reference samples of  $(\text{PDMA})\text{Pb}(\text{I}_{1-x}\text{Br}_x)_4$  thin films ( $x = 0, 0.1, 0.2, 0.3, 0.4, 0.5, 0.6, 0.7, 0.8, 0.9, 1$ ) (see **Figure A2.5**). The reference absorption spectra were collected at different temperatures (corresponding to the same temperatures used in the photo de-mixing experiments) to account for the potential influence of temperature on absorption.

The  $\Delta A$  spectra based on the reference spectra shown in **Figure A.2.5** is calculated. Different de-mixing scenarios involving all relevant combinations of I-rich and Br-rich contributions to  $\Delta A$  is considered. As shown in Equation (1), I assume that, upon complete de-mixing, all of the pristine phase related to  $x_{\text{initial}} = 0.5$  de-mixes and forms two phases with different concentrations and compositions, satisfying mass conservation. Then  $\Delta A_{\text{calc}}$  is a result of the change in absorbance for the newly formed phases and the consumed pristine phase.



$$\Delta A_{\text{calc}} = c_I A_I + c_{\text{Br}} A_{\text{Br}} - A_{0.5} \quad \text{Eq. 6.2}$$

In Eq. 6.2,  $c_I$  and  $c_{\text{Br}}$  are molar ratios of the I- and Br-rich phases, and  $A_I$  and  $A_{\text{Br}}$  are the reference absorbance of the I- and Br-rich phases. By solving the equation of the mass balance

shown in equation 1, the values of  $c_I$  and  $c_{Br}$  as function of the input compositions can be expressed as , where  $x_I$  and  $x_{Br}$  indicate the compositions of the phases used in the calculation.

Here the calculated spectra based on the combination of the composition for I-rich ( $x = 0, 0.1, 0.2, 0.3, 0.4$ ), Br-rich ( $x = 0.7, 0.8, 0.9$ ) is investigated (**Figure A.2.6**), which proved to be the ranges of compositions relevant to the de-mixing experiment (**Figure 6.5, Figure 6.6**).

In all cases shown in **Figure A.2.6 (a, c, e, g)**, varying the value of  $x_{Br}$  results in a clear trend in the peak position of at short wavelengths. The formation of the I-rich phase with different composition and the consumption of the  $x_{initial} = 0.5$  phase have limited influence on the determination of the Br-rich composition in the calculated spectra. Based on this analysis, the value and uncertainty associated with  $x_{Br}$  using these data is estimated. It is also noted that the sharpness of the peak of the  $A_{calc}$  at short wavelengths varies when considering different combinations of I-rich and Br-rich compositions. In order to account for this effect, we use the 95% of the peak intensity to determine the error associated to the peak position. Furthermore, for the case of A spectra where the peak associated with the Br-rich phase absorption and the peak due to the absorption contribution from the I-rich domain at short wavelengths (see **Figure A.2.5, A.2.6**) are not well separated (see example in **Figure A.2.7a**), we extract the peak position after fitting a double Gaussian to describe the observed feature. The comparison of the calibrated compositions with and without the fitting shows consistency between the two approaches (**Figure A.2.7b** and Table 1), with the two methods yielding calibrated compositions that are similar within the error range. For I-rich phases, the extraction of the characteristic wavelengths involved the identification of the (negative) peak for the derivative of  $A_{calc}$  ( $d(A) / d\lambda$ ) as discussed above. The complete calibration dataset that was used to identify the values of  $x_{Br}$  and  $x_I$  is shown in **Figure A.2.8**. These values were extracted by inverting the equation of the fitting line to the calibration data, by using the photon energy associated with the peak of the experimental ( $d(A) / d\lambda$ ) or the photon energy associated with the peak of A at short wavelengths for  $x_I$  and  $x_{Br}$  respectively. The data referring to the calibration of  $x_I$  are similar when considering different  $x_{Br}$  values. On the other hand, the data referring to the calibration of  $x_{Br}$  are slightly different when considering different  $x_I$  values. Therefore, an average between the two values of  $x_{Br}$  was used. The two values were obtained by inverting the equation of two calibration fitting lines associated to values of  $x_I$  defining the relevant range (e.g., if the extracted value of  $x_I = 0.12$ , the value of  $x_{Br}$  was extracted by averaging the values obtained from the calibration fitting line obtained for  $x_I = 0.1$  and  $x_I = 0.2$ ).

$T = 40\text{ }^{\circ}\text{C}$ ,  $X_{\text{initial}} = 0.5$

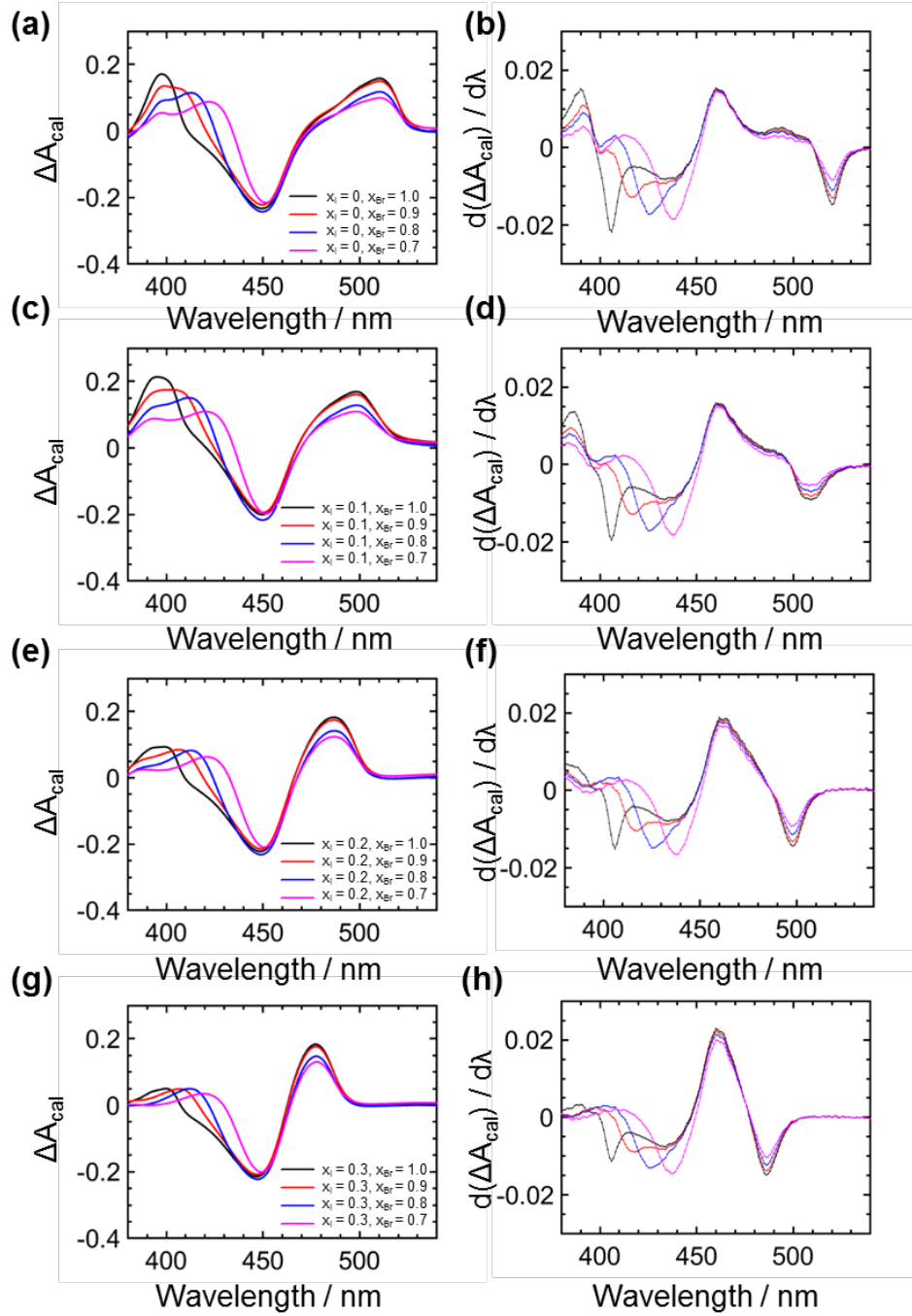


**Figure A.2.6.**  $A_{\text{calc}}$  spectra (a, c, e, g) assuming de-mixed composition of I-rich ( $x = 0, 0.1, 0.2, 0.3$ ). In each graph, spectra associated with different compositions of the Br-rich phase ( $x=0.7, 0.8, 0.9, 1$ ) are shown. The calculated spectra are based on the reference spectra measure at  $40\text{ }^{\circ}\text{C}$  shown in **Figure A.2.5**. (b, d, f, h) are the corresponding first derivatives for  $A_{\text{calc}}$  ( $d(A_{\text{calc}} / d\lambda)$ ) in (a, c, e, g) respectively.



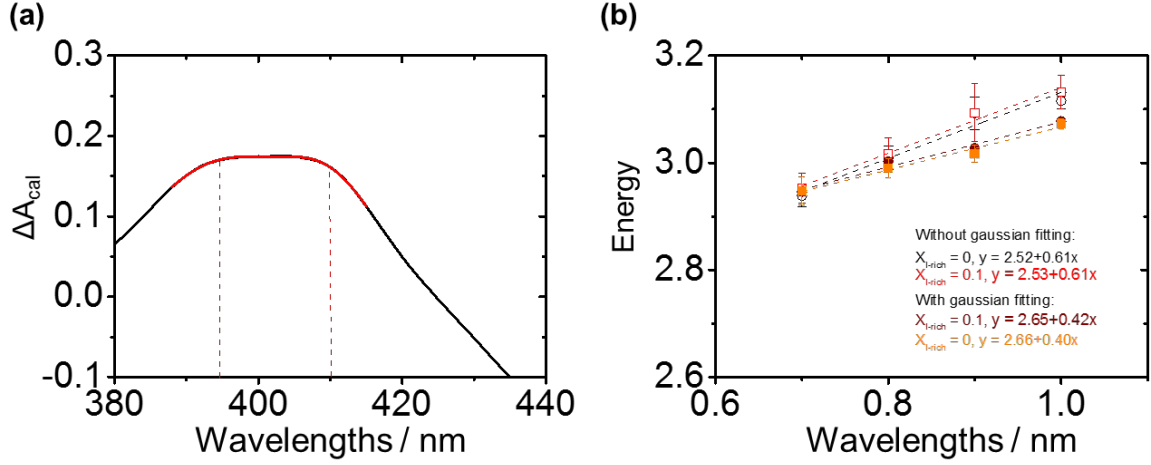


**Figure A.2.7.** (a)  $A_{\text{calc}}$  spectrum ( $x_{\text{initial}} = 0.5$ ,  $x_{\text{I}} = 0.1$ ,  $x_{\text{Br}} = 0.9$  shown in Figure A.2.6c) and its fitting with double Gaussian,  $A_1 = 0.1656$ ,  $A_2 = 0.0962$ ,  $x_1 = 394.9$  nm,  $x_2 = 411.0$  nm. (b) Photon energy calculated from two methods: according to method 1, the values of characteristic wavelengths of Br-rich phase is obtained from peak position at which the highest intensity is in the calculated spectra (empty symbols); as for method 2, the peak wavelengths are obtained from fitting two Gaussian to the data and using the position of the Gaussian peak at long wavelengths (filled symbols).

**Table A.2.1.** Comparison of the calibrated Br-rich compositions using method 1 and method 2 (described in Figure A.2.7).

T	X <sub>Br</sub> , method 1		X <sub>Br</sub> , method 2	
	x_avr	Err_x	x_avr	Err_x
60	0.74	-0.04	0.74	-0.06
40	0.74	-0.04	0.755	-0.06

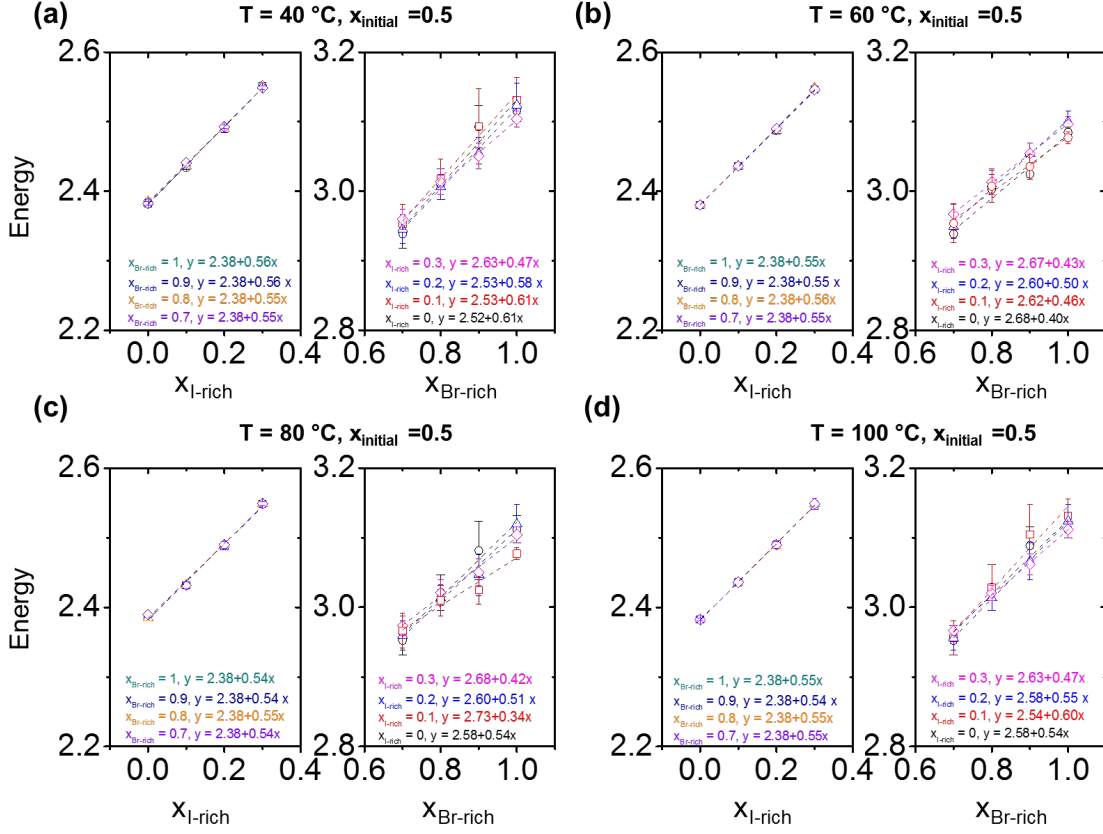
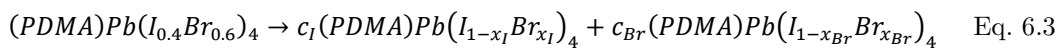


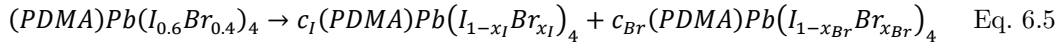
**Figure A.2.8.** Photon energy corresponding to the characteristic absorption wavelengths for I-rich and Br-rich compositions extracted from calculated  $A_{calc}$  and  $(d(A_{calc} / d\lambda))$  de-mixed spectra. The absorbance of the different combinations of I-rich and Br-rich compositions are based on reference spectra shown in **Figure 5.7** at different temperatures (a) 40 °C; (b) 60 °C; (c) 80 °C; (d) 100 °C. For each panel: the left graph shows the photon energy corresponding to the peak of the slope of  $A_{calc}$  ( $d(A / d\lambda)$ ) as a function of  $x_I$ , and for different values of  $x_{Br}$  ( $x_{Br} = 0.7, 0.8, 0.9, 1.0$ ); the right graph shows the photon energy of the peak of  $A_{calc}$  at short wavelengths as a function of  $x_{Br}$  and for different values of  $x_I$  ( $x_I = 0, 0.1, 0.2, 0.3$ ). All graphs refer to a value of the initial composition  $x_{initial} = 0.5$ . The details on the estimation of the errors are described in the text in this section.

The same method is used for determining the Br-rich and I-rich compositions when using different initial composition of the pristine film (see reactions and mass conservation equations below). The corresponding calculated energy in relation with I-rich and Br-rich compositions are shown in **Figure A.2.9** ( $x_{initial} = 0.6$ ) and **Figure A.2.10** ( $x_{initial} = 0.4$ ), respectively. Based on this analysis, the miscibility gaps with different initial compositions are mapped, as shown in **Figure 5.3b**.



$$\Delta A_{calc} = c_I A_I + c_{Br} A_{Br} - A_{0.6} \quad \text{Eq. 6.4}$$

$$c_I = \frac{x_{Br} - 0.6}{x_{Br} - x_I}, \quad c_{Br} = \frac{0.6 - x_I}{x_{Br} - x_I}$$



$$\Delta A_{\text{calc}} = c_I A_I + c_{Br} A_{Br} - A_{0.4} \quad \text{Eq. 6.6}$$

$$c_I = \frac{x_{Br}-0.4}{x_{Br}-x_I}, \quad c_{Br} = \frac{0.4-x_I}{x_{Br}-x_I},$$

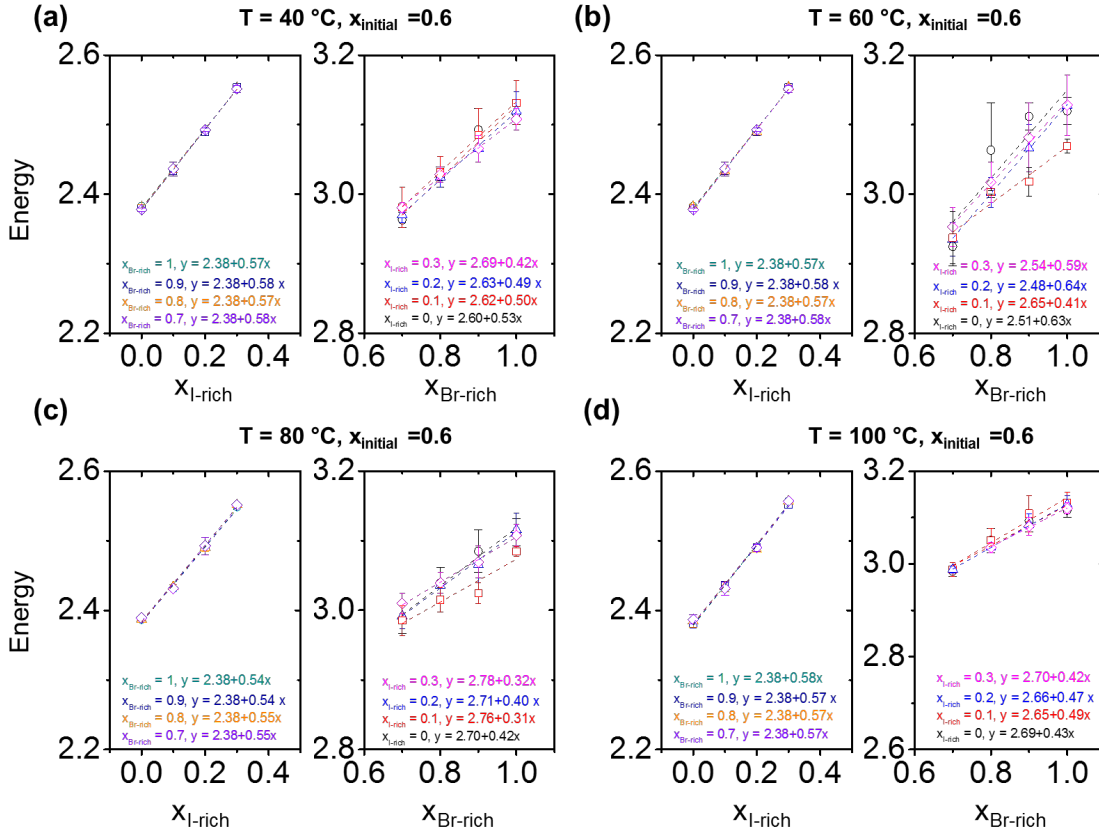


**Figure A.2.9.** Photon energy corresponding to the characteristic absorption wavelengths for I-rich and Br-rich compositions extracted from calculated  $A_{\text{calc}}$  and  $(d(A_{\text{calc}} / d\lambda))$  de-mixed spectra. The absorbance of the different combinations of I-rich and Br-rich compositions are based on reference spectra shown in Figure 5.7 at different temperatures (a) 40 °C; (b) 60 °C; (c) 80 °C; (d) 100 °C. For each panel: the left graph shows the photon energy corresponding to the peak of the slope of  $A_{\text{calc}}$  ( $d(A_{\text{calc}} / d\lambda)$ ) as a function of  $x_I$ , and for different values of  $x_{Br}$  ( $x_{Br} = 0.7, 0.8, 0.9, 1.0$ ); the right graph shows the photon energy of the peak of  $A_{\text{calc}}$  at short wavelengths as a function of  $x_{Br}$  and for different values of  $x_I$  ( $x_I = 0, 0.1, 0.2, 0.3$ ). All graphs refer to a value of the initial composition  $x_{\text{initial}} = 0.6$ . The details on the estimation of the errors are described in the text in this section.

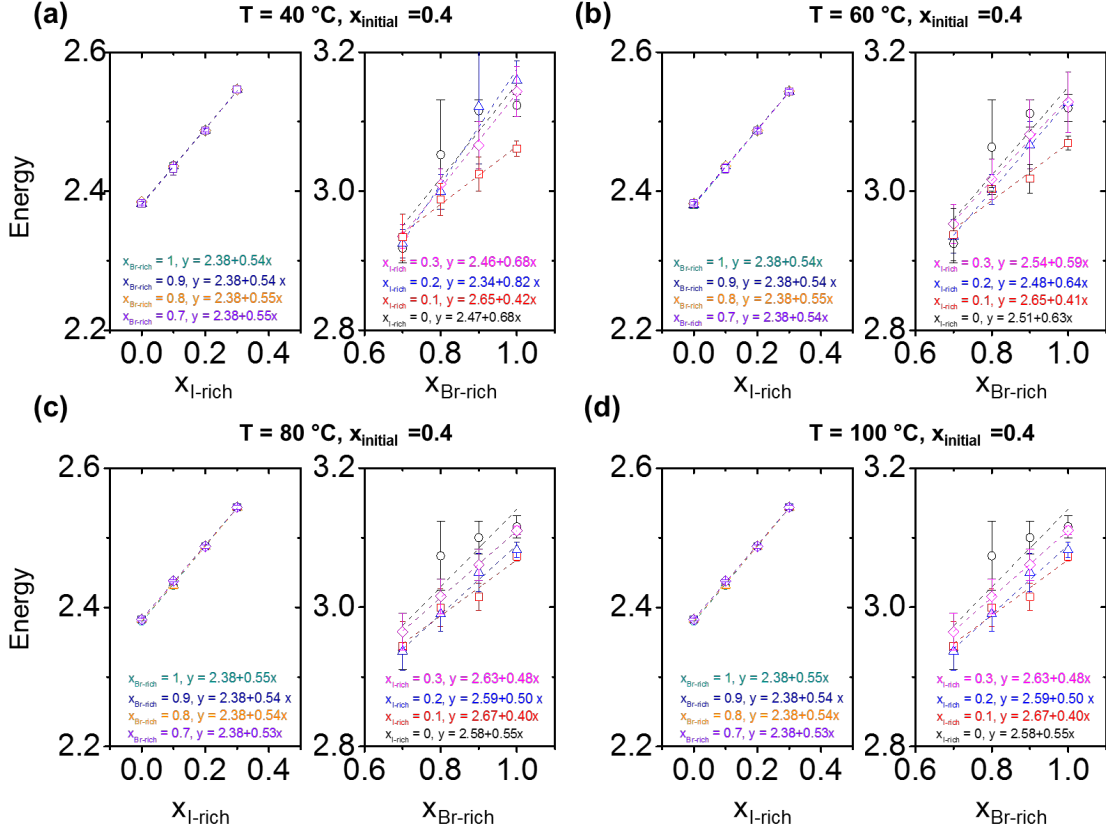


**Figure A.2.10.** Photon energy corresponding to the characteristic absorption wavelengths for I-rich and Br-rich compositions extracted from calculated  $A_{\text{calc}}$  and  $(d(A_{\text{calc}} / d\lambda))$  de-mixed spectra. The absorbance of the different combinations of I-rich and Br-rich compositions are based on reference spectra shown in **Figure 5.7** at different temperatures (a) 40 °C; (b) 60 °C; (c) 80 °C; (d) 100 °C. For each panel: the left graph shows the photon energy corresponding to the peak of the slope of  $A_{\text{calc}}$  ( $d(A / d\lambda)$ ) as a function of  $x_I$ , and for different values of  $x_{Br}$  ( $x_{Br} = 0.7, 0.8, 0.9, 1.0$ ); the right graph shows the photon energy of the peak of  $A_{\text{calc}}$  at short wavelengths as a function of  $x_{Br}$  and for different values of  $x_I$  ( $x_I = 0, 0.1, 0.2, 0.3$ ). All graphs refer to a value of the initial composition  $x_{\text{initial}} = 0.4$ . The details on the estimation of the errors are described in the text in this section.

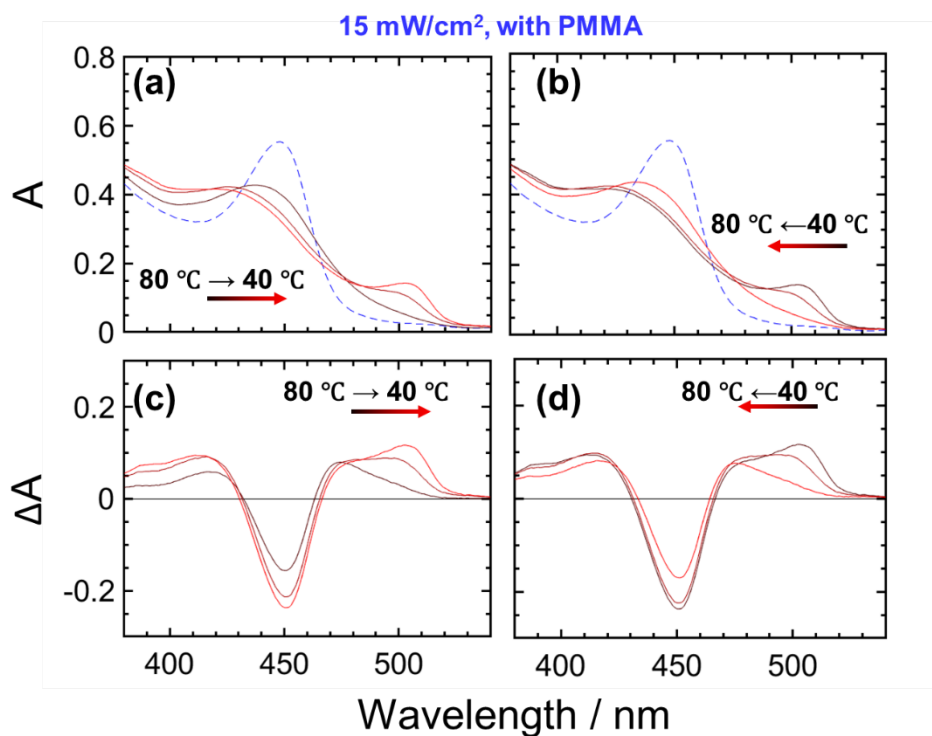


**Figure A.2.11.** Temperature dependence UV-Vis spectra of (PDMA)Pb(I<sub>0.5</sub>Br<sub>0.5</sub>)<sub>4</sub> thin film (with PMMA encapsulation) under light (15 mW/cm<sup>2</sup>) (a) at temperature from 100 °C to 80 to 60 and to 40 °C for 20 h (b) at temperature from 40 °C to 60 to 80 and to 100 °C for 20 h. The gradient from black to red denotes the time sequence of the temperature step. Dashed blue line denotes the absorption spectrum of the pristine (PDMA)Pb(I<sub>0.5</sub>Br<sub>0.5</sub>)<sub>4</sub> phase (50:50). (c) and (d) are the  $\Delta A$  spectra (obtained by subtracting the reference spectrum of the pristine sample from each absorption spectrum).

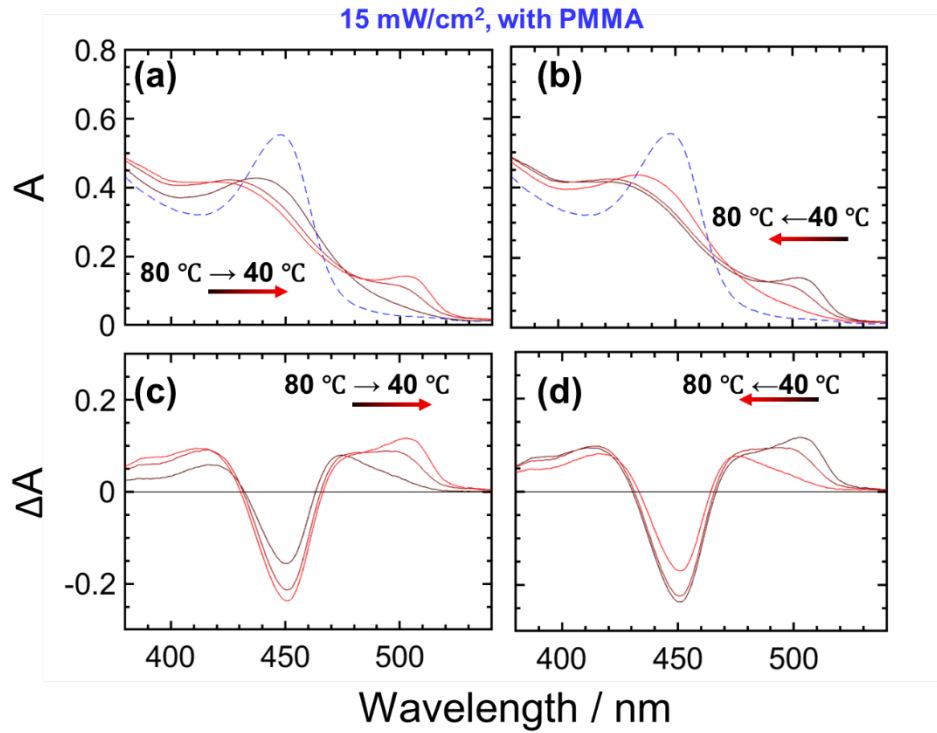


**Figure A.2.12.** Temperature dependence UV-Vis spectra of (PDMA)Pb(I<sub>0.5</sub>Br<sub>0.5</sub>)<sub>4</sub> thin film (with PMMA encapsulation) under light (15 mW/cm<sup>2</sup>) (a) at temperature from 100 °C to 80 to 60 and to 40 °C for 20 h (b) at temperature from 40 °C to 60 to 80 and to 100 °C for 20 h. The gradient from black to red denotes the time sequence of the temperature step. Dashed blue line denotes the absorption spectrum of the pristine (PDMA)Pb(I<sub>0.5</sub>Br<sub>0.5</sub>)<sub>4</sub> phase (50:50). (c) and (d) are the  $\Delta A$  spectra (obtained by subtracting the reference spectrum of the pristine sample from each absorption spectrum).

### A.3 supporting material for Chapter 7

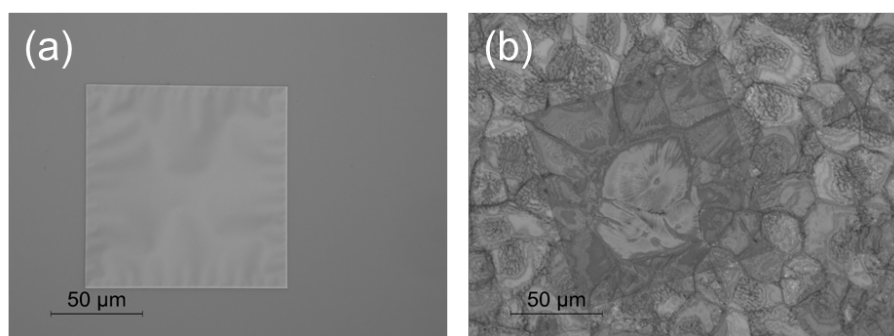


**Figure A.3.1** Microscope image of the (a) bare  $\text{Si}_3\text{N}_4$  membrane substrates (b)  $(\text{PDMA})\text{Pb}(\text{I}_{0.5}\text{Br}_{0.5})_4$  thin films deposited on top of the membrane substrates shown in (a).

The morphology of the perovskites thin film prior to illumination on the window area and non-window area are shown in **Figure 7.2**. Compared with the non-window area, films on the window area show more cracks. This can be due to the more favorable release of the strain (generated from different thermal expansion coefficient between the perovskites thin film and substrate during preparation process) to bulk Si compared with thin film  $\text{Si}_3\text{N}_4$ .

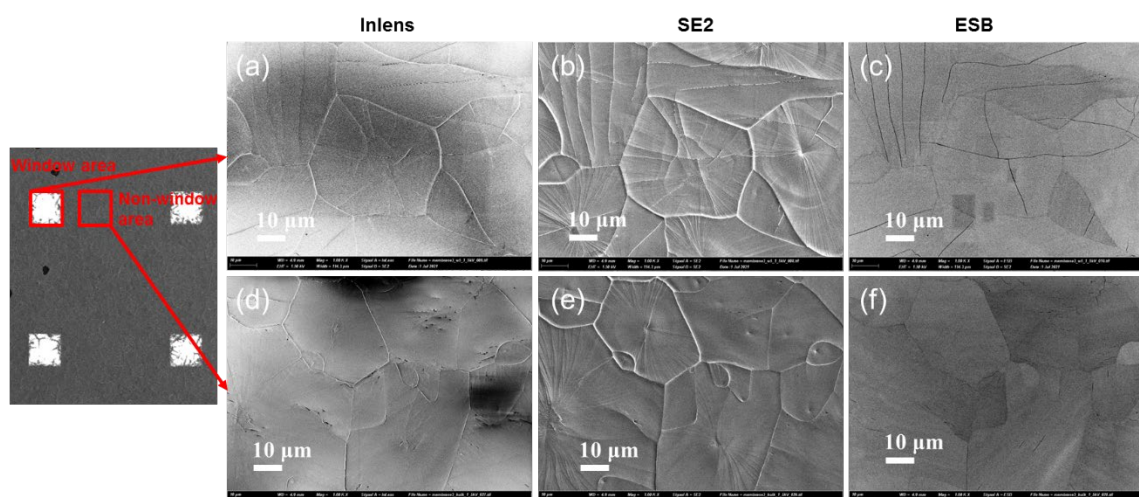


**Figure A.3.2.** SEM of pristine  $(\text{PDMA})\text{Pb}(\text{I}_{0.5}\text{Br}_{0.5})_4$  thin film (a-c) window area; (d-f) Non window area. (a), (d) InLens; (b), (e)SE2; (c), (f)BSE detectors. Magnification: 1K.



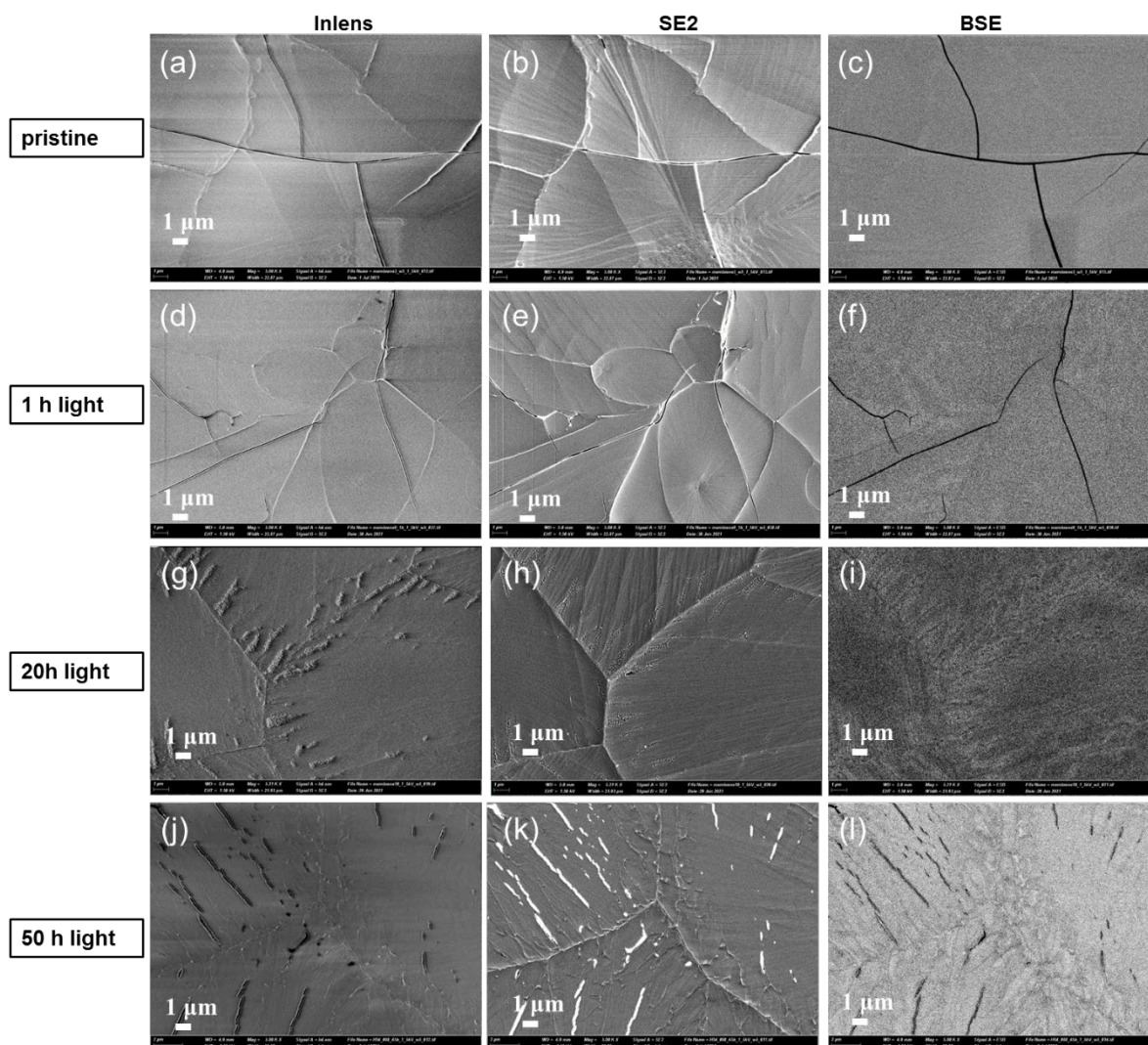


**Figure A.3.3** SEM of  $(\text{PDMA})\text{Pb}(\text{I}_{0.5}\text{Br}_{0.5})_4$  thin film with different de-mixing time (illumination intensity  $1.5 \text{ mW}/\text{cm}^2$  at  $80^\circ\text{C}$ ). (a-c) pristine; (d-f) de-mixed for 1 h; (g-i) de-mixed for 20 h; (j-l) de-mixed for 50 h. (a, d, g, j) InLens; (b, e, h, k) SE2; (c, f, i, l) BSE detectors. The imaging was conducted in window area. Magnification: 5K.



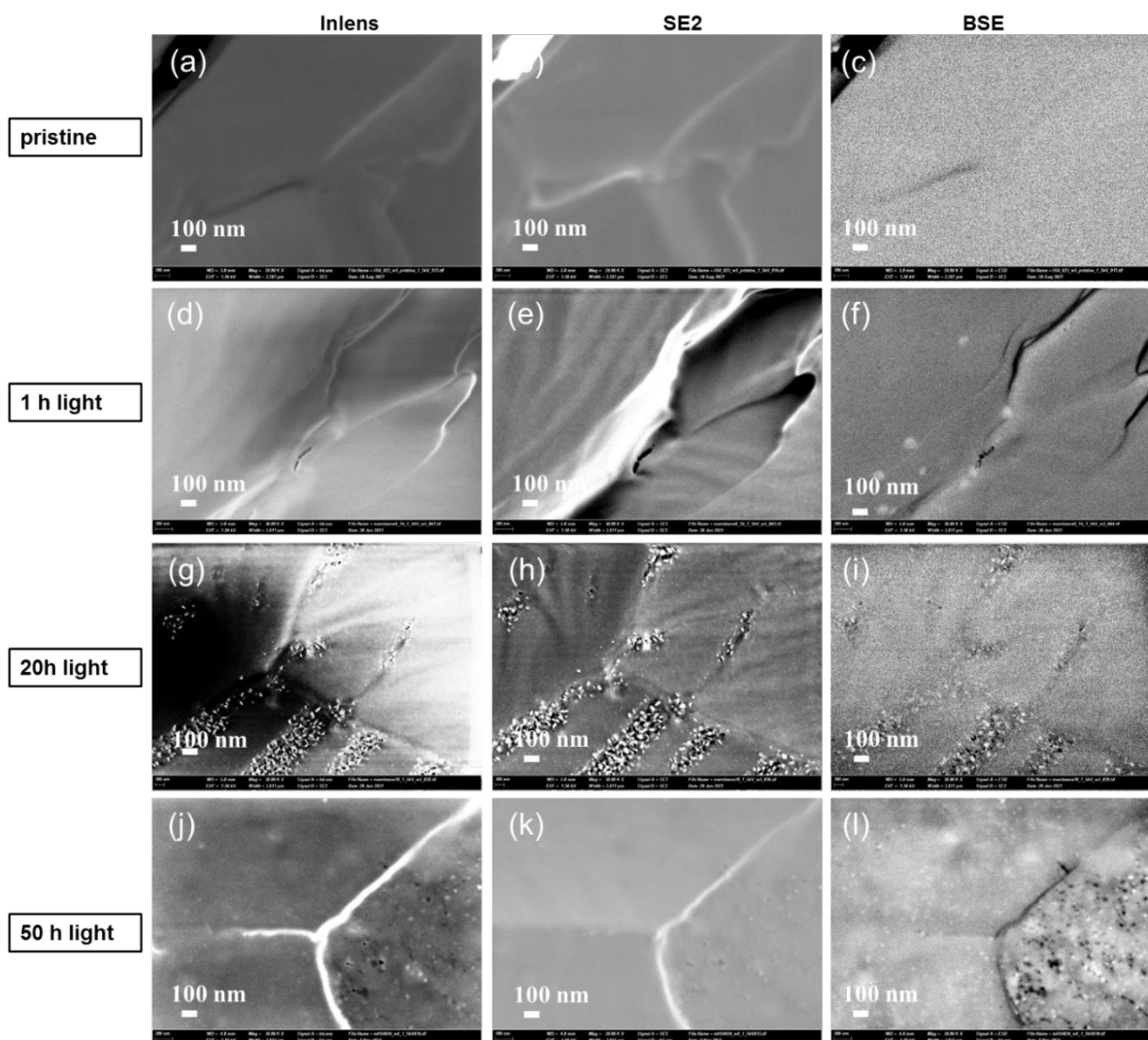


**Figure A.3.4** SEM of  $(\text{PDMA})\text{Pb}(\text{I}_{0.5}\text{Br}_{0.5})_4$  thin film with different de-mixing time (illumination intensity  $1.5 \text{ mW}/\text{cm}^2$  at  $80^\circ\text{C}$ ). (a-c) pristine; (d-f) de-mixed for 1 h; (g-i) de-mixed for 20 h; (j-l) de-mixed for 50 h. (a, d, g, j) InLens; (b, e, h, k) SE2; (c, f, i, l) BSE detectors. The imaging was conducted in window area. Magnification: 30K.

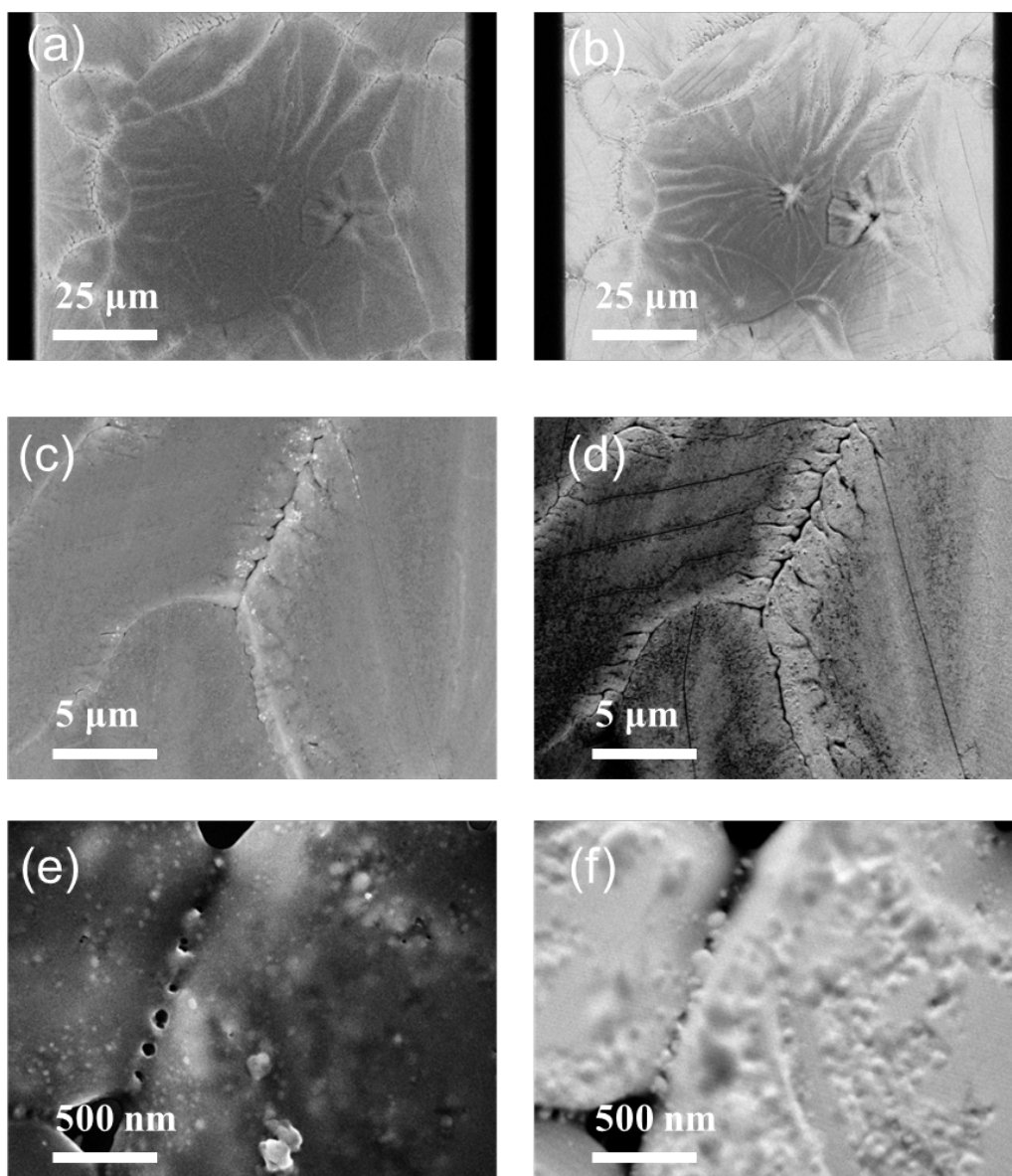


**Figure A.3.5** (a, c, e) SEM (SE2) and (b, d, f) forescatter diodes in imaging for  $(\text{PDMA})\text{Pb}(\text{I}_{0.5}\text{Br}_{0.5})_4$  thin film that had been de-mixed for 50 h at  $1.5 \text{ mW}/\text{cm}^2$  at  $80^\circ\text{C}$ . The imaging was conducted in window area.

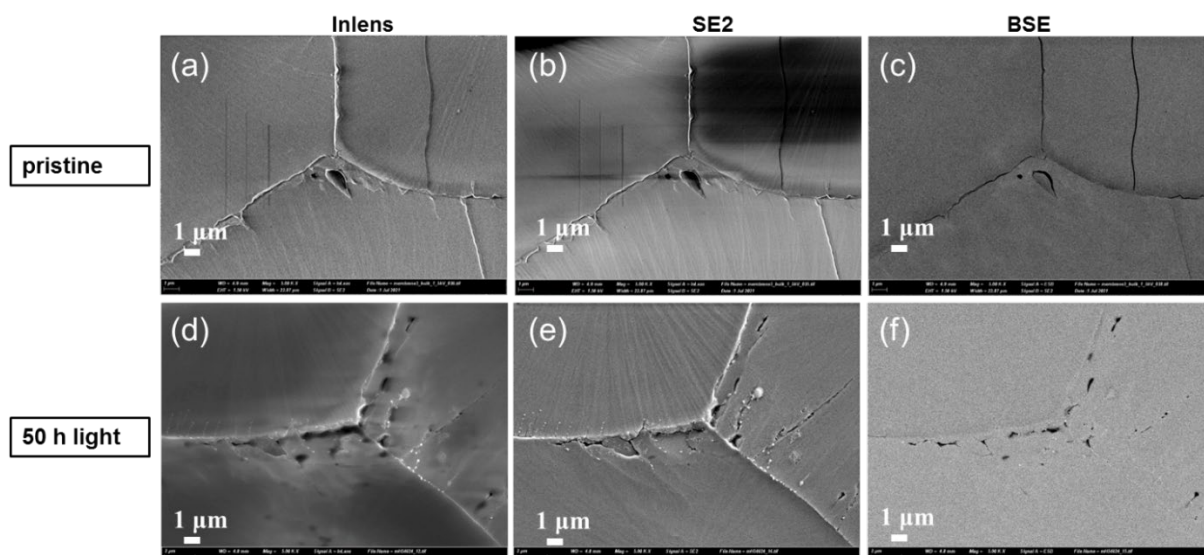


**Figure A.3.6** SEM for  $(\text{PDMA})\text{Pb}(\text{I}_{0.5}\text{Br}_{0.5})_4$  thin film time. (a-c) pristine; (d-f) de-mixed for 50 h at  $1.5 \text{ mW}/\text{cm}^2$  at  $80^\circ\text{C}$ . (a, d) InLens; (b, e) SE2; (c, f) BSE detectors. The imaging was conducted in non-window area. Magnification: 5K.

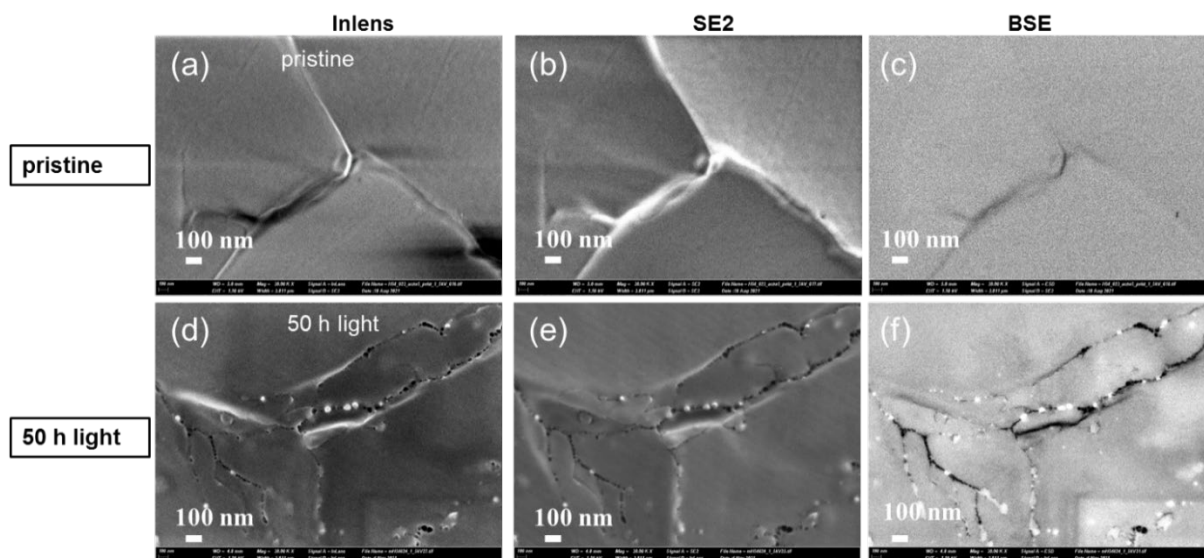


**Figure A.3.7** SEM for  $(\text{PDMA})\text{Pb}(\text{I}_{0.5}\text{Br}_{0.5})_4$  thin film time. (a-c) pristine; (d-f) de-mixed for 50 h at  $1.5 \text{ mW}/\text{cm}^2$  at  $80^\circ\text{C}$ . (a, d) InLens; (b, e) SE2; (c, f) BSE detectors. The imaging was conducted in non-window area. Magnification: 30K.

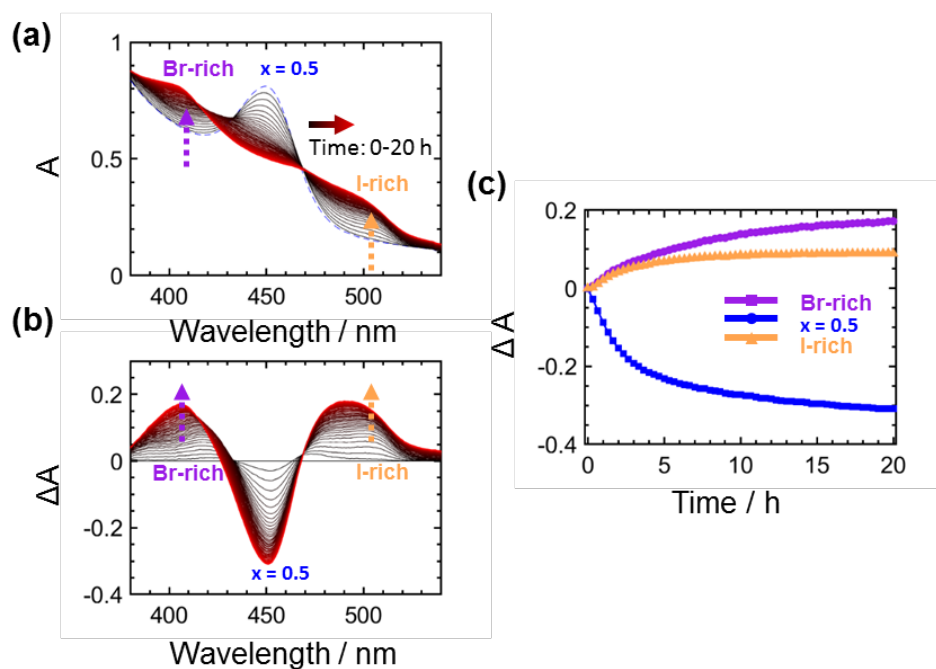


**Figure A.3.9** UV-Vis spectra evolution of (PDMA)Pb(I<sub>0.5</sub>Br<sub>0.5</sub>)<sub>4</sub> thin films (without PMMA encapsulation and in Ar atmosphere) during photo de-mixing under light (1.5 mW/cm<sup>2</sup>) at 80 °C for 20 h (a) Absorbance and (b) Change in absorbance obtained by subtracting the reference spectrum of the pristine sample from each absorbance spectrum shown in (a); (c) Kinetics of the photo de-mixing highlighting the change in absorbance at wavelengths associated to (PDMA)Pb(I<sub>0.5</sub>Br<sub>0.5</sub>)<sub>4</sub> (450 nm, blue), Br-rich (406 nm, purple) and I-rich (515nm, yellow) phases.

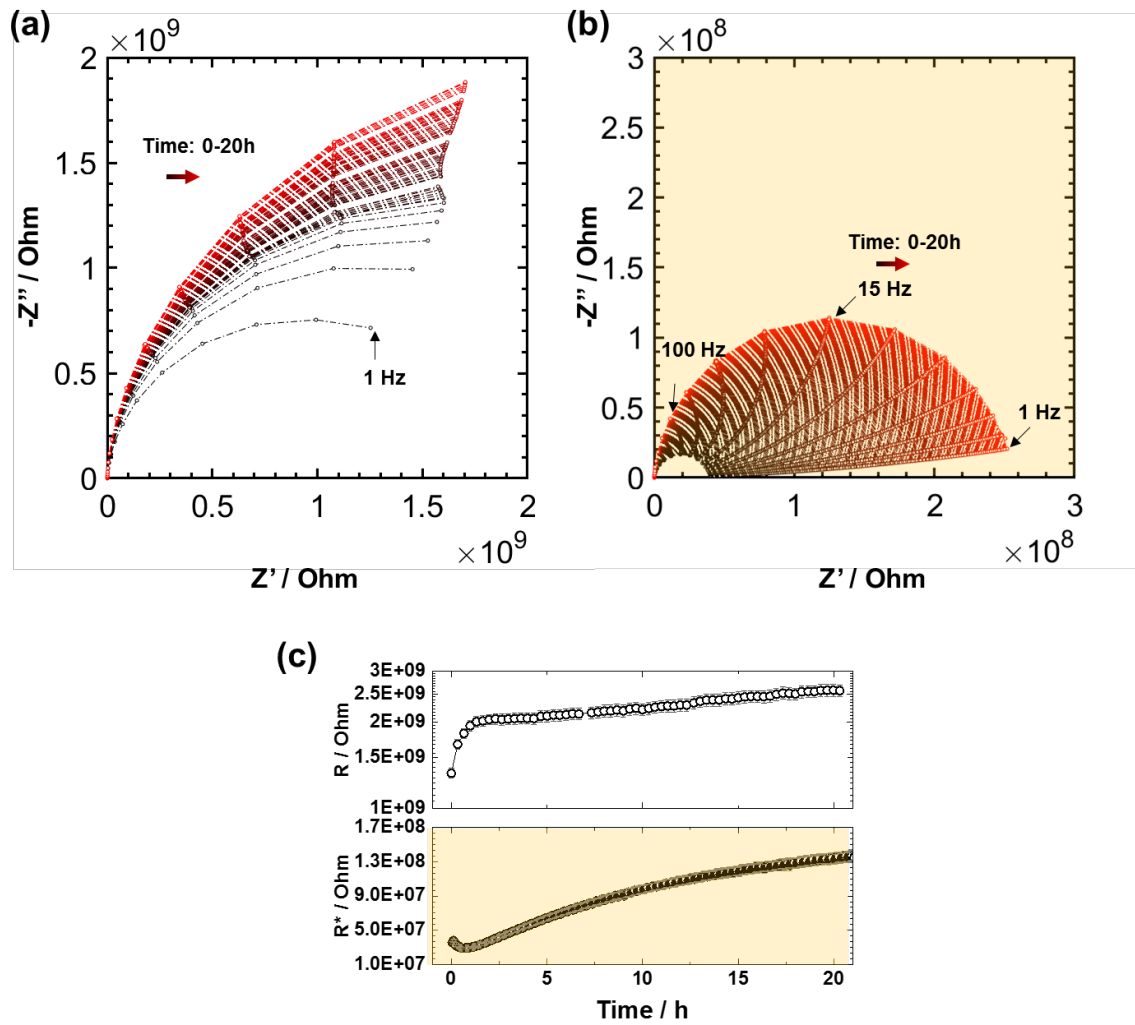


**Figure A.3.10** Impedance spectra of (PDMA)Pb(I<sub>0.5</sub>Br<sub>0.5</sub>)<sub>4</sub> thin film (without PMMA encapsulation, in Ar atmosphere) during photo de-mixing (at 80 °C for 20 h) (a) measured in the dark (b) measured under light (1.5 mW/cm<sup>2</sup>); The measurement frequency range is from 1E06 to 1 Hz(c) Change in resistance in dark(R) and under light(R\*).

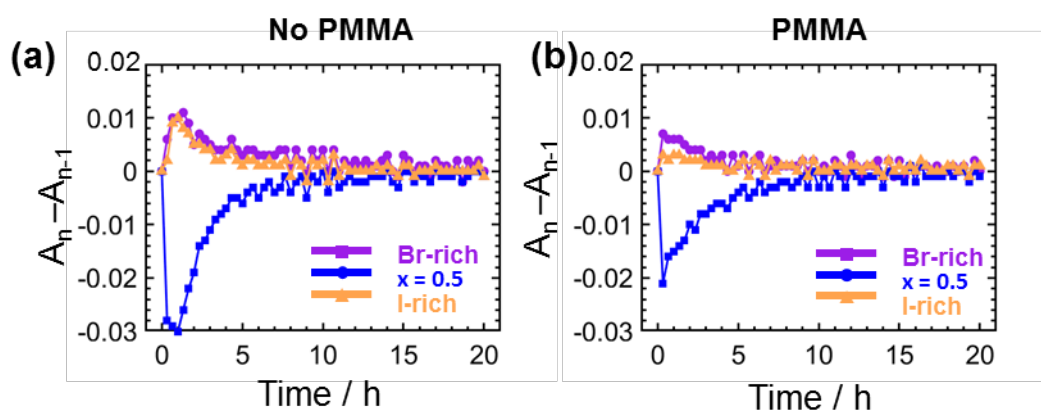


**Figure A.3.11** Change in absorption spectra by subtracting the reference spectrum of the pristine sample from last absorbance spectrum ( $A_n - A_{n-1}$ ); during photo de-mixing (a) without encapsulation of PMMA, subtracted from absorption data shown in Figure A3.3a. (PDMA)Pb(I<sub>0.5</sub>Br<sub>0.5</sub>)<sub>4</sub> (450 nm, blue), Br-rich (406 nm, purple) and I-rich (515nm, yellow) phases.(b) With PMMA encapsulation on surface prior to illumination, subtracted from absorption data shown in Figure 7.12. (PDMA)Pb(I<sub>0.5</sub>Br<sub>0.5</sub>)<sub>4</sub> (450 nm, blue), Br-rich (416 nm, purple) and I-rich (517 nm, yellow) The photo de-mixing are conducted under same experimental condition: LED light illumination 1.5 mW/cm<sup>2</sup>) at 80 °C for ~20 h.

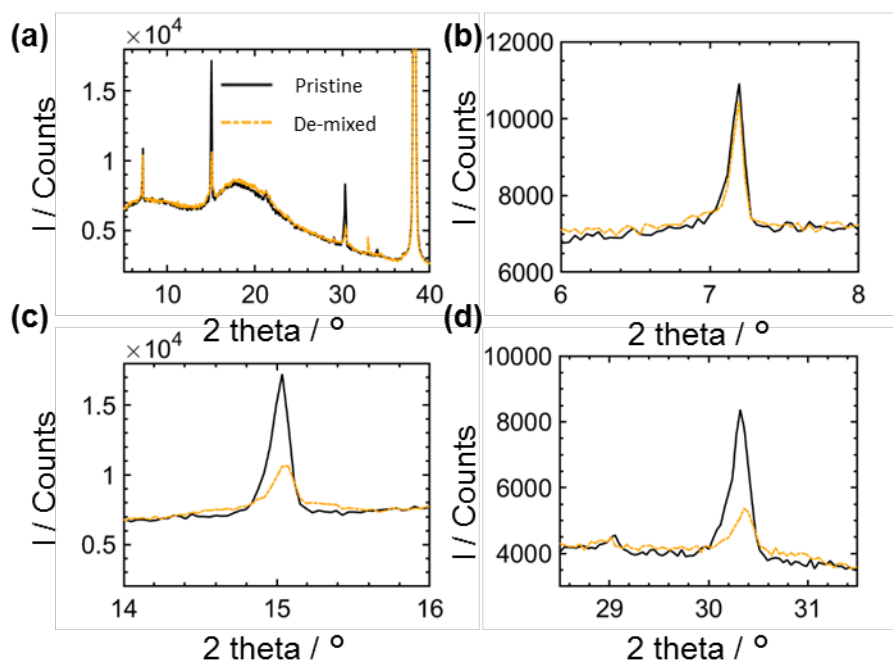


**Figure A.3.12** XRD measurements of (PDMA)Pb(I<sub>0.5</sub>Br<sub>0.5</sub>)<sub>4</sub> thin film (without PMMA encapsulation, in Ar atmosphere) before (black solid line) and after photo de-mixing (yellow dashed line, cold white LED illumination with 1.5 mW /cm<sup>2</sup> for 20 h at 80°C). (a)  $2\theta = 5^\circ - 40^\circ$ ; The peaks are highlighted at (b)  $2\theta = 6^\circ - 9^\circ$ ; (c)  $2\theta = 14^\circ - 16^\circ$ ; (d)  $2\theta = 13^\circ - 17^\circ$ .



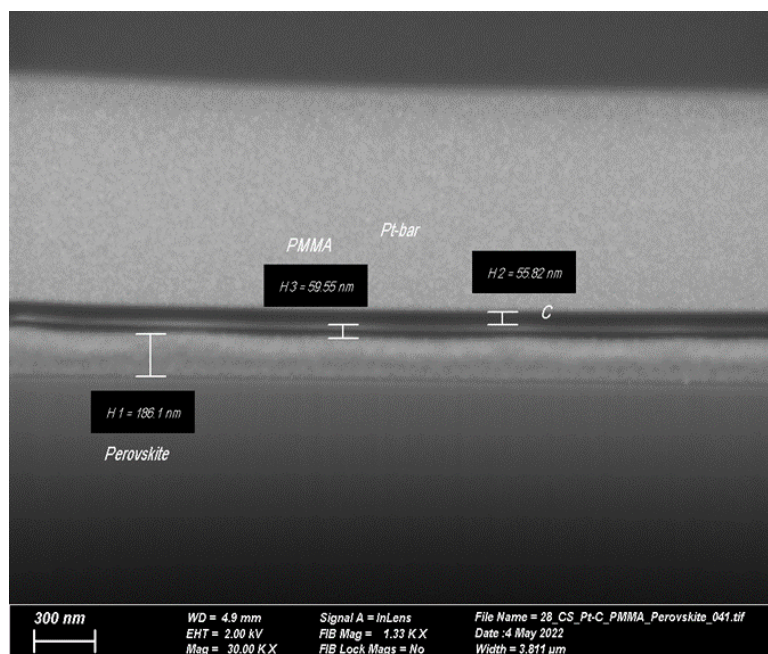


**Figure A.3.13.** Cross sectional image of (PDMA)Pb(I<sub>0.5</sub>Br<sub>0.5</sub>)<sub>4</sub> film on quartz substrates with PMMA encapsulation. From bottom to up, the layer are substrates (quartz), perovskites (186 nm), PMMA (60 nm), carbon and Pt-bar. The carbon and Pt bar are used for creating a conducting surface and protection layer when cross sectional are cut.

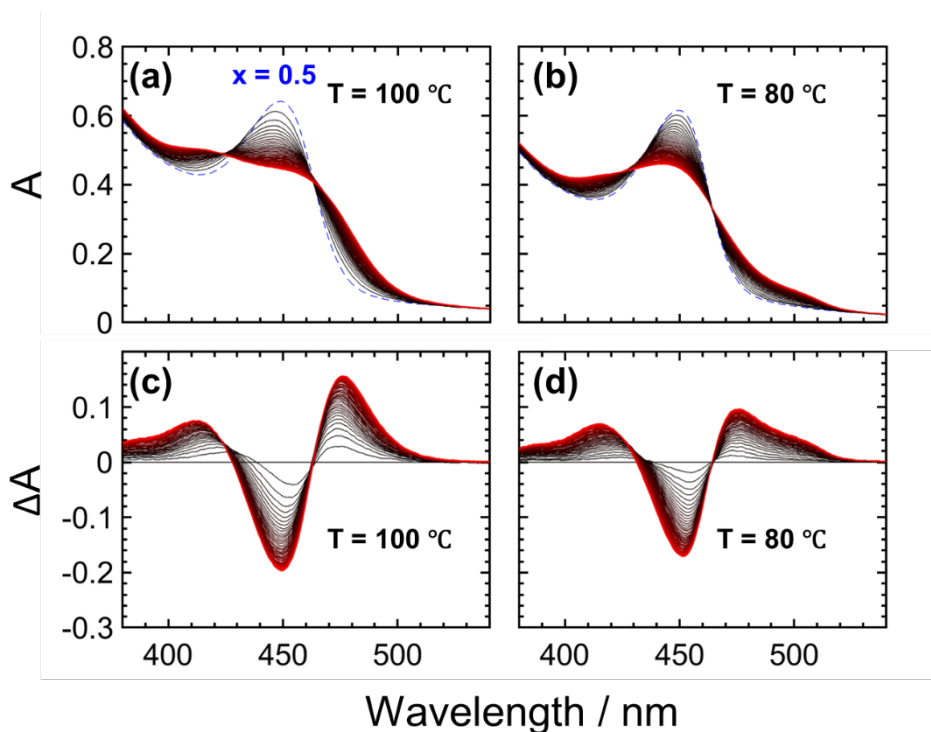


**Figure A.3.14.** Temperature dependent UV-Vis spectra of a (PDMA)Pb(I<sub>0.5</sub>Br<sub>0.5</sub>)<sub>4</sub> thin film (with PMMA encapsulation) under light (1.5 mW/cm<sup>2</sup>) (a) at 100 °C and (b) at 80 °C for 20 hours. (c) and (d) are the  $\Delta A$  spectra (obtained by subtracting the reference spectrum of the pristine sample from each absorption spectrum).

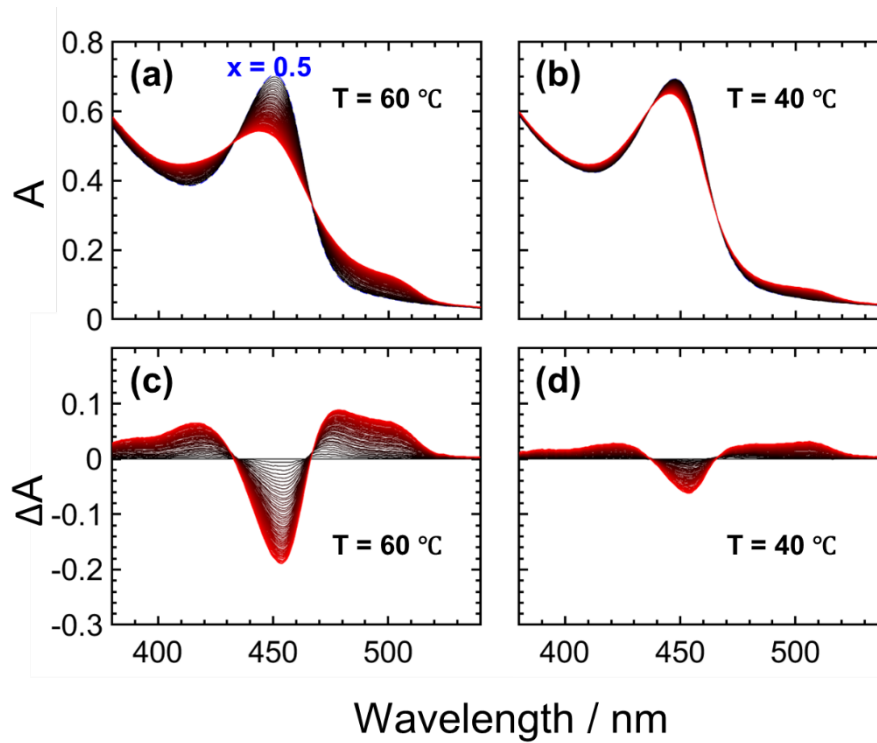


**Figure A.3.15.** Temperature dependent UV-Vis spectra of  $(\text{PDMA})\text{Pb}(\text{I}_{0.5}\text{Br}_{0.5})_4$  thin film (with PMMA encapsulation) under light ( $1.5 \text{ mW}/\text{cm}^2$ ) (a) at  $60 \text{ }^\circ\text{C}$  and (b) at  $40 \text{ }^\circ\text{C}$  for 20 hours. (c) and (d) are the  $\Delta A$  spectra (obtained by subtracting the reference spectrum of the pristine sample from each absorption spectrum).



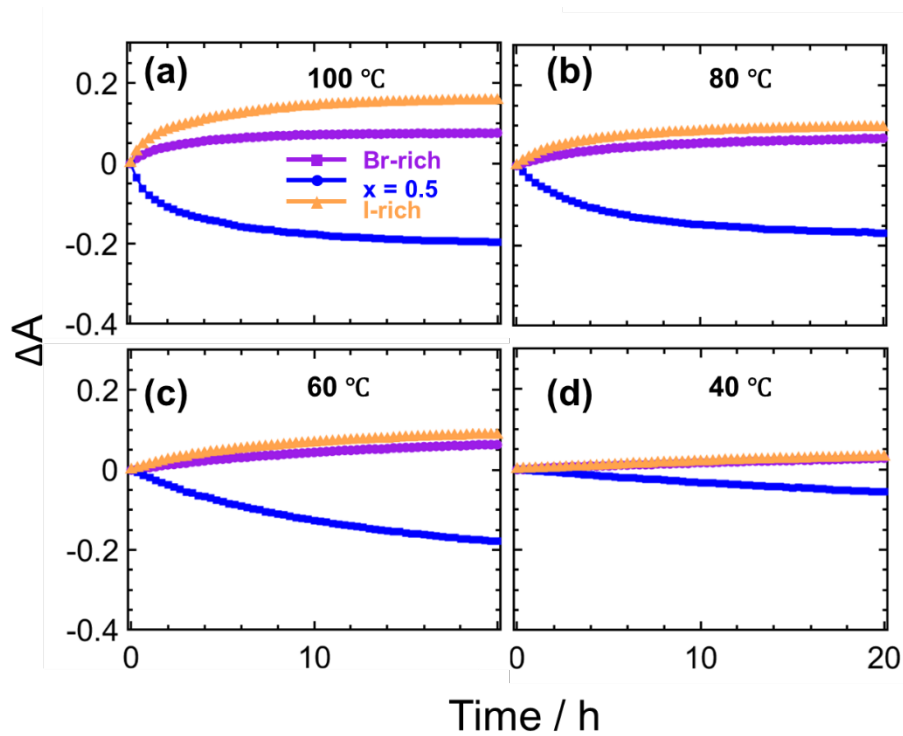


**Figure A.3.16.** Kinetics of photo de-mixing experiments performed at different temperatures at (a) 100 °C (b) 80 °C (c) 60 °C and (d) 40 °C. The characteristic wavelengths of the Br-rich,  $x = 0.5$  and I-rich phases are shown. Data extracted from **Figure A.3.14** and **Figure A.3.15**.

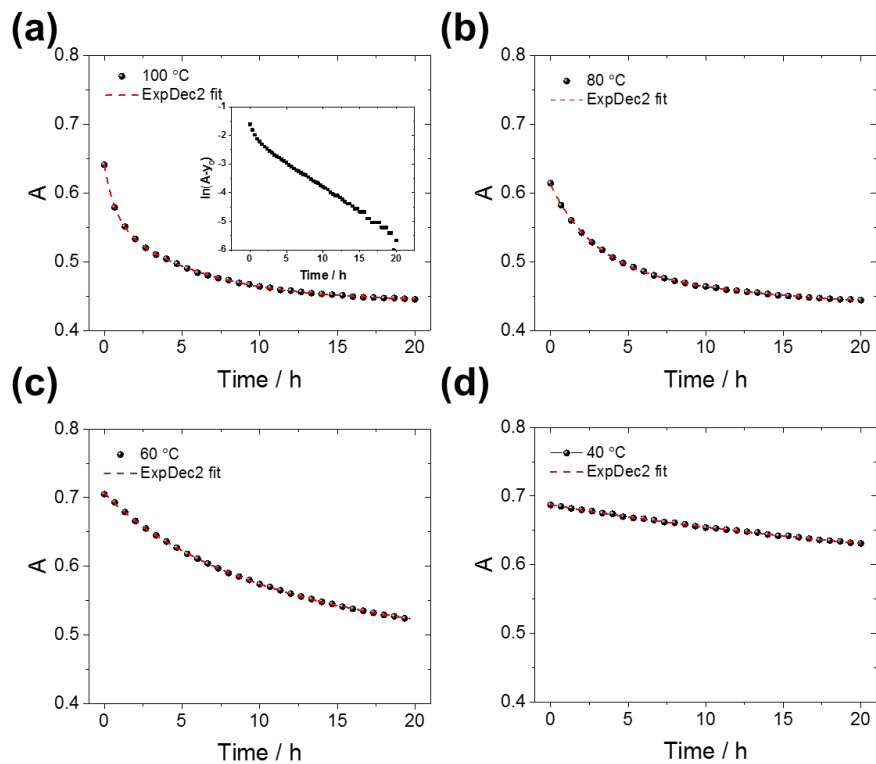


**Figure A.3.17.** (a-c) Kinetics of the change in absorbance at the peak absorption wavelength corresponding to the  $x = 0.5$  phase (450 nm) under light at different temperatures. We fitted a bi-exponential to the data (see also inset in (a)). For the fit of the data we apply the

constraint that the ratio of the initial absorbance and the absorbance that is reached at steady-state is the same value at different temperatures. Such value is obtained from fitting an unconstrained bi-exponential to the data collected at 100 °C.

**Table A.1.3.2.** Fitting parameters for de-mixing kinetics shown in Figure A.3.16 at different temperatures using a bi-exponential function  $y = A_1 e^{\frac{-x}{\tau_1}} + A_2 e^{\frac{-x}{\tau_2}} + y_0$ . For the case of 60 °C and 40 °C, a single exponential was fitted.

$T_{\text{de-mixing}}$	$A_1$	$A_2$	$\tau_1$ (h)	$\tau_2$ (h)	$t_{1/2}$ (h)
100 °C	0.08	0.12	0.4	3.0	1.6
80 °C	0.08	0.09	1.1	3.9	3.2
60 °C	0.11	0.11	5.4	5.4	7.5
40°C	0.06	0.06	16.7	16.7	17.3

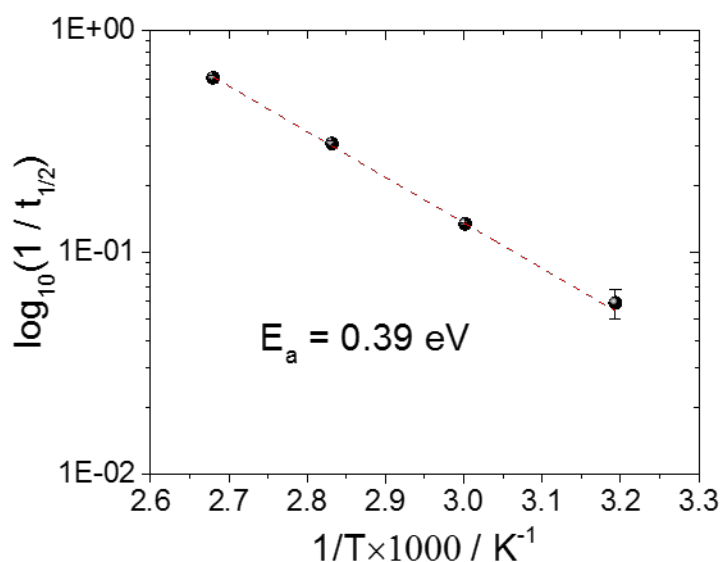


**Figure A.3.18.** Half-time associated to the changes in absorbance shown in Figure A.3.14 and Figure A.3.15 and Table A.3.1 displayed in an Arrhenius plot. The line corresponds to the a linear fit to the data, from which we obtain an activation energy for the photo de-mixing experiment shown in in Figure A.3.14 and Figure A.3.15 of  $E_a = 0.39$  e

#### A.4 supporting material for Chapter 8

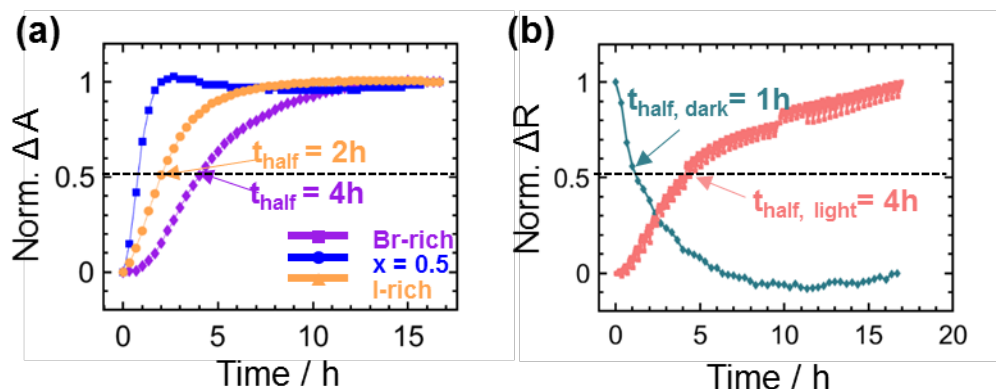


**Figure A.4.1** (a) Normalized kinetics on change in absorbance during photo de-mixing process at wavelengths associated to  $\text{MAPb}(\text{I}_{0.5}\text{Br}_{0.5})_3$  (623 nm, blue), Br-rich (523 nm, purple) and I-rich (663 nm, yellow) phases; (b) Normalized kinetics of change in resistance in the dark (dark green) and under light (orange).

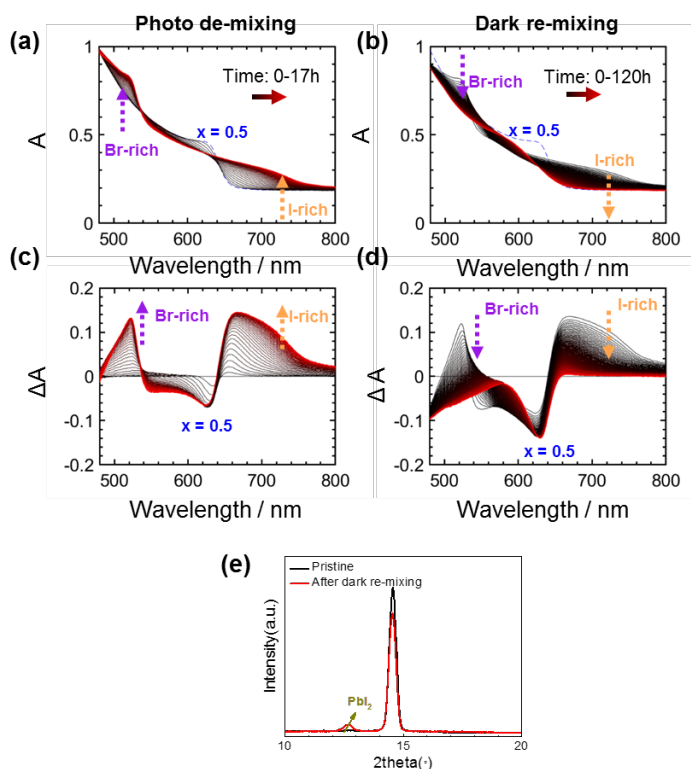


**Figure A.4.2** UV-Vis spectra evolution of  $\text{MAPb}(\text{I}_{0.5}\text{Br}_{0.5})_3$  thin films (without PMMA encapsulation and in Ar atmosphere to exclude possible degradation) (a) under light ( $1.5 \text{ mW/cm}^2$ ) at  $40^\circ\text{C}$  for 17 h and (b) in the dark at  $40^\circ\text{C}$  for  $\sim 160$  h with 1 h time interval between spectra. For the case under light, within each interval, spectra were collected by switching off the bias light for 300 s (see Figure 4.3 from the Material and Methods). (c, d) Change in absorbance obtained by subtracting the reference spectrum of the pristine sample from each absorbance spectrum shown in (a) and (b), respectively. (e) Change in X-ray diffraction patterns between the pristine state and the sample after dark re-mixing.



## B Bibliography

1. V. Bhatt, M. Kumar, P. Yadav, M. Kumar and J.-H. Yun, *Mater. Res. Bull.*, 2018, **99**, 79-85.
2. D. Y. Liu and T. L. Kelly, *Nat. Photonics*, 2014, **8**, 133-138.
3. A. Younis, C.-H. Lin, X. Guan, S. Shahrokhi, C.-Y. Huang, Y. Wang, T. He, S. Singh, L. Hu, J. R. D. Retamal, J.-H. He and T. Wu, *Adv. Mater.*, 2021, **33**, 2005000.
4. K. O. Ogunniran and N. T. Martins, *IOP Conference Series: Earth and Environmental Science*, 2021, **655**, 012049.
5. D. Wang, M. Wright, N. K. Elumalai and A. Uddin, *Sol. Energy Mater. Sol. Cells*, 2016, **147**, 255-275.
6. S. Ruan, M.-A. Surmiak, Y. Ruan, D. P. McMeekin, H. Ebendorff-Heidepriem, Y.-B. Cheng, J. Lu and C. R. McNeill, *J. Mater. Chem. C*, 2019, **7**, 9326-9334.
7. Q. Meng, Y. Chen, Y. Y. Xiao, J. Sun, X. Zhang, C. B. Han, H. Gao, Y. Zhang and H. Yan, *Journal of Materials Science: Materials in Electronics*, 2021, **32**, 12784-12792.
8. G. Y. Kim, A. Senocrate, T. Y. Yang, G. Gregori, M. Gratzel and J. Maier, *Nat. Mater.*, 2018, **17**, 445-449.
9. Y. Nakamura, N. Shibayama, K. Fujiwara, T. Koganezawa and T. Miyasaka, *ACS Mater. Lett.*, 2022, **4**, 2409-2414.
10. P. S. Mathew, G. Szabo, M. Kuno and P. V. Kamat, *ACS Energy Lett.*, DOI: 10.1021/acseenergylett.2c02026.
11. E. T. Hoke, D. J. Slotcavage, E. R. Dohner, A. R. Bowring, H. I. Karunadasa and M. D. McGehee, *Chem. Sci*, 2015, **6**, 613-617.
12. S. J. Yoon, S. Draguta, J. S. Manser, O. Sharia, W. F. Schneider, M. Kuno and P. V. Kamat, *Acs Energy Letters*, 2016, **1**, 290-296.
13. G. Rose, *Annalen der Physik*, 1839, **124**, 551-573.
14. R. M. Ormerod, *Chem. Soc. Rev.*, 2003, **32**, 17-28.
15. A. J. Jacobson, *Chem. Mater.*, 2010, **22**, 660-674.
16. L. G. Tejuca and J. L. Fierro, *Properties and applications of perovskite-type oxides*, CRC Press, 2000.
17. M. Pena and J. Fierro, *Chem. Rev.*, 2001, **101**, 1981-2018.
18. H. L. Wells, *Zeitschrift für anorganische Chemie*, 1893, **3**, 195-210.
19. D. Weber, *Zeitschrift für Naturforschung B*, 1978, **33**, 862-865.
20. A. Kojima, K. Teshima, Y. Shirai and T. Miyasaka, *J. Am. Chem. Soc.*, 2009, **131**, 6050-6051.
21. N. NREL, *Journal*, 2022.
22. W. Shockley and H. J. Queisser, *J. Appl. Phys.*, 1961, **32**, 510-519.

23. M. Yamaguchi, K.-H. Lee, K. Araki and N. Kojima, *J. Phys. D: Appl. Phys.*, 2018, **51**, 133002.
24. H. Li and W. Zhang, *Chem. Rev.*, 2020, **120**, 9835-9950.
25. Y. Cheng and L. Ding, *SusMat*, 2021, **1**, 324-344.
26. P. Wu, D. Thrithamarassery Gangadharan, M. I. Saidaminov and H. Tan, *ACS Central Science*, 2022, **9**, 14-26.
27. C. Katan, N. Mercier and J. Even, *Chem. Rev.*, 2019, **119**, 3140-3192.
28. J. Chang, S. Zhang, N. Wang, Y. Sun, Y. Wei, R. Li, C. Yi, J. Wang and W. Huang, *J. Phys. Chem.*, 2018, **9**, 881-886.
29. R. L. Hoye, J. Hidalgo, R. A. Jagt, J. P. Correa-Baena, T. Fix and J. L. MacManus-Driscoll, *Adv. Energy Mater.*, 2022, **12**, 2100499.
30. L. Polavarapu, B. Nickel, J. Feldmann and A. S. Urban, *Adv. Energy Mater.*, 2017, **7**, 1700267.
31. J. H. Noh, S. H. Im, J. H. Heo, T. N. Mandal and S. I. Seok, *Nano Lett.*, 2013, **13**, 1764-1769.
32. G. E. Eperon, S. D. Stranks, C. Menelaou, M. B. Johnston, L. M. Herz and H. J. Snaith, *Energy & Environmental Science*, 2014, **7**, 982-988.
33. G. Lanty, K. Jemli, Y. Wei, J. Leymarie, J. Even, J. S. Lauret and E. Deleporte, *J. Phys. Chem. Lett.*, 2014, **5**, 3958-3963.
34. Q. A. Akkerman, V. D'Innocenzo, S. Accornero, A. Scarpellini, A. Petrozza, M. Prato and L. Manna, *J. Am. Chem. Soc.*, 2015, **137**, 10276-10281.
35. M. C. Weidman, M. Seitz, S. D. Stranks and W. A. Tisdale, *ACS Nano*, 2016, **10**, 7830-7839.
36. F. Lehmann, A. Franz, Daniel M. Töbrens, S. Levchenko, T. Unold, A. Taubert and S. Schorr, *RSC Adv.*, 2019, **9**, 11151-11159.
37. N. Kitazawa, M. Aono and Y. Watanabe, *Mater. Chem. Phys.*, 2012, **134**, 875-880.
38. N. Kitazawa, *Jpn. J. Appl. Phys.*, 1996, **35**, 6202-6207.
39. M. G. La-Placa, D. Y. Guo, L. Gil-Escrig, F. Palazon, M. Sessolo and H. J. Bolink, *J. Mater. Chem. C*, 2020, **8**, 1902-1908.
40. D. Solis-Ibarra, I. C. Smith and H. I. Karunadasa, *Chem. Sci*, 2015, **6**, 4054-4059.
41. I. Karimata and T. Tachikawa, *Angewandte Chemie-International Edition*, 2021, **60**, 2548-2553.
42. I. Karimata and T. Tachikawa, *Angew. Chem. Int. Ed.*, 2021, **60**, 2548-2553.
43. G. Nedelcu, L. Protesescu, S. Yakunin, M. I. Bodnarchuk, M. J. Grotevent and M. V. Kovalenko, *Nano Lett.*, 2015, **15**, 5635-5640.
44. H. Jiang, S. Huang, Z. Li, T. Song, Y. Chen and H. Zhong, *The Journal of Physical Chemistry C*, 2021, DOI: 10.1021/acs.jpcc.1c00967.

45. J. Cho, J. T. DuBose, A. N. T. Le and P. V. Kamat, *ACS Mater. Lett.*, 2020, DOI: 10.1021/acsmaterialslett.0c00124.
46. R. M. Kennard, C. J. Dahlman, H. Nakayama, R. A. DeCrescent, J. A. Schuller, R. Seshadri, K. Mukherjee and M. L. Chabinye, *Acs Applied Materials & Interfaces*, 2019, **11**, 25313-25321.
47. Akriti, E. Shi, S. B. Shiring, J. Yang, C. L. Atencio-Martinez, B. Yuan, X. Hu, Y. Gao, B. P. Finkenauer, A. J. Pistone, Y. Yu, P. Liao, B. M. Savoie and L. Dou, *Nat. Nanotechnol.*, 2021, **16**, 584-591.
48. J. Mizusaki, K. Arai and K. Fueki, *Solid State Ionics*, 1983, **11**, 203-211.
49. H. J. Snaith, A. Abate, J. M. Ball, G. E. Eperon, T. Leijtens, N. K. Noel, S. D. Stranks, J. T.-W. Wang, K. Wojciechowski and W. Zhang, *J. Phys. Chem.*, 2014, **5**, 1511-1515.
50. H.-S. Kim, I.-H. Jang, N. Ahn, M. Choi, A. Guerrero, J. Bisquert and N.-G. Park, *J. Phys. Chem.*, 2015, **6**, 4633-4639.
51. E. L. Unger, E. T. Hoke, C. D. Bailie, W. H. Nguyen, A. R. Bowring, T. Heumüller, M. G. Christoforo and M. D. McGehee, *Energy & Environmental Science*, 2014, **7**, 3690-3698.
52. H.-S. Kim, I. Mora-Sero, V. Gonzalez-Pedro, F. Fabregat-Santiago, E. J. Juarez-Perez, N.-G. Park and J. Bisquert, *Nat. Commun*, 2013, **4**, 2242.
53. R. S. Sanchez, V. Gonzalez-Pedro, J.-W. Lee, N.-G. Park, Y. S. Kang, I. Mora-Sero and J. Bisquert, *J. Phys. Chem.*, 2014, **5**, 2357-2363.
54. A. Dualah, T. Moehl, N. Tétreault, J. Teuscher, P. Gao, M. K. Nazeeruddin and M. Grätzel, *ACS Nano*, 2014, **8**, 362-373.
55. T. Y. Yang, G. Gregori, N. Pellet, M. Gratzel and J. Maier, *Angew. Chem. Int. Ed. Engl.*, 2015, **54**, 7905-7910.
56. A. Senocrate, I. Moudrakovski, G. Y. Kim, T. Y. Yang, G. Gregori, M. Gratzel and J. Maier, *Angew. Chem. Int. Ed. Engl.*, 2017, **56**, 7755-7759.
57. A. Senocrate, T. Y. Yang, G. Gregori, G. Y. Kim, M. Gratzel and J. Maier, *Solid State Ionics*, 2018, **321**, 69-74.
58. C. Eames, J. M. Frost, P. R. F. Barnes, B. C. O'Regan, A. Walsh and M. S. Islam, *Nat. Commun*, 2015, **6**, 7497.
59. A. Senocrate, I. Moudrakovski, G. Y. Kim, T. Y. Yang, G. Gregori, M. Gratzel and J. Maier, *Angew. Chem. Int. Ed.*, 2017, **56**, 7755-7759.
60. G. Y. Kim, A. Senocrate, Y.-R. Wang, D. Moia and J. Maier, *Angew. Chem. Int. Ed.*, 2021, **60**, 820-826.
61. G. Meyrick and G. W. Powell, *Annu. Rev. Mater. Sci.*, 1973, **3**, 327-362.
62. T. Mullin, *Science*, 2002, **295**, 1851-1851.
63. L. M. Robeson, *A Comprehensive review*, 2007, **641**.

64. W. D. Kingery, H. K. Bowen and D. R. Uhlmann, *Introduction to ceramics*, John Wiley & Sons, 1976.
65. R. A. Swalin and J. Arents, *J. Electrochem. Soc.*, 1962, **109**, 308C.
66. H. N. V. Temperley, *Changes of state: a mathematical-physical assessment*, Cleaver-Hume Press, 1956.
67. J. R. Partington, *An advanced treatise on physical chemistry*, Longmans, Green, 1951.
68. G. F. Samu, C. Janaky and P. V. Kamat, *ACS Energy Lett.*, 2017, **2**, 1860-1861.
69. X. Wang, Y. C. Ling, X. J. Lian, Y. Xin, K. B. Dhungana, F. Perez-Orive, J. Knox, Z. Z. Chen, Y. Zhou, D. Beery, K. Hanson, J. Shi, S. C. Lin and H. W. Gao, *Nat. Commun.*, 2019, **10**, 7.
70. H. C. Zhang, X. Fu, Y. Tang, H. Wang, C. F. Zhang, W. W. Yu, X. Y. Wang, Y. Zhang and M. Xiao, *Nat. Commun.*, 2019, **10**, 8.
71. W. Rehman, R. L. Milot, G. E. Eperon, C. Wehrenfennig, J. L. Boland, H. J. Snaith, M. B. Johnston and L. M. Herz, *Adv. Mater.*, 2015, **27**, 7938-7944.
72. Y.-M. Xie, B. Yu, C. Ma, X. Xu, Y. Cheng, S. Yuan, Z.-K. Wang, H. T. Chandran, C.-S. Lee, L.-S. Liao and S.-W. Tsang, *J. Mater. Chem. A*, 2018, **6**, 9081-9088.
73. C. H. Zhou, Q. D. Ou, W. J. Chen, Z. X. Gan, J. Wang, Q. L. Bao, X. M. Wen and B. H. Jia, *Advanced Optical Materials*, 2018, **6**, 9.
74. W. Rehman, D. P. McMeekin, J. B. Patel, R. L. Milot, M. B. Johnston, H. J. Snaith and L. M. Herz, *Energy & Environmental Science*, 2017, **10**, 361-369.
75. C. M. Sutter-Fella, Q. P. Ngo, N. Cefarin, K. L. Gardner, N. Tamura, C. V. Stan, W. S. Drisdell, A. Javey, F. M. Toma and I. D. Sharp, *Nano Lett.*, 2018, **18**, 3473-3480.
76. P. Gratia, G. Grancini, J. N. Audinot, X. Jeanbourquin, E. Mosconi, I. Zimmermann, D. Dowsett, Y. Lee, M. Gratzel, F. De Angelis, K. Sivula, T. Wirtz and M. K. Nazeeruddin, *J. Am. Chem. Soc.*, 2016, **138**, 15821-15824.
77. I. L. Braly, R. J. Stoddard, A. Rajagopal, A. R. Uhl, J. K. Katahara, A. K. Y. Jen and H. W. Hillhouse, *ACS Energy Lett.*, 2017, **2**, 1841-1847.
78. N. Klein-Kedem, D. Cahen and G. Hodes, *Acc. Chem. Res.*, 2016, **49**, 347-354.
79. K. Suchan, A. Merdasa, C. Rehermann, E. L. Unger and I. G. Scheblykin, *J. Lumin.*, 2020, **221**, 117073.
80. M. C. Brennan, S. Draguta, P. V. Kamat and M. Kuno, *Acs Energy Letters*, 2018, **3**, 204-213.
81. C. G. Bischak, C. L. Hetherington, H. Wu, S. Aloni, D. F. Ogletree, D. T. Limmer and N. S. Ginsberg, *Nano Lett.*, 2017, **17**, 1028-1033.
82. W. Mao, C. R. Hall, A. S. R. Chesman, C. Forsyth, Y. B. Cheng, N. W. Duffy, T. A. Smith and U. Bach, *Angew. Chem. Int. Ed. Engl.*, 2019, **58**, 2893-2898.



83. G. Y. Kim, A. Senocrate, Y. R. Wang, D. Moia and J. Maier, *Angew. Chem. Int. Ed.*, 2021, **60**, 820-826.
84. R. G. Balakrishna, S. M. Kobosko and P. V. Kamat, *ACS Energy Lett.*, 2018, **3**, 2267-2272.
85. M. C. Brennan, A. Ruth, P. V. Kamat and M. Kuno, *Trends Chem.*, 2020, **2**, 282-301.
86. D. J. Slotcavage, H. I. Karunadasa and M. D. McGehee, *Acs Energy Letters*, 2016, **1**, 1199-1205.
87. A. F. Gualdrón-Reyes, S. J. Yoon and I. Mora-Seró, *Curr Opin Electrochem*, 2018, **11**, 84-90.
88. P. V. Kamat and M. Kuno, *Acc. Chem. Res.*, 2021, **54**, 520-531.
89. R. A. Kerner, Z. J. Xu, B. W. Larson and B. P. Rand, *Joule*, 2021, **5**, 2273-2295.
90. Y. Wang, X. Quintana, J. Kim, X. Guan, L. Hu, C.-H. Lin, B. T. Jones, W. Chen, X. Wen, H. Gao and T. Wu, *Photonics Res.*, 2020, **8**, A56-A71.
91. S. Draguta, O. Sharia, S. J. Yoon, M. C. Brennan, Y. V. Morozov, J. S. Manser, P. V. Kamat, W. F. Schneider and M. Kuno, *Nat Commun*, 2017, **8**, 200.
92. K. Datta, B. T. van Gorkom, Z. H. Chen, M. J. Dyson, T. P. A. van der Pol, S. C. J. Meskers, S. X. Tao, P. A. Bobbert, M. M. Wienk and R. A. J. Janssen, *Acs Applied Energy Materials*, 2021, **4**, 6650-6658.
93. S. G. Motti, J. B. Patel, R. D. J. Oliver, H. J. Snaith, M. B. Johnston and L. M. Herz, *Nat. Commun*, 2021, **12**.
94. S. D. Stranks, G. E. Eperon, G. Grancini, C. Menelaou, M. J. P. Alcocer, T. Leijtens, L. M. Herz, A. Petrozza and H. J. Snaith, *Science*, 2013, **342**, 341-344.
95. S. Tao, I. Schmidt, G. Brocks, J. Jiang, I. Tranca, K. Meerholz and S. Olthof, *Nat. Commun*, 2019, **10**, 2560.
96. P. Nandi, Z. Li, Y. Kim, T. K. Ahn, N. G. Park and H. Shin, *ACS Energy Lett.*, 2021, **6**, 837-847.
97. C. G. Bischak, A. B. Wong, E. Lin, D. T. Limmer, P. D. Yang and N. S. Ginsberg, *J. Phys. Chem. Lett.*, 2018, **9**, 3998-4005.
98. H. X. Dang, K. Wang, M. Ghasemi, M. C. Tang, M. De Bastiani, E. Aydin, E. Dauzon, D. Barrit, J. Peng, D. M. Smilgies, S. De Wolf and A. Amassian, *Joule*, 2019, **3**, 1746-1764.
99. M. Saliba, T. Matsui, J.-Y. Seo, K. Domanski, J.-P. Correa-Baena, M. K. Nazeeruddin, S. M. Zakeeruddin, W. Tress, A. Abate and A. Hagfeldt, *Energy & environmental science*, 2016, **9**, 1989-1997.
100. S. Wieghold, A. S. Bieber, M. Mardani, T. Siegrist and L. Nienhaus, *J. Mater. Chem. C*, 2020, **8**, 9714-9723.
101. S. Svanstrom, T. J. Jacobsson, T. Sloboda, E. Giangrisostomi, R. Ovsyannikov, H. Rensmo and U. B. Cappel, *J. Mater. Chem. A*, 2018, **6**, 22134-22144.

102. S. Feldmann, S. Macpherson, S. P. Senanayak, M. Abdi-Jalebi, J. P. H. Rivett, G. Nan, G. D. Tainter, T. A. S. Doherty, K. Frohna, E. Ringe, R. H. Friend, H. Sirringhaus, M. Saliba, D. Beljonne, S. D. Stranks and F. Deschler, *Nat. Photonics*, 2020, **14**, 123-128.
103. A. F. Gualdrón-Reyes, S. J. Yoon, E. M. Barea, S. Agouram, V. Muñoz-Sanjose, A. M. Melendez, M. E. Nino-Gomez and I. Mora-Sero, *ACS Energy Lett.*, 2019, **4**, 54-62.
104. L. Hu, X. Guan, W. Chen, Y. Yao, T. Wan, C.-H. Lin, N. D. Pham, L. Yuan, X. Geng, F. Wang, C.-Y. Huang, J. Yuan, S. Cheong, R. D. Tilley, X. Wen, D. Chu, S. Huang and T. Wu, *ACS Energy Lett.*, 2021, **6**, 1649-1658.
105. M. Hu, C. Bi, Y. Yuan, Y. Bai and J. Huang, *Advanced Science*, 2016, **3**, 1500301.
106. Y. Zhou, Y.-H. Jia, H.-H. Fang, M. A. Loi, F.-Y. Xie, L. Gong, M.-C. Qin, X.-H. Lu, C.-P. Wong and N. Zhao, *Adv. Funct. Mater.*, 2018, **28**, 1803130.
107. J. T. DuBose and P. V. Kamat, *J. Am. Chem. Soc.*, 2020, **142**, 5362-5370.
108. R. A. Belisle, K. A. Bush, L. Bertoluzzi, A. Gold-Parker, M. F. Toney and M. D. McGehee, *ACS Energy Lett.*, 2018, **3**, 2694-2700.
109. G. F. Samu, Á. Balog, F. De Angelis, D. Meggiolaro, P. V. Kamat and C. Janáky, *J. Am. Chem. Soc.*, 2019, **141**, 10812-10820.
110. M. Abdi-Jalebi, Z. Andaji-Garmaroudi, S. Cacovich, C. Stavarakas, B. Philippe, J. M. Richter, M. Alsari, E. P. Booker, E. M. Hutter, A. J. Pearson, S. Lilliu, T. J. Savenije, H. Rensmo, G. Divitini, C. Ducati, R. H. Friend and S. D. Stranks, *Nature*, 2018, **555**, 497-501.
111. D. W. deQuilettes, S. Koch, S. Burke, R. K. Paranjai, A. J. Shropshire, M. E. Ziffer and D. S. Ginger, *ACS Energy Lett.*, 2016, **1**, 438-444.
112. F. Brivio, C. Caetano and A. Walsh, *J. Phys. Chem. Lett.*, 2016, **7**, 1083-1087.
113. Y.-R. Wang, A. Senocrate, M. Mladenović, A. Dučinskas, G. Y. Kim, U. Röthlisberger, J. V. Milić, D. Moia, M. Grätzel and J. Maier, *arXiv preprint arXiv:2107.01260*, 2021.
114. I. M. Pavlovec, A. Ruth, I. Gushchina, L. Ngo, S. Zhang, Z. Zhang and M. Kuno, *ACS Energy Lett.*, 2021, DOI: 10.1021/acsenergylett.1c00790, 2064-2071.
115. A. Ruth, M. C. Brennan, S. Draguta, Y. V. Morozov, M. Zhukovskiy, B. Janko, P. Zapol and M. Kuno, *ACS Energy Lett.*, 2018, **3**, 2321-2328.
116. S. J. Yoon, M. Kuno and P. V. Kamat, *ACS Energy Lett.*, 2017, **2**, 1507-1514.
117. T. Elmelund, B. Seger, M. Kuno and P. V. Kamat, *ACS Energy Lett.*, 2020, **5**, 56-63.
118. D. T. Limmer and N. S. Ginsberg, *J. Chem. Phys.*, 2020, **152**, 11.
119. W. Mao, C. R. Hall, A. S. R. Chesman, C. Forsyth, Y.-B. Cheng, N. W. Duffy, T. A. Smith and U. Bach, *Angew. Chem. Int. Ed.*, 2019, **58**, 2893-2898.
120. W. Mao, C. R. Hall, S. Bernardi, Y. B. Cheng, A. Widmer-Cooper, T. A. Smith and U. Bach, *Nat. Mater.*, 2020, DOI: 10.1038/s41563-020-00826-y, 55-61.
121. Z. Chen, G. Brocks, S. Tao and P. A. Bobbert, *Nat. Commun*, 2021, **12**, 2687.
122. Z. Chen, G. Brocks, S. Tao and P. A. Bobbert, *Phys. Rev. B*, 2022, **106**, 134110.

123. Z. Chen, H. Xue, G. Brocks, P. A. Bobbert and S. Tao, *ACS Energy Lett.*, 2023, DOI: 10.1021/acseenergylett.2c02463, 943-949.
124. A. J. Knight, J. B. Patel, H. J. Snaith, M. B. Johnston and L. M. Herz, *Adv. Energy Mater.*, 2020, **10**, 11.
125. P. Nandi, C. Giri, D. Swain, U. Manju, S. D. Mahanti and D. Topwal, *Acs Applied Energy Materials*, 2018, **1**, 3807-3814.
126. A. Senocrate, I. Moudrakovski and J. Maier, *Phys. Chem. Chem. Phys.*, 2018, **20**, 20043-20055.
127. E. A. Guggenheim, *Mixtures: the theory of the equilibrium properties of some simple classes of mixtures, solutions and alloys*, Clarendon Press, 1952.
128. T. Nishizawa, I. Ohnuma and K. Ishida, *JPE*, 2001, **22**, 269.
129. J.-H. Im, C.-R. Lee, J.-W. Lee, S.-W. Park and N.-G. Park, *Nanoscale*, 2011, **3**, 4088-4093.
130. Y. Li, J. V. Milic, A. Ummadisingu, J. Y. Seo, J. H. Im, H. S. Kim, Y. Liu, M. I. Dar, S. M. Zakeeruddin, P. Wang, A. Hagfeldt and M. Gratzel, *Nano Lett.*, 2019, **19**, 150-157.
131. R. E. Honig, *Vapor pressure data for the more common elements*, David Sarnoff Research Center, 1957.
132. C. Wagner, *Zeitschrift für Elektrochemie, Berichte der Bunsengesellschaft für physikalische Chemie*, 1956, **60**, 4-7.
133. J. Maier, *Journal of the American Ceramic Society*, 1993, **76**, 1212-1217.
134. J. Maier, *Physical Chemistry of Ionic Materials: Ions and Electrons in Solids*, Wiley, 2023.
135. K. Kiukkola and C. Wagner, *J. Electrochem. Soc.*, 1957, **104**, 308.
136. D. Moia, M. Jung, Y.-R. Wang and J. Maier, *Phys. Chem. Chem. Phys.*, 2023, **25**, 13335-13350.
137. J. Maier and G. Schwitzgebel, *Mater. Res. Bull.*, 1983, **18**, 601-608.
138. J. JAIER, *ChemInform*, 1995, **26**.
139. A. Senocrate, G. Y. Kim, M. Gratzel and J. Maier, *ACS Energy Lett.*, 2019, **4**, 2859-2870.
140. D. Moia and J. Maier, *ACS Energy Lett.*, 2021, **6**, 1566-1576.
141. A. Dučinskas, G. Y. Kim, D. Moia, A. Senocrate, Y.-R. Wang, M. A. Hope, A. Mishra, D. J. Kubicki, M. Siczek, W. Bury, T. Schneeberger, L. Emsley, J. V. Milić, J. Maier and M. Grätzel, *ACS Energy Lett.*, 2021, **6**, 337-344.
142. L. R. Chen, H. Wang and Y. C. Shao, *Chinese Physics B*, 2022, **31**.
143. R. L. Z. Hoye, J. Hidalgo, R. A. Jagt, J. P. Correa-Baena, T. Fix and J. L. MacManus-Driscoll, *Adv. Energy Mater.*, 2022, **12**.

144. X. W. Guan, Z. H. Lei, X. C. Yu, C. H. Lin, J. K. Huang, C. Y. Huang, L. Hu, F. Li, A. Vinu, J. B. Yi and T. Wu, *Small*, 2022, **18**.
145. N. K. Tailor, Yukta, R. Ranjan, S. Ranjan, T. Sharma, A. Singh, A. Garg, K. S. Nalwa, R. K. Gupta and S. Satapathi, *J. Mater. Chem. A*, 2021, **9**, 21551-21575.
146. W. Ware, T. Wright, A. Davita, E. Danilov and B. Gautam, *International Journal of Photoenergy*, 2021, **2021**.
147. Y. Lin, Y. Bai, Y. Fang, Q. Wang, Y. Deng and J. Huang, *ACS Energy Lett.*, 2017, **2**, 1571-1572.
148. A. Visnapuu, *Conversion of Il-menite to Rutile by a Carbonyl Process. BuMines RI*, 1973, **7719**, 20.
149. E. M. W. Janssen and G. A. Wiegers, *Journal of the Less Common Metals*, 1978, **57**, P47-P57.
150. J. H. Kennedy, F. Chen and R. C. Miles, *J. Electrochem. Soc.*, 1973, **120**, 171.
151. A. Burawoy and C. S. Gibson, *Journal of the Chemical Society (Resumed)*, 1935, 217-218.
152. A. Visnapuu, B. C. Marek and J. W. Jensen, *Dissociation and Vaporization of Gold Chlorides and Gold Bromides*, US Department of Interior, Bureau of Mines, 1971.
153. Y. W. Woo, Y.-K. Jung, G. Y. Kim, S. Kim and A. Walsh, *Discover Materials*, 2022, **2**, 8.
154. A. Senocrate, E. Kotomin and J. Maier, *Helv. Chim. Acta*, 2020, **103**, 8.
155. X. Xiao, J. Dai, Y. J. Fang, J. J. Zhao, X. P. Zheng, S. Tang, P. N. Rudd, X. C. Zeng and J. S. Huang, *ACS Energy Lett.*, 2018, **3**, 684-688.
156. J. Cho, J. T. DuBose, A. N. T. Le and P. V. Kamat, *ACS Mater. Lett.*, 2020, **2**, 565-570.
157. A. J. Knight, J. B. Patel, H. J. Snaith, M. B. Johnston and L. M. Herz, *Adv. Energy Mater.*, 2020, **10**, 1903488.
158. A. J. Knight, A. D. Wright, J. B. Patel, D. P. McMeekin, H. J. Snaith, M. B. Johnston and L. M. Herz, *ACS Energy Lett.*, 2019, **4**, 75-84.
159. Y. Zhou, L. You, S. Wang, Z. Ku, H. Fan, D. Schmidt, A. Rusydi, L. Chang, L. Wang, P. Ren, L. Chen, G. Yuan, L. Chen and J. Wang, *Nature Communications*, 2016, **7**, 11193.
160. T.-C. Wei, H.-P. Wang, T.-Y. Li, C.-H. Lin, Y.-H. Hsieh, Y.-H. Chu and J.-H. He, *Adv. Mater.*, 2017, **29**, 1701789.
161. M. C. Gélvez-Rueda, P. Ahlawat, L. Merten, F. Jahanbakhshi, M. Mladenović, A. Hinderhofer, M. I. Dar, Y. Li, A. Dučinskas, B. Carlsen, W. Tress, A. Ummadisingu, S. M. Zakeeruddin, F. Schreiber, A. Hagfeldt, U. Rothlisberger, F. C. Grozema, J. V. Milić and M. Graetzel, *Adv. Funct. Mater.*, 2020, **30**, 2003428.

162. Y. Li, J. V. Milić, A. Ummadisingu, J.-Y. Seo, J.-H. Im, H.-S. Kim, Y. Liu, M. I. Dar, S. M. Zakeeruddin, P. Wang, A. Hagfeldt and M. Grätzel, *Nano Lett.*, 2019, **19**, 150-157.
163. A. Ummadisingu, A. Mishra, D. J. Kubicki, T. LaGrange, A. Dučinskas, M. Siczek, W. Bury, J. V. Milić, M. Grätzel and L. Emsley, *Small*, 2022, **18**, 2104287.
164. M. Baranowski and P. Plochocka, *Adv. Energy Mater.*, 2020, **10**, 1903659.
165. F. Babbe and C. M. Sutter-Fella, *Adv. Energy Mater.*, 2020, **10**, 1903587.
166. W. X. Huang, S. J. Yoon and P. Sapkota, *Acs Applied Energy Materials*, 2018, **1**, 2859-2865.
167. P. S. Mathew, J. T. DuBose, J. Cho and P. V. Kamat, *ACS Energy Lett.*, 2021, **6**, 2499-2501.
168. Y.-R. Wang, G. Y. Kim, E. Kotomin, D. Moia and J. Maier, *JPhys Energy*, 2022, **4**, 011001.
169. A. Dučinskas, 2022.
170. A. J. Knight and L. M. Herz, *Energy & Environmental Science*, 2020, **13**, 2024-2046.
171. J. Cho, P. S. Mathew, J. T. DuBose and P. V. Kamat, *Adv. Mater.*, 2021, **33**, 2105585.
172. S. Sidhik, Y. Wang, M. De Siena, R. Asadpour, A. J. Torma, T. Terlier, K. Ho, W. Li, A. B. Puthirath, X. Shuai, A. Agrawal, B. Traore, M. Jones, R. Giridharagopal, P. M. Ajayan, J. Strzalka, D. S. Ginger, C. Katan, M. A. Alam, J. Even, M. G. Kanatzidis and A. D. Mohite, *Science*, 2022, **377**, 1425-1430.
173. A. Caiazzo, A. Maufort, B. T. van Gorkom, W. H. M. Remmerswaal, J. F. Orri, J. Y. Li, J. K. Wang, W. T. M. van Gompel, K. Van Hecke, G. Kusch, R. A. Oliver, C. Ducati, L. Lutsen, M. M. Wienk, S. D. Stranks, D. Vanderzande and R. A. J. Janssen, *Acs Applied Energy Materials*, 2023, **6**, 3933-3943.
174. Q. Zhou, B. B. Liu, X. Shai, Y. L. Li, P. He, H. Yu, C. Chen, Z. X. Xu, D. Wei and J. Z. Chen, *Chem. Commun.*, 2023, **59**, 4128-4141.
175. G. Y. Kim, A. Senocrate, T.-Y. Yang, G. Gregori, M. Grätzel and J. Maier, *Nat. Mater.*, 2018, **17**, 445-449.
176. R. A. Evarestov, E. A. Kotomin, A. Senocrate, R. K. Kremer and J. Maier, *Phys. Chem. Chem. Phys.*, 2020, **22**, 3914-3920.
177. R. A. Evarestov, A. Senocrate, E. A. Kotomin and J. Maier, *Phys. Chem. Chem. Phys.*, 2019, **21**, 7841-7846.
178. A. J. Barker, A. Sadhanala, F. Deschler, M. Gandini, S. P. Senanayak, P. M. Pearce, E. Mosconi, A. J. Pearson, Y. Wu, A. R. Srimath Kandada, T. Leijtens, F. De Angelis, S. E. Dutton, A. Petrozza and R. H. Friend, *ACS Energy Lett.*, 2017, **2**, 1416-1424.
179. Y. Zhong, C. A. M. Luna, R. Hildner, C. Li and S. Huettner, *APL Mater.*, 2019, **7**, 041114.

180. D. W. deQuilettes, W. Zhang, V. M. Burlakov, D. J. Graham, T. Leijtens, A. Osherov, V. Bulović, H. J. Snaith, D. S. Ginger and S. D. Stranks, *Nat. Commun.*, 2016, **7**, 11683.
181. Y. Liu, M. Wang, A. V. Ievlev, M. Ahmadi, B. Hu and O. S. Ovchinnikova, *arXiv preprint arXiv:2107.00786*, 2021.
182. S. Meloni, G. Palermo, N. Ashari-Astani, M. Grätzel and U. Rothlisberger, *J. Mater. Chem. A*, 2016, **4**, 15997-16002.
183. R. A. Kerner, Z. Xu, B. W. Larson and B. P. Rand, *Joule*, 2021, **5**, 2273-2295.
184. B. Philippe, T. J. Jacobsson, J.-P. Correa-Baena, N. K. Jena, A. Banerjee, S. Chakraborty, U. B. Cappel, R. Ahuja, A. Hagfeldt, M. Odellius and H. Rensmo, *J. Phys. Chem. C*, 2017, **121**, 26655-26666.
185. L. Kantorovich, A. Stashans, E. Kotomin and P. W. M. Jacobs, *Int. J. Quantum Chem.*, 1994, **52**, 1177-1198.
186. A. J. Knight, J. Borchert, R. D. Oliver, J. B. Patel, P. G. Radaelli, H. J. Snaith, M. B. Johnston and L. M. Herz, *ACS Energy Lett.*, 2021, **6**, 799-808.
187. D. W. Ferdani, S. R. Pering, D. Ghosh, P. Kubiak, A. B. Walker, S. E. Lewis, A. L. Johnson, P. J. Baker, M. S. Islam and P. J. Cameron, *Energy & Environmental Science*, 2019, **12**, 2264-2272.
188. A. M. Stoneham, *Theory of defects in solids: electronic structure of defects in insulators and semiconductors*, Oxford University Press, 2001.
189. Y.-R. Wang, M. Mladenović, U. Rothlisberger, D. Moia and J. Maier, 2024.
190. M. Wagemaker, D. P. Singh, W. J. H. Borghols, U. Lafont, L. Haverkate, V. K. Peterson and F. M. Mulder, *J. Am. Chem. Soc.*, 2011, **133**, 10222-10228.
191. C. B. Zhu, X. K. Mu, J. Popovic, K. Weichert, P. A. van Aken, Y. Yu and J. Maier, *Nano Lett.*, 2014, **14**, 5342-5349.
192. O. Delmer, P. Balaya, L. Kienle and J. Maier, *Adv. Mater.*, 2008, **20**, 501-+.
193. J. Jamnik and J. Maier, *Phys. Chem. Chem. Phys.*, 2003, **5**, 5215-5220.
194. Y. Yamada, T. Yamada, L. Q. Phuong, N. Maruyama, H. Nishimura, A. Wakamiya, Y. Murata and Y. Kanemitsu, *J. Am. Chem. Soc.*, 2015, **137**, 10456-10459.
195. C. A. López, M. C. Alvarez-Galván, M. V. Martínez-Huerta, F. Fauth and J. A. Alonso, *CrystEngComm*, 2020, **22**, 767-775.
196. G. S. Rohrer, *J. Mater. Sci.*, 2011, **46**, 5881-5895.
197. M. Lai, A. Obliger, D. Lu, C. S. Kley, C. G. Bischak, Q. Kong, T. Lei, L. Dou, N. S. Ginsberg and D. T. Limmer, *Proc. Natl. Acad. Sci.*, 2018, **115**, 11929-11934.
198. B. Chen, T. Li, Q. Dong, E. Mosconi, J. Song, Z. Chen, Y. Deng, Y. Liu, S. Ducharme, A. Gruverman, F. D. Angelis and J. Huang, *Nat. Mater.*, 2018, **17**, 1020-1026.

199. H. Tsai, R. Asadpour, J.-C. Blancon, C. C. Stoumpos, O. Durand, J. W. Strzalka, B. Chen, R. Verduzco, P. M. Ajayan, S. Tretiak, J. Even, M. A. Alam, M. G. Kanatzidis, W. Nie and A. D. Mohite, *Science*, 2018, **360**, 67-70.
200. B. Cao, S. Zeng, X. Lv, W. Gao, Y. Wang, G. Yuan and J.-M. Liu, *ACS Appl. Mater. Interfaces*, 2021, **13**, 32263-32269.
201. H. Qiu and J. M. Mativetsky, *Nanoscale*, 2021, **13**, 746-752.
202. L. S. Darken, R. W. Gurry and M. B. Bever, *Physical chemistry of metals*, McGraw-Hill, 1953.
203. J. Eshelby, *New York*, 1956, 79.
204. S. Ryu, J. H. Noh, N. J. Jeon, Y. Chan Kim, W. S. Yang, J. Seo and S. I. Seok, *Energy & Environmental Science*, 2014, **7**, 2614-2618.
205. D. Meggiolaro, S. G. Motti, E. Mosconi, A. J. Barker, J. Ball, C. Andrea Riccardo Perini, F. Deschler, A. Petrozza and F. De Angelis, *Energy & Environmental Science*, 2018, **11**, 702-713.
206. L. A. Frolova, S. Y. Luchkin, Y. Lekina, L. G. Gutsev, S. A. Tsarev, I. S. Zhidkov, E. Z. Kurmaev, Z. X. Shen, K. J. Stevenson, S. M. Aldoshin and P. A. Troshin, *Adv. Energy Mater.*, 2021, **11**.
207. S. Svanström, T. J. Jacobsson, T. Sloboda, E. Giangrisostomi, R. Ovsyannikov, H. Rensmo and U. B. Cappel, *J. Mater. Chem. A*, 2018, **6**, 22134-22144.
208. J. Hu, R. A. Kerner, I. Pelczer, B. P. Rand and J. Schwartz, *ACS Energy Lett.*, 2021, **6**, 2262-2267.
209. D. W. de Quilettes, S. M. Vorpahl, S. D. Stranks, H. Nagaoka, G. E. Eperon, M. E. Ziffer, H. J. Snaith and D. S. Ginger, *Science*, 2015, **348**, 683-686.
210. X. Yang, Y. Fu, R. Su, Y. Zheng, Y. Zhang, W. Yang, M. Yu, P. Chen, Y. Wang, J. Wu, D. Luo, Y. Tu, L. Zhao, Q. Gong and R. Zhu, *Adv. Mater.*, 2020, **32**, 2002585.
211. T. Chen, W.-L. Chen, B. J. Foley, J. Lee, J. P. C. Ruff, J. Y. P. Ko, C. M. Brown, L. W. Harriger, D. Zhang, C. Park, M. Yoon, Y.-M. Chang, J. J. Choi and S.-H. Lee, *Proc. Natl. Acad. Sci.*, 2017, **114**, 7519-7524.
212. Y. Mastrikov, N. Chuklina, M. Sokolov, A. Popov, D. Gryaznov, E. A. Kotomin and J. Maier, *J. Mater. Chem. C*, 2021, DOI: 10.1039/D1TC01731D.





## Ya-Ru Wang

Heisenbergstraße 1, 70569, Stuttgart, Germany | Ya-Ru\_Wang@outlook.com

---

### EDUCATION

Max Planck Institute for Solid State Research, Stuttgart, Germany

Ph.D. in Chemistry

Department of Physical chemistry of Solid

Advisor: Prof. Joachim Maier

Thesis: Defect Chemistry and Photo-Ionic Effects in Iodide and Bromide Perovskites

February 2019 – July 2023

East China University of Science and Technology, Shanghai, China.

M. Sc. in Materials Science and Engineering

The laboratory of Advanced Energy Storage Materials

Advisor: Prof. Shiyu Guan

Thesis: Molecular Structure Design and Electrochemical Performance of Aromatic Imide for Lithium Ion Battery

September 2015-June 2018

Taiyuan University of Technology, Taiyuan, China.

B. S. in Chemical Engineering

The laboratory of New Energy Materials and Devices

Thesis: Preparation and Characterization of Graphene / Iron Ferrocyanide nanocomposites

September 2011-June 2015

### PUBLICATIONS

1. **Wang, Y.-R.**; Senocrate, A.; Mladenović, M.; Dučinskas, A.; Kim, G. Y.; Rothlisberger, U.; Milić, J. V.; Moia, D.\*; Grätzel, M.; Maier, J.\*, Photo De-Mixing in Dion-Jacobson 2D Mixed Halide Perovskites. *Adv. Energy Mater.* 2022, 12(26), 2200768.
2. **Wang, Y.-R.**; Kim, G. Y.; Kotomin, E.; Moia\*, D.; Maier, J.\*, Photo de-mixing in mixed halide perovskites: the roles of ions and electrons. *JPhys Energy* 2022, 4 (1), 011001.
3. Dučinskas, A.; Kim, G. Y.; Moia, D.; Senocrate, A.; **Wang, Y.-R.**; Hope, M. A.; Mishra, A.; Kubicki, D. J.; Siczek, M.; Bury, W.; Schneeberger, T.; Emsley, L.; Milić, J. V.\*; Maier\*, J.; Grätzel, M.\*, Unravelling the Behavior of Dion–Jacobson Layered Hybrid Perovskites in Humid Environments. *ACS Energy Lett.* 2021, 6 (2), 337-344.
4. Kim, G. Y.; Senocrate, A.; **Wang, Y.-R.**; Moia, D.; Maier, J.\*, Photo-Effect on Ion Transport in Mixed Cation and Halide Perovskites and Implications for Photo-Demixing\*\*. *Angew. Chem. Int. Ed.* 2021, 60 (2), 820-826.
5. Moia, D.\*; Jung, M.; **Wang, Y.-R.**; Maier, J., Ionic and electronic polarization effects in horizontal hybrid perovskite device structures close to equilibrium. *Phys. Chem. Chem. Phys.*, 2023, 25, 13335-13350.

6. Yan, X.<sup>1</sup>; **Wang, Y.-R.**<sup>1</sup>; Yu, T.; Chen, H.; Zhao, Z.; Guan, S.\*; Polyimide binder by combining with polyimide separator for enhancing the electrochemical performance of lithium ion batteries. *Electrochim. Acta* 2016, 216, 1-7.
7. **Wang, Y.-R.**; Liu, Z.; Liu, H.; Liu, H.; Li, B.; Guan, S.\*; A Novel High-Capacity Anode Material Derived from Aromatic Imides for Lithium-Ion Batteries. *Small* **2018**, 14 (17), 1704094.
8. Liu, H.<sup>1</sup>; **Wang, Y.-R.**<sup>1</sup>; Liu, H.; Sun, Y.; Guan, S.\*; Homology and isomerism effect of aromatic imides as organic anode materials of lithium-ion batteries. *J. Electroanal. Chem.* 2019, 848, 113289.

#### **PATENTS**

1. Guan, S; Yan, X, **Wang, Y.-R.**, Zhao Z., Polyimide, lithium ion battery, preparation method and application of lithium ion battery. P. CN201610289109.0
2. Guan, S.; **Wang, Y.-R.**, Lin S., Negative electrode material for lithium ion batteries and preparation method. P. CN110277558B

#### Notes:

<sup>1</sup>Two authors contributed equally

\*Correspondence author